

**Faculty of Engineering and Science**

**Integrated Petrography, Geochemistry and Petrophysical Characteristics of  
Miri Formation, Sarawak, Malaysia**

**Abdulmajid Muhammad Ali  
0000-0002-8103-9059**

**This thesis is presented for the Degree of  
Master of Philosophy (Geology)  
of  
Curtin University**

**January 2022**

# Declaration

To the best of my knowledge and belief, this thesis contains no material previously published by any other person except where due acknowledgment has been made.

This thesis contains no material which has been accepted for the award of any other degree or diploma in any university.

Signature:.....

Date: 31/01/2022

## **Acknowledgement**

First and foremost, I would like to give my deepest appreciation to my mentor and principal supervisor, Dr. R. Nagarajan for his patience, guidance, encouragement, moral support, constant inspiration and affection through the course of my research. He motivated me to finish my thesis and push me to achieve more than what I can ever imagined. I thank him for the financial support from his Curtin Sarawak Research Incentive fund towards, bulk rock geochemistry, SEM analysis. I thank him for spending so much of his time guiding me in writing my thesis and for being there for me anytime even after working hours to consult him.

I would like to express my deepest appreciation and gratitude to my associate supervisors Dr. Numair Siddiqui, and Dr. Joel Ben-Awuah. They have shown unceasing patience, guidance, encouragement, motivation, moral support, and constant inspiration throughout my studies. I thank them for their immense knowledge, alongside insightful comments and critical reviews of my studies. Their continuous support has led and enlightened me in all the time of research and writing of this thesis and publications, especially during the challenging moments. I would like to extend sincere gratitude to the thesis chair Dr. AjaOgboo Chikere for the encouragement, support and help he provided during my study period.

I would like to express my sincere appreciation to Mr. Rick Carter for his immense contribution and for proofreading my whole thesis. I would also like to thank my fellow friends and university colleagues who have been supportive and encouraging throughout all times of research and thesis writing, also for all the good times working together before deadlines and all the fun we had. I would like to thank the Dean, Faculty of Engineering and Science, and The Director, Graduate School, Curtin University for the partial tuition fee waiver support during my research. Many thanks to our lab staff members, Ms. Marilyn and Ms. Rassti for their support in ensuring that the storage and facilities are well maintained throughout my research. Also, I would thank former Applied Geology undergraduate students for helping during thin sections preparations.

I am extremely thankful to my family for their continuous motivation, support and love throughout my life which were the backbone to overcome the various hurdles during my studies.

Finally, I am indebted to God for giving me the strength and peace amidst rains and storms, to complete the journey and finish this thesis.

# Abbreviations

CBS- Circular Backscatter Detector  
CIA – Chemical Index of Alteration  
CIW- Chemical index of Weathering  
GPS - Global Positioning System  
HFSE – High Field Strength Elements  
ICP – Inductively Coupled Plasma  
LILE- Large Ion Lithophile Elements  
LVD- Low Vacuum Detector  
PAAS- Post Archean Australian Shale  
PIA- Plagioclase index of Alteration  
PPL- Plane Polarized Light  
Ppm- Part per million  
QFL- Quartz-Feldspar-Lithic Fragments  
RGB- Red-Green-Blue  
REE- Rare Earth Elements  
SEM- Scanning Electron Microscope  
TTE- Transition Trace Elements  
UCC- Upper Continental Crust  
Wt%-Weight percentage  
XPL- Cross Polarized Light  
XRD- X-ray Diffractor  
XRF- X-ray Fluorescence

## Abstract

The Onshore Baram Delta is known to be a petroleum prolific basin. Miri Formation (Middle-Late Miocene) consists predominantly of shallow marine sandstone and mudstone successions with an estimated thickness of 6000 feet in Miri and Seria fields, which is mostly constrained to the coastal zone between Miri city in the Sarawak Basin and Jerudong area in Brunei. An integrated approach is proposed in this study to investigate the petrographic, geochemical and petrophysical characteristics of the Miri Formation to gain insights into the architecture and orogenic processes of the Miri Formation and its potential as a petroleum reservoir. The objectives of this research are to reconstruct the provenance, paleo weathering, and tectonic setting and assess the effects of diagenesis on the reservoir quality of sandstone using petrography, mineralogy and geochemistry. In addition, the research analyses the petrophysical characteristics of the Miri Formation and its implications for reservoir quality. To achieve the objectives of this study, four outcrops were selected, namely, the Miri Hospital, Bomba, Taman Awam and Tanjung Lobang outcrops in order to achieve the set objectives of the research. Based on the geochemical classification, the clastic rocks of the Miri Formation are classified as quartz arenite, sublitharenite, litharenite, wacke and Fe-sandstone, which are well supported by the petrographic study. Based on the grain shape and grain size analyses, the sandstone of the Miri Formation is found to be sub-angular to sub-rounded in shape with very fine to medium grain sizes. Sandstones show enrichment in  $\text{SiO}_2$  content and depletion in many elemental concentrations compared to other lithotypes and UCC and mudstones show enrichment of many elements and depletion in  $\text{SiO}_2$  content. All the lithotypes are depleted in  $\text{Na}_2\text{O}$ ,  $\text{CaO}$ ,  $\text{Sr}$  and  $\text{Mo}$ , while enriched in  $\text{TiO}_2$  and  $\text{Zr}$  compared to UCC. The REE content in sandstone and sandstone interbedded mudstone are recorded lower compared to UCC and PASS while mudstone is comparable to the PAAS. Various weathering indices and weathering diagrams are used based on geochemistry, which reveals that the source area underwent moderate to intensive chemical weathering, which led the sediments to be chemically mature. Petrographically and geochemically, the sediments of the Miri Formation were derived from recycled sedimentary/metasedimentary sources and deposited in an evolving active to passive margin setting. The sediments are mainly recycled from the Rajang Group of sedimentary to Meta-sedimentary rocks and other older age rocks exposed in the source region. The geochemistry discriminant diagram and REE pattern suggest the source rocks of felsic to intermediate rocks. The provenance model revealed that the

Miri Formation sediments were associated with the mixing of sediments derived from granitoids combined with a mixture of sedimentary to meta-sedimentary rocks and felsic volcanic rocks. Based on the mixing model, the Miri Formation REE pattern was comparable to a mixture of source rocks composition of granite, TTG and Kelalan Formation (Paleocene to Eocene) in the ratio of 15:30:55. Based on the various analyses, the sediments of the Miri Formation are derived from the Rajang Group of Formations which have undergone moderate weathering and tectonic activities. The diagenetic influences on the reservoir quality of the Miri Formation are studied through an integrated approach. Based on the petrophysical analysis, the reservoir rocks are divided into four quality classes namely; Class numbers I-IV; Class I (high), II (moderate), III (low) and (IV) very low-quality reservoir rocks. Factors controlling the different quality classes were confirmed through petrography, SEM, XRD and bulk geochemistry. Diagenetic events such as grain coating chlorites preserve the pore throats yielding a Class I high reservoir quality rock, while the reservoir quality is negatively influenced by diagenetic events including compaction, pore-blocking diagenetic minerals, calcite cement, iron oxide cement and bioturbation.

**Keywords:** Weathering, Provenance, Recycled, Passive margin, Active continental margin, reservoir quality, diagenesis

# Table of Contents

<b>1</b>	<b>CHAPTER 1</b>	<b>INTRODUCTION.....</b>	<b>1</b>
1.1	Background.....		1
1.2	Problem Statement.....		3
1.3	Aim and Objectives.....		4
1.4	Significance.....		4
1.5	Regional Geology.....		5
1.6	General Section of the Study Area.....		7
1.7	Outline of the Thesis.....		8
<b>2</b>	<b>CHAPTER 2</b>	<b>LITERATURE REVIEW.....</b>	<b>9</b>
2.1	Introduction.....		9
2.2	Siliciclastic Sedimentary Rocks.....		9
2.2.1	Sandstone Composition.....		9
2.2.2	Mudstone Composition.....		10
2.3	Provenance.....		12
2.4	Tectonic settings.....		14
2.5	Paleo weathering.....		16
2.6	Quartz Microtextures.....		18
2.7	Diagenesis.....		19
2.7.1	Mechanical Compaction.....		21
2.7.2	Dissolution.....		21
2.7.3	Cementation.....		22
2.7.3.1	Silica.....		22
2.7.3.2	Iron oxide.....		23

2.7.3.3	Carbonate cement.....	23
2.7.4	Clay Minerals.....	24
2.8	Porosity and Permeability.....	25
2.9	Petrography.....	27
2.9.1	Quartz.....	28
2.9.2	Feldspar.....	29
2.9.3	Rock Fragments.....	30
2.10	Bulk Rock Geochemistry.....	31
2.11	Previous work on the Miri Formation.....	33
2.12	Summary.....	37
<b>3</b>	<b>CHAPTER 3</b>	
	<b>RESEARCH METHODOLOGY.....</b>	<b>38</b>
3.1	Introduction.....	38
3.2	Field studies and Sample collection.....	40
3.2.1	Sample collection.....	41
3.3	Sample Preparation.....	41
3.3.1	Thin Section Preparation.....	42
3.3.2	SEM sample preparation.....	45
3.3.2.1	Quartz grains microtexture analysis.....	45
3.3.2.2	Coin shaped samples.....	46
3.3.3	Sample preparation for XRD and Geochemical analysis.....	47
3.3.4	Sample preparation for petrophysical analysis.....	48
3.4	Analysis.....	49
3.4.1	Thin Section Analysis.....	49
3.4.1.1	Optical Mineralogical Analysis.....	50
3.4.1.2	Grain Size and Grain shape.....	50
3.4.2	SEM Analysis.....	51
3.4.3	Mineralogy (XRD) Analysis.....	52
3.4.4	Geochemical Analysis.....	53



3.4.5	Petrophysical Analysis.....	55
3.4.5.1	Permeability.....	55
3.4.5.2	Porosity.....	56
3.4.6.	Data Interpretation.....	58
<b>4</b>	<b>CHAPTER 4 RESULTS AND DISCUSSION.....</b>	<b>61</b>
4.1	Introduction.....	61
4.2	Studied Outcrops.....	61
4.2.1	Hospital Outcrop.....	62
4.2.2	Bomba Outcrop.....	65
4.2.3	Taman Awam Outcrop.....	68
4.2.4	Tajung Lobang Outcrop.....	71
4.3	Samples Description.....	73
4.4	Petrography.....	73
4.4.1	Petrographic Classification/modal composition.....	73
4.4.1.1	Quartz.....	77
4.4.1.2	Feldspar.....	78
4.4.1.3	Lithic fragments.....	80
4.4.1.4	Other minerals.....	81
4.4.1.5	Matrix and Cement.....	83
4.4.2	Grain size and grain shape analysis.....	84
4.4.3	Quartz grain Microtexture analysis.....	87
4.4.3.1	Mechanical Origin.....	89
4.4.3.2	Mechanical/Chemical Origin.....	91
4.4.3.3	Chemical Origin.....	93
4.4.4	Diagenetic features.....	95
4.4.4.1	Compaction.....	95
4.4.4.2	Cementation, clay minerals and dissolution.....	96
4.5	X-Ray Diffraction (XRD).....	100
4.6	Reservoir Properties.....	101

4.7	Geochemistry .....	104
4.7.1	Major Oxides .....	104
4.7.2	Trace Elements.....	109
4.4.2.1	TTE (Sc, V, Cr, Mn, Co, Ni, Cu and Zn).....	109
4.7.2.1	LILE (Rb, Cs, Ba, Sr and Be).....	110
4.7.2.2	HFSE (Zr, Hf, Nb, Ta, Y, Th, U, and W) .....	110
4.7.2.3	Rare Earth Elements (REEs).....	111
4.8	Discussion.....	114
4.8.1	Paleo weathering.....	114
4.8.2	Sediment Sorting and Recycling.....	119
4.8.3	Source-rock Composition .....	123
4.8.4	The possible provenance area .....	129
4.8.5	Tectonic setting.....	133
4.8.6	Influential parameter on the Miri Formation reservoir properties. ....	137
4.8.6.1	Textural influence on the reservoir properties. ....	137
4.8.6.2	Diagenetic influences on reservoir quality. ....	140
<b>5</b>	<b>CHAPTER 5 CONCLUSION AND FUTURE RECOMMENDATIONS.....</b>	<b>144</b>
5.1	Introduction.....	144
5.2	Conclusion .....	144
5.3	Future Recommendations .....	146
<b>6</b>	<b>References.....</b>	<b>147</b>
	<b>Appendix 1.0.....</b>	<b>164</b>

# List of Figures

Figure 1.1. A. Structural provinces of Sarawak Basin, B. Generalized Stratigraphy framework for Onshore Northwest Sarawak, including the upper and lower Miri Formation (i.e L= Late, E= Early, M= Middle, and I, II, III, IV, V represent the sedimentary cycle boundaries) (Siddiqui et al., 2017).  
 ..... 6

Figure 1.2 Geology map of the northern Sarawak which shows the present study area (after Liechti et al., 1960). Adapted from (Nagarajan et al., 2015) ..... 7

Figure 2.1. Provenance discriminant diagrams; A- Discriminant function diagram using major elements after Roser and Korsch (1988); The discriminant functions are: discriminant function 1 =  $(-1.773 \times \text{TiO}_2) + (0.607 \times \text{Al}_2\text{O}_3) + (0.760 \times \text{Fe}_2\text{O}_3) + (-1.500 \times \text{MgO}) + (0.616 \times \text{CaO}) + (0.509 \times \text{Na}_2\text{O}) + (-1.224 \times \text{K}_2\text{O}) + (-9.090)$ ; discriminant function 2 =  $(0.445 \times \text{TiO}_2) + (0.070 \times \text{Al}_2\text{O}_3) + (-0.250 \times \text{Fe}_2\text{O}_3) + (-1.142 \times \text{MgO}) + (0.438 \times \text{CaO}) + (1.475 \times \text{Na}_2\text{O}) + (1.426 \times \text{K}_2\text{O}) + (-6.861)$ . B- Scatter diagram of  $\text{TiO}_2$  vs. Zr after Hayashi et al. (1997), C- La/Th vs. Hf diagram after Floyd and Leveridge (1987), D- Ternary Ni-V-La\*4 diagram shows the fields of different source rocks (after Bracciali et al., 2007). ..... 14

Figure 2.2 Tectonic setting discriminant diagrams A- QFL after Dickinson (1970), B- Discriminant-function multi-dimensional diagram (Verma and Armstrong-Altrin, 2013), C-  $\text{K}_2\text{O}/\text{Na}_2\text{O}$  vs.  $\text{SiO}_2$  tectonic discrimination diagram for siliciclastic rocks of the Miri Formation (Roser and Korsch, 1986), D and E- Trace elements discriminant diagrams after Bhatia and Crook (1986), F- Discrimination diagram based on major oxides and trace elements after Verma and Armstrong-Altrin (2016). ..... 16

Figure 2.3 Different stages of diagenesis and the links between various diagenetic realms (adapted from Worden and Burley, 2003). ..... 20

Figure 3.1 Flowchart of the methods used to achieve the objectives in the study. .... 39

Figure 3.2 Selected outcrops for the present study within the Miri Formation (Modified from Wannier et al., 2011). ..... 40

Figure 3.3 Images of A. Lapidary trim saw, B. Hot plate, C. Hillquist thin section grinder, D. Vacuum pot and E. Ingram ward thin section machine. ....	44
Figure 3.4 Images of A. Hydrochloric acid 1M, B. 1:1 solution with sample soaked for 24hrs, C. Examining quartz grains under the binocular microscope.....	46
Figure 3.5 A. Illustration of cone and quartering technique (Adapted from Pitard, 1993), B. Agate mortar.....	48
Figure 3.6 Optical microscope equipped with digital imaging software (Nikon NIS Element)...	49
Figure 3.7 Thermo scientific quattro s located in Curtin BioValley Pilot Plant.....	52
Figure 3.8 TKA-290 gas permeameter located in petrophysics laboratory, Curtin University Malaysia.....	56
Figure 3.9 TPI-219 helium porosimeter available at Petrophysics laboratory, Curtin University Malaysia.....	57
Figure 4.1 Image of A-Hospital outcrop, the red bar represents the stratigraphic log section, B- stratigraphic log section showing the location of samples collected, C- Legend for sample analysis. ....	63
Figure 4.2 Stratigraphic log of the Hospital outcrop, showing the details of the four sedimentary units (I to IV) with description and facies photos.....	64
Figure 4.3 Image of A. The Bomba outcrop mainly consists of thick sandstone beds and thin mudstone beds, the red bar represents the stratigraphic log section. B. stratigraphic log section showing the location of samples collected.....	66
Figure 4.4 Stratigraphic log of the Bomba outcrop, showing the details of the four sedimentary units (I to IV) with description and facies photos.....	67
Figure 4.5 Image of A.Taman Awam outcrop, Images are stacked from bottom to top bed, length of the outcrop is about 100m with a thickness of 22m. B. stratigraphic log section showing the location of samples collected.....	69

Figure 4.6 Stratigraphic log of the Taman Awam outcrop, showing the details of the five sedimentary units (I to V) with description and facies photos.....	70
Figure 4.7. Image of The Tanjung Lobang outcrop (a cross-laminated and bioturbated sandstone facies) the red bar represents the stratigraphic log section. ....	71
Figure 4.8 Stratigraphic log of the Tanjung Lobang outcrop, showing the details of the three sedimentary units (I to III) with description and facies photos. ....	72
Figure 4.9 Microphotographs (in XPL) of the siliciclastic rocks of the Miri Formation, A (S22 Top), B (S24 Top), C- (S11)- Fe-rich sublitharenite, D- (S24 Bottom), E- (S26 Bottom) Quartz arenite, and F- (HO3 Top)- Sublitharenite.....	75
Figure 4.10. Microphotographs (under XPL) of the siliciclastic rocks of the Miri Formation, G- Fe-rich sublitharenite (S11), H and I- poorly sorted sublitharenite, (HO2 Bottom and HO3 Bottom respectively), J- calcite cement (B2 Top), K- organic laminated siltstone (S1 Top), and L- interbedded sandstone (S1 Bottom). ....	76
Figure 4.11 Q-F-L ternary plot: Petrographic classification of the Miri Formation sandstones (Folk, 1974). ....	77
Figure 4.12 Micro (under XPL) and SEM photographs of the siliciclastic rocks of the Miri Formation, A-Quartz with the inclusion of zircon and rutile (B4cBottom). B- (S24Bottom), C- (S24Top)- Quartz overgrowth and D- SEM image of a sub-rounded quartz grain (S22) .....	78
Figure 4.13 The Microphotographs (under XPL) show the feldspar types, A- Plagioclase feldspar (S3 Top), B –cloudy altered feldspar (S24 Top), C- Microcline (S32 Top) and D- Plagioclase feldspar (B2Top).....	79
Figure 4.14. An illustration of extinction angle (under XPL) (Sample S3 from Taman Awam outcrop) confirms their type as albite to andesine. ....	80
Figure 4.15. Common lithic fragments observed on study samples (A, B, D - under XPL; B-under PPL); A-Blue arrow metasedimentary lithic fragment, red arrow sedimentary lithic fragments (S15)-. B-blue arrow metasedimentary lithic fragment, red arrow sedimentary lithic fragments	

(S15). C- igneous lithic fragment with iron oxide around the grain boundary (S6). D- igneous lithic fragment (Ho5Top). .....	81
Figure 4.16. A. subhedral zircon grain in the sandstone (Ho6H), B. euhedral zircon grain with colour zonation in a sandstone (Ho6H), C. SEM image shows a zircon grain (Ho2Top),, D. banded mica in calcite cemented sandstone (Ho5Top), E. SEM image shows a monzonite grain and F. EDS spot analysis data of Monzonite. ....	82
Figure 4.17. A. Blue arrow shows silica cement, Red arrow shows matrix (Ho6H), B. Clay mineral matrix (Ho2Top)- silica cement C. SEM image of pore-filling clay minerals, and D. Red arrow shows Calcite cement (B2top). ....	83
Figure 4.18. Mean grain size distribution (with error bars) of the studied sandstones of the Miri Formation.....	84
Figure 4.19. Grain shape distribution (Roundness vs Sphericity) of the analysed sandstones of the Miri Formation (modified from Krumbein and Sloss, 1951). ....	85
Figure 4.20. Mechanical origin microtexture: A. Large Conchoidal fracture (S22), B. Medium conchoidal fracture (S26), C. Small conchoidal fracture (S24), D. Straight striations (S15) E. Straight striations with pits (S26), F. Curved striations (Yellow arrow) small pits (S22), G. V-shaped marks (S22), H. Closeup V-shaped marks with linear striations (S22), I. Straight steps (S15), J. Arcuate steps (S15), K. Sub-rounded grain outline (S15), L. Sub-angular grain outline (S22).....	90
Figure 4.21. A. Elongated depression (S22), B. Fracture plane (red arrow) (S22), C. Adhering particles (red arrows) (S15), D. Low relief (S15), E. High relief (S22), F. Medium relief (S24). 92	
Figure 4.22. A. Oriented dissolution etching (S15), B. Close-up of the oriented dissolution etching (S15), C. Solution pits (S15), D. Silica precipitation (S24), E. Quartz overgrowth (S22), and F. Silica precipitation (dendritic pattern) (S22). ....	94
Figure 4.23. Thin-section photography of sandstones showing A. Point contact (S33T), B. Line contact (S22T), C. Deformed mica (red arrow) and pseudomatrix (blue arrow) (Ho5T) and D. Sutured contact (HO4 T).....	95

Figure 4.24 A. A thin section shows the overgrowth within detrital quartz grain (under PPL), B. SEM image shows pore filling illite (I) pattern that resembles kaolinite (S32 T), C. Pore bridging illite (I) (S3), D. Kaolinite (K), E. Grain coating chlorite (S22 B), F. Pore filling chlorite (C) and illite (I) (Ho4 T). ..... 98

Figure 4.25 G. SEM image showing pore filling mixed layer of illite (I)-smectite (S) (S24 T), H. SEM image shows calcite and mica cement (Ho2M), I. A thin section photo shows pore-filling calcite cement (B2T; under XPL), J. Pyrite (P) within pore space (Ho1T), K&L a thin section image showing dissolution feldspar and iron oxide cement (S20; under PPL and XPL respectively). ..... 99

Figure 4.26. X-ray diffractogram of the selected samples (Sample Number: S7 and Ho5 Top), showing the main peaks of important minerals. .... 100

Figure 4.27 Porosity versus the log of permeability cross plot of the Miri Formation sandstones from all four studied outcrops. The cross plot shows four reservoir rock classes: high quality (class I), moderate quality (class II), low quality (class III) and very low quality (class IV). Class I: Medium-grained mature sandstone; low clay minerals, well to very well sorted, Avg. Illite = 0.4% (S22B, S22T, S24B, S24T, S26B and S26T); Class II: Very fine to fine-grained mature sandstone; 5-10% of clay minerals; moderately well sorted - well-sorted, Avg. Illite = 9.58% (T1B, T1T, T2B, T2T, T3T, Ho2B, Ho6H, S3,S8, S10B and S20); Class III: Very fine -fine-grained, mature sandstone; >10% of clay minerals, and moderately well sorted - well-sorted, Avg. Illite = 11.45% (T3T, B4cT, B4dT, Ho4T, S1T, S13, S14T, S29B and B4cT); Class IV: Very fine -fine-grained mature – immature sandstone 10 - 15% of clay minerals, moderately well sorted - well-sorted, calcite cement and bioturbated, Avg. Illite = 13.57% (B2T, Ho1T, Ho3M and Ho6G). ..... 103

Figure 4.28 Geochemical Classification Plot of Siliciclastic rocks of the Miri Formation using Log (Fe<sub>2</sub>O<sub>3</sub>/K<sub>2</sub>O) vs Log (SiO<sub>2</sub>/Al<sub>2</sub>O<sub>3</sub>) (Herron, 1988). ..... 109

Figure 4.29A- UCC-normalized multi-elements plot based on the average oxide/elemental composition of various lithotypes of the Miri Formation. B- UCC-normalized multi-elements plot for different lithotypes of the Miri Formation. .... 111

Figure 4.30. Chondrite normalized REE pattern for the siliciclastic rocks of the Miri Formation (A – sandstone; B. sandstone interbedded mudstone and C. mudstone) .....	113
Figure 4.31 (A) A-CN-K and (B) A-CNK-FM (after Nesbitt and Young, 1984; Nesbitt and Wilson, 1992) plots showing the weathering trend for the siliciclastic rocks of the Miri Formation.....	116
Figure 4.32. A- $M^{+}-4Si-R^{2+}$ diagram shows the changes in sediments of the Miri Formation due to the dissolution of primary components, B. $M^{+}-4Si-R^{2+}$ diagram shows the changes in sediments of the Miri Formation due to the effect of illitization, C. $M^{+}-4Si-R^{2+}$ diagram shows all sediments plot in the grey area, which represents the domain of kaolinite-illite and pyrite. D- $\Delta 4Si$ versus $R^{3+}/(R^{3+}+R^{2+}+M^{+})$ shows the majority of samples plotted in the physical mixture and few samples follow the trend of chemical weathering (after Meunier et al., 2013). .....	118
Figure 4.33 Th/Sc versus Zr/Sc diagram for the siliciclastic rocks of the Miri Formation (after McLennan et al., 1993). The concentration of zircon due to sediment sorting and recycling can be seen along with the second Trend (increasing Zr/Sc ratios).....	120
Figure 4.34 SEM images of sandstone show the presence of zircon minerals .....	120
Figure 4.35 $Al_2O_3$ -Zr-TiO <sub>2</sub> plot showing the sorting trend for the siliciclastic rocks of the Miri Formation. (after Garcia et al., 1994) .....	121
Figure 4.36. CIA versus ICV plot showing the intensity of weathering and maturity of the siliciclastic rocks of the Miri Formation (Long et al., 2012). (please refer 4.35 for the legend of the samples' symbols).....	123
Figure 4.37. A. Major oxide-based provenance discrimination plot for the siliciclastic rocks of the Miri Formation (after Roser and Korsch, 1988). B. Hf vs. La/Th bi-plot shows the major provenance fields for the siliciclastic rocks of the Miri Formation (after Floyd and Leveridge, 1987). .....	125
Figure 4.38 A- Co/Th vs. La/Sc and B- Co/Th vs. Sc/Th plots show the provenance characters of the Miri Formation studied samples. ....	129



Figure 4.39 A. Chondrite normalized REE pattern for the siliciclastic rocks of the Miri Formation compared with mixed pattern ratio of 40:10:50 (granite: TTG: Kelalan Formation). B. Chondrite normalized REE pattern for the siliciclastic rocks of the Miri Formation compared with mixed pattern ratio of 15:30:55 (granite: TTG: Kelalan Formation). C. Chondrite normalized REE pattern for the siliciclastic rocks of the Miri Formation compared with mixed pattern ratio of 50:50 (Cratonic sandstone: Kelalan Formation). ..... 132

Figure 4.40. QFL Diagram (after Dickinson, 1970) for determination of tectonic settings. Showing the majority of the sandstone samples falling in the recycled orogenic and two samples falling on the craton interior. .... 133

Figure 4.41 A- $K_2O/Na_2O$  vs.  $SiO_2$  tectonic discrimination diagram for Siliciclastic rocks of the Miri Formation (Roser and Korsch 1986). B-Discriminant-function multi-dimensional diagram (Verma and Armstrong-Altrin, 2013) showing the tectonic setting for the Miri Formation. .... 134

Figure 4.42. A-Th–Sc–Zr/10 ternary plot shows the major tectonic fields for the siliciclastic rocks of the Miri Formation. B-La–Th–Sc ternary plot showing the major tectonic area of the sediments with the possible source rocks ..... 135

Figure 4.43 Tectonic setting discrimination diagram based on major oxides and major oxides and trace elements. (A) Oxides  $DF(A-P) M = (3.0005 \times ilr1TiM) + (-2.8243 \times ilr2AlM) + (-1.0596 \times ilr3FeM) + (-0.7056 \times ilr4MnM) + (-0.3044 \times ilr5MgM) + (-0.6277 \times ilr6CaM) + (-1.1838 \times ilr7NaM) + (1.5915 \times ilr8KM) + (0.1526 \times ilr9PM) - 5.9948$ , and (B) based on trace element  $DF(A-P)MT = (3.2683 \times ilr1TiMT) + (5.3873 \times ilr2AlMT) + (1.5546 \times ilr3FeMT) + (3.2166 \times ilr4MnMT) + (4.7542 \times ilr5MgMT) + (2.0390 \times ilr6CaMT) + (4.0490 \times ilr7NaMT) + (3.1505 \times ilr8KMT) + (2.3688 \times ilr9PMT) + (2.8354 \times ilr10CrMT) + (0.9011 \times ilr11NbMT) + (1.9128 \times ilr12NiMT) + (2.9094 \times ilr13VMT) + (4.1507 \times ilr14YMT) + (3.4871 \times ilr15ZrMT) - 3.2088$  for the Miri Formation (after Verma and Armstrong-Altrin, 2016). ..... 136

Figure 4.44. A. Porosity and permeability cross plot of the Miri Formation based on grain size, B. Porosity and permeability cross plot of the Miri Formation based on sorting. .... 139

Figure 4.45 A- Cross plot shows the studied sandstones relationship of porosity Vs illite %, B- Cross plot shows the relationship of permeability Vs illite %. .... 143

Figure 7.1. SEM images of grain shape of quartz grains from the Miri Formation (SA= sub-angular, SR= sub- rounded) .....	197
Figure 7.2. SEM images of grain shape of quartz grains from the Miri Formation (SA= sub-angular, SR= sub- rounded) .....	198
Figure 7.3. SEM images showing pore throat, microfractures and illite in S1T .....	199
Figure 7.4. SEM images showing overall grains with clay minerals, (chlorite and illite) in S3	199
Figure 7.5. SEM images showing overall grains with clay minerals and pore space, chlorite and illite in S10B .....	200
Figure 7.6 SEM images showing overall grains with less clay minerals and pore space, chlorite and illite in S22B .....	200
Figure 7.7. SEM images showing overall grains with less clay minerals and pore space, grain coating chlorite, smectite and illite in S24T .....	201
Figure 7.8 SEM images showing overall grains with less clay minerals and pore space, grain coating chlorite and illite in S26T.....	201
Figure 7.9. SEM images showing overall grains with clay minerals mostly illite in S29B .....	202
Figure 7.10. SEM images showing overall grains with clay minerals and pore space, grain coating chlorite and pore-blocking illite in S32T .....	202
Figure 7.11 SEM images showing overall grains with clay minerals and pore space, grain coating chlorite, pore-blocking pyrite and illite in HO1T .....	203
Figure 7.12 SEM images showing calcite cement, pore-blocking illite and pore-blocking chlorite in HO2.....	203
Figure 7.13 SEM images showing overall grains with clay minerals and pore space, pore-blocking chlorite and illite in HO4T .....	204

Figure 7.14 SEM images showing overall grains with high clay minerals and less pore space, pore-blocking illite in HO5 .....	204
Figure 7.15 SEM images showing pore-blocking illite and chlorite in T1 T .....	205
Figure 7.16 SEM images showing overall grain with pore space, pore-blocking clay minerals in T2 T.....	205
Figure 7.17. SEM images showing overall grain with pore space, pore-blocking illite and Chlorite in T3 T.....	206
Figure 7.18. SEM images showing pore-blocking calcite and illite in B2 T.....	206
Figure 7.19. SEM images showing pore-blocking illite in B4C T .....	207
Figure 7.20 Bi-plot showing the correlation of Rb with K <sub>2</sub> O, TiO <sub>2</sub> , Al <sub>2</sub> O <sub>3</sub> , Ba, Ga, Cs. ....	220
Figure 7.21: stratigraphic log legend of the Miri Formation. ....	221

# List of Tables

Table 2.1 Porosity range and practical cutoff (Taib and Donaldson, 2015). .....	25
Table 3.1 List of oxides and elements analyzed, unit, minimum detection limit and methods. ...	54
Table 4.1 The petrographic framework of the sandstone samples from the Miri Formation. ....	74
Table 4.2. Plagioclase extinction angle for studied samples of the Miri Formation .....	79
Table 4.3. Grain size analysis with the mean, median and standard deviation of the analysed sandstones of the Miri Formation. ....	86
Table 4.4. Grain Shape analysis results show the area, maximum ferret, perimeter, roundness, shape factor and sphericity of the sandstone samples of the Miri Formation.....	87
Table 4.5. Observed microtextures, their morphological features in the quartz grains and their origin. ....	88
Table 4.6. Porosity and permeability data based on TPI- 219 Helium porosimeter and TKA-209 gas permeameter with the grain size parameters and lithology/facies.....	102
Table 4.7a The major oxides (in Wt.%) trace element concentration (in ppm) of sandstones (n=17) of the Miri Formation.....	105
Table 4.8: Statistical summary of REE values of the three lithotypes in the Miri Formation....	112
Table 4.9 The corrected composition of the Miri Formation after subtraction of illite contribution. ....	117
Table 4.10: Range of elemental ratios of siliciclastic rocks of the Miri Formation, compared with those fine fractions derived from felsic and mafic source rocks, Upper Continental Crust (UCC), and Post-Archaean Australian Shale (PAAS).....	126
Table 4.11 Range of elemental ratios of siliciclastic rocks of the Miri Formation, compared with published data from Nagarajan et al. (2017a) of the Sibuti and Lambir Formations. ....	127

Table 4.12 Range of REE of siliciclastic rocks of the Miri Formation, compared with published data from Nagarajan et al. (2017b) of the Tukai Formations.....	128
Table 4.13 Trace element abundances (ppm) of the end members used in mixing calculations.	130
Table 4.14 Comparison of end members mixing calculation of the Miri Formation with the possible source rocks. ....	131
Table 7.1 XRD results for the studied samples of the Miri Formation.....	208
Table 7.2 Geochemical parameters for tectonic setting, paleoweathering, sorting and provenance. ....	212
Table 7.3 Normalized major oxides composition of the Miri Formation samples.....	214
Table 7.4 Isometric log-transformed ratios and discriminant function (DF <sub>(A-P)M</sub> ) of the normalized major oxides of the Miri Formation samples. ....	215
Table 7.5 Normalized major (%) and trace element (ppm) of the Miri Formation samples. ....	216
Table 7.6 Product and 16Root of normalized oxides and trace elements of the Miri Formation. ....	217
Table 7.7 Isometric log-transformed ratios of the normalized major oxides (%) and trace (ppm) of the Miri Formation samples. ....	218
Table 7.8 Isometric log-transformed ratios and discriminant function (DF <sub>(A-P)MT</sub> ) of the normalized major oxides and trace elements of the Miri Formation samples. ....	219
Table 7.9 REE values of the Miri Formation studied samples. ....	222

## List of equations

<b>Equation No.</b>	<b>Description</b>	<b>Page No.</b>
3.1	Roundness RD	51
3.2	Circularity	52
3.3	Form Factor Sphericity	52
3.4	Permeability to gas	56
3.5	Gas Viscosity	56
3.6	Porosity by Grain Volume Measurement	58
3.7	Porosity by Direct Pore Volume Measurement	58
3.8	Bulk volume	58
3.9	Chemical Index of Alteration (CIA)	59
3.10	CaO* - Carbonate in silicate fraction	59
3.11	Chemical Index of Weathering (CIW)	59
3.12	Plagioclase Index of Weathering (PIA)	59
3.13	Index of Compositional Variability (ICV)	60
3.14	Eu Anomaly	60
3.15	Discriminant Function DF1	60
3.16	Discriminant Function DF1	60
3.17	Tectonic Setting discrimination based on Major Oxides	60
3.18	Tectonic Setting discrimination based on trace elements	60

# CHAPTER 1

## INTRODUCTION

### 1.1 Background

The exposed rocks in the Miri area consist of uplifted oil-rich sedimentary strata of the Miri Field and could be deemed onshore analogues for the offshore fields of the Sarawak Basin as well (Jia and Rahman, 2009; Ulfa et al., 2011; Siddique et al., 2016; Adepehin et al., 2019). The Miri Formation consists predominantly of shallow marine sandstone and mudstone successions with an estimated thickness of 6000 feet in Miri and Seria fields. The Miri Formation has been an attractive area to many researchers and explorers due to its unique Miocene sediments and sedimentary structures. The discovery of oil and gas in 1910 by Royal Dutch Shell in the onshore Baram delta (Canada hill Miri) initiated the drilling of several prospects in the Miri field. Production from the Miri field yielded approximately 80 Million barrels of oil before being abandoned in 1972, which was due to the rapid pressure loss caused by many production wells in the area (Jong et al., 2017).

Provenance study via geochemistry and petrography of the Miri Formation aims to aid the reconstruction of the source history of the sediments that comprise this Formation. Many researchers have used major oxide geochemistry of rocks to infer the provenance of sediments or sedimentary rocks using discrimination diagrams (Roser and Korsch, 1986; Bhatia and Crook, 1986; Condie, 1993; Xinlu et al., 2015; Kunming et al., 2015; Ben-Awuah et al., 2017; Nagarajan et al., 2017a&b, Nagarajan et al., 2020). The provenance of sediments can be better elucidated when multiple methods are combined, where each method is supporting each other, and thus an accurate information of the provenance area can be achieved. Many researchers have used bulk geochemistry with the combination of bulk mineralogy (Madhavaraju et al., 2017; Bessa et al., 2018; Pang et al., 2018; Chougong et al., 2021), clay mineralogy (Baldermann et al., 2020; He et al., 2020), mineralogy of heavy minerals and/or mineral chemistry (Nagarajan et al. 2017b; O'Sullivan et al., 2018; Garzanti et al., 2021), Zircon morphology and geochronology etc. (Xiong et al., 2018; Deng et al., 2019). Indeed, it is the opinion of various authors that studying provenance and tectonic setting based on the combination of major oxides and trace elements is

the most appropriate approach to study (Armstrong-Altrin et al., 2013; 2014; 2015, Nagarajan et al., 2014, 2015, 2017a, b; 2021; Paole et al. 2017).

The majority of the world's petroleum reserves are found in ancient sandstones which have good porosity and permeability (Bjørlykke and Jahren, 2010; Zou et al., 2017). When a sufficient amount of hydrocarbon can be extracted from sandstone by known technology, it is referred to as a sandstone reservoir. Sandstone reservoirs are normally composed of a matrix of stable minerals (e.g., primarily quartz, feldspar and rock fragments), together with smaller quantities of accessory minerals and saturated with fluids between the pores. Individual sand grains must be between 63 microns and 2 mm in diameter for the sandstone to be classified as sandstone. The quantity of pore volume and the nature of the interconnections between pores depend on the controlling factors related to the primary processes under which the sandstone accumulated, or they may be related to secondary changes (diagenesis) that are post-depositional. Researchers interested in the origins of sedimentary rocks are fortunate in that they can take advantage of the current conditions and processes that cause sediment to accumulate and utilise their findings to explain the origins of ancient sediments. Researchers seek to increase the quality of their work by expanding the collective scientific knowledge base about the processes and products of the many depositional and diagenetic systems that exist on our planet today by employing modern surroundings of deposition as natural laboratories.

Diagenesis is a factor that affects the reservoir quality in sandstones. Diagenesis is a process in which the original sedimentary features change as a result of physical, chemical and biological post-depositional processes (Worden and Burley, 2003). Therefore, diagenesis is an important aspect to study when analysing reservoir rocks. A detailed study of the diagenetic processes will increase our understanding of the controls on reservoir quality. However, diagenesis can also either reduce or improve reservoir rock quality (Worden and Morad, 2003; Ali et al., 2010 Baiyegunhi et al., 2020; Bukar et al., 2021). In this regard, there is still a research gap between the understanding of the Miri Formation reservoir properties and the influences that govern the quality of the reservoir rocks.

With the aim of answering the research gap, this research is taken into account the geochemical, mineralogical, petrographic and petrophysical properties of the rocks in the Miri Formation to reconstruct the provenance, paleo weathering and tectonic setting and to illustrate



the reservoir characteristics and also define how the diagenetic features, petrophysical parameters and detrital composition affect the reservoir quality.

In the sight of this, no integrated approach has been made in the Miri Formation to understand the history of the formation and the diagenetic effects on its reservoir rocks. Therefore, studying the reservoir quality of the Miri Formation using an integrated approach, such as the petrographic, bulk mineralogy, geochemical and petrophysical characteristics will provide a clearer understanding of the provenance, paleo weathering, possible tectonic setting and also how the reservoir rocks of the Miri Formation have been affected due to diagenesis.

## **1.2 Problem Statement**

Previous studies on the Miri Formation have focused on sedimentology, stratigraphy, fault evolution and facies analysis (Abieda et al., 2005; Jia and Rahman 2009; Ulfa et al., 2011; Togunwa et al., 2015; Siddiqui et al., 2017; Togunwa and Abdullah, 2017; Rahman and Tahir, 2017; Ismail and Abdul Rahman, 2017; Cheng, 2019; Van der Zee and Urai, 2005; De Rosa et al., 2018). No study is available in the current literature, which addresses the integrated petrography, geochemistry and petrophysical characteristics of the Miri Formation. However, other studies for other formations of northern Borneo do reference the Miri Formation as a potential reservoir. Even though Siddiqui et al. (2017) reported the presence of a diagenetic alteration in the Miri Formation reservoir rocks, a detailed study on diagenesis has not been yet carried out.

There has been a lack of knowledge on the integrated mineralogy, petrography, petrophysical and geochemistry aspects to address the diagenetic alterations, provenance, paleo-weathering, tectonic settings and reservoir potential by considering the lithology of the selected outcrops in the Miri Formation.

This study will use methods such as major and trace element geochemistry, X-ray diffraction spectrometry and helium/mercury porosimetry to study the mineralogical composition, geochemical composition and hydrocarbon reservoir potential of the clastic rocks of the Miri Formation. The additional knowledge from this research will enable the diagenetic history, provenance, weathering history, and reservoir potential of the Miri Formation to be determined (Khidir and Catuneanu, 2010; Descourvieres et al., 2011; Nagarajan et al., 2014; Ben-Awuah et al., 2017). This new additional information from this research is important due to the active

exploration efforts in the onshore and offshore Sarawak Basin, particularly in the Baram Delta Province. Hence, accurate characterisation and classification of facies is vital in portraying the potential reservoir characteristics and can be integrated as input in the optimisation of the stimulation of a reservoir.

### **1.3 Aim and Objectives**

The present study aims to use an integrated approach to elucidate the geochemical, sedimentological, mineralogical characteristics and petrophysical properties of the Miri Formation and their implications to provenance, paleo weathering, tectonic setting and diagenesis. Siliciclastic sediments are an important source of information to understand the diagenetic, provenance and tectonic evolution of a basin. This thesis reports an attempt to reconstruct the provenance of the Baram Delta province (Miri Formation), which is one of the prolific hydrocarbon basins from the Sarawak Basin. The provenance study is proposed through an integrated approach of petrography and geochemistry together with XRD and SEM analyses. Provenance analysis will help in reconstructing the climatic-physiographic condition as well as the source rock assemblage from where the sediments were originated.

The proposed objectives are;

1. To identify the mineralogical composition of the rocks in the Miri Formation and its implications on diagenesis.
2. To study the geochemical composition of the rocks in the Miri Formation and its implication on paleoweathering, sediment provenance and possible tectonic setting.
3. To assess the petrophysical characteristics of the rocks in the Miri Formation and its implications for reservoir quality.

### **1.4 Significance**

In order to constrain the tectonic evolution of the Sarawak Basin (Subis Limestone, Sibuti, Setap Shale, Lambir, Miri, Tukai, Seria and Liang formations), a complete study of the Tertiary sedimentary successions in the basin such as the Onshore West Baram Delta Province, Miri Formation is required. The West Baram delta is important because of its immense oil and gas potential. Recent studies on this formation have contributed a few details on facies analysis, petrophysical properties with very little geochemistry (Abieda et al., 2005; Jia and Rahman 2009;

Ulfa et al., 2011; Togunwa et al., 2015; Siddiqui et al., 2017; Tongunwa and Abdullah, 2017; Ismail and Abdul, 2017; Ismail and Abdul, 2018; Cheng, 2019). There is therefore a lack of knowledge on the integrated petrographic, geochemical and petrophysical aspects of the Miri formation. This project pursues to bridge this knowledge gap by providing a comprehensive study of the mineralogy, petrography, geochemistry and petrophysical characteristics of the Miri Formation. This new knowledge will further enhance hydrocarbon exploration success in the Sarawak Basin. The provenance, paleoclimate condition, paleoweathering, tectonic setting and also the reservoir properties of the study area will be revealed based on this study, which could enhance the understanding of the architecture and orogenic processes of the Miri Formation.

## 1.5 Regional Geology

Borneo is the world's third-largest island, and it consists of three countries: Malaysia (Sarawak and Sabah), Brunei and Indonesia (Kalimantan). The island is termed as tectonically active and has experienced major tectonic events onshore and offshore from the Miocene until today (Menier et al., 2014; Mathew et al., 2016a; Mathew et al., 2016b).

The orogenic uplift and folding of the Cretaceous to Eocene eugeosynclinal sediments initiated the formation of the Tertiary Basin of the Baram Delta Province during the Late Eocene (Rijks, 1981; Hutchison, 2005). The northwest-heading prograding West Baram Delta was formed during the Middle Miocene times. The periods of the delta were disjointed by prompt transgressions, which are signified by intervals of marine shale intervals that molded the base of the eight sedimentary cycles (Tan et al., 1999; Hutchison, 2005). Coastal-fluvio marine sands to neritic and marine shale characterized the regressive sequences of each depositional cycle northwestwards, followed by Early Miocene tectonic occurrences, an uplift and erosion processes, and these were supplemented by the sedimentation of a dense number of clastic deposits, which prograded seaward through the Neogene times. Eroded sediments, mostly sandstones, settled in the coastal plain, deltaic and coastal environmental settings. The entire sequence comprises up to 9-10 km of sedimentary deposits and the main source area is primarily from the catchment extent of the modern Baram River (Ibrahim and Light, 2012). The Tertiary succession covers the Setap Shale, Sibuti, Lambir, Miri, Tukai, Seria and Liang formations (**Fig 1.1 B**).

The study area, Miri Formation, is situated in the West Baram Delta Province (Fig 1.1 A) found in the onshore Sarawak Basin (Togunwa and Abdullah, 2017) located within the Sarawak Basin. The siliciclastic succession of the Miri Formation comprises of coarsening upwards clay-sand series.

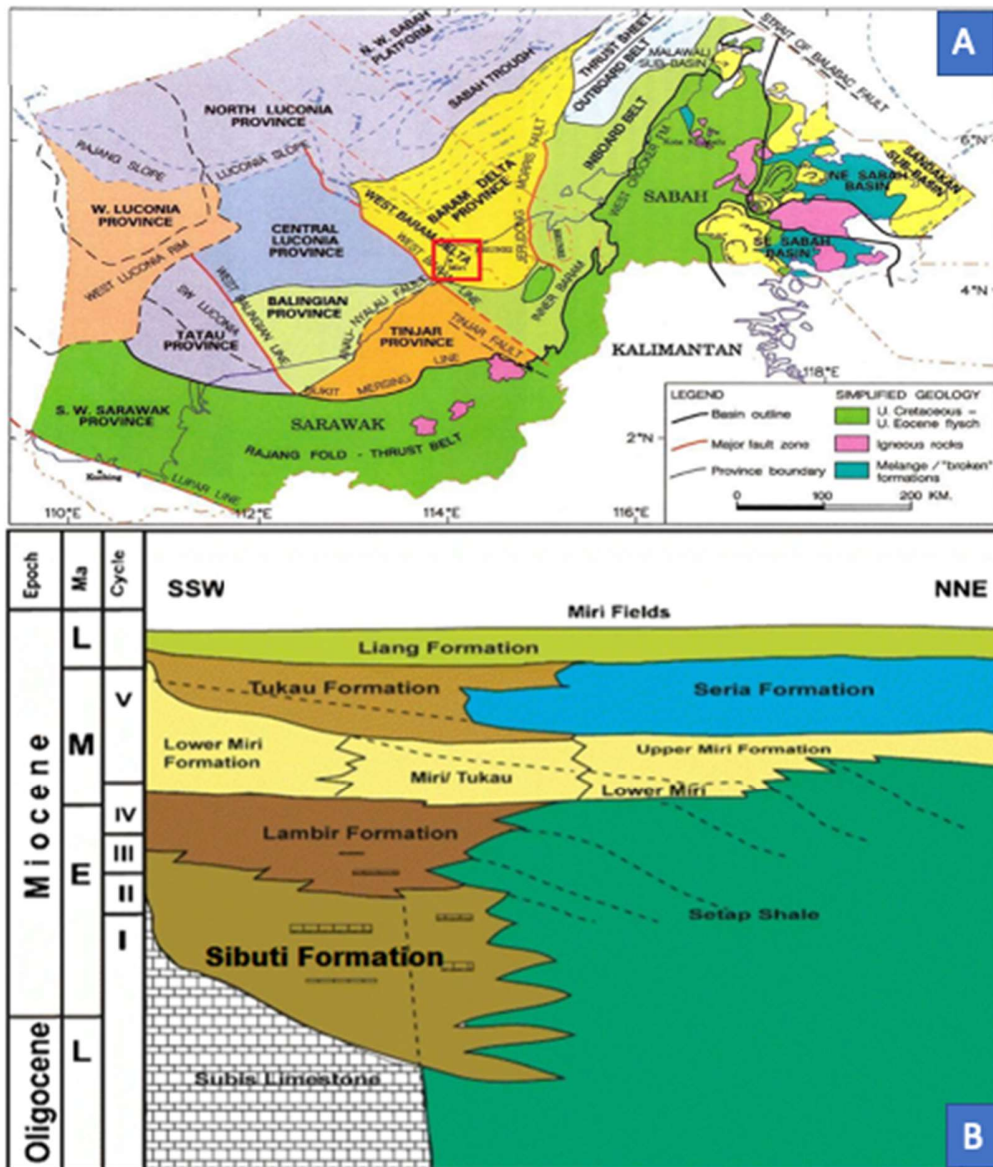
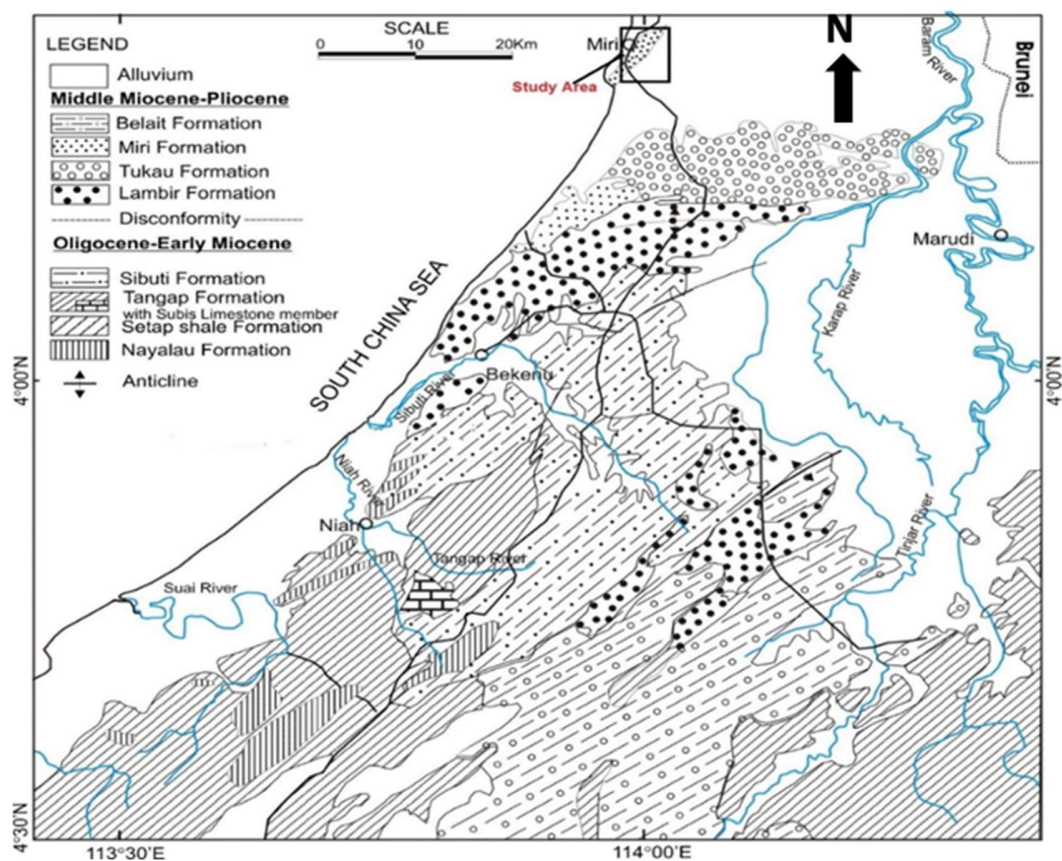


Figure 1.1. A. Structural provinces of Sarawak Basin, B. Generalized Stratigraphy framework for Onshore Northwest Sarawak, including the upper and lower Miri Formation (i.e L= Late, E= Early, M= Middle, and I, II, III, IV, V represent the sedimentary cycle boundaries) (Siddiqui et al., 2017).

## 1.6 General Section of the Study Area

The Miri Formation (Middle-Late Miocene) consists of coarsening upwards clay-sand packages that are constrained to the coastal zone between Miri city in the Sarawak Basin and Jerudong area in Brunei. The outcrops that are studied are positioned within the coastal region of Miri city. The Miri Formation is the uplifted part of the subsurface, oil-bearing sedimentary strata of the Miri oilfield perhaps resembles upper Cycle IV to Cycle V of the offshore stratigraphic elements (Tan et al., 1999; Wannier et al., 2011). Looking at the lithological variances and micropaleontology, the Miri Formation was split into the Lower Miri Formation that comprises of interbedded shale and sandstone placed on top of the Setap Shale Formation, whereas the Upper Miri Formation is described by the irregular sandstone and shale fluctuations (**Fig 1.2**) (Tan et al., 1999; Hutchison, 2005; Wannier et al., 2011).



**Figure 1.2** Geology map of the northern Sarawak which shows the present study area (after Liechti et al., 1960). Adapted from (Nagarajan et al., 2015)

## **1.7 Outline of the Thesis**

Chapter 1 Includes the introduction of the study, background, problem statement, significance of the research, regional geology of the study area and general information on the study area.

Chapter 2 Summarizes the comprehensive literature review of rock types in the study area, provenance, tectonic settings, paleoweathering, quartz microtextures, diagenesis, porosity and permeability, bulk rock geochemistry and previous studies carried out in the study area.

Chapter 3 explains all the methods used in the research, which includes fieldwork, sample collection, sample preparation and all the analyses carried out.

Chapter 4 reports all the results obtained from this study and interpretation of multiple datasets have been discussed, in detail and addressed the proposed objectives.

Chapter 5 concludes the major findings of the present research and highlighted potential future research required in the near future for the enhanced understanding of the Sarawak Basin.

# CHAPTER 2

## LITERATURE REVIEW

### 2.1 Introduction

This chapter provides a comprehensive literature review which was carried out to first identify the research gap and secondly to select the right methods used in this research by reviewing the existing works/publications for the study area. Based on this literature review, the aim of the research was to (i) identify the mineralogical composition of the Miri Formation and the implications for diagenesis, (ii) to study the geochemical composition of the formation and its implication on weathering, sediment provenance, tectonic setting and (iii) also assess the petrophysical characteristics of the reservoir rocks and their implications on the reservoir quality of the sandstones. All is made possible by interpreting the multiple datasets from mineralogy, petrography, geochemistry and petrophysical studies in an integrated approach.

### 2.2 Siliciclastic Sedimentary Rocks

Siliciclastic sedimentary rocks are non-carbonate rocks that are created from the older fragments of pre-existing rocks, such as metamorphic, igneous and sedimentary rocks, through several geological processes such as physical, chemical and biological weathering, erosion, transportation, sedimentation and lithification. Sandstone and mudstone are the most common siliciclastic sedimentary rocks. Sandstone consists of almost silicon, either as a form of quartz or other silicate minerals.

#### 2.2.1 Sandstone Composition

Sandstones are the fourth most important sedimentary rocks distributed worldwide. This rock is considered to be a significant economic resource and important oil, gas, and water reservoir (Nowrouzi et al., 2014). The composition of sandstone indicates modifications of the tectonic settings or provenance of terranes (Dickinson, 1985), hence it is a valuable group of

siliciclastic sedimentary rocks for provenance analysis. Furthermore, sandstones are considered good pointers for weathering processes and as a provenance of source area terranes (Roser and Korsch, 1986; Cullers, 2000; Getaneh, 2002; Zhiming et al., 2003; Ohta, 2004; Tijani et al., 2010; Armstrong-Altrin et al., 2013; Nowrouzi et al., 2014; Nagarajan et al., 2014; Ali et al., 2014; Galin et al., 2017, 2020). The composition of the sandstone enhances the understanding of the rock type, provenance and field characteristics of sandstones provide important information on depositional environments of the rock types (Pettijohn, 1975). So far, the affiliation between the tectonic locality and composition of sandstone has been focused primarily on the prevailing structural framework (Bhatia, 1983). Due to its rather straightforward approach (Schieber, 1992), sandstone petrography is commonly used to presume the provenance and tectonic settings (i.e. Dickinson, 1970; Hossain et al., 2010; Saminpanya et al., 2014; Malaza et al., 2016). The knowledge on provenance is obtained through extensive analyses of the sandstone compositional and textural features (Schieber, 1992).

Studies have been carried out using sandstone detrital (mineralogy and geochemistry) to conclude the provenance and tectonic settings at various stratigraphic intervals. These include Precambrian (Schieber, 1992; Osae et al., 2006; Nagarajan et al., 2007a, b; Paikaray et al., 2008; Dumoulin, 2018); Paleozoic (Cawood, 1983; Dickinson et al., 1983; Bassis et al., 2016; Li et al., 2016; Anani et al., 2018; Casas-Peña et al., 2021), Mesozoic (Ingersoll, 1983; Asiedu et al., 2000; Caja e al., 2007; Bakkiaraj et al., 2010; Armstrong-Altrin et al., 2013; Rodrigues and Goldberg, 2014; Yang et al., 2019; Hou et al., 2020; Zhang et al., 2020; Zaid, 2020; Chaudhuri et al., 2021), and Cenozoic (Jalal and Ghosh, 2012; Van Hattum et al., 2013; Nagarajan et al., 2015, 2017; Ben-Awuah et al., 2017; Ramkumar et al., 2018; Kettanah et al., 2020; Kattanah et al., 2021; Nagarajan et al., 2021). Previous researchers have used the sandstone's chemical components to link it to the sedimentary basin tectonic settings (e.g., Tawfik et al., 2017; Zaid, 2017; Nagarajan et al., 2017; Nagarajan et al., 2021).

## **2.2.2 Mudstone Composition**

Mudstone is the term applied to any rocks that consist of silt and/or clay. Mudstones are present in almost every major sedimentary deposit. Considering their quantity, there is limited



research on these types of rock compared to sandstone and carbonate rocks (Church et al, 2005). Intriguingly, details about the past depositional system and how it has evolved over the entire geological period can be expressed by the composition of mudstones.

Sandstones provide useful knowledge on tectonics and the sediments' transport record. In contrast, mudstones supplement the information obtained from sandstone evaluation by offering information about the past levels of oxygen, paleoclimates, provenance, weathering and depositional environment of the rock (Church et al, 2005; Potter et al., 2005; Bracciali et al., 2007). Under certain circumstances, mudstones may sometimes be better candidates than sandstones in terms of studying sedimentary environments (Grimes et al., 2015; Zau et al., 2020).

The use of mudstones for the analysis of provenance aims to compare if the sandstone and mudstone units originate from the same source that has experienced the same forms of transportation and other depositional environment-related matters (Potter et al., 2005). Bjorlykke (2014) stated that mudstones are generally defined by the observations from the outcrops and the composition of their organic matter, depending on the physical characteristics. Nevertheless, the most interesting insight of their clay mineralogy is that it offers information regarding their transport, deposition and compaction (Potter et al., 2005).

Reconstruction of provenance using clay mineralogy is therefore advantageous for samples, which comprise higher amounts of mud. According to Potter et al. (2005), the proportion of clay had undergone; a) chemical and mineralogical alteration by the processes of weathering and diagenesis, b) the distance travelled may have triggered the mixing of particles from various sources. The combining of the multiple types of sources collected from the content of the muds will portray the origin of a wider region in a wider time frame (Wronkiewicz and Condie, 1987; Cullers and Podkovyrov, 2000). It compares with features derived from sandstones as it represents data from additional immediate origins. It assists researchers to evaluate the provenance details of a terrigenous segment with a variety of data from two distinct rock types. The geochemistry of mudstone is the best compared to sandstone to reconstruct the provenance, paleo weathering and redox conditions (Grimes et al., 2015; Zau et al., 2020).

## 2.3 Provenance

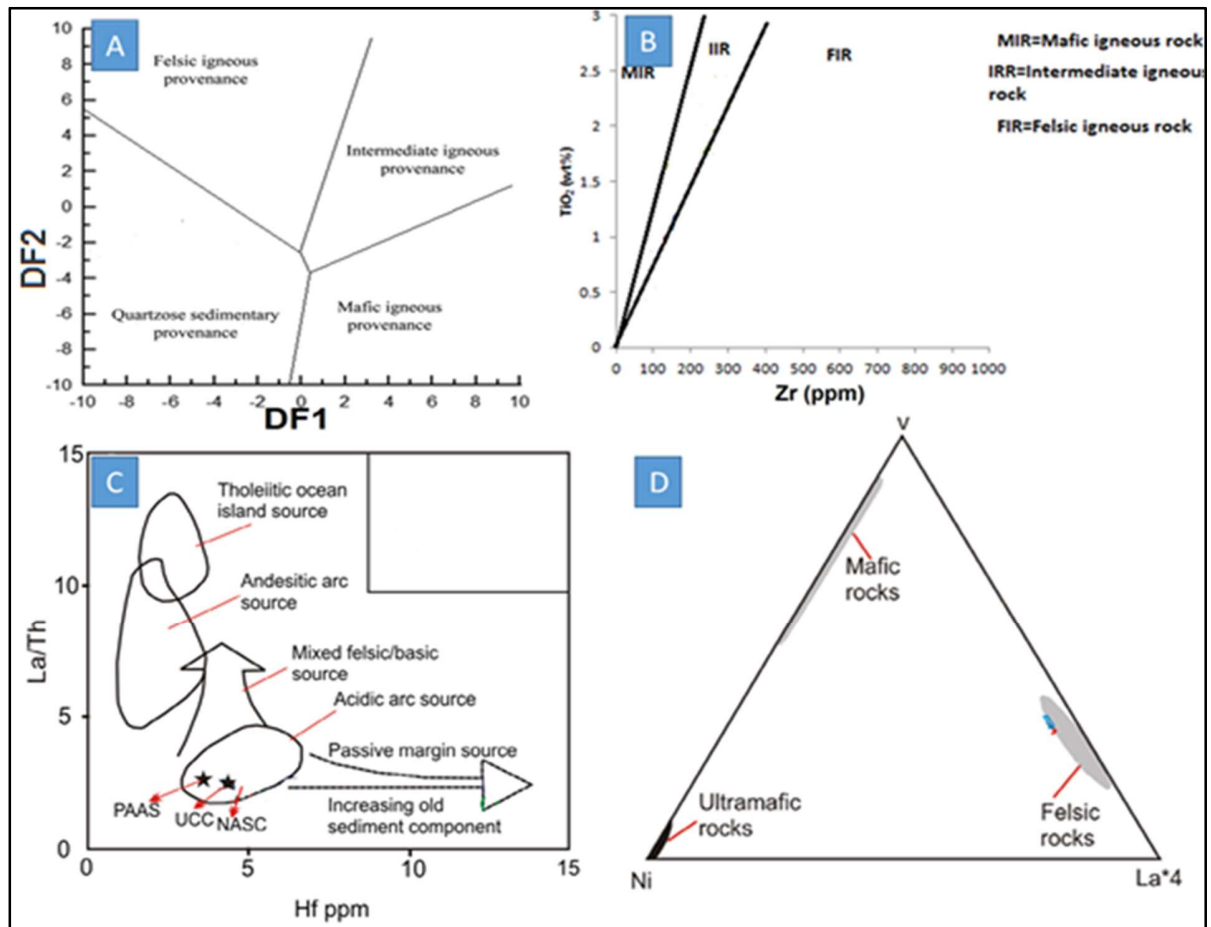
Provenance study is an important approach to understand the paleogeography of sediments and reconstruct the origin of the sediments (Weltje and von Eynatten, 2004; Garzanti et al., 2007; Mazumder, 2017). The term “provenances” originates from the Latin word “Provenire”, even though it indicates the origin or the source rock from which the sediments were generated (Cottingham, 1951). Provenance is not only focused on the source, but it also includes all aspects associated with the production of sediment and “*specific reference to the composition of the parent rocks as well as the physiography and climate of the source area*” (Weltje and Eynatten, 2004).

Before sediment deposition, sediments undergo various physical and chemical changes from the source to sink depending on transportation mechanisms and climate influences, for example, sediment abrasion, chemical weathering and, grain size and shape (Nesbitt et al., 1996; Saminpanya et al., 2014; Malaza et al., 2016; Bhattacharya et al., 2016; Li et al., 2020; Li et al., 2021). These provide researchers the ability to interpret the mechanism of sediment transportation, the climate condition, environment, diagenesis/ lithification, sediment composition and geochemistry in which the local tectonism can have a significant influence (Weltje and Eynatten, 2004). Provenance study data is essential in determining paleogeographic changes, understanding the pattern of lateral shifts in orogens, distinguishing the overburden crust, subsurface interrelationship and also guessing reservoir quality (Weltje and Eynatten, 2004; Garzanti et al., 2014; Bhattacharya et al., 2016).

The petrographic approach has been the pillar of provenance studies for many decades have been identifying minerals as small as 20 micrometres in siliciclastic rocks (sandstones; Dickinson and Suczek, 1979; Dickinson et al., 1983) and sands (Potter, 1994; Augustsson, 2021). The results of the petrographic analysis are normally plotted in the QFL triangle (Dickinson and Suczek, 1979; Pettijohn, 1975; Folk, 1980; Dickinson et al., 1983) for classifying the sandstones and to interpret the climate and tectonic conditions (Suttner and Dutta, 1986) and classify the type of sandstone (Folk, 1981; Pettijohn et al., 1987). The approach has been modified by many researchers for the past 100 years because rock fragments in sandstone defied the original description. The most common approach used by researchers is known as the Gazzi- Dickson method (Ji et al., 2019;

Mohammadi et al., 2020), it has proven to be useful and is widely used (Basu, 2017). Data collected using point counting methods can be plotted in the Dickinson diagram that identifies all easily altered minerals such as feldspar even if they are altered into clay minerals as long as they still maintain the detrital grain, outlines and twinning. Similarly, lithic fragments (L/RF) should exclude carbonate and other mono-mineralic polycrystalline grains (Augustsson, 2021).

Geochemical and mineralogical data of siliciclastic rocks are used to reassemble the provenance of the rocks (Taylor and McLennan, 1985; McLennan et al., 1993; Nagarajan et al., 2007a, b; Nagarajan et al., 2014; Ben-Awuah et al., 2017; Nagarajan et al., 2017; Armstrong-Altrin et al. 2013; Jafarzadeh and Hosseini-Barzi 2008; Akinlua et al. 2016; Zaid, 2012; Nagarajan et al., 2021; Denge and Gaiyegunhi, 2021; Kettanah et al., 2021). Siliciclastic sediments or/and rocks provide tools for provenance study to examine the evolution of sedimentary basins. Major and trace element geochemistry of siliciclastic residues is responsible for providing data regarding the source rock types, paleo weathering settings, hydraulic grain sorting and the magnitude of recycling in the tectonic enlargement of geological basins (Nesbitt and Young, 1982; Cullers, 1995; Cullers and Podkovyrov, 2000; Armstrong-Altrin et al., 2004; Armstrong-Altrin, 2015; Nagarajan et al., 2017). The proposed discrimination diagrams that are utilized by researchers is depending on the geochemical information acquired to categorize the origin of sediments or/and sedimentary rocks (**Fig 2.1**) (Roser and Korsch, 1986; Roser and Korsch 1988; Floyd and Leveridge, 1987; McLennan et al. 1993; Fralic and Kronberg, 1997; Hayashi et al., 1997; Bracciali et al., 2007).



**Figure 2.1. Provenance discriminant diagrams; A- Discriminant function diagram using major elements after Roser and Korsch (1988); The discriminant functions are: discriminant function 1 =  $(-1.773 \times \text{TiO}_2) + (0.607 \times \text{Al}_2\text{O}_3) + (0.760 \times \text{Fe}_2\text{O}_3) + (-1.500 \times \text{MgO}) + (0.616 \times \text{CaO}) + (0.509 \times \text{Na}_2\text{O}) + (-1.224 \times \text{K}_2\text{O}) + (-9.090)$ ; discriminant function 2 =  $(0.445 \times \text{TiO}_2) + (0.070 \times \text{Al}_2\text{O}_3) + (-0.250 \times \text{Fe}_2\text{O}_3) + (-1.142 \times \text{MgO}) + (0.438 \times \text{CaO}) + (1.475 \times \text{Na}_2\text{O}) + (1.426 \times \text{K}_2\text{O}) + (-6.861)$ . B- Scatter diagram of  $\text{TiO}_2$  vs.  $\text{Zr}$  after Hayashi et al. (1997), C-  $\text{La}/\text{Th}$  vs.  $\text{Hf}$  diagram after Floyd and Leveridge (1987), D- Ternary  $\text{Ni}-\text{V}-\text{La}^*4$  diagram shows the fields of different source rocks (after Bracciali et al., 2007).**

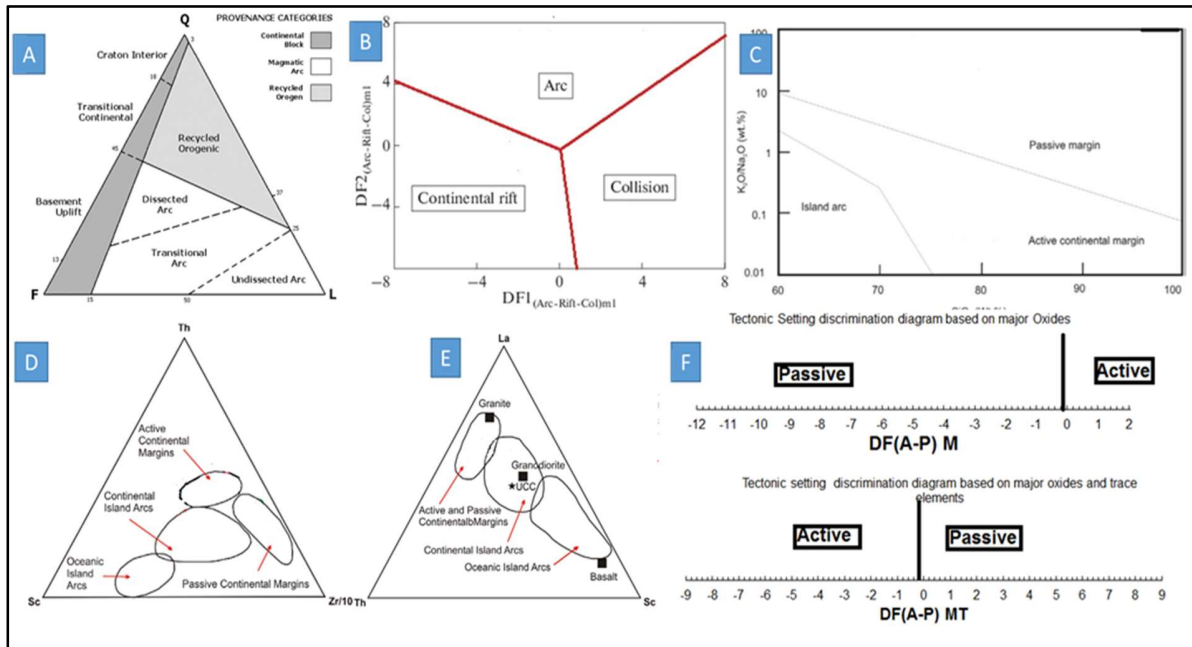
## 2.4 Tectonic settings

The geochemical composition of rocks in a sedimentary basin is governed principally by the tectonic zone of the provenance, thus it is consequently conceivable to disclose the tectonic region of the provenance and the locality of the source rocks established from the data from the geochemical composition of the deposits (Zhiming et al., 2003).

In sedimentary geochemistry, many researchers (Bhatia, 1983; Bhatia and Crook, 1986; Roser and Korsch, 1986) have proposed the tectonic discrimination diagrams which are now been extensively applied to classify the tectonic site of unknown geological basins (Jafarzadeh and Hosseini-Barzi, 2008; Dostal and Keppie, 2009; Nagarajan et al., 2014; Guadagnin et al., 2015; Zaid, 2015; Zaid et al., 2015; Xie and Chi, 2016), even though these tectonic discrimination diagrams have been reported that they do not carry out satisfactorily (Armstrong-Altrin and Verma, 2005; Weltje, 2006; Ryan and Williams, 2007; Maslov et al., 2016). Besides, few researchers (Armstrong-Altrin and Verma, 2005; Verma and Armstrong-Altrin, 2013; Armstrong-Altrin, 2015) assessed the effectiveness of these major and trace elements demonstrated by discrimination diagrams with Neogene sedimentary grains and exhibited a little accomplishment for the diagrams developed by Bhatia (1983) and Roser and Korsch (1986). Verma and Armstrong-Altrin (2013) proposed two discriminant tectonic setting diagrams as silica high and low, which can classify the three major tectonic settings (arc, collision and rift setting). The effectiveness of these diagrams was assessed by Maslov et al. (2016) based on the geochemical databases from different known tectonic settings and found that the diagrams proposed by Verma and Armstrong-Altrin (2013) show a difference in the minimum DF2 values (-8) in the diagram but the dataset has recorded the DF values  $< -8$  and up to  $-13$ , in particular for rift-related compositions. Overall these diagrams are discriminating their provenances though the samples usually over into rift and collision provenances (Maslov et al., 2016).

The most recent breakthrough done by Verma and Armstrong-Altrin (2016) in which they established two new discriminant plots regarding the multidimensional illustrations for the discrimination of active and passive margin environmental settings using isometric log-ratio makeovers of major and major-trace element applications. These two figures projected by Verma and Armstrong-Altrin (2016) were constructed depending on the isometric log-ratio and linear discrimination investigation of a wide-ranging geochemical record worldwide data reported for Neogene-Quaternary siliciclastic residues from well-known tectonic areas. The active margin region comprises the remains from arc and collision environmental settings, whereas the passive margin zone consists of deposits from the rift depositional settings. Verma and Armstrong-Altrin (2016) proved 77% - 100% exceptional presentation of these two diagrams through 11 case studies carried out using worldwide data of Quaternary to Holocene siliciclastic sedimentary deposits from

identified continental margins. They suggested that these diagrams are to be used as a supplement for effective study on the tectonic setting of ancient sedimentary geological basins (Fig.2.2).



**Figure 2.2** Tectonic setting discriminant diagrams A- QFL after Dickinson (1970), B- Discriminant-function multi-dimensional diagram (Verma and Armstrong-Altrin, 2013), C- K<sub>2</sub>O/Na<sub>2</sub>O vs. SiO<sub>2</sub> tectonic discrimination diagram for siliciclastic rocks of the Miri Formation (Roser and Korsch, 1986), D and E- Trace elements discriminant diagrams after Bhatia and Crook (1986), F- Discrimination diagram based on major oxides and trace elements after Verma and Armstrong-Altrin (2016).

## 2.5 Paleo weathering

The degree of chemical weathering is correlated with the environment, where humid and warm climates produce strong chemical weathering, while arid environments are related to poor chemical weathering (Nesbitt and Young, 1982). The magnitude of chemical weathering in sedimentary rocks is measured with the aid of the chemical index of alteration (CIA) and plagioclase index of alteration (PIA). They are dimensionless parameters from 0 to 100 and a quantitative approximation of secondary aluminous clay minerals in regard to primary feldspars grains (Nesbitt and Young, 1982).

The degree of weathering has been studied and reported by many researchers in order to understand the intensity of weathering in the source rock area by using various geochemical

weathering indicators such as the Chemical Index of Alteration (CIA), which was proposed by Nesbitt and Young (1982), the Chemical Index of Weathering (CIW) by Harnois (1988), the Plagioclase Index of Alteration (PIA) by Fedo et al. (1995), weathering index (WIP) by Parker (1970), CIX (Garzanti et al., 2014), the concentration of K<sub>2</sub>O divided by Na<sub>2</sub>O (K<sub>2</sub>O/Na<sub>2</sub>O) by Nesbitt and Young (1984) and also Lindsey (1999), Al/Na by Selvaraj and Chen (2006), K/Al ratio by Yarincik et al. (2000); and Th/U and Rb/Sr ratios by McLennan et al. (1993). These proposed approaches have been used by several researchers (Selvaraj and Chen, 2006; Armstrong-Altrin et al., 2013; Armstrong-Altrin et al., 2014; Armstrong-Altrin et al., 2015; Nagarajan et al., 2015; Ben-Awuah et al., 2017; Nagarajan et al., 2017; Nagarajan et al., 2021) to evaluate the intensity of weathering in their study regions and have been successfully addressed the intensity of weathering. Recently, Zhao and Zheng (2015) proposed some new proxies [(log(Th/Ca), log(Sc/Ca), log(Th/(Na/5+Ca) and log[Sc/(Na/5+Ca)]] for chemical weathering based on the fact that the selected elements such as Th, Sc, Ca, and Na are not amenable to changes in sedimentary provenance. Also, they tested their ability in assessing the intensity of chemical weathering using Triassic age sediments from South China. However, the applicability needs to be checked on each studied profile and can be suitable for calcareous clastic sediments.

The weathering intensity scale (WIS) proposed by Meunier et al. (2013) is an alternative approach to the CIA and other indices. The WIS is based on the  $M^{+}-4Si-R^{2+}$  system ( $M^{+} = Na^{+} + K^{+} + 2Ca^{2+}$ ;  $4Si = Si/4$ ;  $R^{2+} = Fe^{2+} + Mg^{2+}$  and  $R^{3+}/(R^{3+}+R^{2+}+M^{+})$  versus  $\Delta 4Si\%$  that takes divalent metallic elements, alkaline earth elements and silica into account. The approach was proposed to tackle the problems faced when dealing with sediments of different weathering intensity and different source rock compositions. The correction of diagenetic illitization is also taken into account when samples are plotted in the illitization trend due to K metasomatism. Based on the study, sediments derived from different sources (felsic to ultra-mafic) are considered, different sources plot in the different fields on the  $M^{+}-4Si-R^{2+}$  and samples with progressive weathering tend to plot towards the 4Si point (kaolinite).

## 2.6 Quartz Microtextures

For the past decades, researchers have tried to connect quartz microtextures observed on quartz grains with provenance and deposition environment. Transmission electron microscopy (TEM) was the first method used to observe the quartz microtextures but had some complications (Krinsley and Takahashi, 1964). Scanning electron microscopy (SEM) is a more accurate and direct method to observe the quartz grains, which became the preferred approach to use.

The characteristics observed on the surfaces of quartz grains may be categorized as mechanical or chemical characteristics or combinations of both. The quantity, strength and spatial arrangement of the above three characteristics can be successfully used to delineate a variety of different deposition and weather environments (Krinsley, 1980).

Quartz microtextures provide valuable information about the impressions caused by the sedimentary processes that work on the sediments throughout transportation and subsequently during deposition (Krinsley and Takahashi, 1964; Krinsley and Funnell, 1965; Krinsley and Donahue, 1968; Doornkamp and Krinsley, 1971; Mahaney et al., 2001; Madhavaraju et al., 2006; Madhavaraju et al., 2009; Peterknecht and Tietz, 2011; Armstrong-Altrin and Natalhy-Pineda, 2014; Kalińska-Nartiša et al., 2017). The mechanical and chemical distinguishing parameters and their consequences have been recognized by many researchers (Krinsley and Donahue, 1968; Whalley and Krinsley, 1974; Al-Saleh and Khalaf, 1982; Rahman and Ahmed, 1996; AL-Hurban and Gharib, 2004; Madhavaraju et al., 2006; Peterknecht and Tietz, 2011; Armstrong-Altrin and Natalhy-Pineda, 2014; Vos et al., 2014; Kanhaiya et al., 2017; Itamiya et al., 2019; Hossain et al., 2020; Srivastava et al., 2020; Ramos-Vazques and Armstrong-Altris, 2020). The surface texture study of quartz grains is therefore used as a valuable method for identifying provenance, transport processes and the diagenetic background of detrital residues (Krinsley et al., 1973; Madhavaraju and Ramasamy, 1999; Abu-Zeid et al., 2001; Madhavaraju et al., 2004, 2006; Armstrong et al., 2005; Kanhaiya et al., 2017; Itamiya et al., 2019; Ramos-Vázquez, and Armstrong-Altrin, 2021).

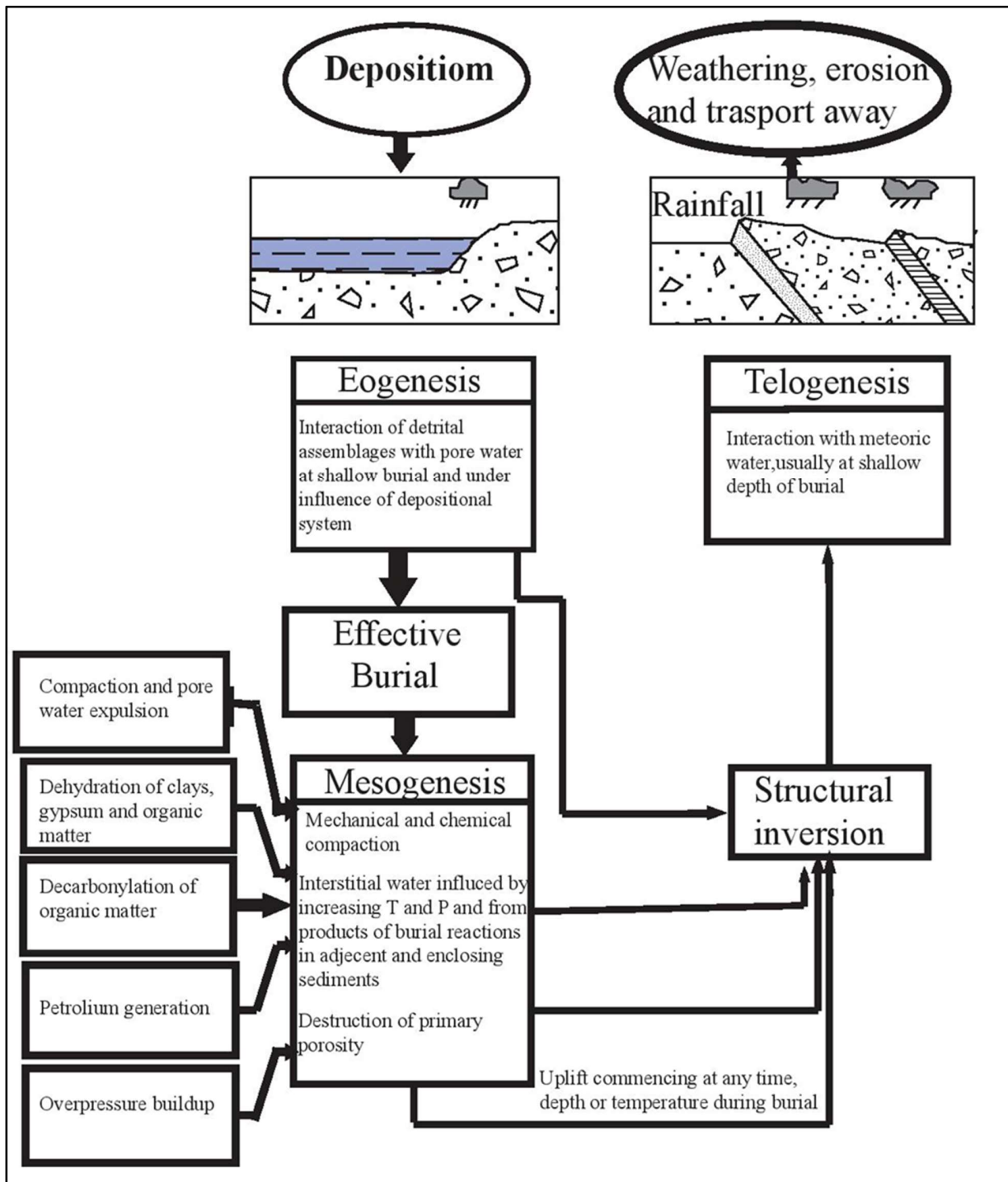


## 2.7 Diagenesis

Diagenesis covers a wide variety of post-depositional physical, chemical, and biological processes in which the deposited sediments and their pore waters react with the surrounding environment to achieve their texture and geochemical equilibrium (Worden and Burley, 2003). Diagenetic processes can affect both porosity and permeability due to cementation and compaction which are common in nature. In sandstones, the concept of diagenesis is a fairly new phenomenon that was introduced by researchers in the 1950s and has continued to be studied to this day. It emerged from the definition of grain shapes and textures, total sediment composition with increasing depth and temperatures (Worden and Burley, 2003). This evolution is due to interest and funding from the oil industry where geologists and engineers require this knowledge to quantify the distribution of sandstone porosity and permeability that regulates the hydrocarbon migration routes and production (Worden and Burley, 2003).

The diagenetic features regarding, and its implications on reservoir quality of siliciclastic sedimentary rocks, have been studied by many researchers via multiple approaches such as petrography and geochemistry. The petrographic analysis is the most crucial approach to understand the relationship between the textural and compositional maturity and immaturity of sediments and it is also an important tool to reconstruct the diagenetic history in most sandstone reservoirs (Burley and Worden., 2009; Morad et al., 2010; Zhang et al., 2011; Shalaby et al., 2014; Cao et al., 2017; Ben-Awuah et al., 2017; Heidsiek et al., 2020; Usman et al., 2020). Geochemistry gives the opportunity to understand the water chemistry involved in the process of diagenesis as well as the prediction of conditions that form diagenetic illite, various cement types, and the temperature and the composition of diagenetic fluids (Hood et al., 2018; Deng et al., 2019; Fantle et al., 2020).

Diagenesis is divided into three parts; early diagenesis (eogenesis), burial diagenesis (mesogenesis) and uplift influenced diagenesis (telogenesis) (Worden and Burley, 2003) (**Fig. 2.3**).



**Figure 2.3** Different stages of diagenesis and the links between various diagenetic realms (adapted from Worden and Burley, 2003).

## 2.7.1 Mechanical Compaction

Compaction decreases the volume of rocks resulting in the displacement of pore waters due to the shear-compressional stress of  $\sigma_3$  commensurate with the rising overburden load or younger sediments (Worden and Burley, 2003). This load is the efficient stress that distinguishes between lithostatic and fluid pressure. Because of these processes, sandstone compaction takes place; grain rearrangement, ductile compound plastic deformation, dissolution, and brittle fracturing. The compaction of sediments is duly controlled by the grain composition and burial depth and pore pressure. Highly ductile grains such as micas and lithic fragments in sandstones tend to experience more extensive compaction due to their ductile nature (Pittman and Larese, 1991; Paxton et al., 2002; Worden and Burley, 2003; Li et al., 2006). Mechanical compaction typically occurs within 1000 m of depth, equal to 25-30% of porosity, and corresponds to Worden's theoretical value when the further burial occurs in 2000-4000 m depth (Worden and Burley, 2003). Pittman and Larese (1991) reported that even at 2000 m of burial, much loss of porosity may occur during mechanical compaction due to displacement or ductile grains (clay-rich weathered volcanic residues, mud intraclast or metapelite rock residues that may lead to extreme plastic deformation) caused by the more rigid grains. In addition to mechanical compaction, loss of porosity and permeability from authigenic mineral growth also occurred (Kassab et al., 2014).

## 2.7.2 Dissolution

Dissolution describes the process where the rock minerals are exposed to pore fluids and suffer damage by dissolution, which results in the creation of additional rock porosity, at various scales. (Worden and Burley, 2003). Dissolution usually involves unstable rock fragments, for instance, feldspar and volcanic deposits (Kassab et al., 2014). It can occur in many different situations depending upon the burial history of the sediments. Examples include; when grains/minerals are in contact with a fluid such as surface (meteoric) water at a shallow depth (Yuan et al., 2019), or hotter fluids formed during burial, by organic matter (releasing acids), or lastly clay mineralisation at a higher depth (Taylor 1996, 2010; Kassab et al., 2014; Bukar et al., 2021). When the pressure and temperature rise, silicate minerals can appear to dissolve more quickly (Worden and Burley, 2003) and the process of “pressure solution” can be observed for rocks that have undergone significant burial stresses. These sandstones that are subjected to high

burial stresses can undergo pressure dissolution at the microscopic scale such that the grain to grain contacts area is increased (Worden and Burley, 2003). To accommodate these high stresses, the grains' boundaries change from straight to elongated to concave to convex at the points of contact and finally sutured contacts are observed (Worden and Burley, 2003; Baiyegunhi et al., 2017).

Matter and Ramseyer (1985) observed that the onset of pressure solution is greatly affected by mineralogy, mineral chemistry and structure, as can be seen by the differential dissolution pressure of the dissolved minerals and also the differential solubility of detrital quartz grain. Effective stress decreases when the fluid pressure is greater than the hydrostatic pressure, thus reducing relative sandstone pressure and also affecting mechanical and chemical compaction (Worden and Burley, 2003). Compaction may be concluded as an association of function of burial depth, lithology (rigid ductile grain ratio, mineralogy) and pressure of the fluid (Worden and Burley, 2003).

### **2.7.3 Cementation**

Cementation is the development or precipitation of minerals inside the pore spaces. Common cementations on sandstone include quartz (silica), iron oxide, clay minerals and calcareous (Kassab et al., 2014). The types of cementations can be identified mainly through SEM analysis and geochemical analysis (Ben-Awuah et al. 2017; Chima et al., 2018; Makeem et al., 2021).

#### **2.7.3.1 Silica**

Globally, Quartz cement is the most important factor that destroys porosity in sandstone reservoirs. Cementation takes place in two distinct phases: an early minor phase during which a few percentages of authentic quartz are precipitated, followed by a fairly rapid beginning of major deep burial cementation, which can lead to a reduction in porosity of up to 20%. Massive cementation of quartz usually commences at  $90 \pm 10^\circ \text{C}$  (Giles et al., 2000). According to Kassab et al. (2014), quartz overgrowth has a similar environment in which it can develop in shallow-buried sandstone, although they differ in their opinion that quartz overgrowth can occur through the formation of silcrete (Worden and Burley, 2003; Kelly et al., 2007).

However, Worden and Morad (2003) stated that the overgrowth of quartz usually occurs in deep-burial diagenesis, although it has the same temperature range as 70-130°C (Baig et al., 2016). The primary source of this overgrowth is the dissolution of K-feldspar (Baig et al., 2016). As a result, simple quartz cement can form in a variety of forms, it can also result in silica cement, which then develops into a quartz overgrowth (Worden and Burley, 2003).

### **2.7.3.2 Iron oxide**

Iron oxides cement is the weathering product of iron-rich minerals, like laterite in the upland regions, transported and laid beside other sediments, which are subsequently transformed into hematite in favourable humid tropical or subtropical environmental conditions. This iron oxide comes in the manner of a reddish-brown cement, is produced as cement that fills up the pore spaces, thin coatings that surround the outer layer of detrital grains (Beitler et al., 2005; Parry, 2011), deposit inside mica flakes and runs through cracks boundaries (Carroll, 1958; Chima et al., 2018). Iron oxide is also bordered on the transported and overgrowth quartz, suggesting that the sandstone had a few diagenesis stages (Kassab et al., 2014). The oxidizing environment can also affect iron oxide cement during eogenesis occurring before compaction and overlapping overgrowth of quartz (Kassab et al., 2014). Goethite and hematite are examples of iron oxide, in which goethite occurs in the form of rosettes, is formed as clusters and is often distributed randomly, while hematite occurs between the grain spaces (Kassab et al., 2014).

### **2.7.3.3 Carbonate cement**

Carbonate cementation is well known for destroying both permeability and porosity in sandstone reservoirs. The most common situation for carbonate cementation is found in sandstones either interbedded with carbonate beds or sandstones that contain detrital carbonate material such as marine fossils. The carbonate cements can be found in areas such as inside pore spaces, replacement of sand grains with calcite and minor dolomite and carbonate cement in intergranular pores. Pore-filling cements tend to get trapped in fairly wide pore spaces or replace grains inside a structure. Eogenetic cement is supported by framework sediments and prevents compaction,

ensuing in a floating grain texture and a large volume of “minus-cement” porosity. Pore-filling cement is normally precipitated prior to substantial compaction and therefore can imply an eogenetic source (Lai et al., 2017).

Calcite, dolomite and siderite are commonly formed during mesogenesis as quartz, and prominent carbonates (Worden and Burley, 2003). However, eogenetic cementation leads to pore-filling cement fabric that amounts up to < 40% composed of fine microspar crystals (Worden and Burley 2003). Wilkinson (1991) argued that eogenetic calcite nodules or discrete layers are commonly interlocking with shallow marine sandstones. This is due to the dissolution and re-precipitation of shell detritus as non-ferroan calcite (Worden and Burley, 2003).

#### **2.7.4 Clay Minerals**

Clay minerals often found in sandstone are usually the sandstone cementing agent. This type of cement grows like tiny, ragged, abraded crystals and naturally fills rock pores that form tangential grain coatings and pore-bridging fabrics, despite the fact that these minerals can significantly affect reservoir quality (Worden and Burley, 2003). A reservoir's porosity and permeability are highly dependent upon the quality of clay minerals even though they contribute to the rock's bulk composition insignificantly (Worden and Burley, 2003). While hydrodynamic sorting inclines to avoid co-deposition of sand sediments and clay minerals, both forms of clay may occur as detrital components (Worden and Burley, 2003).

Baig et al. (2016) and Worden and Burley (2003) have documented that kaolinite, illite, and chlorite are the common clay minerals in sandstone and smectite is less common. Kaolinite normally fills in the pore space but this would have a significance on vertical permeability and slightly affect the horizontal permeability as well (Mode et al., 2016; Worden and Burley, 2003). Fibrous illite develops hair-like coating all around the mineral grains, which often grows as a barrier between the porous throats causes a substantial decrease in permeability by blocking pore throats and increasing in wettability (Mode et al., 2016), whereas chlorite consists of euhedral interlocking plates that prevent further diagenesis of the grains that normally enclose the grains (Worden and Burley, 2003). Mode et al. (2016) also mentioned that swelling of smectites can both fill pores and could destroy the mechanical integrity of the formation.

## 2.8 Porosity and Permeability

Sand and carbonate particle sedimentation in sandstone and carbonate reservoirs never fits perfectly together due to high forms of irregularities (Tiab and Donaldson, 2015). The void spaces created between grains are called pore spaces, and fluids usually occupy them when buried below the local water table (Tiab and Donaldson, 2015). Porosity is the volume-to-bulk ratio of pores (Tiab and Donaldson, 2015). However, the effective porosity and total porosity which are determined by the water interaction with the many frequently occurring minerals vary in porosity (Kennedy, 2015).

Porosity is usually expressed as the percentage of the bulk rock volume. The porosity of sedimentary rocks typically ranges from 0 to 50% (including carbonates) while porosity values in sandstones are rarely over 35% (Tiab and Donaldson, 2015). A petroleum reservoir porosity ranges from 0% to 30% (Table 2.1). Reservoirs with a porosity of less than 5% are not economical, and more than 35% are uncommon (Tiab and Donaldson, 2015).

**Table 2.1 Porosity range and practical cutoff (Tiab and Donaldson, 2015).**

Description	Range (%)
Negligible	0-5
Poor	5-10
Fair	10-15
Good	15-20
Very good	>20
Practical cutoff for oil sandstone	~ 8
Cut off for gas reservoir	< 5

Tiab and Donaldson (2015) noted the following factors influencing porosity:

1. Grain size uniformity: Uniformity is the grain class range. The variations in grain size influence the effective porosity at which finer grains fill the spaces of the pores.
2. Degree of cementation or consolidation: The higher the cementing degree, the lower the sandstone porosity. Cementation happens both during lithification and alteration. By filling pore spaces with mineral materials this process decreases porosity.

3. Compaction rate before and after deposition: Compaction allows grains to be closer to each other resulting in lower volume available for the pores. In addition, compaction also expels fluids in pore spaces.
4. Mode at which packing occurred: The progressive modification from random packing to closer packing of poorly sorted angular sand grains occurs when overburden pressure increases. There is some crushing of the sand particle and some plastic deformation which reduces porosity.

Permeability is the capability of rock to conduct fluid through its porous spaces (Tiab and Donaldson, 2015). A rock's permeability is influenced by the rock's effective porosity, which in turn is a function of grain size, shape, sorting, packing, degree of consolidation and cementation (Tiab and Donaldson, 2015). In addition to this, the formation of clay minerals and cementation plays a major role in reducing permeability particularly when water is present (Tiab and Donaldson, 2015). Different types of clay react to freshwater differently. Smectites and montmorillonites tend to swell in freshwater and cause a blockage to the pores (Tiab and Donaldson, 2015).

Based on the K value, the permeability values are categorized into four for quantifying the reservoir quality (Levorsen, 1967):

- Fair - 1 to 10 mD
- Good - 10 to 100 mD
- Very good - 100 to 1000 mD
- Excellent - > 1000mD

According to Tiab and Donaldson (2015), the following factors affect the permeability are:

1. Grain shape and size: Permeability generally ranges from horizontal to vertical, and the latter is typically lower. Rock reservoir permeability is typically small if the grains of sand are offline and irregular in form. Many oil reservoirs fall into this group.



2. Lamination: Muscovite or shale laminations typically serve as a barrier to permeability to the vertical. Often the vertical permeability due to fractures may be higher than the horizontal permeability.
3. Cementation: Cement can block porous spaces and reduce access to pores. Therefore, the permeability reduces.
4. Fracturing and solution: Fracturing is not a significant cause of its secondary permeability in sandstone except when the sandstones are interbedded with shale, calcareous and dolomites.

## 2.9 Petrography

The petrographic study of the Miri Formation will provide detailed information that will be useful to interpret the sediment provenance, reservoir quality, mineral composition, amount of detrital and diagenetic components and the microstructures. The mineralogical composition can be used to reconstruct the provenance and classify the rock type, it is an instrument used to examine the development of sedimentary basins (Crook, 1974; Dickinson and Suczek, 1979; Dickinson, 1985; Zuffa, 1985). The mineral composition is plotted on QFL triangular diagram (Dickinson and Suczek, 1979; Dickinson, 1985) to reconstruct the provenance and can be plotted on a QFL diagram (Folk, 1981; Pettijohn et al., 1987) to name the rock.

The petrographic modal composition of sands and sandstones includes data on the composition and texture of polycrystalline minerals, which are essential for provenance examinations as they can be ascribed to the parent-rock aggregations in the source region. The background of petrography was initiated in 1828 by a Scottish scientist named William Nicol. Through the incorporating of prisms made from calcite in Iceland Spar, which would then transform a normal microscope into a polarizing microscope, he developed a technique called the Nicol prisms, and it is used to generate polarized light. With the implementation of thin sections by Sorby (1880) and other scholars, the growth of petrography was accelerated mostly during 1840s. The process was later introduced as the traditional procedure for rock analysis.

The point-counting method practiced in petrography testing is a common technique for counting the frame content of sandstones (Dickinson, 1985). Dickinson also recommended using

the point-counting method especially for rock specimens with similar grain sizes to determine provenance. The point-counting technique in Glagolev-Chayes method system typically involves around 300 to 600 counts per thin section (Chayes, 1949, 1956). Two separate sedimentary petrography ideologies adapted the Glagolev-Chayes method system, it was later divided into two sets of classification models, the Indiana scheme and the Gazzi-Dickinson strategy. A recent study by Augustsson (2021), reported that the geological and non-geological factors influence the use of point counting in provenance studies of sand and sandstones. Non-geological influences on the point-counting method can be avoided when one person performs the operation on all the studied samples or all samples analysed by many operators. The geological factors include the wrong usage of methods and discriminant diagram, which can be avoided by using proper methods suited for discriminant diagram and also specifying the matrix cut-off size. The misinterpretation of pseudomatrix as lithic fragment can lead to the misinterpretation of provenance. Understating the diagenetic effect on studied samples can improve the identification of source indicators in sandstone compositions.

The Indiana point-counting approach is ideal for the study of provenance, history of transport and post-depositional changes (Suttner, 1974; Suttner et al., 1981). The Indiana method is utilized to identify weathering and transportation variations in the composition of sandstones. The Gazzi-Dickinson method was established to lessen the effects of grain-size differences in sandstone composition.

The Indiana and Gazzi-Dickinson strategies display two resemblances: a) both methods developed ternary diagrams are created based on the percentage of identified quartz and feldspar grains, and lithic fragments. The Indiana method categorized them as QFR, while the Gazzi-Dickinson method classified them as QFL, and b) carbonate fragments are not known in either technique and are classified in the Gazzi-Dickinson method as lime clasts.

### **2.9.1 Quartz**

The quartz inclusion analysis was first used to determine the provenance by Mackie (1897). Afterward, Krynine (1940, 1946) and Folk (1974) enhanced the use of quartz as the identifier of provenance. To distinguish them from their presumed parent rocks, both authors included the undulatory extinction and polycrystallinity characteristics of quartz. The

mineralogical maturity of sedimentary rocks was also assessed using quartz. Rocks that contain larger numbers of quartz grains are termed as 'mineralogically mature'. Maturity research studies have been carried out by targeting multiple classes of minerals (Cozzens, 1931; Friese, 1931; Woodruff, 1937; Thiel, 1940) based on quartz and still being used for recent studies (Bhattacharyya and Das, 2015; Akinlua et al., 2016; Chima et al., 2018; Baiyegunhi et al., 2020)

The northern Borneo studies have recently used quartz to evaluate provenance (Nagarajan et al., 2015), porosity and permeability (Ben-Awuah and Eswaran, 2015) and diagenetic processes (Ben-Awuah et al., 2015; Usman et al., 2020). That being said, using geochemical methods, the detection of quartz as the principal component in sandstone was achieved indirectly. Nagarajan et al. (2015) adapted the X-ray diffraction (XRD) approach to distinguish the sandstone mineralogy in the Sibuti Formation and used petrography to characterize the sandstones in the Lambir Formation (Nagarajan et al., 2017). Ben-Awuah and Eswaran (2015) identified quartz grains using the Energy-dispersive X-ray spectroscopy (EDX) method in the Baram Delta. Ben-Awuah et al. (2017) also adopted SEM and petrographic approach in their research to evaluate the authigenic quartz cement that occurred in their study samples mainly as overgrowths and the abundance of quartz overgrowth is associated with diagenetic processes (Khidir and Catuneanu, 2010).

## **2.9.2 Feldspar**

The use of feldspar as a reference to study the provenance was generally not noticed as equally important as quartz. This is because feldspar content is lesser upon increasing maturity, in comparison to quartz. Hence, this principle does not extend to sediments generated in feldspar-poor cratons (Pettijohn, 1975). Conversely, a few experiments have been done in which feldspar has been effectively utilized for the identification of provenance. Pittman (1963) proposed that many forms of feldspar that come from various tectonic habitats. Plagioclase feldspar was used as a provenance proxy in sedimentary rocks. Naturally, plagioclase feldspar holds hosting elements such as Na and Ca as an unstable mineral and is vulnerable to weathering. The fragile features allowed plagioclase feldspar to get more use in the evaluation of younger rock sequences and situations concerning rapid deposition (Pittman, 1970). Pittman (1963, 1970) proposed to use the twinning and zoning properties of plagioclase feldspar to determine the provenance of the rock (Shruti et al., 2017). Trevena and Nash (1981) distinguished the source rocks for both volcanic

and plutonic rocks, based on the potassium (K) content in plagioclase feldspars. Maynard (1984) streamlined the Trevena and Nash (1981) classification by splitting it into high and low potassium (K) contents. The classification of Maynard (1984) was more accurate as he claimed that a High-K category would be deemed volcanic in nature, while a Low-K category has plutonic-metamorphic origin. Besides, Maynard (1984) also reported that island arc-derived sediments are abundant in Ca-plagioclase whereas passive continental margin sediments are rich in Na-based plagioclase (i.e. albite).

According to Yuan et al. (2018), feldspar alteration has a significant impact on the subsurface microorganisms and hydrocarbon degradation in which biodegradation of hydrocarbon promotes the alteration of feldspar in hydrocarbon reservoirs. Degradation of feldspars into clay minerals also increases the CIA and PIA value to about 100 (Nesbit and Young., 1982; 1984; Fedo et al., 1995).

The variation of feldspar to kaolinite is related to climate. This alteration is an early stage of diagenesis due to the meteoric water released by sediments (Bjorlykke, 1998 as cited by Ben-Awuah et al., 2017).

### **2.9.3 Rock Fragments**

Besides quartz and feldspar particles, rock fragments are the successful element for provenance studies. Rock fragments or lithic fragments are classified as bits of other rocks that are broken down into sand grain sizes via sedimentary processes, and they exist as sand-sized grains in sedimentary rocks and can be extracted from present sedimentary, igneous and metamorphic rocks. Sandstone provenance can be known if the rock pieces contained in the rock are related to a particular source region (Tucker, 2009). Rock fragments thus have a higher interest in assessing provenance as they are derived from the source and/or parent rock (Boggs, 1968). Potter (1978) and Dickinson and Suczek (1979) have deliberated the significance of rock fragments for interpreting provenance.

There are still some disadvantages to using rock fragments for provenance studies. It is because of their smaller particle size, which has made it is harder to distinguish their parent rock. In hand samples, rocks are typically classified based primarily on their textures, structures, mineral composition and geological prevalence. The probability that these products will be observed declines when the grain size is decreased due to abrasion during transport and deposition cycles.

## **2.10 Bulk Rock Geochemistry**

Bulk rock geochemistry has been a successful and relatively quick and inexpensive approach in studying the geochemistry of rocks (Caracciolo, 2020). Methods have been developed to study sedimentary rocks based on variations in major oxides (Bhatia, 1983), trace elements. (Bhatia and Crook, 1986) and also rare earth elements (McLennan et al., 1989). The geochemical method allows a large sample number to be analyzed more quickly. The geochemical approach provides several findings compared to regular optical microscopy without compromising the outcome. However, geochemistry alone may mislead the provenance interpretation when particular rocks are significantly modified by the diagenesis (Caracciolo et al., 2019, Caracciolo, 2020). A clear example of an effective geochemical process is the rare earth element quantification (McLennan et al., 1989; Mounteney et al., 2018).

The integrated approach is considered for this research, which gives room for an improved understanding of the link between the petrographic and geochemical approaches. Framework modes are applied in a petrographic tactic to understand the association between sandstone composition and provenance. The introduction of the geochemical approach (bulk chemistry) has advantages in cases where fine-grained sedimentary rocks (mudstone and siltstone), and the petrographic approaches are not suitable (Totten et al., 2000). In addition, the use of log-ratio transformation of geochemical data is recommended to produce a correlation matrix and to relate the mineral phases through geochemistry (Caracciolo, 2020).

Classification of sedimentary rocks using geochemical data have been proposed by many researchers Pettijohn et al. (1972); Blatt et al. (1972); Folk (1974); Herron (1988); and the geochemical classification of Lindsey (1999) and have been adopted by many researchers over the past decades. Pettijohn et al. (1972) and Herron (1988) are the most widely used classification schemes. The Pettijohn et al. (1972) classification is proposed based on the  $\text{SiO}_2/\text{Al}_2\text{O}_3$  and

Na<sub>2</sub>O/K<sub>2</sub>O. The use of the Na<sub>2</sub>O/K<sub>2</sub>O ratio is not a suitable approach in distinguishing between lithic fragments and feldspars. Misleading classification might arise in arkose samples containing albite or orthoclase, which will result in high and low ratios of Na<sub>2</sub>O/K<sub>2</sub>O. Therefore, the use of Pettijohn et al.'s (1972) classification scheme can be omitted to avoid shortcoming/misleading classification. Herron's (1988) classification scheme uses the SiO<sub>2</sub>/Al<sub>2</sub>O<sub>3</sub> and Fe<sub>2</sub>O<sub>3</sub>/K<sub>2</sub>O ratios, where the Fe<sub>2</sub>O<sub>3</sub>/K<sub>2</sub>O ratio is an indicator of mineralogical stability and is effective in distinguishing feldspar from the lithic fragment.

Major elements have been used for the past decades in identifying tectonic settings (Schwab, 1975; Bhatia, 1983; Roser and Korsch, 1986). Their research was the foundation of modern applications of geochemical methods. With respect to that, sedimentary rocks are affected by many sedimentary processes that reflect the chemistry of the sediments. Major elements are subjected to many changes in their composition such as enrichment of SiO<sub>2</sub> in basins will show a reduction of Na<sub>2</sub>O and CaO in analyzed samples compared to the source rock composition.

While trace elements are utilized to classify igneous rocks as either mafic or felsic. The most suitable trace elements are the low mobile trace elements (La, Th, Y, Zr, Ti, Co and Ni) and geochemical ratios of immobile elements (i.e. Y/Ni, Cr/V, Zr/Sc and Th/Sc etc. McLennan et al., 1993), which are more suitable for decimating sandstones formed in a continental island arc, an active continental margin, or a passive continental margin and oceanic island arc settings (Bhatia and Crook, 1986).

Rare Earth Elements (REE) are also important trace elements, they are imprints of the provenance of sedimentary rocks (Taylor and McLennan, 1985; Yang et al., 2002; Song and Choi, 2009). REEs present in very low concentrations and are relatively insoluble in most geological conditions, which make them essential for provenance studies.

Diagenesis is one of the aspects that might influence the interpretation of provenance using bulk rock geochemistry (Milliken et al., 1994; Caracciolo, 2020). These can show variants in elements, for example, Fe<sub>2</sub>O<sub>3</sub>, K<sub>2</sub>O, MgO and SiO<sub>2</sub>. In addition, the post-depositional alteration leads to grain replacement and dissolution of the framework minerals and the consequent

precipitation of the authigenic phase consolidates the sands to rock. The clay minerals (some authigenic phases in addition to the weathering products) and carbonate cementation may be misleading the researchers to obtain the wrong values of indices used for weathering (Caracciolo, 2020). Therefore, consideration of detrital mineralogy and diagenetic processes must be taken into account while making interpretations.

As mentioned earlier, many discriminant diagrams have been proposed based on bulk rock geochemistry for provenance, tectonic settings and paleowethering, and researchers have adopted them based on the scope of their study and need caution to select the suitable diagrams and indices are essential.

## **2.11 Previous work on the Miri Formation**

Previous studies on the Miri Formation have mainly focused on the facies distribution and depositional controls on the reservoir rocks. Abieda et al. (2005) did a study on the depositional controls of the Miri Formation, particularly on the petrophysical properties and based on this work, twelve lithofacies were identified. The lithofacies were split into two facies associations: 1. the estuarine, tide-dominated and the shoreface-offshore transition and 2. storm-and wave-dominated facies associations. The estuarine lithofacies were described by their distinctive tidal features such as; tidal dune cross-bedding with mud draped cosets and fore sets, as well as mud couplets, herringbone cross-bedding, rhythmic stratifications, flaser, wave and lenticular bedding structures. While the shoreface-offshore transition, storm-and-wave facies association were characterized by only sandstone builds with indications of storm and wave made sedimentary structures such as; swaley cross-stratified sandstones, amalgamated hummocky cross-stratified sandstones, bioturbated sandstones and mudstone inter-bedding with parallel stratified to hummocky cross-stratified sandstones. The petrophysical properties of the six facies were determined, which are; Facies A (trough cross-stratified sandstone with mud drapes), Facies B (parallel stratified sandstone with mud drapes), Facies F (homogenous coarse-grained sandstone), Facies G (Swaley cross-stratified sandstone), Facies I (fine-grained bioturbated sandstone) and Facies L (mudstone inter-bedding with parallel stratified to hummocky cross-stratified sandstone). The porosity was acquired by means of water immersion in a vacuum method and permeability was regulated by a

gas permeability practice proposed by Monicard (1980). The study was also sustained by twelve standard thin sections that represented the six sandstone lithofacies. The lithofacies were categorized by an extensive variety of permeability rates, ranging from 0.35 to 287 mD, whereas porosity shows variation of less than 10 % in all lithofacies. Lithofacies A and F were logged to have the best reservoir properties with porosities of 23.3 to 29.7% and permeability was in the range of 9.64 to 287 mD. Lithofacies G displayed wide-ranging porosity and permeability rates that are sorted from high to low reservoir properties; the porosity values were 23.5 to 27.5% and permeability values were 3.4 to 45 mD. Lower shoreface and offshore transition (lithofacies I and L respectively) exhibited the lowest reservoir properties; the porosity values were 13.5 to 24.5% and permeability values were 0.35-3.4 mD. Generally, the good reservoir quality of the Miri sandstones was related to the coarser grain size, low clay content and better-sorted grains. Abieda et al. (2005) concluded that broad clay drapes, bioturbation and an abundant amount of very fine grains caused a substantial reduction in permeability in both tide- and wave-generated lithofacies.

Jia and Rahman (2009) also did a comparative sedimentological and the petrophysical characteristics (porosity, permeability, density, sonic velocity) of sandstones in the Miri Formation and Nyalau Formation. The study investigated and determined the facies characteristics and reservoir properties of the diverse sorts of sandstone rocks, and also established the relationships between the facies characteristics and petrophysical properties. Based on lithology, sedimentary structures, bed geometry and fossil traces, four lithofacies were identified in the Miri Formation. These lithofacies are (i) hummocky cross-stratified sandstones (HCS); (ii) trough cross-bedding sandstones (TCB); (iii) bioturbated sandstones; and (iv) swaley cross-stratified sandstones (SCS). The petrophysical properties of the lithofacies were determined based on laboratory petrophysical testing and measurements and were reported respectively. The porosity value of HCS was reported to be 19.84 to 21.21% and the average porosity percentages of about 20%, permeability value of ~14 mD and density was measured more than 2 g/cm<sup>3</sup>; 2.07 to 2.16 g/cm<sup>3</sup>, velocities from 2191 to 2472 m/s. TCB shows the porosity values as 20.77 to 23.50%, permeability as 6.49 to 14.57 mD, densities as 1.86 to 2.04 g/cm<sup>3</sup> and average velocity of the facies as ~2000 m/s. The bioturbated sandstones show a porosity value of 18.84 to 19.02%, with a wide range of permeability values, ranging from 6.53 to 11.91 mD, densities of more than 2 g/cm<sup>3</sup>; 2.25 to 2.62 g/cm<sup>3</sup> and velocities ranging from 2191 to 2806 m/s. SCS also shows a wide range porosity (9.74 to 39.90%),



permeability (0.06 to 16.12mD), densities ( $2 \text{ g/cm}^3$ ;  $2.15$  to  $2.51 \text{ g/cm}^3$ ) and average velocity of is 1917 m/s.

Ulfa et al. (2011), also did a study on the influence of tide and storm on facies deposition in the Miri formation. The principal objective of their study was to deliver added clarification on the stratigraphy of the Miri Formation in the Miri Field with the new information collected from new outcrops in the area. According to the lithology, sedimentary structures, bedding geometry and trace fossils, the deposits of the Miri Formation were assembled into fourteen lithofacies; Facies A (hummocky cross-stratified sandstones), Facies B (massive sandstone), Facies C (swaley cross-stratified sandstone), Facies D (rhythmic parallel stratified sandstone and laminated siltstone), Facies E (trough cross stratified sandstone with mud-drapes), Facies F (parallel stratified sandstone with mud-laminas), Facies G (wavy-bedded sandstone), Facies H (rhythmic stratified sandstone and mudstones), Facies I (lenticular bedding), Facies J (interbedded to bioturbated sandstone and siltstone), Facies K (bioturbated sandstone), Facies L (mudstone interbedding with parallel to hummocky cross-stratified sandstone), Facies M (flaser bedded sandstone) and Facies N (bioturbated siltstone). Two facies associations were recognized, which denoted the past environmental settings of the Miri Formation. The facies associations are: (i) tide-dominated estuary and (ii) wave-and-storm dominated. These facies associations described the combined tide and storm effect on the facies deposition of the Miri Formation, where the tide-dominated estuary illustration of the Miri Formation comprises of (i) estuary mouth or tidal channel and sand bars (facies E); (ii) estuary channel or upper flow regime of sand flat (facies F); (iii) mixed-tidal flat (facies G and facies M); and (iv) mud-tidal flat (facies H and facies I) that demonstrates sporadic sand or mud layering in dissimilar dimension associated with the tidal stages of interchanging current and slack water movement and the storm-and-wave dominated modal figure of the Miri Formation contains: (i) lower to middle shoreface (facies A and D); (ii) upper shoreface (facies C); (iii) lower shoreface (facies J); and (iv) offshore transitional (facies L and facies K). They concluded that the depositional processes in the shoreface depositional setting and are typically controlled by waves, and generally diminished by the rising water depth. The upper shoreface (0 to 2 meters of water depth) specified an area with high wave energy and low organism productivity, reflected by the sedimentation of facies C. Lower wave energy but greater organism productivity imitates by the sedimentation of facies A and D in the middle to lower shoreface (below water depth of 2 meters). Lower shoreface (facies J) demonstrates low wave energy and high organism

productivity. The lower shoreface and offshore regions are not disturbed by waves, hence fine-grained residues were deposited from suspension with the likelihood of reworking process are found in those regions. The sedimentation of facies L and facies K in the offshore transitional proves fluctuation episodes of fair-weather and storm actions.

Togunwa et al. (2015), studied the organic-rich remains of Neogene West Baram Delta Province via organic geochemistry and petrography in order to know its associations for source rock and hydrocarbon prospective. Geochemical analyses were carried out for total organic carbon (TOC) content, bulk pyrolysis, pyrolysis-GC and elemental analyses, while petrographic analysis involved vitrinite reflectance measurements and microscopical kerogen analysis done on polished blocks and thin section slides. The results based on organic geochemistry and petrography show that the total organic carbon (TOC) contents of the Neogene sediments were ranging from 1.06 to 11.11 wt. % and Hydrogen Index (HI) values were generally below 105 mg HC/g TOC, signifying that the grains were organic-rich and consist of Type III kerogen gas. The result of the kerogen type was sustained by the plentiful terrestrial constituents, such as vitrinite phytoclasts, spores and pollen), low atomic hydrogen-to-carbon atomic (H/C) ratio and a large quantity of aromatic hydrocarbons in Pyrolysis GC pyrograms and would probably produce predominantly condensate and gas. The examined samples had a vitrinite reflectance between 0.39 and 0.48 % Ro and pyrolysis  $T_{max}$  was between 401 and 434°C. This specifies that the Neogene deposits have immature to very early-mature organic matter. Concluding that the onshore deposits were not buried to a sufficient depth, but the offshore stratigraphic equivalent of these deposits was famous for their deeper burial and could then behave as an effective petroleum source rock for natural gas.

According to the most recent study carried out by Siddiqui et al. (2017) who analysed the static connectivity and facies quality of the sandstones from the Miri Formation. They analysed well-exposed outcrops in the Miri Formation, to illustrate reservoir properties, for example, grain size, petrography, pore-perm and static connectivity, of dissimilar sandstone facies and to create a 2D intermediate-scale figure of the sandstone distribution and connectivity. They reported seven diverse sorts of sandstones facies: (i) hummocky cross-stratified sandstones (HCSS), (ii) herringbone cross-bedded (HBCBS), (iii) trough cross-bedded sandstones (TCBS), (iv) wavy- to flaser-bedded (W-FBS), (v) cross-bedded sandstone (CS), (vi) bioturbated sandstone (BS), and (vii) massive sandstone (MS). Based on their results, the sandstones of HCSS and HBCBS are

well sorted, have slight mud content, and demonstrate an accumulative vertical and lateral connectivity caused by the depositional forms, especially in bioturbated sandstones. The sandstones of BS and CB have poor grain sorting and poro-perm, though TCB and MS sandstone facies have less lateral and vertical extent. They also did a 2D outcrop-based illustration that provided extra visions into the importance of small-scale heterogeneity and static connectivity of shallow marine sandstone sedimentations which can be correspondent for subsurface reservoir quality study. Siddiqui et al. (2017) also mentioned that all seven sandstone facies had some diagenetic alteration and clay minerals penetration, and distress porosity and permeability.

## **2.12 Summary**

Previous studies on the Miri Formation have mainly focused on the structural aspects (Van der zee and Urai, 2005), stratigraphy (Jia and Rahman, 2009; Ulfa et al., 2011) sedimentology and reservoir quality (Abieda et al., 2005; Siddiqui et al., 2017) of the Miri Formation. However, the petrography, mineralogy and geochemistry and their implications on provenance, chemical maturity, paleo-weathering and tectonic setting of the Miri Formation have not been reported yet. Due to multiple factors such as chemical weathering, sorting and diagenesis controlling the petrographic, geochemical and petrophysical characteristics of sedimentary rocks, an integrated approach is proposed for the current study using petrography, mineralogy, geochemistry and petrophysics to investigate the characteristics of the Miri Formation and deduce their provenance, tectonic setting, the intensity of weathering as well as the diagenetic factors affecting the reservoir characteristics of the Miri Formation. Knowing the provenance, paleoweathering and tectonic setting of the study area could enhance the understanding of the architecture of the petroliferous Sarawak Basin through the Miri Formation.

# CHAPTER 3

## RESEARCH METHODOLOGY

### 3.1 Introduction

An integrated approach combining petrography, mineralogy, geochemistry and petrophysical parameters was used to achieve the research objectives of this project (**Fig 3.1**). The combination of petrography, XRD and geochemistry was used in this research to identify the mineralogical and geochemical composition of the Miri Formation sedimentary rocks in order to elucidate their implications for diagenesis, weathering and sediment provenance. Similarly, the petrophysical characteristics are accessed via a combination of petrography, geochemistry, SEM analysis and petrophysical analysis to understand the possible controls on the reservoir quality of the sandstones.

A combination of methods has been adopted by many researchers (Jafarzadeh and Hosseini-Barzi 2008; Nagarajan et al., 2014; He et al., 2015; Nagarajan et al., 2015; Armstrong-Altrin et al., 2015; Akinlua et al., 2016; Nagarajan et al., 2017; Nagarajan et al., 2021) to understand the implication on provenance and weathering in their study area. Combining data from various methods can yield more valuable information to elucidate. The methodology adopted in the present study is presented as a flow chart (**Fig. 3.1**). In addition, each step of the various methods has been explained separately in the following sections.

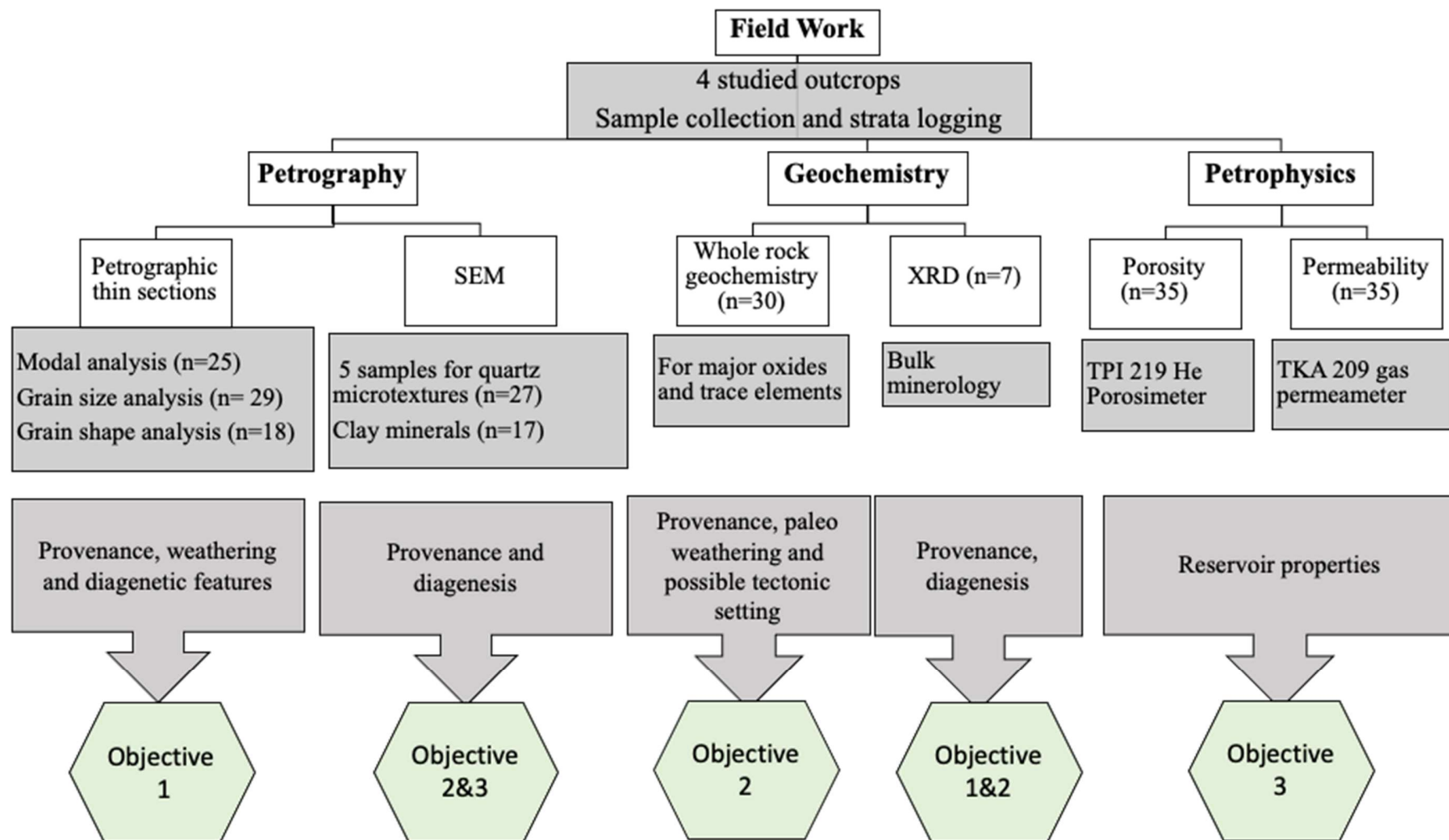


Figure 3.1 Flowchart of the methods used to achieve the objectives in the study.

### 3.2 Field studies and Sample collection

Field study and sample collection are the most crucial step to acquire relevant data for every geological study. Most of the fieldwork carried out in this research involves field observation, data collection, sample collection and strata logging of each outcrop. The fieldwork was carried out in a span of one month due to difficulty in sample collection and weather conditions. Four well-exposed outcrops were chosen around Miri city (Fig 3.2), two outcrops are newly exposed recently due to construction work taking place. The outcrops for the study are selected based on the outcrop exposure and also to cover the upper and lower sections of the Miri Formation.

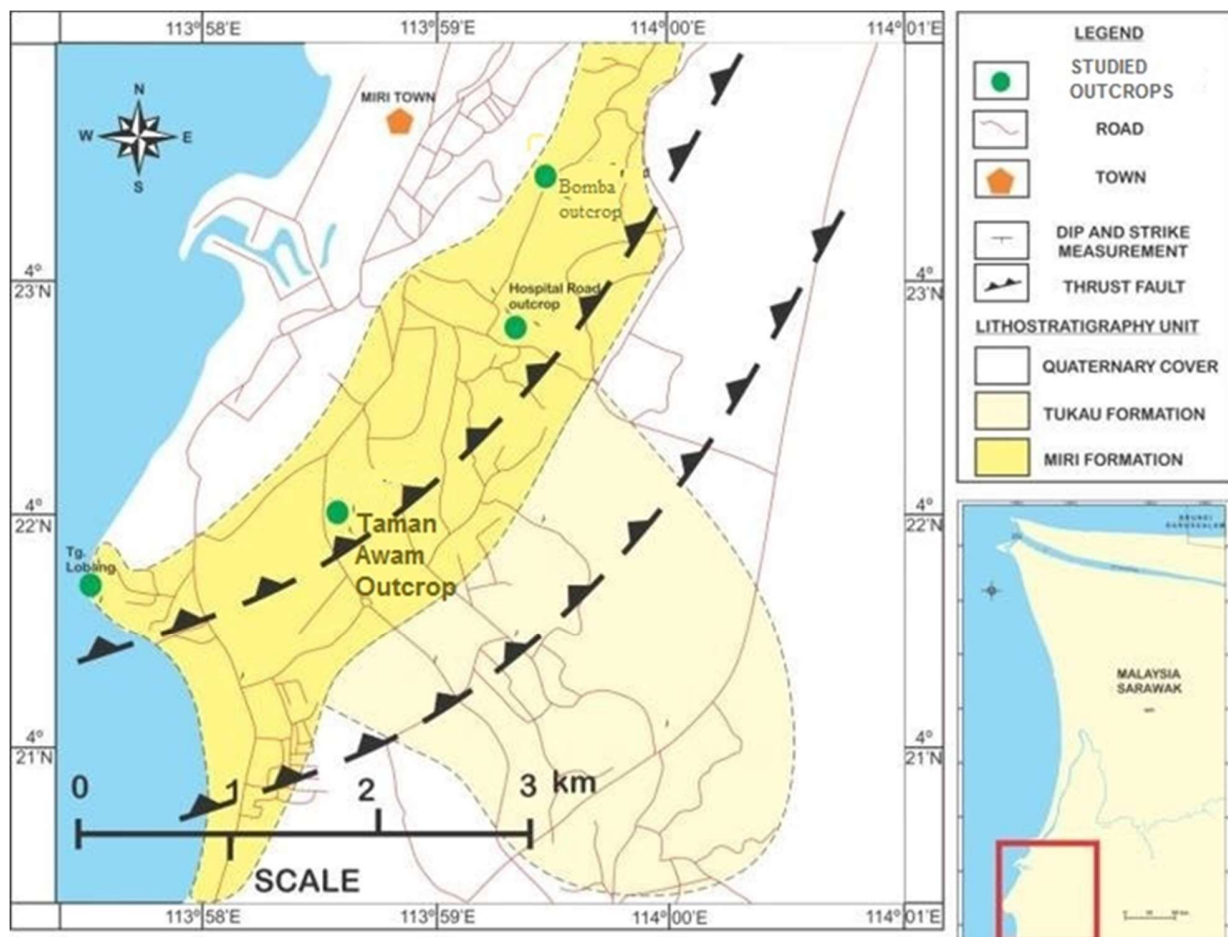


Figure 3.2 Selected outcrops for the present study within the Miri Formation (Modified from Wannier et al., 2011).

All observations and data collected in the field were recorded in the geological field notebook and pictures were also taken for reference and further observation. The lithologs were generated using adobe illustrator.

### **3.2.1 Sample collection**

All sample collection was done using (SHAW Backpack Drill) portable core drill to obtain fresher and cylindrical shaped samples. Samples were collected in every bed depending on the bed size, larger bed samples included the top, middle and bottom, medium size beds included top and bottom while for smaller beds one repetitive sample was collected. All samples collected were core samples, which were at least 1Kg. The samples were labelled and well preserved in polythene zip-lock sample bags for further analysis.

Usage of the portable core drill has its advantages and disadvantages. Some of the advantages include; (i) fresher samples can be obtained by drilling deeper into the sedimentary bed, (ii) sample processing (preparation in the laboratory) is made easier and (iii) no sample contaminations. The main disadvantage of this equipment is the fact that to collect 5 or 6 good quality core samples requires a supply of 15 gallons (or 68 litres) of clean freshwater weighing 68kg. The logistics and labour required for carrying out outcrop drill core sampling, therefore, requires an adequate supply of water which is usually not the case for outcrop geology. Secondly, collecting mudstone samples can be problematic as the mud slurry created during operating the drill can cause the core drill water pump to suffer blockages.

### **3.3 Sample Preparation**

Sandstone was the primary sample for the petrographic analysis but some of the mudstone samples were included as well. Due to the nature of the studied samples, the petrography method used in the sample preparation was modified from Niki et al. (2019), unlike sample preparation for harder rocks that requires the availability of the required equipment and materials. The equipment used for the preparation of samples for this project includes (i) a Trim Saw, (ii) an Ingram-WARD trim saw with a grinder, (iii) a Hillquist polishing machine, located in the Sedimentology Lab, Curtin University, Malaysia.

### **3.3.1 Thin Section Preparation**

#### **STEP 1: Cutting**

Rock samples were cut into smaller pieces using the trim saw (**Fig 3.3 A**). Depending on the user, samples can be resized and reshaped into any suitable shape. For this research, all samples were cut into cubic slabs with the same dimensions as the glass slide available. All samples are labelled after attaining the perfect shape and size.

#### **STEP 2: Impregnation**

Samples were then heated up in a hot plate (**Fig 3.3 B**) to a temperature of 80°C for at least 5 minutes. Impregnating solution was then prepared by mixing 50ml of resin, 50ml of hardener and 50ml of acetone (i.e., change of mixture proportion was done to suit the nature of studied samples). At this stage, one scoop (small spatula) of blue dye was added to the mixture for the samples used for porosity analysis. The prepared solution was then divided into three or four disposable cups (6oz size). Heated samples were submerged and soaked in the solution, and then placed in a vacuum pot (**Fig 3.3 D**) for about 20 minutes. Samples were then removed and placed on the hot plate at a temperature of 40°C and kept for between 5-24 hours to harden.

#### **STEP 3: Polishing rock slab**

At this stage, the hardened samples were first polished using the Hillquist polishing machines (**Fig 3.3 C**) with 45 and 30µm disks respectively for at least 5 minutes on each disk. Samples were then polished on a glass plate with 800, 1000, 1500 and 2000 grit carborundum powder until a well-polished surface was achieved. Samples were then washed and dried in an oven at 100°C for 1 hour. If the sample was not well impregnated, step 2 was repeated.

#### **STEP 4: Mounting sample to the glass slide**

Rock sample and glass slide were first heated on the hot plate at about 70°C, the glue (Loctite Hysol 0151 epoxy glue) was mixed 2:1 ratio and applied evenly on the polished rock slab sample surface and the glass was mounted. Glass was pressed gently with fingers to remove all bubbles. The mounted sample was then put back on the hot plate at 65°C for 2 hours to speed the curing of the mounted glass slide on the rock.



The glue was first crushed to a powder form before use. The glass slides and rock samples were heated on the hot plate at 100°C, the powdered glue (hard Canada Balsam glue) was spread on the glass slide and heated at the same temperature. Once the glue was heated enough (using a pin to touch the glue and pinching it, it turns into a white powder and that's how to know the glue was heated enough). The glass slide was then mounted to the polished rock slab surface and slowly pressed with a finger to remove all bubbles. The cure for this glue was achieved within 5 minutes.

#### **STEP 5: Cutting rock sample from the glass slide**

The rock slab was cut from the glass slide using the Ingram-WARD trim saw (**Fig 3.3 D**).

#### **STEP 6: Polishing thin section**

The thin section was first polished using the Hillquist polishing machines with 45 and 30micron disks respectively for at least 5 minutes on each disk. Samples were then polished on a glass plate with 800, 1000,1500 and 2000 grit carborundum powder until a well-polished surface was achieved.

#### **STEP 7: Polishing Thin section using Sandpaper**

For better results, a 2000 grid sandpaper was used to further polish the thin section. The final thickness of the thin section was determined by observing the quartz grains interference color and comparing it with the Michael- Levy interference chart.



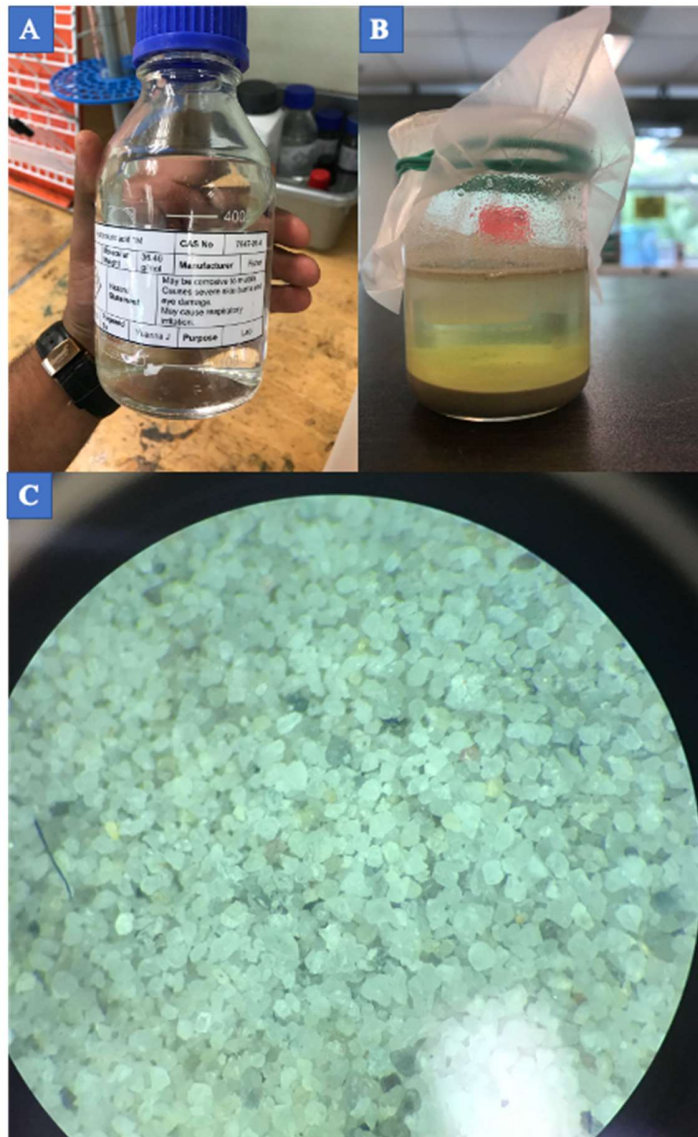
**Figure 3.3 Images of A. Lapidary trim saw, B. Hot plate, C. Hillquist thin section grinder, D. Vacuum pot and E. Ingram ward thin section machine.**

### **3.3.2 SEM sample preparation**

For SEM analysis, two sets of samples were prepared based on the analysis to be carried out. Two types of SEM analyses were carried out in this research, the first one was the quartz grain microtexture analysis and the second analysis was on coined shaped samples to determine the cement composition, pore types and diagenetic features.

#### **3.3.2.1 Quartz grains microtexture analysis**

The coarser-grained samples were chosen for this analysis, two samples from the study area were chosen and prepared accordingly. About 20 g of each sample was treated using 1:1 solution HCl (**Fig 3.4A**), the samples were soaked for 24 hrs in the HCl solution to dissolve carbonates and to remove iron stains from the quartz grains (**Fig 3.4B**). The samples were then washed several times with distilled water in a 70 $\mu$ m sieve to obtain grains only bigger than 70  $\mu$ m. Treated samples were then dried in an oven at 70°C till fully dry. Quartz grains were examined under a binocular microscope (**Fig 3.4 C**) and the cleanest samples were selected for SEM analysis at Curtin BioValley Pilot Plant. This preparation was a modified approach of Kinsley and Doornkamp (1973) and Helland and Holmes (1997).



**Figure 3.4 Images of A. Hydrochloric acid 1M, B. 1:1 solution with sample soaked for 24hrs, C. Examining quartz grains under the binocular microscope.**

### 3.3.2.2 Coin shaped samples

As mentioned earlier all samples were collected as core samples, the samples for SEM analysis were washed with distilled water and dried in the oven at 40°C for 24 hours. Samples are impregnated with a prepared solution of 50 ml of Resin, 50 ml of Hardener and 20 ml of acetone. This is to harden the walls of the core sample. The impregnation process is the same as the one

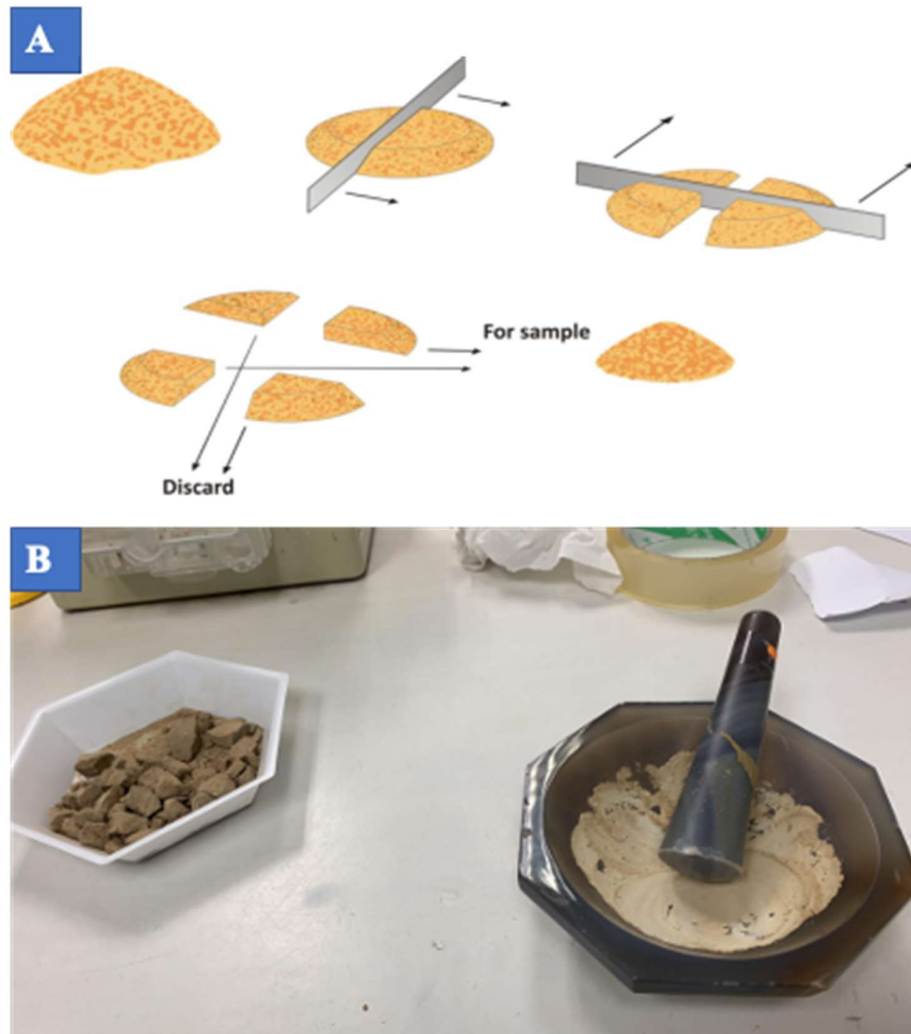
explained earlier in step 2 of thin section preparation (see section 3.3.1 STEP 2) but here 20 ml of acetone was used to reduce deep penetration of the solution.

After samples were hardened, the samples were cut into small coin shapes for easier analysis. The shape and size of the sample were followed as per the laboratory's guidelines to carry out the analysis.

### **3.3.3 Sample preparation for XRD and Geochemical analysis**

Samples for XRD and bulk geochemistry analyses were prepared as powdered samples with grain size less than 63  $\mu\text{m}$ . Rock samples are first washed with distilled water to remove all dirt and oven-dried at 60-70°C for 24 hrs. Once dried, the samples were broken into smaller pieces. The smaller pieces were subjected to cone and quartering technique (**Fig.3.5A**) to evenly distribute the samples and 50g were then ground with agate mortar and pestle to <63  $\mu\text{m}$  (**Fig 3.5 B**). The samples were then sieved with a 63  $\mu\text{m}$  sieve, if the sample does not pass through the sieve the sample was ground again until the initial 50g grained sample was fully obtained.

Samples were clearly labelled and kept in zip bags before sending for analysis. 20g of sample was sent for XRD analysis and another 10g for geochemical analysis to outsourced laboratories (Monash University, West Malaysia and ACME Lab Canada).



**Figure 3.5 A. Illustration of cone and quartering technique (Adapted from Pitard, 1993), B. The image of Agate mortar with the sample.**

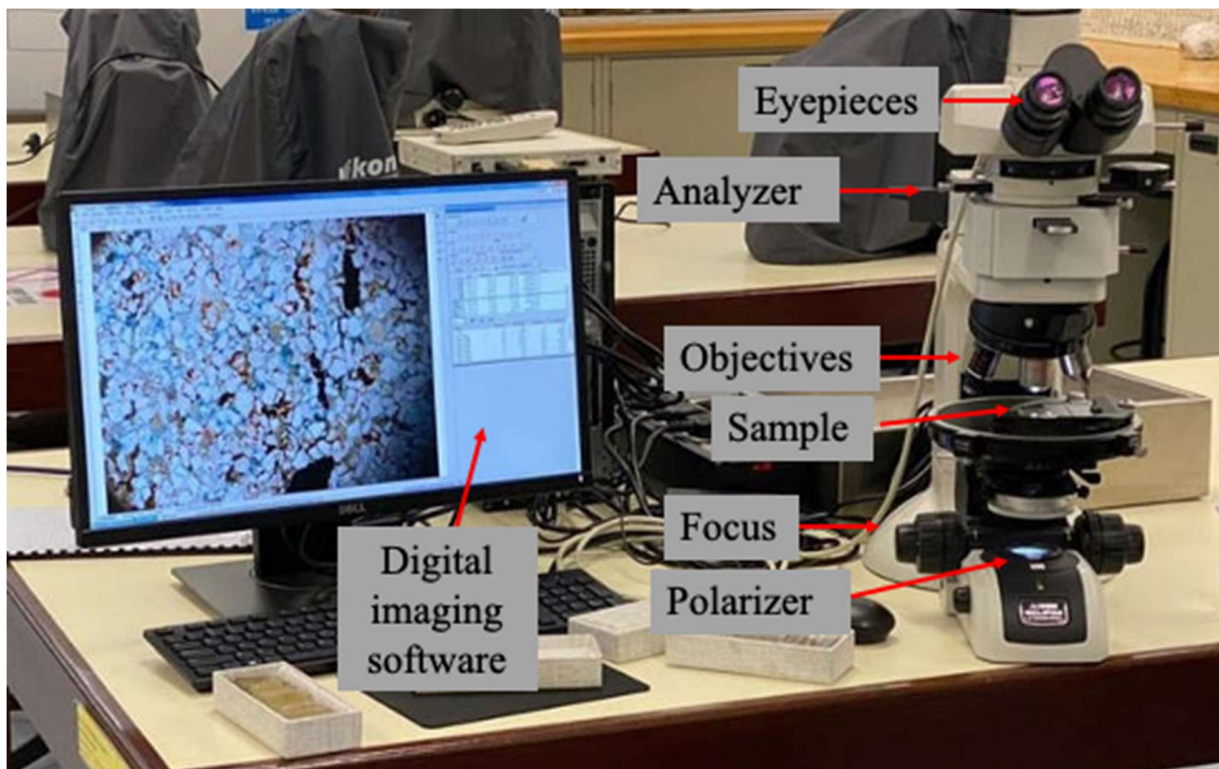
### **3.3.4 Sample preparation for petrophysical analysis**

Core samples were cut using the trim saw to a length range of 1.5-3 inches and the diameter was 2.5 inches constant for all samples. The surfaces of the core samples were evenly smoothing with the Hillquist polishing machines using the 30  $\mu\text{m}$  disk. The samples were then washed with distilled water and oven-dried at 60-70°C for 24 hrs. Samples were analyzed in the petrophysics laboratory at Curtin University Malaysia.

## 3.4 Analysis

### 3.4.1 Thin Section Analysis

The thin section analysis was carried out in the mineralogy laboratory at Curtin University Malaysia. The laboratory is equipped with a polarizing microscope and the microscope is also equipped with Nikon NIS Elements (Digital imaging software) which allows analysis of thin section digital image features such as grain size and grain shape (**Fig 3.6**). Petrographic study point counting was implemented using the updated Gazzi-Dickinson method (Osae et al., 2006). A minimum of 300 points were counted per thin section.



**Figure 3.6** Optical microscope equipped with digital imaging software (Nikon NIS Element).

### **3.4.1.1 Optical Mineralogical Analysis**

All the optical properties of minerals were observed in both PPL and XPL in order to determine the mineralogy of sample, diagenetic features, cement and visual pore spaces. Mineralogical composition of each sample was conducted after examining the optical properties of minerals present and at least 300 points were counted on each thin section in order to evaluate the QFL composition. QFL by Pettijohn (1975) and Folk (1980) as mentioned in chapter 2, was then used to determine the provenance of the studied samples.

Other features observed such as the diagenetic features, cements types and pores were analysed through the captured images using the digital imaging software (Nikon NIS Elements). The results are reported below in section 4.4. of this report.

### **3.4.1.2 Grain Size and Grain shape**

The grain size was first estimated in the field using a hand lens and grain size chart. Measuring grain size in sediments is a basic tool for understanding sedimentary strata and depositional structures (Switzer and Pile, 2015). The grain size of the sediments reflects relative hydrodynamic energy, which is one of the key environmental factors that control sediment particle erosion, transport and deposition (Switzer and Pile, 2015).

One of the most common methods of measuring grain size and grain size distribution is the sieving method. However, since this method would require difficult and time-consuming disaggregation of the collected samples, an alternative digital method was used for this research. This digital image approach was used to analyze at least 300 different grains on each sample, where the Nikon NIS Elements (Digital imaging software) allows grain size measurement. Grain distribution histograms were generated after all-grain analysis using Microsoft Excel.

The grain shape was also estimated using the same software and at least >100 grains on each thin section were considered. After the analysis was done, a data spreadsheet was automatically generated with different parameters such as the area of grain, EqDiameter, Perimeter, MinFerret, MaxFerret, etc. Three parameters were applied to the equations below to calculate the sphericity and roundness of the grains respectively (Liu et al., 2015; Cassel et al., 2018; Berrezueta et al., 2019).



$$\text{Roundness (RD)} = \frac{4A_p}{\pi D_{\text{maxferet}}^2} \quad (\text{Eq. 3.1})$$

$$\text{Circularity (Circ)} = \frac{P_p}{2\sqrt{\pi A_p}} \quad (\text{Eq. 3.2})$$

$$\text{Form factor Sphericity} = \frac{4\pi A_p}{P_p^2} \quad (\text{Eq. 3.3})$$

Where  $A_p$  is the area of the particle,  $P_p$  represents the perimeter of the particle, and  $D_{\text{maxferet}}$  represents the maximum Feret diameter.

### 3.4.2 SEM ANALYSIS

All SEM analyses were carried out in Curtin BioValley Pilot Plant. The analysis was carried out using the Thermo scientific quattro s equipped with wavelength dispersive X-ray spectroscopy (WDS), X-ray spectroscopy (EDS) and electron backscatter diffractor that allows the analysis of samples in their natural state (**Fig 3.7**). Both quartz grain microtextures and diagenetic clay minerals images were captured at different magnification with the voltage of 10-15 kV using either the circular backscatter detector (CBS) or low vacuum detector (LVD).

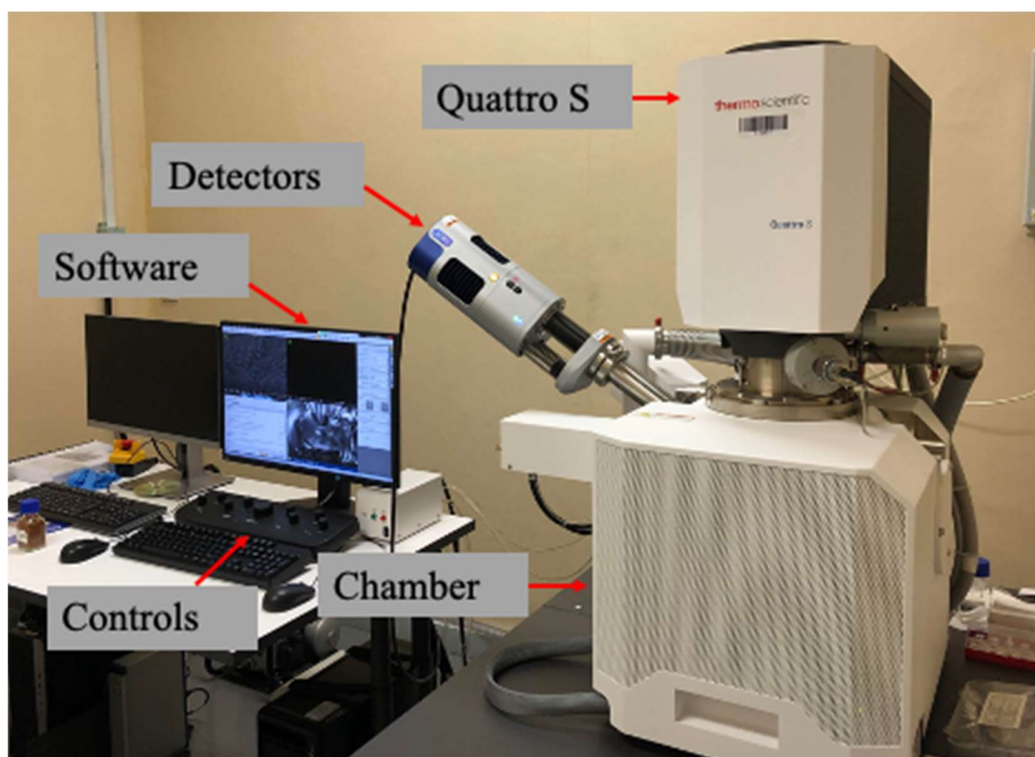


Figure 3.7 Thermo scientific quattro s located in Curtin BioValley Pilot Plant.

### 3.4.3 Mineralogy (XRD) Analysis

6 powdered samples were sent out for XRD analysis to Monash University, Malaysia. The samples were placed on the XRD plate and run/scan using the XRD device (Bruker D8 Discovery). The analysis was carried out using the following parameters: Parameters – Ni Filtered 0.02mm; Cu-K $\alpha$  radiation ( $k = 1.5418 \text{ \AA}$ ); accelerating voltage = 40kV; emission current = 40mA; Bragg-Brentano Scan; 2-theta range =  $5^\circ - 90^\circ$ ; scan rate =  $3^\circ/\text{min}$ ; step size =  $0.03^\circ/\text{step}$ ; sample rotation =  $10^\circ/\text{min}$ ; temperature =  $25^\circ\text{C}$  (Room temperature).

Results obtained from the analysis were interpreted using the DiffracEVA software with the ICDD database.

### 3.4.4 Geochemical Analysis

30 Powdered samples were sent to Bureau Veritas (ACME LAB) Canada for bulk geochemical analysis. The major, trace and REE analyses were carried out using a lithochemical whole-rock fusion package (LF 202 – whole-rock major and trace elements). The rock pulps were mixed with lithium borate or lithium metaborate ( $\text{LiBO}_2/\text{Li}_2\text{B}_4\text{O}_7$ ) flux and the crucibles were fused in a furnace. The cooled bead was dissolved in nitric acid (ACS grade) and analysed using ICP and/or ICP-MS. Loss of Ignition (LOI) was determined by igniting the sample split then measured the weight loss. The Carbon and Sulphur were analysed using the Leco method (TC003). 14 elements such as Ag, As, Au, Bi, Cd, Cu, Hg, Mo, Ni, Pb, Sb, Se, Tl and Zn were analysed after the aqua regia digestion. A replicate analysis was performed to ensure the precision of the analysis. The accuracy for major oxides was within  $\pm 3\%$  and for trace elements, it was within  $\pm 5\%$ . The elements show more deviation ( $> 10\%$ ) and below the detection limit in many samples were not reported in this study.

**Table 3.1 List of oxides and elements analyzed, unit, minimum detection limit and methods.**

Analyte	Unit	MDL	Method	Analyte	Unit	MDL	Method
SiO <sub>2</sub>	%	0.01	LF200	Y	PPM	0.1	LF200
Al <sub>2</sub> O <sub>3</sub>	%	0.01	LF200	La	PPM	0.1	LF200
Fe <sub>2</sub> O <sub>3</sub>	%	0.04	LF200	Ce	PPM	0.1	LF200
MgO	%	0.01	LF200	Pr	PPM	0.02	LF200
CaO	%	0.01	LF200	Nd	PPM	0.3	LF200
Na <sub>2</sub> O	%	0.01	LF200	Sm	PPM	0.05	LF200
K <sub>2</sub> O	%	0.01	LF200	Eu	PPM	0.02	LF200
TiO <sub>2</sub>	%	0.01	LF200	Gd	PPM	0.05	LF200
P <sub>2</sub> O <sub>5</sub>	%	0.01	LF200	Tb	PPM	0.01	LF200
MnO	%	0.01	LF200	Dy	PPM	0.05	LF200
LOI	%	-5.1	LF200	Ho	PPM	0.02	LF200
Sum	%	0.01	LF200	Er	PPM	0.03	LF200
Ba	PPM	1	LF200	Tm	PPM	0.01	LF200
Sc	PPM	1	LF200	Yb	PPM	0.05	LF200
Be	PPM	1	LF200	Lu	PPM	0.01	LF200
Co	PPM	0.2	LF200	TOT/C	%	0.02	TC000
Cr	PPM	13.7	LF201	TOT/S	%	0.02	TC000
Cs	PPM	0.1	LF200	Mo	PPM	0.1	AQ200
Ga	PPM	0.5	LF200	Cu	PPM	0.1	AQ200
Hf	PPM	0.1	LF200	Pb	PPM	0.1	AQ200
Nb	PPM	0.1	LF200	Zn	PPM	1	AQ200
Rb	PPM	0.1	LF200	Ni	PPM	0.1	AQ200
Sn	PPM	1	LF200	As	PPM	0.5	AQ200
Sr	PPM	0.5	LF200	Cd	PPM	0.1	AQ200
Ta	PPM	0.1	LF200	Sb	PPM	0.1	AQ200
Th	PPM	0.2	LF200	Bi	PPM	0.1	AQ200
U	PPM	0.1	LF200	Ag	PPM	0.1	AQ200
V	PPM	8	LF200	Au	PPB	0.5	AQ200
W	PPM	0.5	LF200	Hg	PPM	0.01	AQ200
Zr	PPM	0.1	LF200	Tl	PPM	0.1	AQ200
				Se	PPM	0.5	AQ200

LF200= Lithium Fusion, AQ200= Aqua Regia- ICP-ES/MS, MDL= minimum detection limit.

### 3.4.5 Petrophysical Analysis

The petrophysical analysis is one of the analyses chosen in order to understand the reservoir characteristics in this research. Porosity and permeability analyses were carried out to have a better understanding of the reservoir quality of the Miri Formation based on the following procedure.

#### 3.4.5.1 Permeability

The permeability of 30 core samples was analysed using the TKA-209 gas permeameter available at Petrophysics laboratory Curtin University Malaysia (**Fig 3.8**). The TKA-209 measures the flow characteristics of Nitrogen gas as a fluid of the core samples. The device used steady-state flow and was operated manually. Measured pressure and flow data from the digital display meters on the front panel of the device were used to calculate permeability when steady-state flow conditions were reached. Excel spreadsheets were also provided in the manual to make the calculations easier and the equation below was used for a manual calculation.

$$Ka = \frac{2\mu.Qb.Pb.L}{A(P1^2 - P2^2)} \times 1000 \quad (\text{Eq. 3.4})$$

The viscosity of Nitrogen,

$$\mu = \frac{(13.85 \times T^{1.5})}{(T+102)} \times 0.0001 \quad (\text{Eq. 3.5})$$

Where,

Ka = Permeability to gas (not corrected for slip), millidarcies

$\mu$  = Gas Viscosity, centipoise (At room temperature)

Qb = Flow rate of gas calculated from meter reading (at room conditions), cc/sec

Pb = Atmospheric pressure, atm

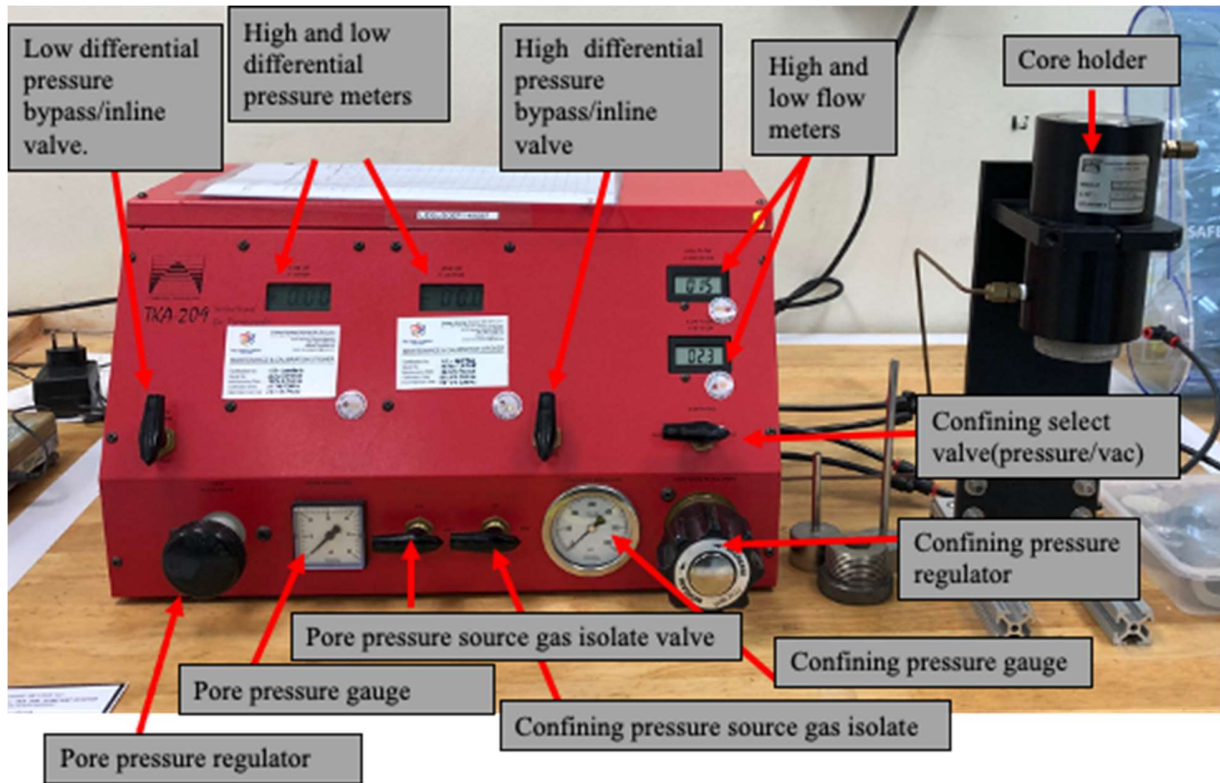
P1 = Inlet pressure, atm

P2 = Outlet pressure, atm

L = Core Sample Length, cm

A = Core Sample Area, cm<sup>2</sup>

T = In Kelvin (degree Celsius + 273)



**Figure 3.8 TKA-290 gas permeameter located in petrophysics laboratory, Curtin University Malaysia.**

### 3.4.5.2 Porosity

The porosity of 30 core samples was analysed using the TPI-219 helium porosimeter available at the Petrophysics laboratory of Curtin University Malaysia (**Fig 3.9**). The TPI-219 helium porosimeter was operated manually primarily used to obtain the grain volume of the core samples. As defined earlier in Chapter 2 the porosity is the volume-to-bulk ratio of pores (Kennedy, 2015; Tiab and Donaldson, 2012). Therefore, applying the Boyle relationship which states; there is an inverse relationship between volume and pressure for the ideal gas in conditions of constant temperature and quantity  $P_1V_1 = P_2V_2$  is applicable when using the helium porosimeter. The relationship  $P_1V_1 = P_2V_2$  allows us to determine the volume of grain using the TPI-219 pressure chamber. Helium gas was used since it's an inert gas with a small atom and can penetrate even the smallest void space in the core sample.

The porosity of the sample was calculated using pore volume and bulk volume. The pore volume can be calculated in two ways and using the following equations.

1. Porosity by Grain Volume Measurement.

$$\text{Porosity} = \left( \frac{\text{Bulk Volume, cm}^3 - \text{Grain Volume, cm}^3}{\text{Bulk Volume, cm}^3} \right) \times 100 \quad (\text{Eq. 3.6})$$

2. Porosity by Direct Pore Volume Measurement

$$\text{Porosity} = \left( \frac{\text{Pore Volume, cm}^3}{\text{Bulk Volume, cm}^3} \right) \times 100 \quad (\text{Eq. 3.7})$$

Bulk volume of core sample was calculated by measuring the diameter and length of the cylindrical core sample with a caliper and calculating the volume of cylinder as equation below:

$$V = \pi r^2 h \quad (\text{Eq. 3.8})$$

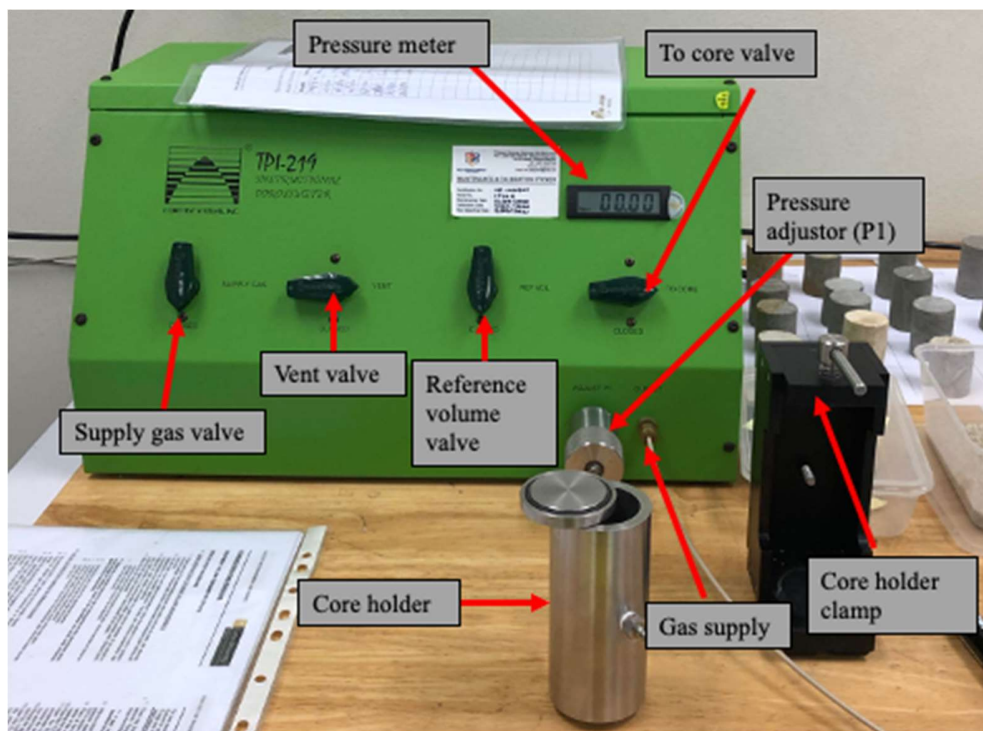


Figure 3.9 TPI-219 helium porosimeter available at Petrophysics laboratory, Curtin University Malaysia.

### 3.4.6. Data Interpretation

The major oxides were recalculated to anhydrous (LOI free) basis before constructing major oxide-based plots and to calculate various geochemical ratios. Various weathering indicators were calculated, in which CIA, CIW and WIP were used for the present study. The CIA values were calculated using the formula (molecular proportion) proposed by Nesbitt and Young (1982).

$$\text{CIA} = [\text{Al}_2\text{O}_3 / (\text{Al}_2\text{O}_3 + \text{CaO}^* + \text{K}_2\text{O} + \text{Na}_2\text{O})] \times 100 \quad (\text{Eq. 3.9})$$

Where, CaO\* represents CaO associated with silicate fractions only. In order to calculate CaO in silicate fraction, CO<sub>2</sub> data is required. But, for the present study, we do not have the CO<sub>2</sub> data. Thus, to estimate the CaO\* data, the assumptions suggested by McLennan (1993) were used (e.g., Bock et al., 1998; Thorpe et al., 2019; Nagarajan et al., 2021). Initially, the carbonate associated with the phosphate minerals was removed using the formula

$$(\text{CaO}^* = \text{CaO} - (\text{P}_2\text{O}_5 * 10/3)). \quad (\text{Eq. 3.10})$$

After calculating these values, which were compared with the molar proportion of Na<sub>2</sub>O, if the CaO\* values equal to or lesser than Na<sub>2</sub>O were considered as it is while the values greater than Na<sub>2</sub>O then CaO\* values were assumed to be equal to Na<sub>2</sub>O. In the present study, only for two samples, the assumption was made while other samples show very low CaO values and thus, this adjustment was not required.

The Chemical Index of Weathering (CIW) proposed by Harnois (1988) was also used in addition to CIA to overcome if there any metasomatic effect on the CIA values. The CIW values were calculated using the formula

$$\text{CIW} = [\text{Al}_2\text{O}_3 / (\text{Al}_2\text{O}_3 + \text{CaO} + \text{Na}_2\text{O}) * 100] \quad (\text{Eq. 3.11})$$

The Plagioclase Index of Alteration (PIA) proposed by Fedo et al. (1995) was also used in this study to strengthen the interpretation of weathering intensity based on CIA. The PIA values were calculated using the formula

$$\text{PIA} = (100) (\text{Al}_2\text{O}_3 - \text{K}_2\text{O}) / (\text{Al}_2\text{O}_3 + \text{CaO}^* + \text{Na}_2\text{O} + \text{K}_2\text{O}) \quad (\text{Eq. 3.12})$$



The Index of Compositional Variability (ICV) can be used to estimate the shales and siltstones' original composition (Cox et al., 1995), in addition, the weathering intensity and chemical maturity also can be established. The ICV values were calculated using the formula

$$\text{ICV} = (\text{Fe}_2\text{O}_3 + \text{K}_2\text{O} + \text{Na}_2\text{O} + \text{CaO} + \text{MgO} + \text{MnO} + \text{TiO}_2)/\text{Al}_2\text{O}_3 \quad (\text{Eq. 3.13})$$

The rare earth elements (REEs) were normalized against the chondrite values (McDonough and Sun, 1995) and various indices were calculated after the normalization. Accordingly, the Eu anomaly was calculated using the formula

$$\text{Eu}/\text{Eu}^* = \text{Eu}_{\text{cn}}/[(\text{Sm}_{\text{cn}})(\text{Gd}_{\text{cn}})]^{1/2} \quad (\text{Eq. 3.14})$$

Where subscript cn refers to chondrite-normalized values (McDonough and Sun, 1995).

Major oxides based provenance discriminant function diagram of Roser and Korsch, (1988) was calculated using the following formula as DF1 and DF2 respectively,

$$\text{The discriminant function 1} = (-1.773 \times \text{TiO}_2) + (0.607 \times \text{Al}_2\text{O}_3) + (0.760 \times \text{Fe}_2\text{O}_3) + (-1.500 \times \text{MgO}) + (0.616 \times \text{CaO}) + (0.509 \times \text{Na}_2\text{O}) + (-1.224 \times \text{K}_2\text{O}) + (-9.090) \quad (\text{Eq. 3.15})$$

$$\text{and discriminant function 2} = (0.445 \times \text{TiO}_2) + (0.070 \times \text{Al}_2\text{O}_3) + (-0.250 \times \text{Fe}_2\text{O}_3) + (-1.142 \times \text{MgO}) + (0.438 \times \text{CaO}) + (1.475 \times \text{Na}_2\text{O}) + (1.426 \times \text{K}_2\text{O}) + (-6.861) \quad (\text{Eq. 3.16})$$

Tectonic setting discrimination diagram (Verma and Armstrong-Altrin, 2016) based on major oxides was calculated using the formula.

$$\text{(A) based on Major Oxides DF(A-P) M} = (3.0005 \times \text{ilr1TiM}) + (-2.8243 \times \text{ilr2AlM}) + (-1.0596 \times \text{ilr3FeM}) + (-0.7056 \times \text{ilr4MnM}) + (-0.3044 \times \text{ilr5MgM}) + (-0.6277 \times \text{ilr6CaM}) + (-1.1838 \times \text{ilr7NaM}) + (1.5915 \times \text{ilr8KM}) + (0.1526 \times \text{ilr9PM}) - 5.9948 \quad (\text{Eq. 3.17})$$

$$\text{and (B) based on trace element DF(A-P)MT} = (3.2683 \times \text{ilr1TiMT}) + (5.3873 \times \text{ilr2AlMT}) + (1.5546 \times \text{ilr3FeMT}) + (3.2166 \times \text{ilr4MnMT}) + (4.7542 \times \text{ilr5MgMT}) + (2.0390 \times \text{ilr6CaMT}) +$$

$$(4.0490 \times \text{ilr7NaMT}) + (3.1505 \times \text{ilr8KMT}) + (2.3688 \times \text{ilr9PMT}) + (2.8354 \times \text{ilr10CrMT}) + \\ (0.9011 \times \text{ilr11NbMT}) + (1.9128 \times \text{ilr12NiMT}) + (2.9094 \times \text{ilr13VMT}) + (4.1507 \times \text{ilr14YMT}) \\ + (3.4871 \times \text{ilr15ZrMT}) - 3.2088 \quad (\text{Eq. 3.18})$$

The detailed procedures for analysis are included in appendix 4.0.

# CHAPTER 4

## RESULTS AND DISCUSSION

### 4.1 Introduction

This chapter reports all the results obtained from the various analyses carried out in the study starting from the field study, petrography (thin sections, SEM of quartz grain microtextures and reservoir properties), bulk mineralogy (XRD), bulk geochemical analysis and petrophysical analysis (porosity and permeability) in order to elucidate the paleo-weathering, provenance, tectonic setting, diagenesis and reservoir characteristics of the sedimentary rocks of the Miri Formation.

### 4.2 Studied Outcrops

A total of four outcrops were selected for this study (**Fig. 3.2**). The four outcrops chosen are; Hospital outcrop (4°22'51.51"N and 113°59'35.21"E), Bomba outcrop (4°23'34.68"N and 113°59'32.25"E), Taman Awam outcrop (4°21'57.03"N and 113°58'45.37"E) and Tanjung Lobang Outcrop (4°22'11.87"N and 113°58'3.67"E) and the outcrops were chosen based on accessibility, safety and geologic relevance to this research project.

## 4.2.1 Hospital Outcrop

Hospital outcrop (**Fig.4.1 A**) is one of the most popular outcrops belonging to the lower Miri Formation. The outcrop is located near the Miri general hospital, thus, called as “hospital outcrop”. The outcrop is located at Lat. 4°22'51.51"N and Long. 113°59'35.21"E. The outcrop is well exposed with a total height of about 32m, however, only 10m of the outcrop was observed due to inaccessibility and safety reasons. A stratigraphic log was produced, and 23 samples were collected from the 4 units observed as shown in figure 4.1 B. The outcrop consists of interbedded sandstone/mudstones and sandstone beds orienting at approximately 044/10°NW, with trace fossils such as *Ophiomorpha* burrows mostly observed in HO2 and HO4 (**Fig 4.2**). The alternating thickness of the beds is observed ranging from 50 to 185cm for sandstone beds and 10-100cm interbedded sandstone- mudstone beds. A fining upward of the lithology was also observed with a perfect/wavy contact boundary between the units. The detailed stratigraphic log is presented in figure 4.2.

Based on the stratigraphic log, the outcrop is divided into four units. The first unit is about 2.5m thick consisting of very fine-grained, bioturbated sandstone with mud clasts, fine-grained, swelling planar cross stratified sandstone and sandstone interbedded with mudstone. Unit II is about 2.5m and it is made up of fine to very fine-grained, massive bioturbated sandstone with significant distribution of trace fossils (*Ophiomorpha*) throughout the unit. Sedimentary structures include planar cross-stratification and parallel lamination. Unit III consists of very fine-grained interbedded sandstone/mudstone with the thickness of sandstone reducing at the top of the unit about 10-20cm. Unit IV is 1m thick and made up of fine to very fine-grained, parallel laminated sandstone with planar bedding.

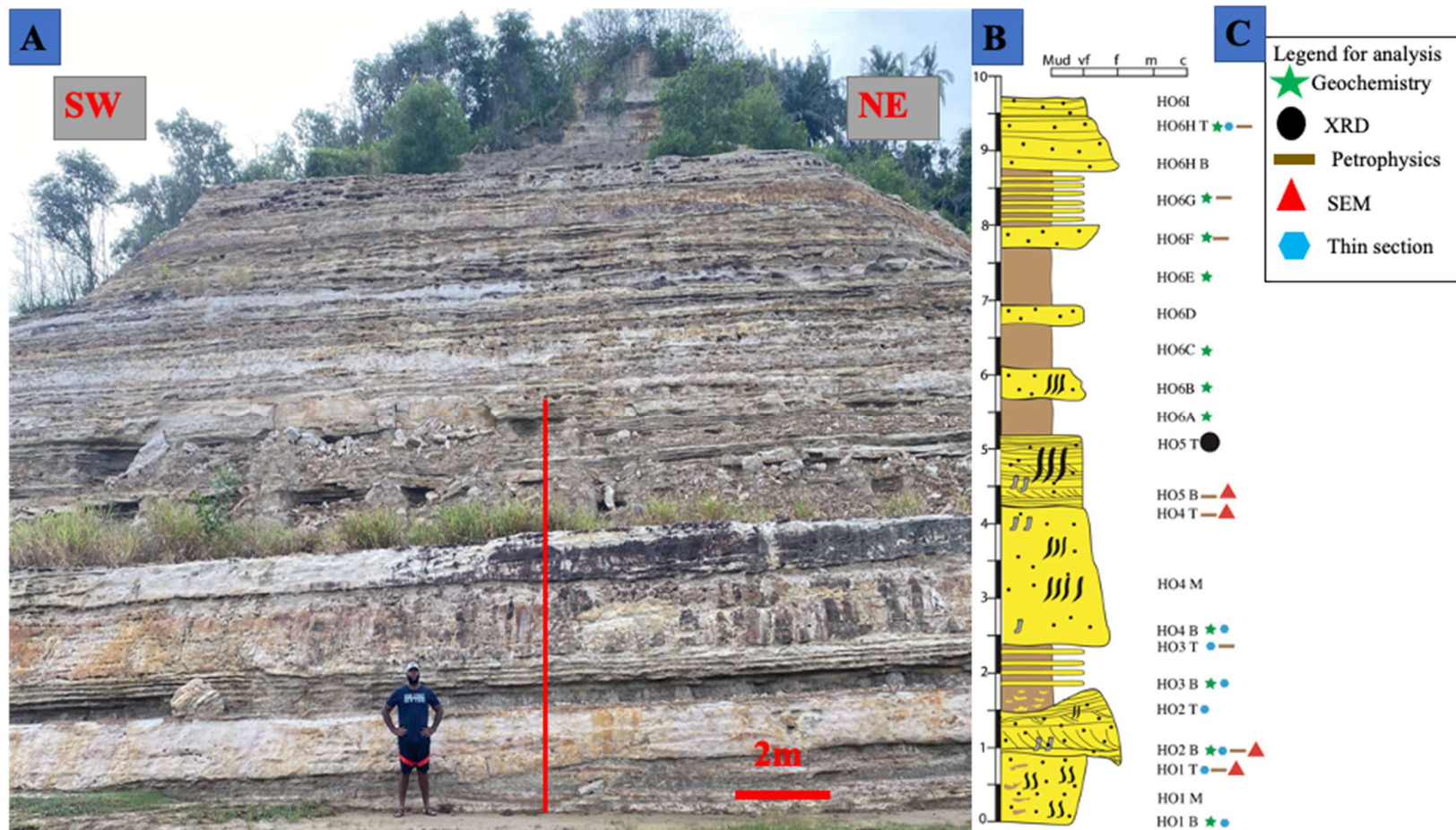


Figure 4.1 Image of A-Hospital outcrop, the red bar represents the stratigraphic log section, B- stratigraphic log section showing the location of samples collected, C- Legend for sample analysis.

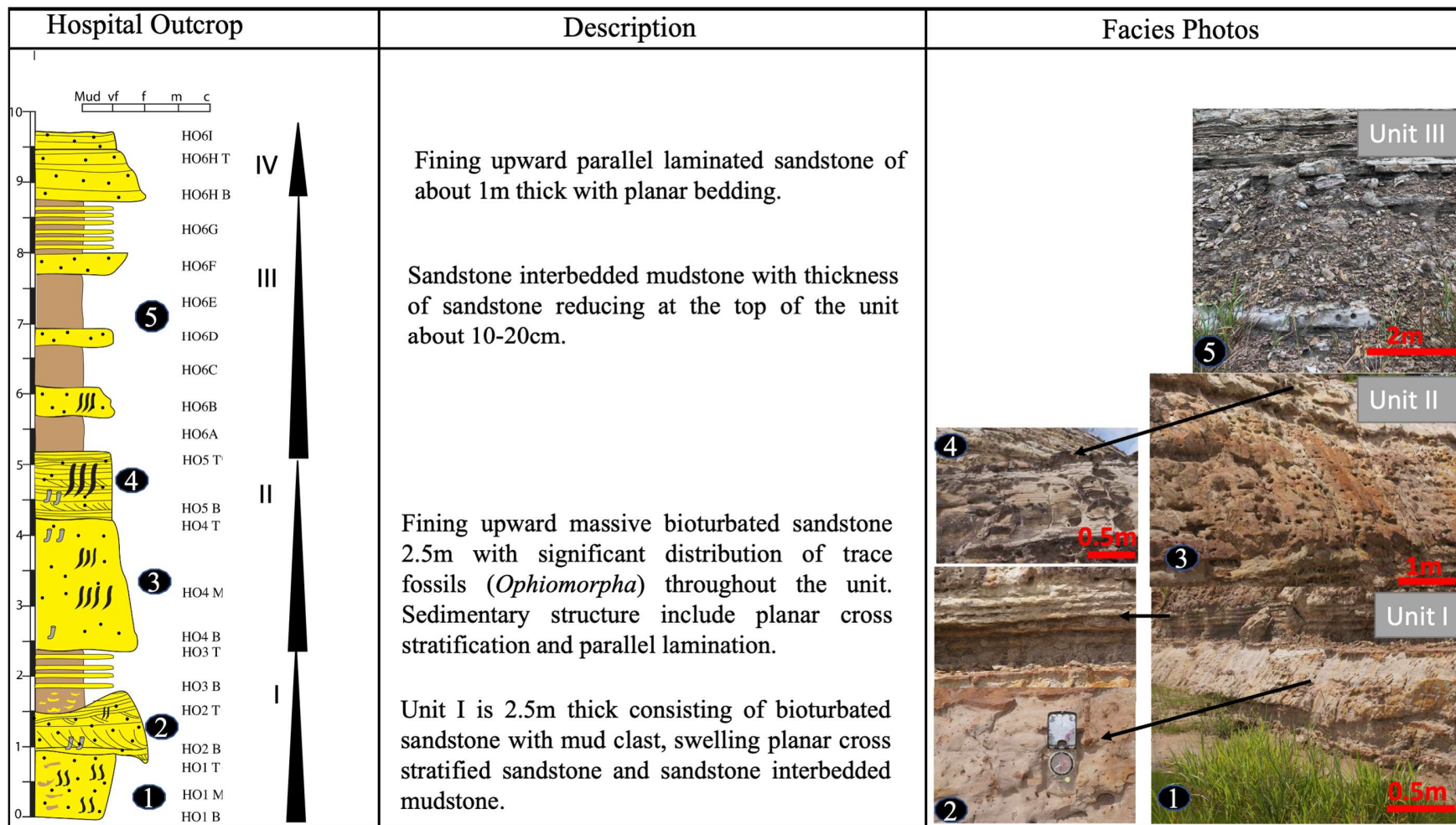


Figure 4.2 Stratigraphic log of the Hospital outcrop, showing the details of the four sedimentary units (I to IV) with description and facies photos.

## 4.2.2 Bomba Outcrop

The Bomba outcrop (**Fig.4.3 A**) is a newly exposed outcrop due to the construction of a new SESCO 33kV electrical substation located at Lat.4°23'34.68"N Long.113°59'32.25"E adjacent to the Miri Bomba station. The outcrop is about 8m high but only 6.7m of the outcrop was observed and logged due to the steepness in the topmost part of the outcrop. The outcrop is dominated by sandstones and minor mudstone layers and is orienting at approximately 082/14°N. The sandstone beds' thickness varies from 0.5 to 2 m, mudstone 0.1 to 0.5 m and interbedded layers of 10 to 20 cm thickness. The sandstone grains are mostly very fine to fine-grained. The stratigraphic log of the outcrop is presented in figure 4.4 with the collected sample positions.

Based on the stratigraphic log (**Fig 4.4**), the outcrop is divided into four units. Unit I is formed by 0.3- 0.5 m of very fine to fine-grained parallel laminated sandstone and mudstone with coal clast. Unit II is 2 m thick cross stratified and parallel laminated sandstone at the top. Unit III is about 1.5 m thick of sandstone interbedded mudstone with a 50/50 proportion. Unit IV is made up of massive fine-grained sandstone with minor bioturbation.

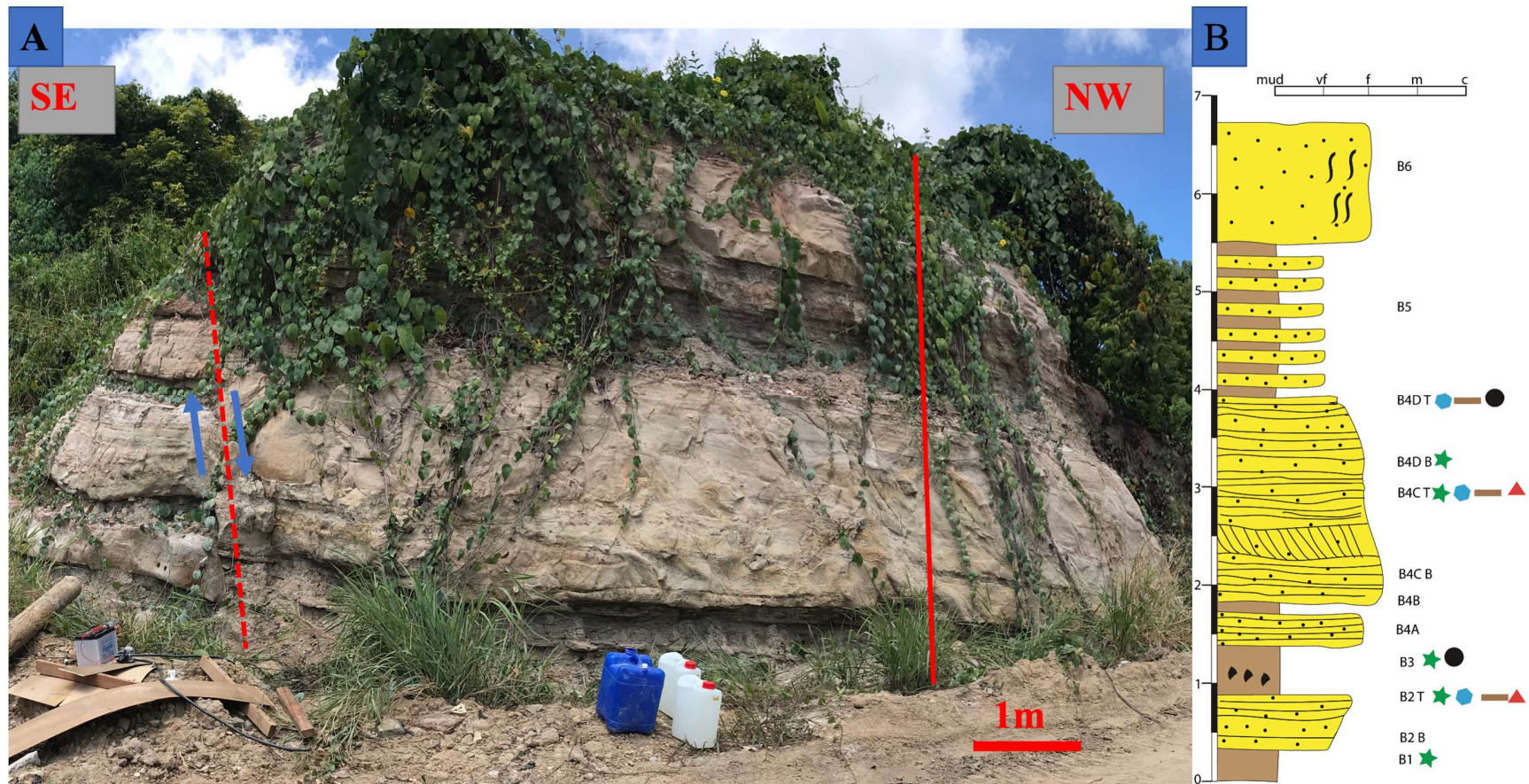
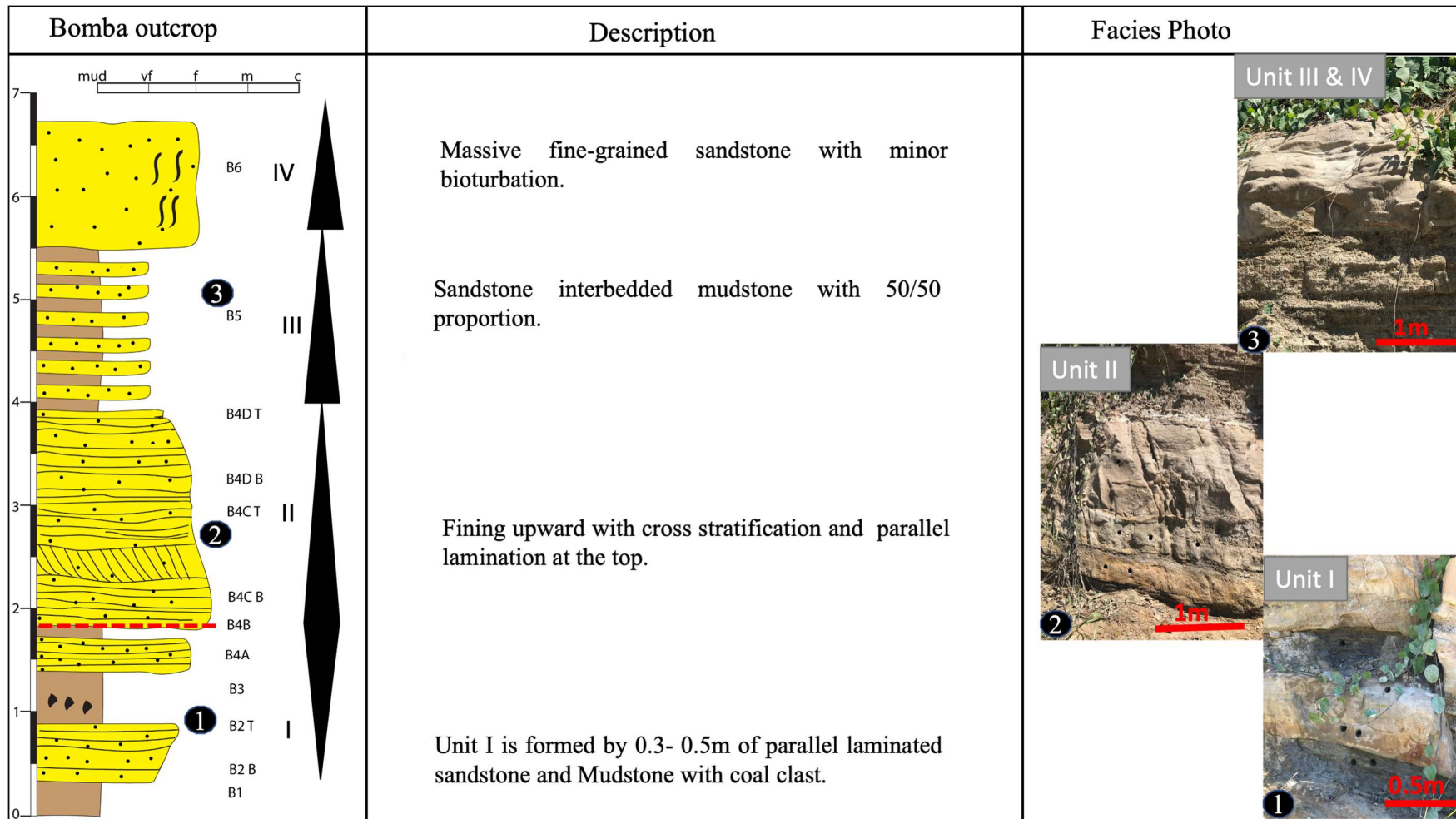


Figure 4.3 Image of A. The Bomba outcrop mainly consists of thick sandstone beds and thin mudstone beds, the red bar represents the stratigraphic log section. B. stratigraphic log section showing the location of samples collected.





**Figure 4.4 Stratigraphic log of the Bomba outcrop, showing the details of the four sedimentary units (I to IV) with description and facies photos.**

### 4.2.3 Taman Awam Outcrop

The Taman Awam outcrop (**Fig 4.5 A**) is also recently exposed outcrop along the airport road ( $4^{\circ}21'57.03''\text{N}$ ,  $113^{\circ}58'45.37''\text{E}$ ) at the Taman Awam park (A geoheritage site). The outcrop is exposed in the S – N direction and dipping towards the SSE yielding a long stretch of about 100 m exposure of the outcrop with an approximate height of 22 m. The outcrop is mostly dominated by different sandstone facies such as massive sandstone, cross-laminated, parallel laminated sandstone and sandstone interbedded mudstone with siltstone and is oriented at  $060/18^{\circ}$  SE. The thickness of the alternating beds ranges from 50 to 200 cm for sandstone beds and 5-10 cm interbedded sandstone mudstone and siltstone beds. Many normal and reverse faults are also observed in the outcrop with a displacement of 10cm for the minor faults and about 50cm for the major faults. Due to the long exposure of the outcrop, a stack image from bottom to top is provided below (**Fig 4.5A**). Figure 4.6 represents the detailed stratigraphic representation and descriptions of the outcrop while the location of the collected samples is represented in Figure 4.5B.

The outcrop is divided into five units. Unit I is 1.8m thick consisting of sandstone interbedded mudstone and siltstone, proportion of sandstone beds at the top is 60/40 sandstone dominated with organic laminae and mud clast. Unit II consist of fine to very fine-grained minor bioturbated sandstone bed with mud clast and interbedded sandstone mudstone. Unit III consists of medium-grained hummocky cross stratified sandstone, sandstone interbedded mudstone, minor bioturbated sandstone, sandstone interbedded mudstone (20-30cm thick) and 2m thick medium-grained sandstone. Unit IV includes thin beds of very fine-grained sandstone interbedded mudstone at a 50/50 proportion and fine to very fine-grained planar cross-stratified sandstone. Unit V includes thin beds of mudstone and massive fine-grained sandstone.



Figure 4.5 Image of A.Taman Awam outcrop, Images are stacked from bottom to top bed, length of the outcrop is about 100m with a thickness of 22m. B. stratigraphic log section showing the location of samples collected

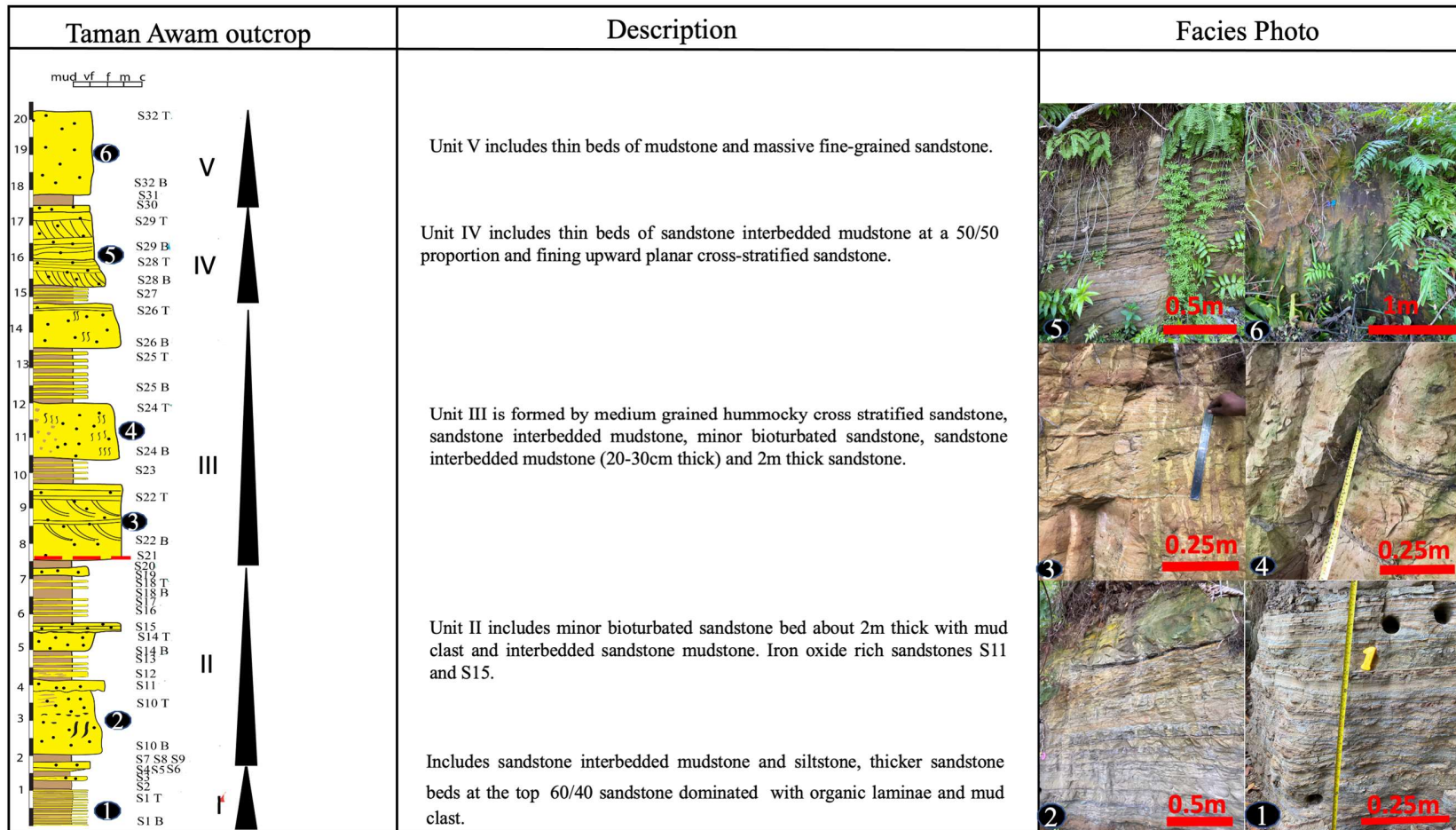


Figure 4.6 Stratigraphic log of the Taman Awam outcrop, showing the details of the five sedimentary units (I to V) with description and facies photos.

## 4.2.4 Tanjung Lobang Outcrop

The Tanjung Lobang outcrop (**Fig 4.7 A**) is a well-exposed outcrop along the coastal line in Tanjung beach. The outcrop is located at Lat:4°22'11.87"N and Long: 113°58'3.67"E. The outcrop is only accessible at low tide, thus the optimum tidal time was chosen for the fieldwork. A total of 3 units are observed in the outcrop starting with a 1-meter-thick sandstone bed, the second unit is a highly bioturbated layer with hummocky cross-stratification. The beds are orienting at 045/20 °NW and possess a fining upward sequence, with trace fossils such as *Ophiomorpha* burrows mostly observed in unit 2. Figure 4.8 is the stratigraphic representation of the outcrop and the location of samples is shown in Figure 4.7B.



**Figure 4.7. Image of The Tanjung Lobang outcrop (a cross-laminated and bioturbated sandstone facies) the red bar represents the stratigraphic log section.**

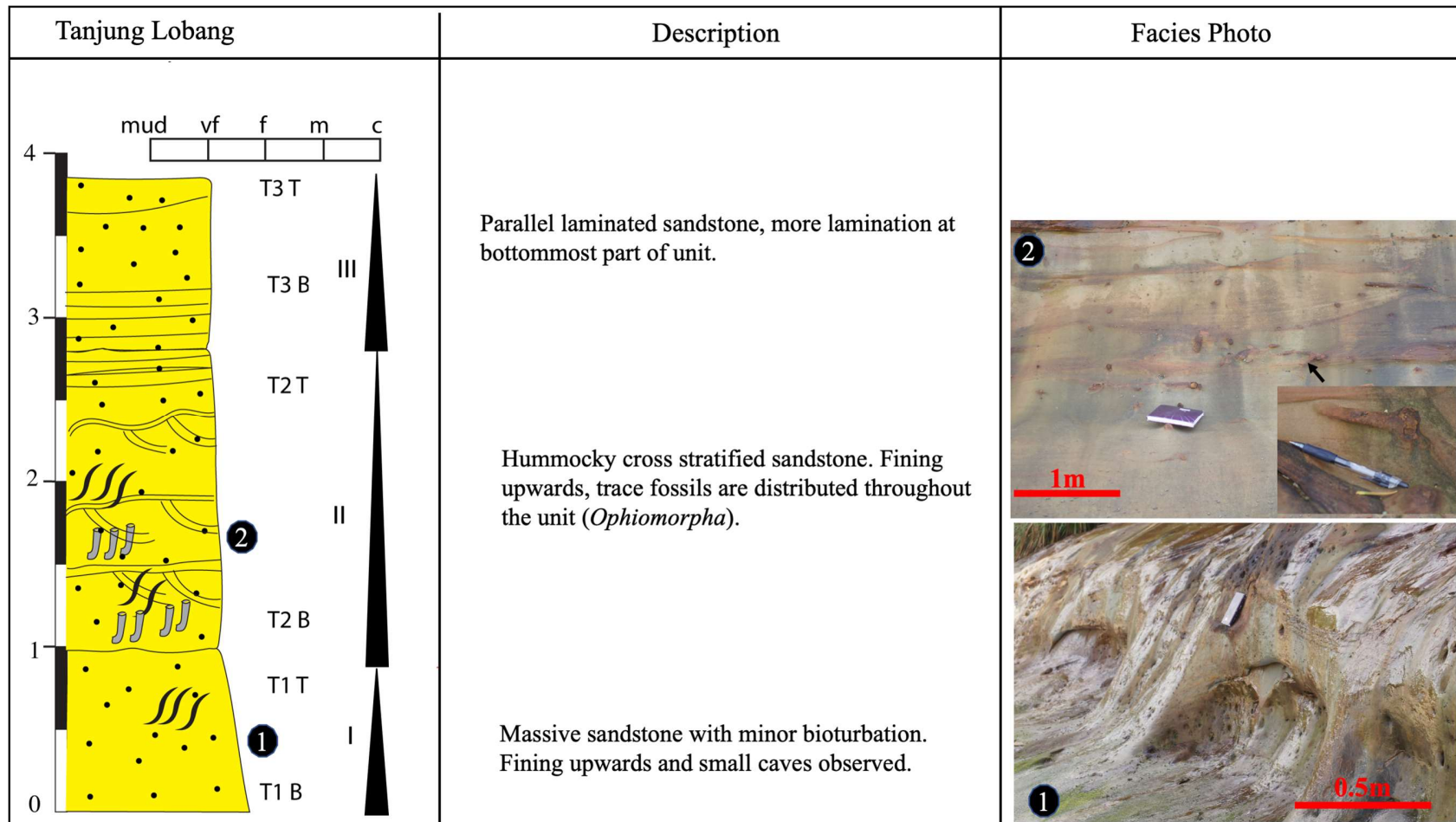


Figure 4.8 Stratigraphic log of the Tanjung Lobang outcrop, showing the details of the three sedimentary units (I to III) with description and facies photos.

## 4.3 Samples Description

All studied samples are first divided into three main groups based on their lithological variations (Pettijohn, 1975; Pettijohn et al., 1987; Tucker, 1991). These include sandstone, sandstone interbedded mudstone and mudstones. The names based on the field classification of the rock samples are used throughout the discussion part of this report. Details of all sample types and analysis carried out are provided in Appendix 6.0, Table 7.10 1 and Table 7.10 2.

## 4.4 Petrography

The petrography of the clastic sedimentary rocks samples of the Miri Formation is analysed via thin sections, SEM and X-ray diffraction (XRD) studies, which are detailed below.

### 4.4.1 Petrographic Classification/modal composition

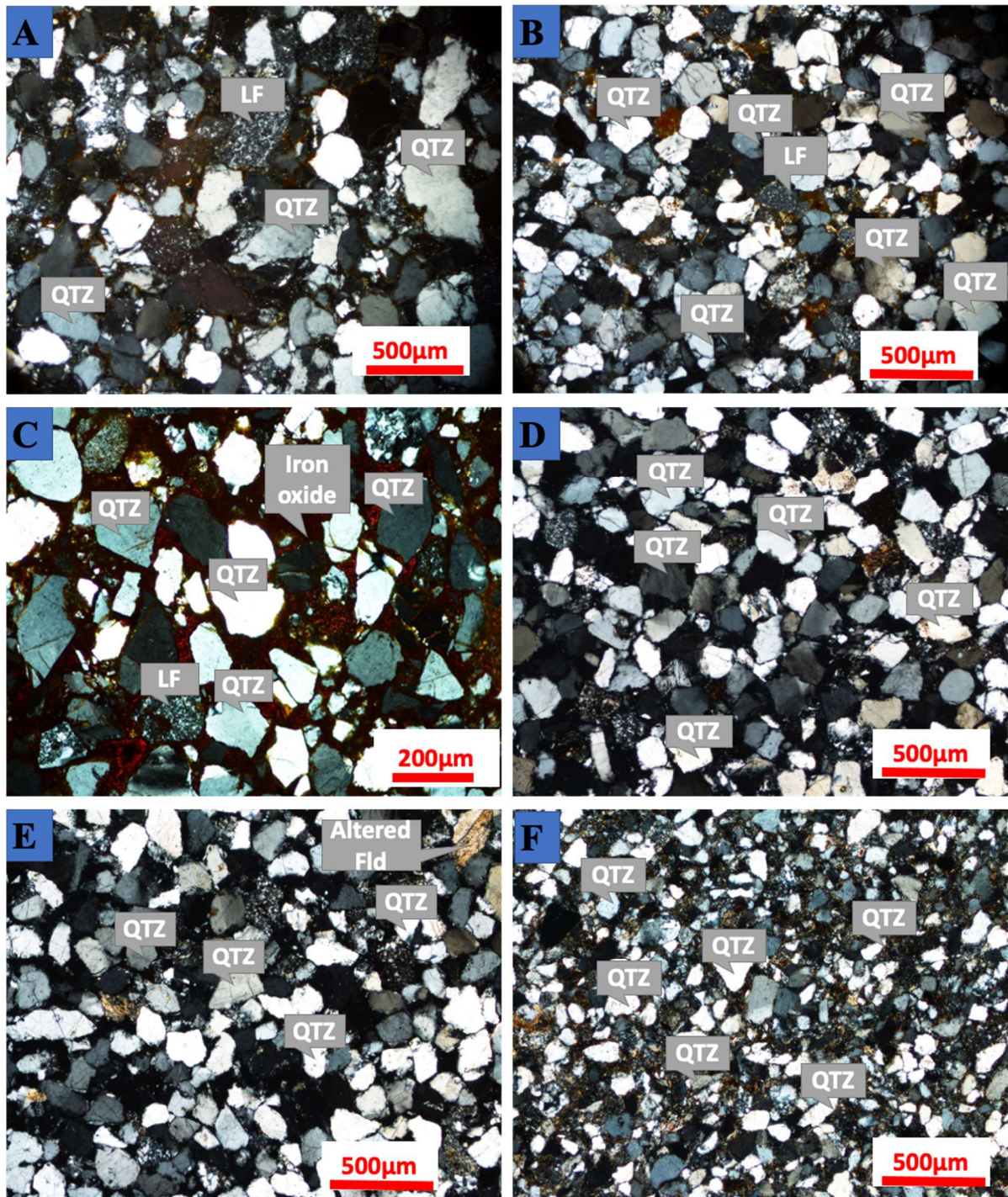
The sandstone samples of the Miri Formation are made up of the framework grains, matrix, cement, accessory minerals and pores. The grains are generally very fine to medium-grained (**Table 4.3**), subangular to subrounded and moderate to well sorted. The common types of grain contact observed in the studied samples include point contact, line contact and in few sutured contacts. However, an abundance of point contact was noted in most of the samples (**Fig. 4.9, 4.10**). The framework grains of the sandstones are composed of quartz (monocrystalline quartz (Qtzm) and polycrystalline quartz (Qtzp), feldspar (Fld) and lithic fragments (LF), while the matrix is mostly clay minerals and the precipitated cement present in the samples are mostly silica, iron oxide in few samples and calcite in only two samples. The mean matrix content of the analysed samples is 3-15%. Based on the Folk (1974) classification, the Miri Formation sandstones are classified as quartz arenite and sublithic arenites (**Fig. 4.11**). The quartz arenites are generally medium-grained, whereas sublithic arenites are very fine to fine-grained.

**Table 4.1 The petrographic framework of the sandstone samples from the Miri Formation.**

Sample No	Qtz m	Qtzp	LF	Fld	TQtz	TLF	TFld	Q%	L%	F%
HO1 Bottom	241	13	16	7	254	16	7	91.7%	5.8%	2.5%
HO1 Top	300	12	16	8	312	16	8	92.9%	4.7%	2.4%
HO2 Middle	277	13	24	2	290	24	2	91.8%	7.6%	0.6%
HO2 Top	274	13	12	3	287	12	3	95%	4%	1%
HO3 Bottom	296	12	11	2	308	11	2	96%	3%	1%
HO3 Top	251	18	42	5	269	42	5	85%	13%	2%
HO4 Bottom	404	13	50	4	417	50	4	89%	11%	1%
S10 Top	356	15	49	5	371	49	5	87%	12%	1%
S11	298	10	19	0	308	19	0	94%	6%	0%
S14 Top	355	10	13	4	365	13	4	96%	3%	1%
S18Top	300	7	35	2	307	35	2	89.2%	10.2%	0.01%
S22Top	250	8	25	1	258	25	1	91%	9%	0%
S24Bottom	294	10	28	0	304	28	0	92%	8%	0%
S26Top	301	9	21	2	310	21	2	93%	6%	1%
S29Top	282	13	44	3	295	44	3	86%	13%	1%
S32 Top	279	10	37	4	289	37	4	88%	11%	1%
T1Top	212	13	55	3	225	55	3	80%	19%	1%
T2Top	229	11	45	5	240	45	5	82.8%	15.5%	1.7%
T3Top	262	8	57	6	270	57	6	81%	17%	2%
B2Top	283	12	56	3	295	56	3	83%	16%	1%
B4DTop	239	11	50	3	250	50	3	82.5%	16.5%	1%
HO2Bottom	229	15	71	4	244	71	4	76.5%	22.2%	1.3%
HO4Bottom	244	10	75	2	254	75	2	77%	23%	1%
HO5Top	268	11	40	5	279	40	5	86%	12%	2%
HO6H Top	217	14	53	7	231	53	7	79.4%	18.2%	2.4%

Qtz m- Quartz monocrystalline, Qtz p- Quartz polycrystalline, LF- lithic fragments, Fld- feldspar, T- Total. Q-quartz, L-Lithics and F-feldspar





**Figure 4.9** Microphotographs (in XPL) of the siliciclastic rocks of the Miri Formation, A (S22 Top), B (S24 Top), C- (S11)- Fe-rich sublitharenite, D- (S24 Bottom), E- (S26 Bottom) Quartz arenite, and F- (HO3 Top)- Sublitharenite

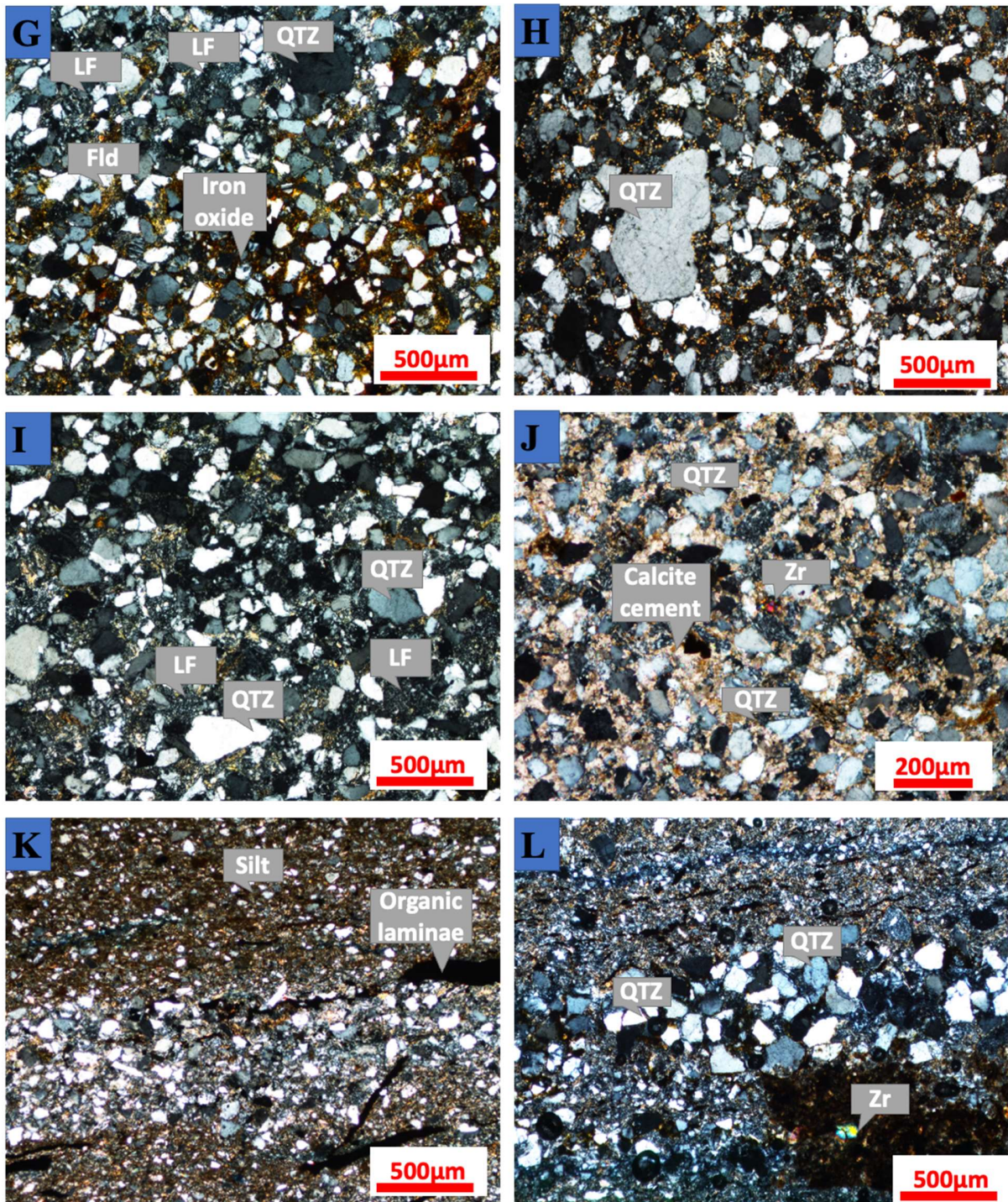


Figure 4.10. Microphotographs (under XPL) of the siliciclastic rocks of the Miri Formation, G- Fe-rich sublitharenite (S11), H and I- poorly sorted sublitharenite, (HO2 Bottom and HO3 Bottom respectively), J- calcite cement (B2 Top), K- organic laminated siltstone (S1 Top), and L- interbedded sandstone (S1 Bottom).

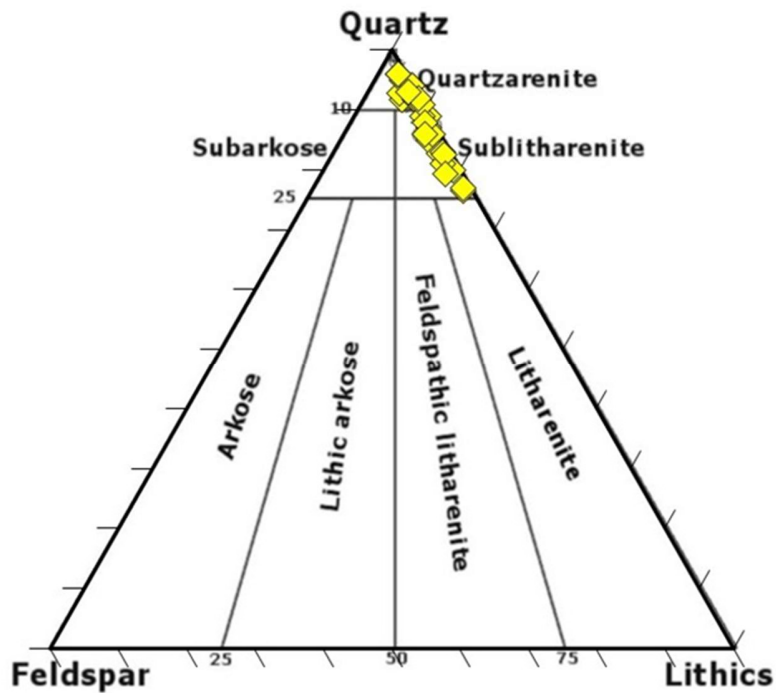
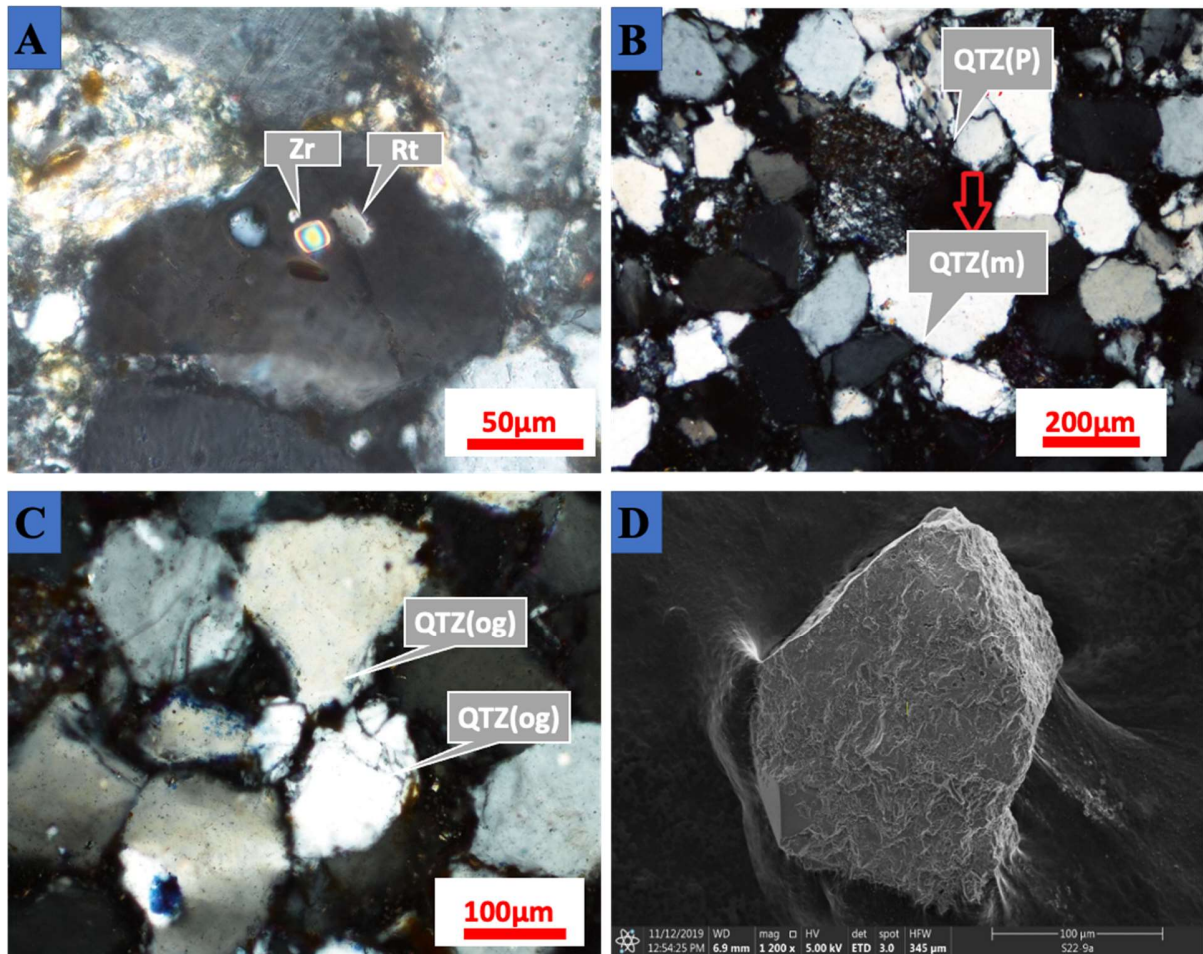


Figure 4.11 Q-F-L ternary plot: Petrographic classification of the Miri Formation sandstones (Folk, 1974).

#### 4.4.1.1 Quartz

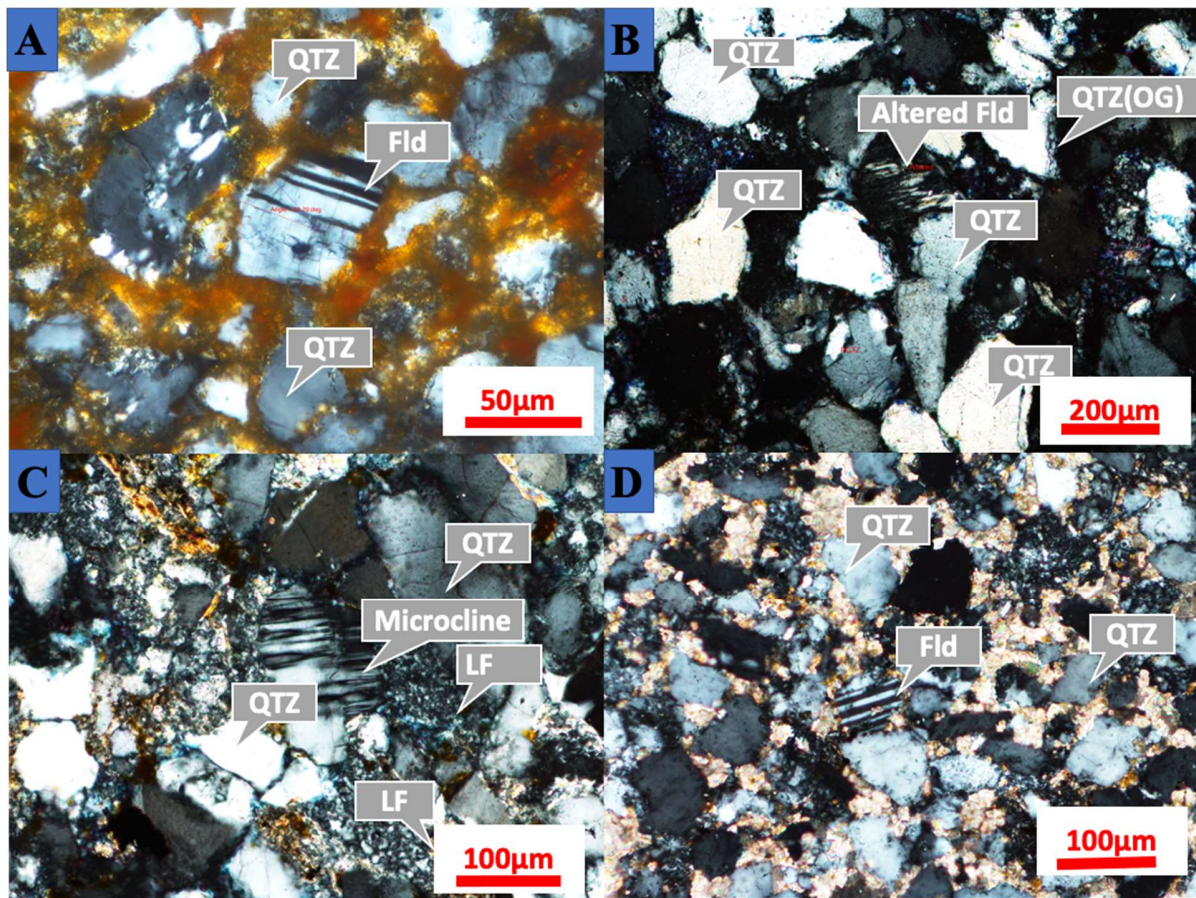
Quartz is the most dominant mineral which constitutes about 76.5-96% of the framework grains in the sandstones. Both monocrystalline and polycrystalline quartz grains are present in the Miri Formation samples, with the monocrystalline quartz dominating the framework composition. The monocrystalline quartz grains are subangular to subrounded, very fine to fine-grained in size with some of the monocrystalline quartz grains showing an undulose extinction. Common features observed on the quartz grains are the inclusion of trace minerals such as zircon and rutile (Fig.4.12 A), and also the precipitation of secondary overgrowth around the original detrital grain boundary (Fig.4.12 B, C). The polycrystalline quartz grains are texturally sub-angular to sub-rounded, very fine to fine-grained in size.



**Figure 4.12** Micro (under XPL) and SEM photographs of the siliciclastic rocks of the Miri Formation, A-Quartz with the inclusion of zircon and rutile (B4cBottom). B- (S24Bottom), C- (S24Top)- Quartz overgrowth and D- SEM image of a sub-rounded quartz grain (S22)

#### 4.4.1.2 Feldspar

Feldspars constitute about 1-3% of the total framework grains present in the Miri Formation sandstones. Plagioclase feldspar (albite and andesine; **Fig. 4.14, 4.14**) and alkali feldspar (orthoclase and microcline) are the common feldspar minerals observed in the study, with the plagioclase being the most abundant found. The feldspars are sub-angular to sub-rounded, very fine to fine-grained. Occasionally, the feldspars tend to be patchy and cloudy and have brownish coatings on the grains and in some cases altered to clay minerals, mica, or replaced by calcite (**Fig. 4.13D**).

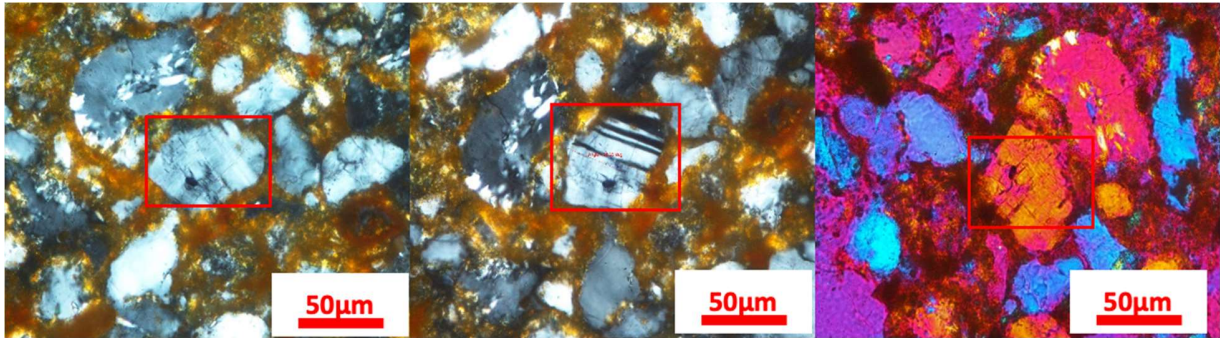


**Figure 4.13** The Microphotographs (under XPL) show the feldspar types, A- Plagioclase feldspar (S3 Top), B –cloudy altered feldspar (S24 Top), C- Microcline (S32 Top) and D- Plagioclase feldspar (B2Top).

The extinction angle of plagioclase feldspar was observed using Michel- Levy’s method (Fig 4.14) and reported in Table 4.2 below

**Table 4.2. Plagioclase extinction angle for studied samples of the Miri Formation**

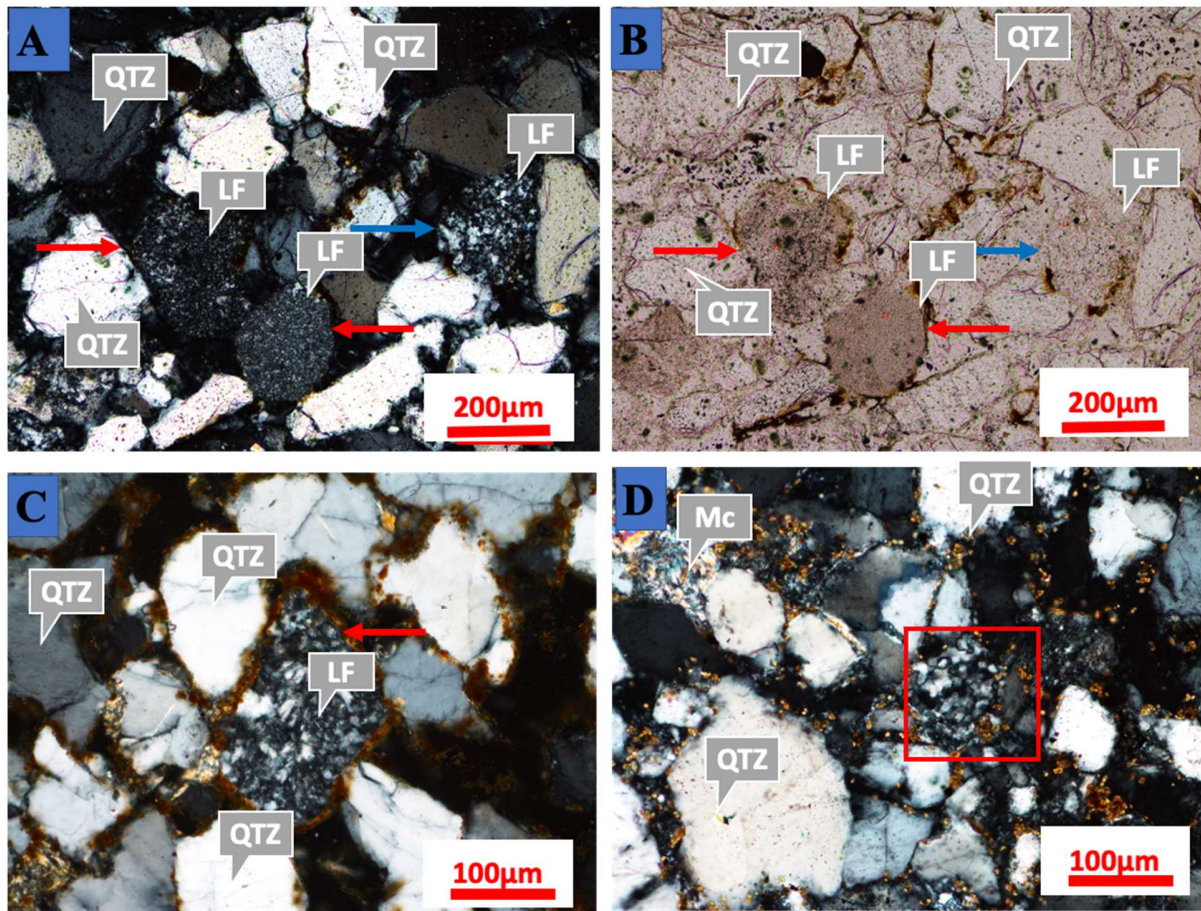
Sample No.	Average extinction angle (degree)	Retardation
B4C Bottom	29	Fast ray
B4D Top	24	Fast ray
Ho6H	26	Fast ray
S3	27	Fast ray
S13	20	Fast ray



**Figure 4.14.** An illustration of extinction angle (under XPL) (Sample S3 from Taman Awam outcrop) confirms their type as albite to andesine.

### 4.4.1.3 Lithic fragments

Lithic fragments are the second dominant in the framework grains constituting about 3-23%. The lithic fragments observed in the Miri Formation sandstones are made up of sedimentary, metamorphic and igneous lithic fragments (**Fig.4.15**). These pieces of fragments are recycled and originated from sedimentary or metamorphic rocks eroded down to smaller sand-sized grains and are now present in the sandstone samples.



**Figure 4.15. Common lithic fragments observed on study samples (A, B, D - under XPL; B- under PPL); A-Blue arrow metasedimentary lithic fragment, red arrow sedimentary lithic fragments (S15)-. B-blue arrow metasedimentary lithic fragment, red arrow sedimentary lithic fragments (S15). C- igneous lithic fragment with iron oxide around the grain boundary (S6). D- igneous lithic fragment (Ho5Top).**

#### 4.4.1.4 Other minerals

The accessory minerals observed in some of the study samples include; mica (muscovite and biotite), zircon, pyrite, magnetite and rutile. Muscovite is more abundant and chemically more stable compared to biotite. The detrital muscovite grains are distinguished by their tabular appearance and high birefringence with individual grains bent due to compaction or deformation between quartz grains (**Fig. 4.16**). Zircon, magnetite and rutile are less abundant in the framework grains and are observed as individual grains as well as inclusions in quartz grains.

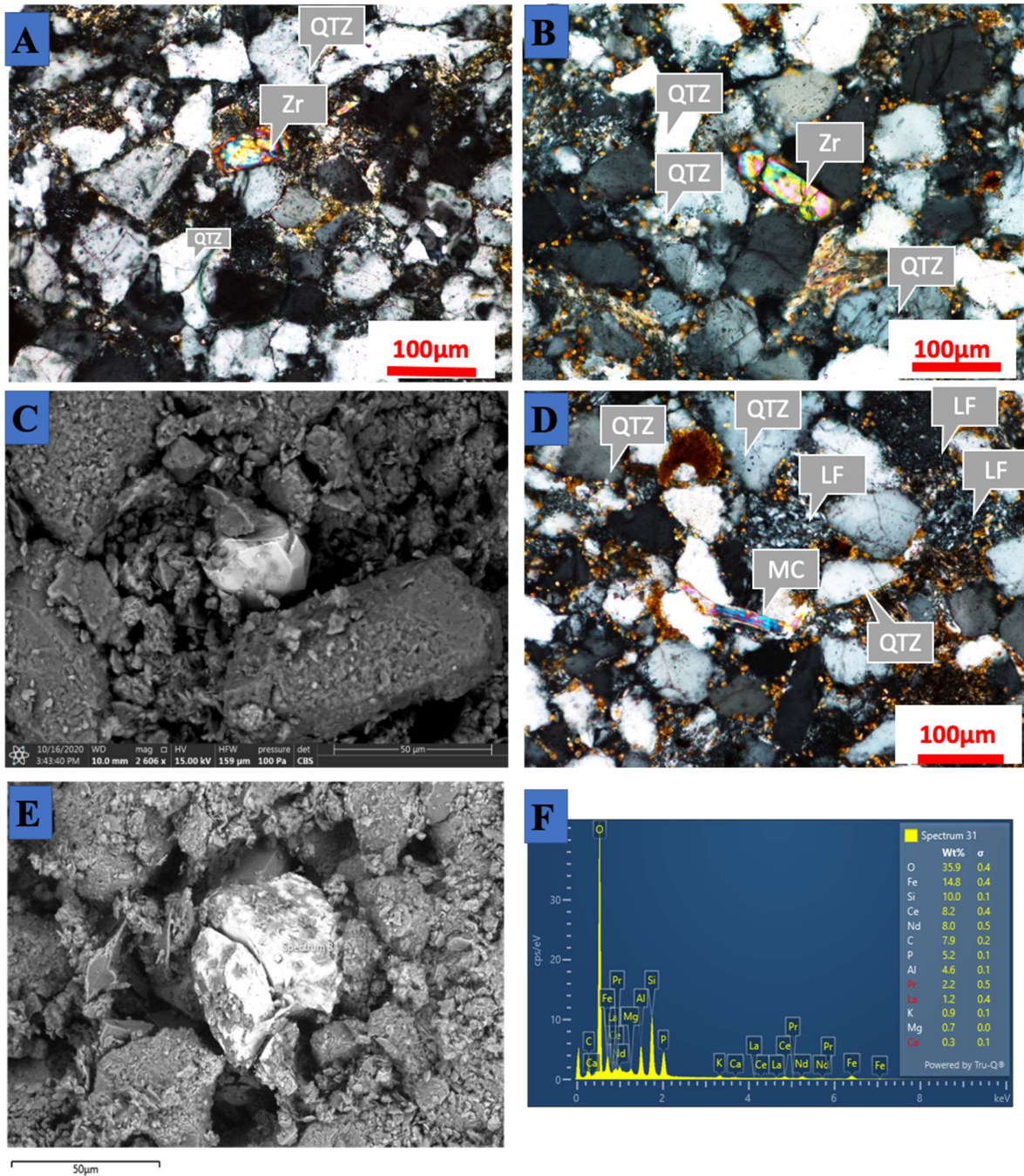


Figure 4.16. A. subhedral zircon grain in the sandstone (Ho6H), B. euhedral zircon grain with colour zonation in a sandstone (Ho6H), C. SEM image shows a zircon grain (Ho2Top), D. bent mica in calcite cemented sandstone (Ho5Top), E. SEM image shows a monzonite grain and F. EDS spot analysis data of Monzonite.



#### 4.4.1.5 Matrix and Cement

The detrital framework grains of the study samples are bounded by a matrix which constitutes about 3-15% of the overall rock composition and cement. The major types of matrix observed in the study samples are mostly clay minerals (Fig. 4.17A-C), which are either detrital or formed due to diagenesis. Diagenetic modified matrix minerals are formed due to alteration and precipitation of the framework grains, as well as the recrystallization of other matrix minerals (Fig 4.17 A blue arrow). Meanwhile, the cements that bind the framework grains are mostly silica, authigenic clay minerals and calcite (Fig. 4.17D). The silica cement mostly forms as overgrowths and pore-fills around quartz grains. The authigenic clay minerals occur as pore-filling cements (Fig. 4.17 B).

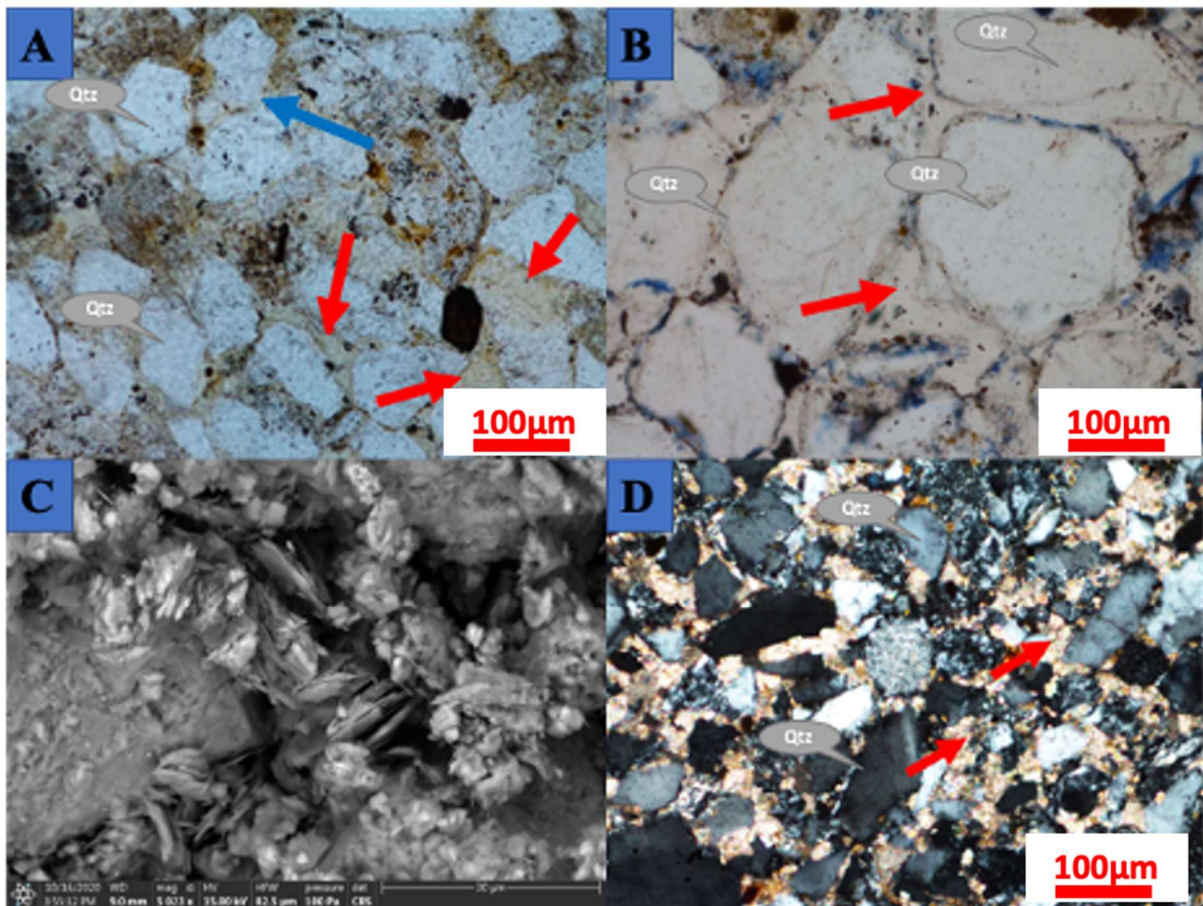
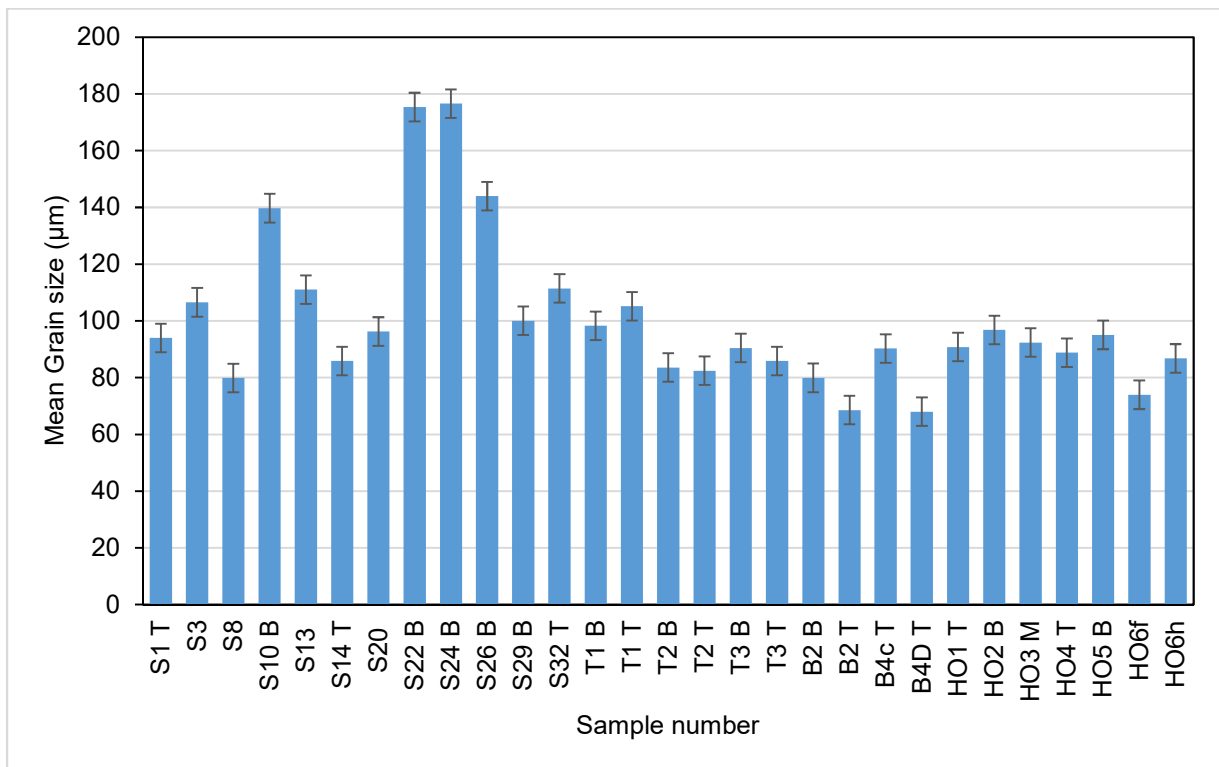


Figure 4.17. A. Blue arrow shows silica cement, Red arrow shows matrix (Ho6H), B. Clay mineral matrix (Ho2Top)- silica cement C. SEM image of pore-filling clay minerals, and D. Red arrow shows Calcite cement (B2top).

#### 4.4.2 Grain size and grain shape analysis

The grain shape and grain size analysis of studies samples were obtained using the NIS-Element software on the thin sections. The statistical summary of the measured grain size and grain shape in the sandstones are summarized in **Table 4.3** and **Table 4.4** respectively. The different thresholds were used as Red, green and blue (RGB) to obtain an accurate measurement. The studied samples are reported to be very fine to medium-grained (**Fig 4.18**) with most of the samples ranging from fine to very fine-grained, moderate to well-sorted and sub-angular to sub-rounded in shape (**Fig 4.19**). The detailed grain size and grain shape analysis data are attached in **Appendix 1.0**.



**Figure 4.18. Mean grain size distribution (with error bars) of the studied sandstones of the Miri Formation.**

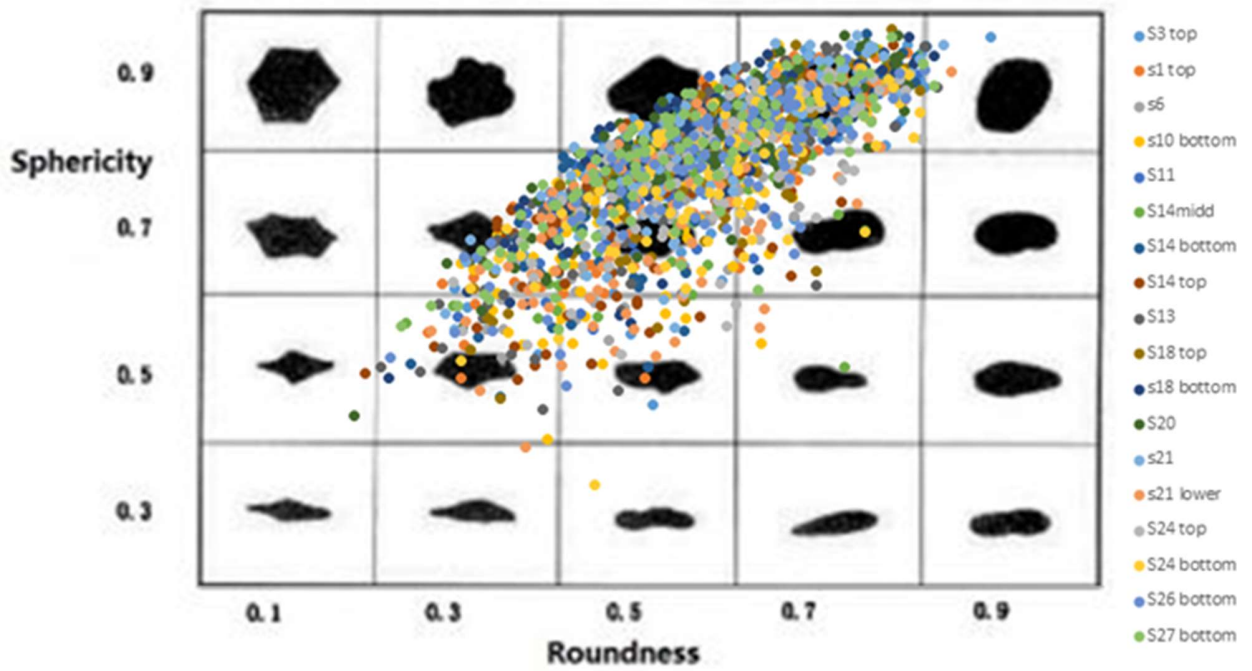


Figure 4.19. Grain shape distribution (Roundness vs Sphericity) of the analysed sandstones of the Miri Formation (modified from Krumbein and Sloss, 1951).

**Table 4.3. Grain size analysis with the mean, median and standard deviation of the analysed sandstones of the Miri Formation.**

<b>Sample No.</b>	<b>Mean (<math>\mu\text{m}</math>)</b>	<b>Median (<math>\mu\text{m}</math>)</b>	<b>S.D</b>	<b>Size</b>
S1 T	93.99	84.95	39.92	Fine
S3	106.57	101.50	30.07	Fine
S8	79.90	75.29	29.03	V. fine
S10 B	139.75	129.70	53.10	Fine
S13	111.05	104.33	37.81	Fine
S14 T	85.90	77.45	35.83	V. fine
S20	96.29	94.09	31.03	Fine
S22 B	175.39	171.65	47.49	Medium
S24 B	176.59	176.40	44.07	Medium
S26 B	143.98	141.43	37.64	Medium
S29 B	100.09	90.97	36.87	Fine
S32 T	111.46	103.69	45.43	Fine
T1 B	98.25	94.95	32.34	Fine
T1 T	105.17	103.98	27.30	Fine
T2 B	83.57	82.57	23.56	Fine
T2 T	82.51	79.26	27.52	V. fine
T3 B	90.49	87.31	26.50	Fine
T3 T	85.83	85.29	23.95	Fine
B2 B	79.93	78.12	18.69	Fine
B2 T	68.57	67.26	19.80	V. fine
B4c T	90.27	90.01	26.79	Fine
B4D T	68.01	64.76	20.98	V. fine
HO1 T	90.86	81.86	52.03	Fine
HO2 B	96.84	88.73	55.99	Fine
HO3 M	92.40	87.06	32.23	Fine
HO4 T	88.79	89.05	29.24	Fine
HO5 B	95.07	87.95	37.07	Fine
HO6f	73.97	71.72	24.02	V. fine
HO6h	86.81	81.62	29.56	Fine

SD = standard Deviation, V.fine= very fine

**Table 4.4. Grain Shape analysis results show the area, maximum ferret, perimeter, roundness, shape factor and sphericity of the sandstone samples of the Miri Formation**

<b>Samples</b>	<b>Area <math>\mu\text{m}^2</math></b>	<b>Max. Feret</b>	<b>Perimeter</b>	<b>Roundness</b>	<b>Shape Factor</b>	<b>Sphericity</b>
S3 Top	6206.8	112.55	312.42	0.58	0.86	0.75
S1 Top	4585.9	100.81	273.82	0.55	0.84	0.74
S6	11652.4	162.49	452.12	0.54	0.81	0.69
S10 Bottom	9836.9	149.92	415.19	0.52	0.75	0.68
S11	7494.3	124.99	335.50	0.56	0.80	0.77
S14 Middle	6066.2	112.60	306.30	0.56	0.79	0.75
S14 Bottom	7640.4	127.23	349.22	0.81	0.73	0.72
S14 top	7699.6	131.15	362.90	0.53	0.76	0.70
S13	6125.5	117.99	323.37	0.55	0.77	0.73
S18 Top	8146.4	133.76	366.68	0.57	0.79	0.74
S18 Bottom	4024.8	96.57	255.88	0.55	0.78	0.76
S20	6802.6	122.63	327.45	0.56	0.79	0.76
S21 Top	4891.7	102.52	275.26	0.57	0.80	0.78
S21 Bottom	15100.6	190.09	536.53	0.52	0.76	0.67
S24 Top	13573.3	168.91	474.94	0.58	0.80	0.73
S24 Bottom	16836.5	185.96	528.45	0.58	0.82	0.72
S26 Bottom	13077.1	167.81	461.81	0.57	0.80	0.74
S27 Bottom	1866.8	66.89	176.33	0.53	0.80	0.73

#### 4.4.3 Quartz grain Microtexture analysis

The quartz grains from the sandstones were studied using the scanning electron microscope (SEM). Different types of microtextural features were observed and grouped into three modes of origin, i.e., mechanical (**Fig. 4.20**), a combination of mechanical and chemical origin (**Fig. 4.21**), and chemical origin (**Fig. 4.22**). The types and characteristics of the microtextures observed are presented in **Table 4.5**. Features of the mechanical origin are more common compared to the chemical origin features observed in the studied samples.

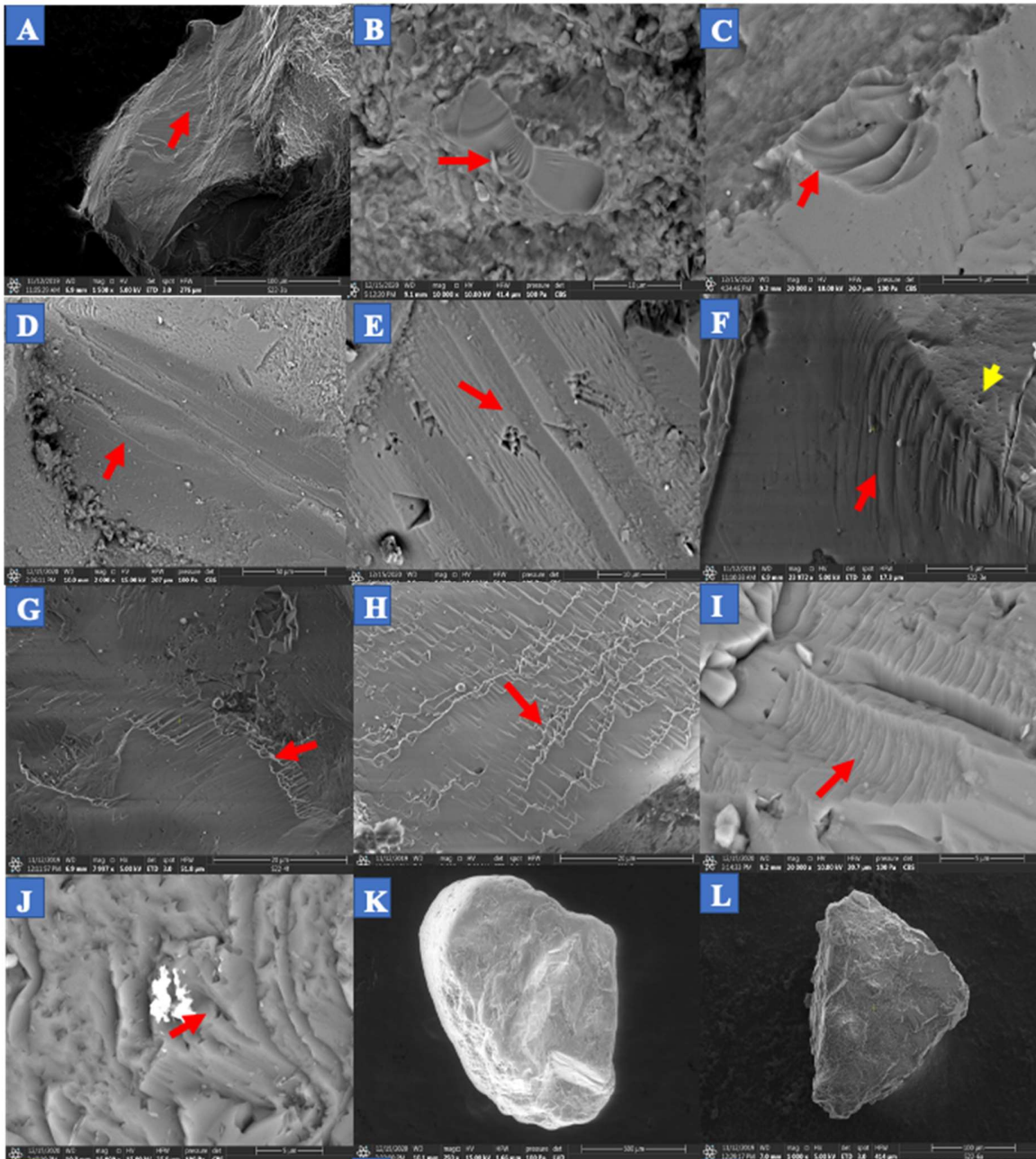
**Table 4.5. Observed microtextures, their morphological features in the quartz grains and their origin.**

<b>Microtexture</b>	<b>Morphological Features</b>	<b>Origin</b>
1. Small conchoidal fracture	Shell like/dish-shaped breakage (<10 $\mu$ m)	Mechanical
2. Medium conchoidal fracture	Shell like/dish-shaped breakage (10-100 $\mu$ m)	Mechanical
3. Large conchoidal fracture	Shell like/dish-shaped breakage (>100 $\mu$ m)	Mechanical
4. Striations	Straight lines	Mechanical
5. V-shaped marks	V-shaped mark/ triangular depressions with straight lines	Mechanical
6. Arcuate steps	Arcuate and successive step-like features	Mechanical
7. Straight steps	Straight and successive step-like features	Mechanical
8. Sub- rounded grains	Sub- rounded grain shape	Mechanical
9. Sub- angular grains	Sub- angular grain shape	Mechanical
1. Fracture plane/plates	Fractures	Mechanical/Chemical
2. Elongated depressions,	Dish-shaped cavities	Mechanical/Chemical
3. Adhering particles	Small particles on the surface of the grain	Mechanical/Chemical
4. Low relief	Smooth surface	Mechanical/Chemical
5. Medium relief	In between low and high relief	Mechanical/Chemical
6. High relief	Irregular surface	Mechanical/Chemical
1. Oriented dissolution etching	Oriented triangular depressions	Chemical (dissolution)
2. Solution pits	Regular and circular holes	Chemical (dissolution)
3. Silica precipitation	Thin layer or droplets of silica precipitation	Chemical (precipitation)
4. Crystal overgrowth	Thick layers of subhedral to euhedral mineral precipitations	Chemical (precipitation)

### 4.4.3.1 Mechanical Origin

A total of nine mechanically originated quartz microtextures are observed in the studied samples (**Table 4.5**). Mechanical features such as conchoidal fracture, striations, V-shaped marks, steps, and grain outlines, which are formed by erosion or weathering processes, collision and abrasions of grains during transportation of the sediments from their source. Conchoidal fractures observed are curved and shell-like in shape and these structures are commonly observed in minerals with no cleavage such as quartz. Different sizes of the conchoidal fractures are observed in the studied samples ranging from small, medium to large (**Fig 4.20 A-C**). The different size ranges of conchoidal fractures observed in quartz grains are common features originating from crystalline rocks (Krinsley and Marshall, 1987; Madhavaraju et al., 2009; Madhavaraju et al., 2021). Striations are produced during transportation and these features have been reported to be the products of ice action by Pettijon (1984), however, they are more abundant in river deposits than glacial deposits (Wentworth, 1936). Striations features (straight and curved) as seen in **Figure 4.20 D, E and F**, which are created during grain to grain collision and abrasion during transportation of the sediments, and are subjected to agitation in a fluvial environment initiated from their sources during a long transportation or sediment recycling (Krinsley and Takahshi, 1962; Mahaney and Kalm, 2000; Krishnan et al., 2015). Pits are randomly observed in a few studied samples and are mostly associated with striations.

V-shaped marks are also observed on the studied samples, they are mostly associated with linear or curved scratches (**Fig 4.20 G and H**). The occurrence of the V-shaped marks is believed to be formed by the collision of grains during transportation (Margolis and Krinsley, 1974). Arcuate and straight steps were also observed in the studied samples. They are mostly associated with conchoidal fractures (**Fig 4.20 C, I and J**). They occur as a result of grain to grain collision and become more abundant due to prolonged agitation in the aqueous environment (Madhavaraju et al., 2021). The observed quartz grain shape is also of mechanical origin. The observed grains are mostly sub-angular to sub-rounded (**Appendix 2.0. A-AB**). The sub-rounded grains show smooth edges while sub-angular grains mostly have blunt edges (**Fig 4.20 K and L**).



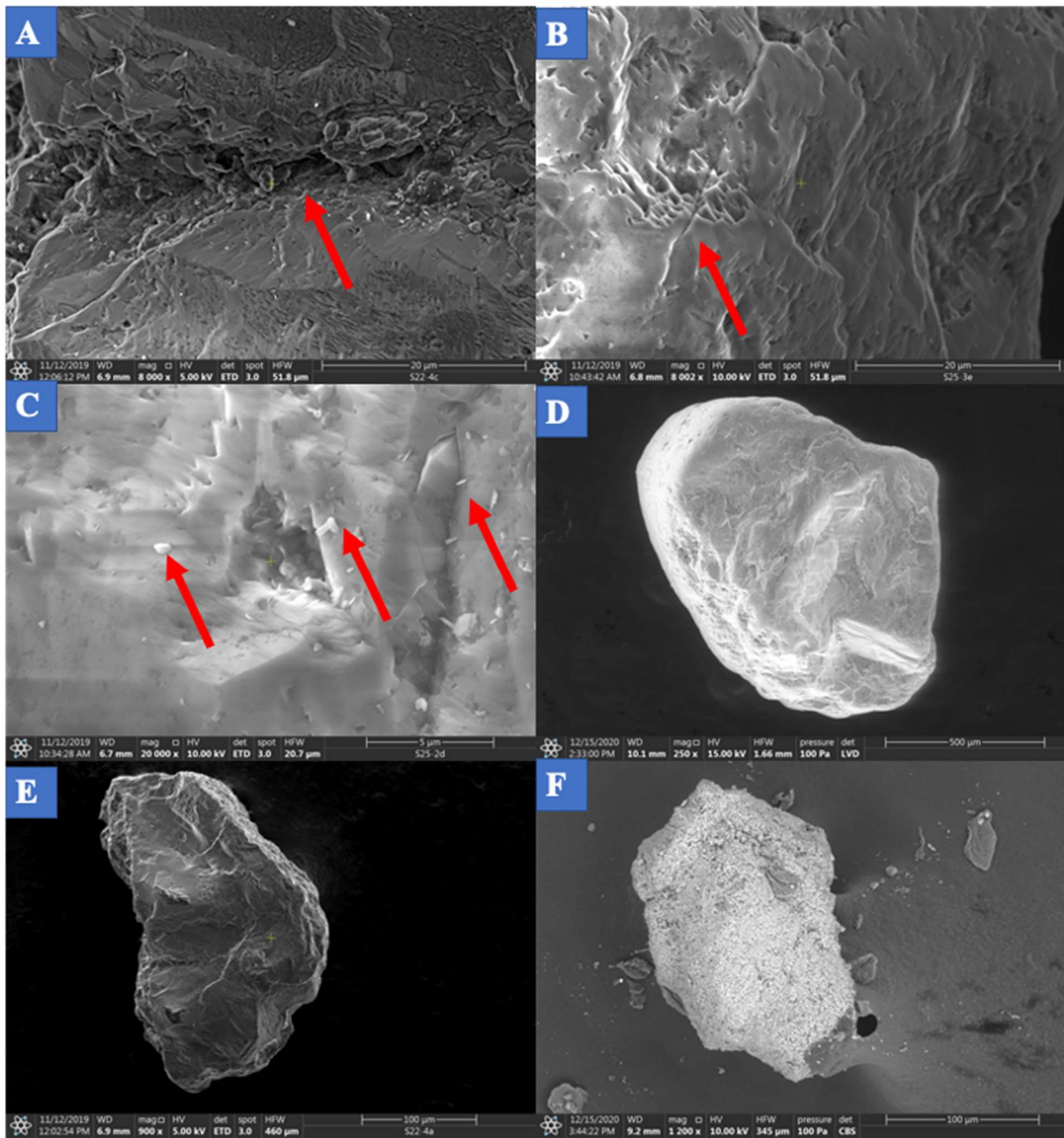
**Figure 4.20. Mechanical origin microtexture: A. Large Conchoidal fracture (S22), B. Medium conchoidal fracture (S26), C. Small conchoidal fracture (S24), D. Straight striations (S15) E. Straight striations with pits (S26), F. Curved striations (Yellow arrow) small pits (S22), G. V-shaped marks (S22), H. Closeup V-shaped marks with linear striations (S22), I. Straight steps (S15), J. Arcuate steps (S15), K. Sub-rounded grain outline (S15), L. Sub-angular grain outline (S22).**



#### 4.4.3.2 Mechanical/Chemical Origin

A combination of mechanical and chemical origin features observed on the quartz grains include fracture plane/plates, elongated depressions, adhering particles and relief. Fracture planes are moderately observed in the studied samples (**Fig 4.21 A**). Elongated depressions are also observed as long dish-shaped cavities on quartz grains (**Fig 4.21 B**). Adhering particles are small fragments observed on the surface of the quartz grains (**Fig 4.21 C**), they are highly distributed in most of the studied samples.

The surface relief of all the studied samples is a result of chemical/mechanical origin. Based on the observed samples, the relief is categorized into low, medium and high relief (**Fig 4.21 D-F**). The high relief samples are mostly having an irregular surface with well-defined depressions and edges while low relief samples have a smooth surface. The most common relief observed in the studied samples is the medium relief. The abundance of medium relief (**Fig 4.21 F**) is associated with the sub-aqueous diagenetic environment (Hossain et al., 2020; Ramos-Vazquez and Armstrong-Altrin, 2020).

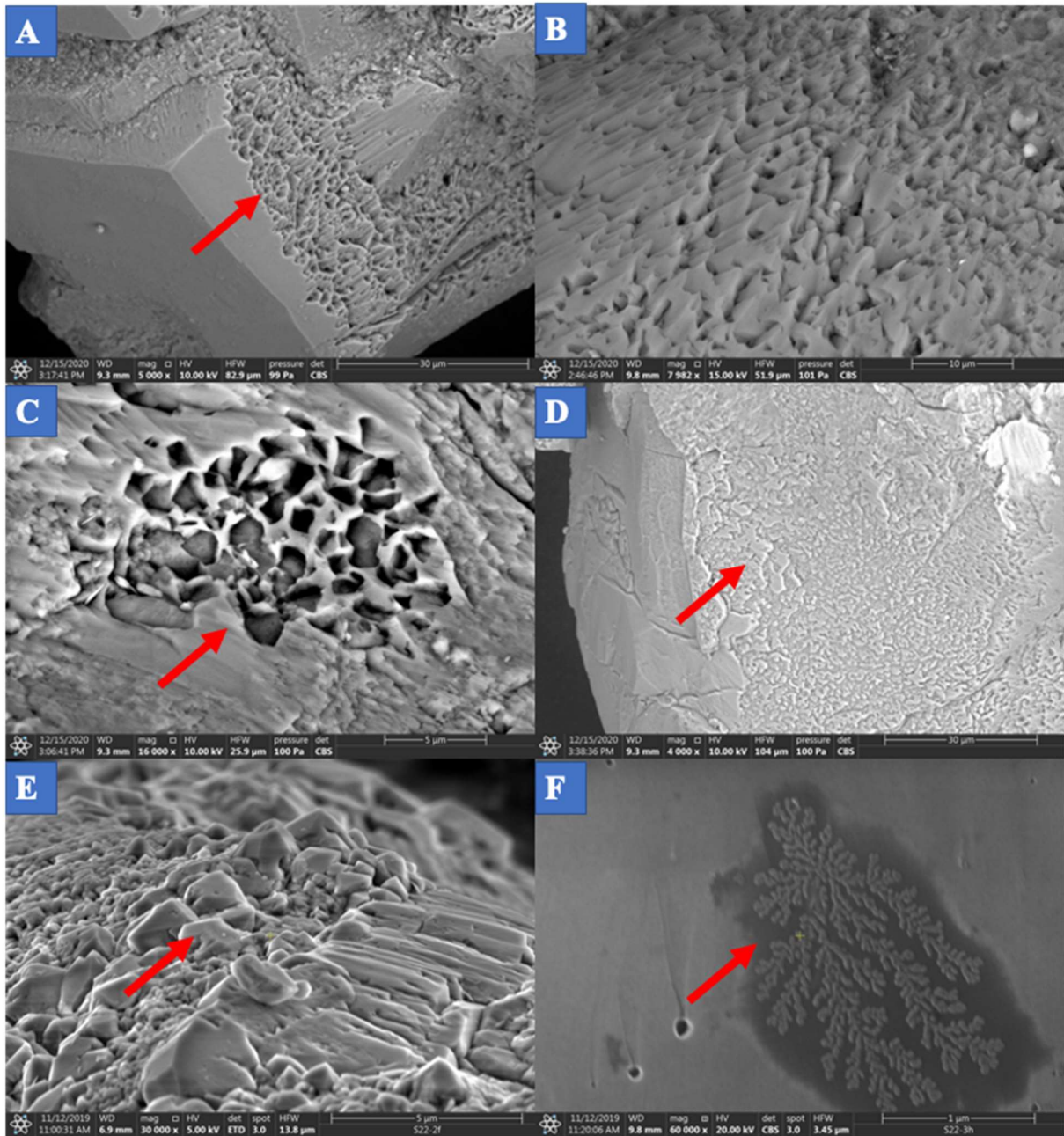


**Figure 4.21. A. Elongated depression (S22), B. Fracture plane (red arrow) (S22), C. Adhering particles (red arrows) (S15), D. Low relief (S15), E. High relief (S22), F. Medium relief (S24).**

### 4.4.3.3 Chemical Origin

The microtextures of the chemical origin are observed in the study samples, which are divided into dissolution and precipitation origins. Samples that exhibit dissolution origin include oriented dissolution etching and solution pits, while samples that exhibit precipitation origin include silica precipitation, crystal overgrowth and dendritic pattern (precipitation). Oriented dissolution etching is the most common microtexture observed in the studied samples, they occur as triangular depressions similar to V-shape marks but are distinguished due to their orientation and regular occurrence (**Fig 4.22A and B**). Solution pits are also observed in the studied samples (**Fig 4.22 C**), they occur as circular or sub-circular depressions caused due to the fluid interaction with quartz or diagenesis (Vos et al., 2014).

Silica precipitation observed (**Fig. 4.22 D and F**) in the study samples are associated with grains in contact with silica saturated fluids during transportation in a low energy environment (Madhavaraju et al., 2006; Hossain et al., 2020), while quartz overgrowth (**Fig 4.22 E**) are associated with burial diagenesis (Vos et al., 2014; Hossain et al., 2020).



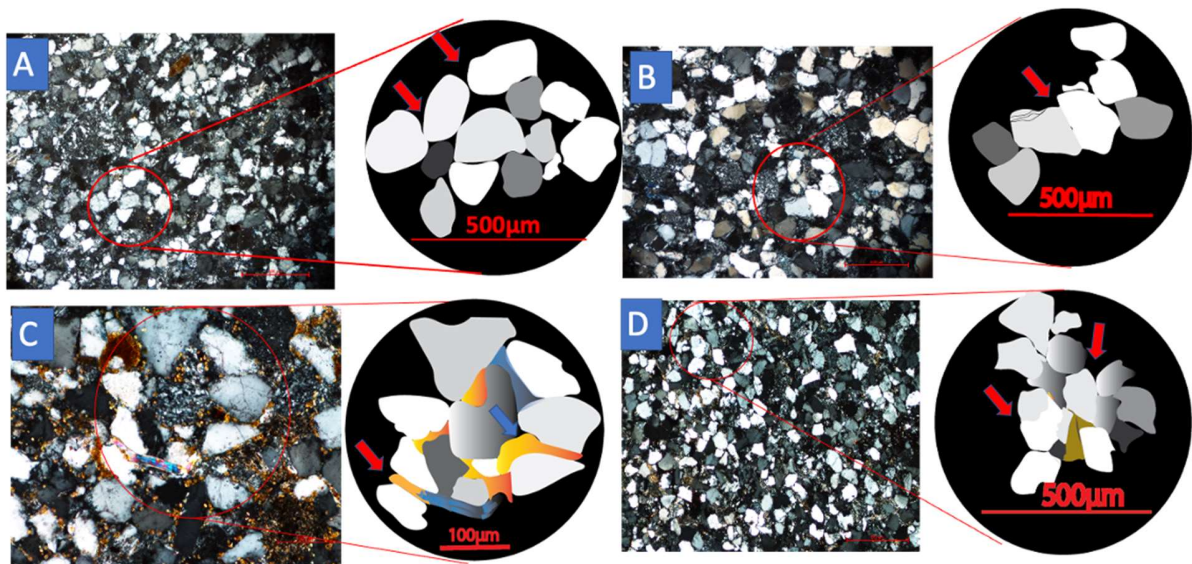
**Figure 4.22. A. Oriented dissolution etching (S15), B. Close-up of the oriented dissolution etching (S15), C. Solution pits (S15), D. Silica precipitation (S24), E. Quartz overgrowth (S22), and F. Silica precipitation (dendritic pattern) (S22).**

#### 4.4.4 Diagenetic features

The diagenetic features and their implications on the reservoir quality are inferred through detailed SEM analysis, petrographic analysis, XRD and geochemistry. Based on the petrographic and SEM analysis, the most common diagenetic features that have positively and negatively influenced the reservoir quality are compaction, cementation and dissolution.

##### 4.4.4.1 Compaction

Compaction of the studied samples is observed via petrographic analysis. The compaction of sandstones at shallow depth are caused by sediment lithostatic pressure which brings about the rearrangement of sediment grains. Based on the grain contact observed, the studied samples are subjected to low to moderate compaction. Based on the petrographic analysis of the studied samples, the rigid grains such as quartz are mostly arranged at point contact (**Fig 4.23A**), line contact (**Fig 4.23B**) and a few sutured contacts (**Fig 4.23D**). Most of the ductile grains such as micas are observed in between rigid grain forming a concave or convex contact and can also be seen forming a pseudomatrix (**Fig 4.23 C**). Some of the mica grains tend to bend or crack, which is a common feature observed in metasedimentary rocks (Nagarajan et al., 2021). This is an indication of former meta-sedimentary rocks that have been recycled.



**Figure 4.23. Thin-section photography of sandstones showing A. Point contact (S33T), B. Line contact 9S22T), C. Deformed mica (red arrow) and pseudomatrix (blue arrow) (Ho5T) and D. Sutured contact (HO4 T).**

#### **4.4.4.2 Cementation, clay minerals and dissolution.**

Cementation is one of the most common diagenetic processes. It is the process in which loose sediments are cemented together to form consolidated rock. Based on thin section, SEM and XRD analyses of the studied samples, different types of cement were observed, which are silica, authigenic clay minerals, calcite and iron oxide cement.

Silica cement are observed as quartz overgrowths and pore filling. Quartz overgrowths (**Fig 4.24 A**) are formed due to feldspar and mica dissolution by leaching pore waters, which lead to the precipitation of silica, thus forming as overgrowths on the available detrital quartz grains. Such cements manifest themselves as euhedral-shaped overgrowths while the more pervasive quartz cements are formed in the pore spaces. The observed quartz overgrowth and quartz cement in the studied samples have a negative effect on the reservoir quality as they are formed within the pore spaces thus reducing the porosity.

Authigenic clay minerals are the most common clay minerals observed in the studied samples. Based on SEM, XRD and geochemistry, the clay minerals observed in the studied samples include illite, illite/smectite, kaolinite and chlorite (Fig 4.24 A, B, D, E and G). These minerals are observed via SEM analysis as pore lining, pore bridging and pore-filling cements. Illite is the most abundant clay mineral observed in all the studied samples. Based on SEM analysis, illite occurs as pore bridging and pore-filling showing a booklet and vermicular stacked plates pattern that resembles kaolinite (Chima et al 2018). This morphology of illite observed in the studied samples has a negative impact on the reservoir quality as it tends to form within the pore spaces thus both reducing porosity and blocking the pore throats, resulting in a negative effect on the sandstone permeability (**Fig 4.24 B and C**). This effect is clearly observed in samples with a high percentage of illite correlating with very low permeability.

A small quantity of kaolinite was observed in the studied samples based on the SEM analysis. Kaolinite occurs as pore-filling minerals having sheets and booklet morphology (**Fig 4.24**

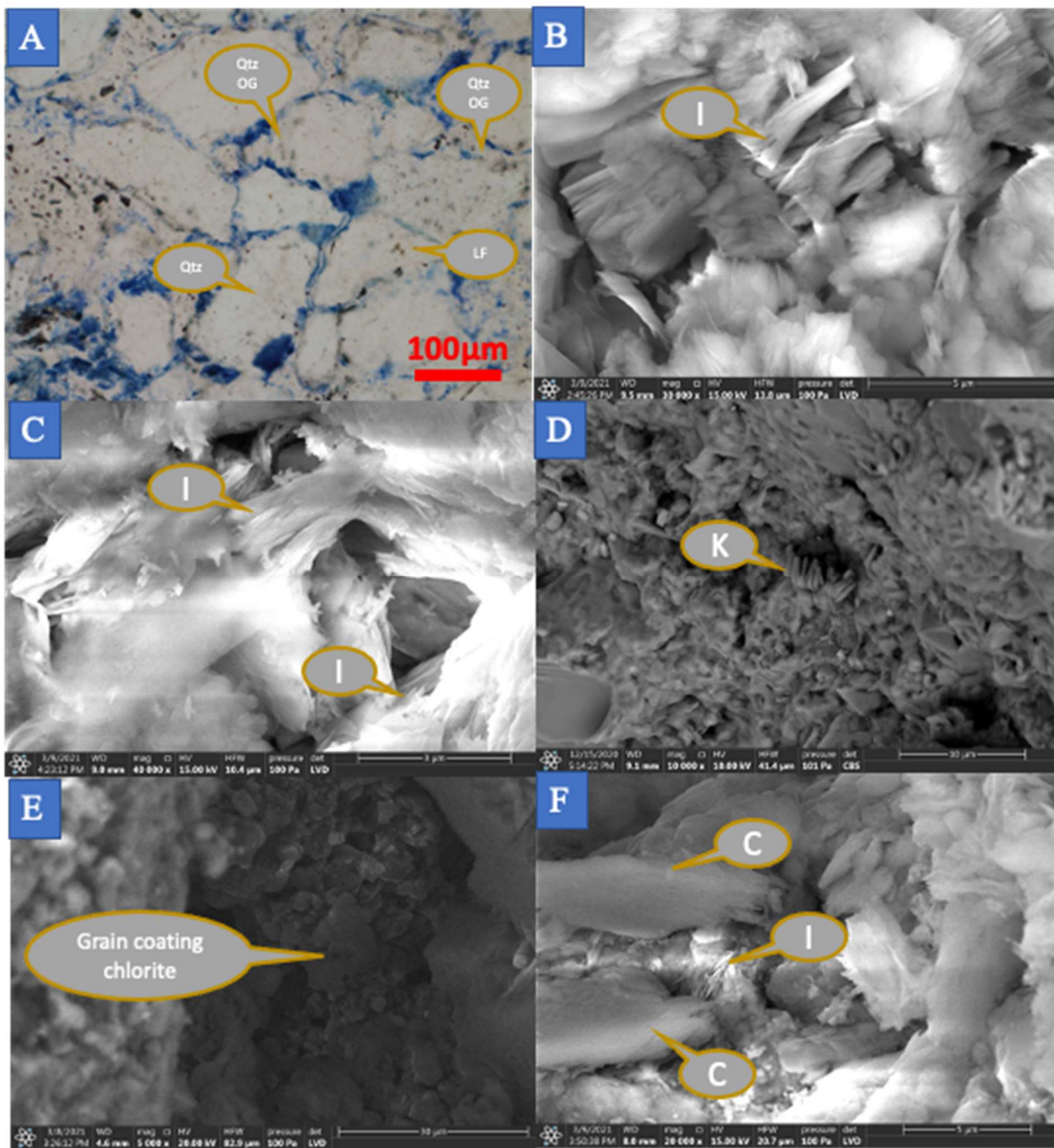
**D).** Due to the less abundant amount of kaolinite observed, a less significant effect on the reservoir porosity is noted.

Chlorite in the studied samples occurs as grain coating minerals around detrital grains and as pore-filling cement with illite. Grain coating chlorite (**Fig 4.24 E**) appears to preserve the pore spaces in the study samples and thus has a positive effect in preserving the reservoir quality. However, the occurrence of chlorite with illite as pore-filling minerals has a negative impact on the reservoir quality (**Fig 4.24 F**).

Smectite based on the SEM analysis occurred in small fractions mostly as grain coating clay mineral around the detrital grains having a honeycomb morphology. Illite is observed on the surface of smectite forming a mixed layer of illite- smectite (**Fig 4.25 G**). The occurrence of mixed illite- smectite in the sandstone pore systems has a negative impact on the potential reservoir permeability of the studied samples.

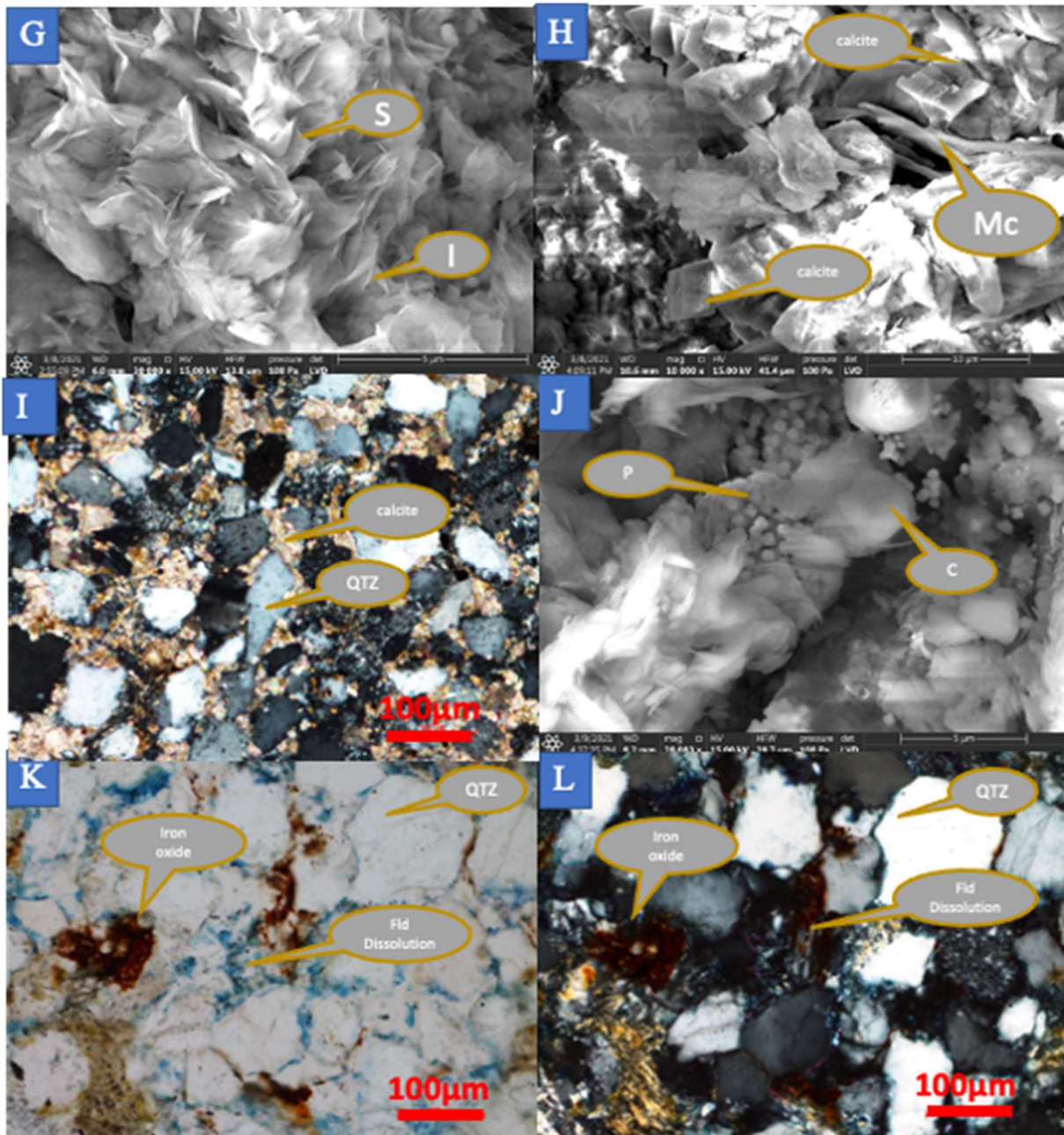
Other diagenetic minerals observed based on SEM and petrographic thin section study include calcite cementation, pore filling pyrite and hematite cementation. Calcite cement is observed in some of the studied samples as pore-filling or mineral replacement (**Fig 4.25 H, I**). Pervasive calcite cement in the studied samples has a very significant influence by reducing the porosity and permeability in the studied samples almost to zero. While pore filling pyrite cement are mostly observed in bioturbated sandstones, where they mostly occur in pore spaces of the studied samples (**Fig 4.25 J**). Hematite (iron oxide) cement are observed via petrographic thin section, having a negative effect on both porosity and permeability (**Fig 4.25 K, L**).

Dissolution is another diagenetic feature observed in the studied samples. Dissolution mostly involves the partial or total removal of the pre-existing reactive minerals creating pore space. The most common dissolution observed in the studied samples is the dissolution of feldspar and lithic fragments (**Fig 4.25 K, L**). Dissolution of feldspar aids the provision of silica source for authigenic quartz cement and overgrowth as mentioned earlier. Feldspar dissolution is minimal in most of the studied samples, thus having less significance on the reservoir properties as it will only contribute to minor additional microporosity in the vicinity of a very few grains.



**Figure 4.24** A. A thin section shows the overgrowth within detrital quartz grain (under PPL), B. SEM image shows pore filling illite (I) pattern that resembles kaolinite (S32 T), C. Pore bridging illite (I) (S3), D. Kaolinite (K), E. Grain coating chlorite (S22 B), F. Pore filling chlorite (C) and illite (I) (Ho4 T).

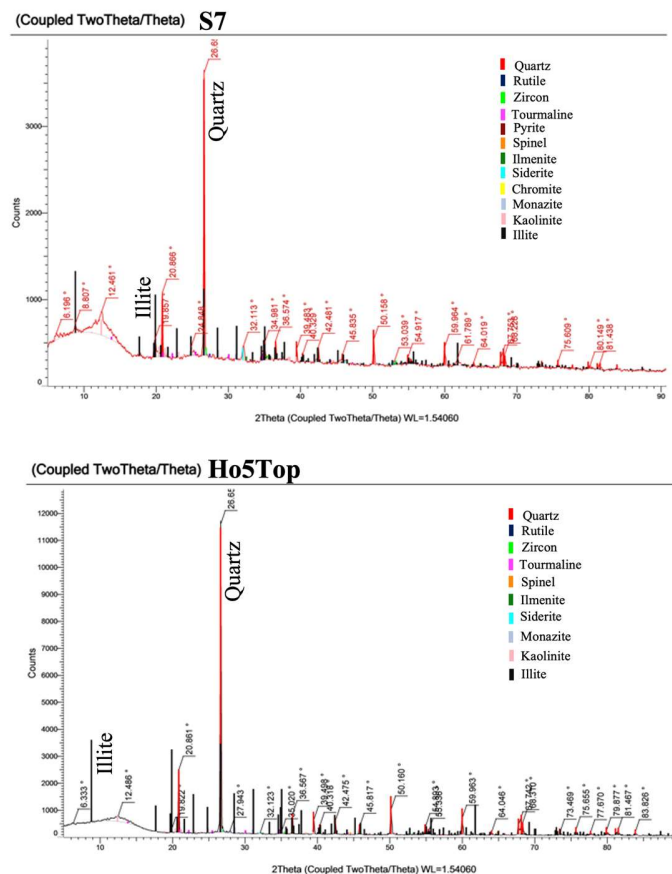




**Figure 4.25 G.** SEM image showing pore filling mixed layer of illite (I)-smectite (S) (S24 T), H. SEM image shows calcite and mica cement (Ho2M), I. A thin section photo shows pore-filling calcite cement (B2T; under XPL), J. Pyrite (P) within pore space (Ho1T), K&L a thin section image showing dissolution feldspar and iron oxide cement (S20; under PPL and XPL respectively).

## 4.5 X-Ray Diffraction (XRD).

Based on the six selected samples analysed for bulk mineral XRD, the major mineral phases are quartz, illite, and kaolinite (**Fig4.26**) and other minerals obtained based on the XRD analysis are tourmaline, spinel, monzonite, zircon, pyrite, ilmenite, rutile and chromite. Feldspars are observed in the petrographic analysis but not reported in the XRD analysis which might be due to their alteration to clay minerals (e.g kaolinite). Appendix 4.0 shows the x-ray diffractograms of all 6 samples analyzed.



**Figure 4.26. X-ray diffractogram of the selected samples (Sample Number: S7 and Ho5 Top), showing the main peaks of important minerals.**

## 4.6 Reservoir Properties

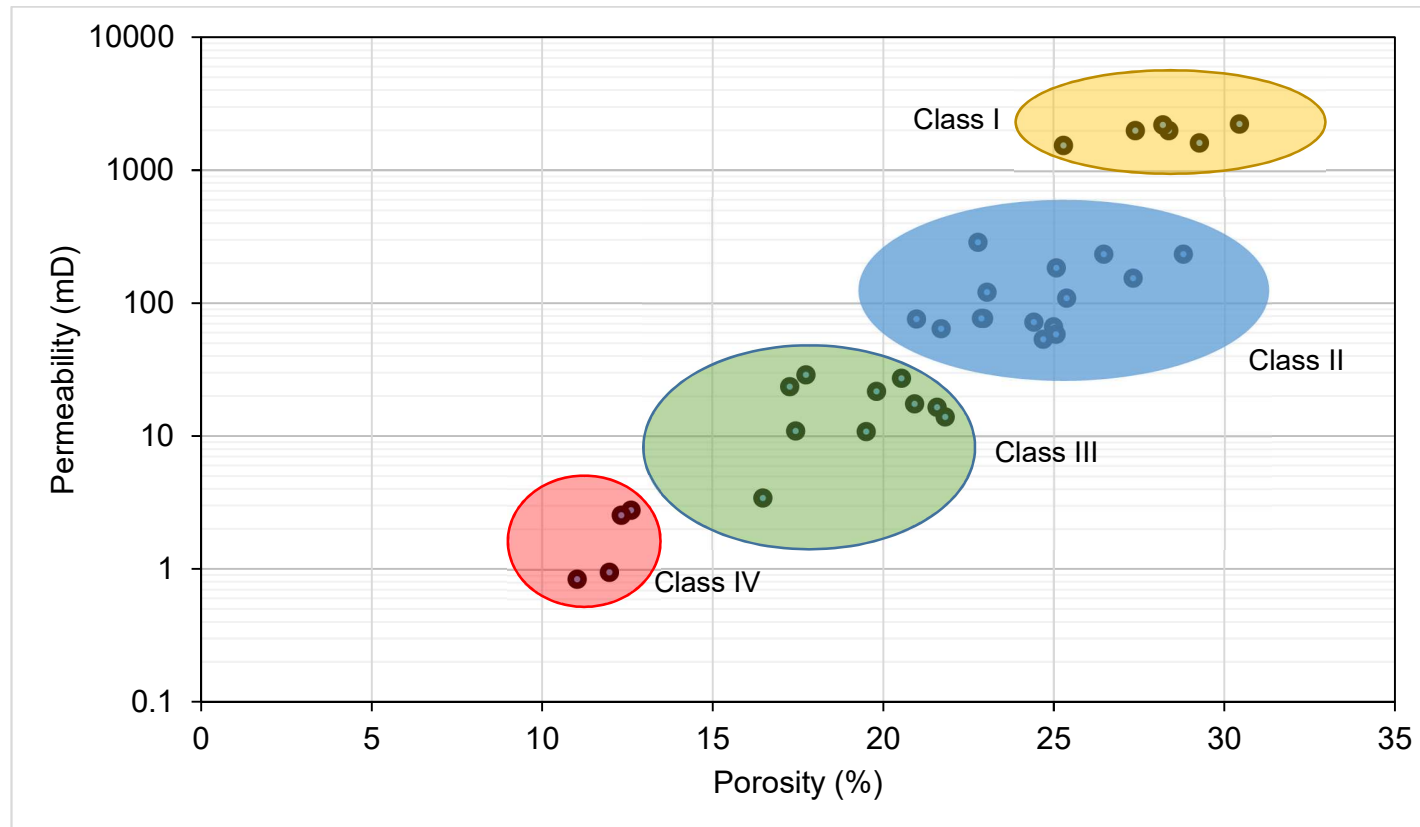
The thin section with blue dye staining was not successful due to the wash off of the blue dye while polishing the thin section. Hence digital analysis of thin section porosity was abandoned. Therefore, only core sample analysis results are considered and reported for the reservoir properties of the studied samples. These core plug measurements are more likely to provide representative values for both porosity and permeability and are a superior data point compared to thin section digital image analysis methods.

Based on the 34 core samples selected from all the four studied outcrops of the Miri Formation, the average porosity and permeability are 22.2% and 390.7 mD, with the ranges of 11.03 to 30.44 % for porosity and 0.85 to 2238.3 mD for permeability respectively (**Table 4.6**). The cross-plot of the examined porosity and permeability of the studied core samples are widely distributed. Based on the porosity and log of permeability values on the cross plot, the studied samples are grouped into four qualitative reservoir rock classes (**Fig 4.27**). Class I: The high reservoir quality sandstones with average porosity and permeability of 28.33% and 1937.74mD includes medium grain mature sandstones, moderately well sorted to very well sorted quartz arenite with a very low percentage of clay minerals (S22T, S22B, S24T, S24B, S26T, S26B). Class II: The moderate reservoir quality sandstones with an average porosity and permeability of 24.29% and 116.57mD includes fine to very fine-grained moderately well sorted to well-sorted sandstone with clay minerals present (S10B, T3T, T1B, T2B, S28T, S8, T1T, T2T, S11, S3, HO2B, S32T, S27T). Class III: The low reservoir quality sandstones with an average porosity and permeability of 19.31% and 17.46mD includes fine to very fine-grained moderately well sorted to well-sorted sandstone with high clay mineral (B4CT, B4DT, HO4T, HO5B, HO6F, S13, S14T, S29B, S1T). Finally, Class IV: The very low reservoir quality sandstones with an average porosity and permeability of 11.98% and 1.78mD includes fine to very fine-grained moderately sorted to moderately well-sorted sandstones with bioturbation and calcite cement present in the samples (B2T, HO1T, HO3M, and HO6G).

**Table 4.6. Porosity and permeability data based on TPI- 219 Helium porosimeter and TKA-209 gas permeameter with the grain size parameters and lithology/facies**

Sample No	Porosity (%)	Permeability (mD)	Grain size	Sorting	Skewness	Kurtosis	Lithology /Facies
T1 B	26.46	233.11	Fine	M. well sorted	C.skewed	V. Leptokutric	Massive FG S.St
T1 T	24.69	53.59	Fine	M. well sorted	VC skewed	V. Leptokutric	Massive FG S.St
T2 B	25.37	109.26	Fine	well sorted	VF skewed	V. Leptokutric	Hummocky
T2 T	24.41	72.16	V.fine	M. well sorted	Fine Skewed	Mesokurtic	Hummocky
T3 B	20.92	17.48	Fine	Well sorted	Symmetrical	V. Leptokutric	Parrallel laminated
T3 T	27.32	153.73	Fine	M. well sorted	VF skewed	V. Leptokutric	Parrallel laminated
B2 T	11.97	0.95	V.fine	M. well sorted	VF skewed	V. platykurtic	Parrallel laminated
B4c T	21.58	16.48	Fine	Well sorted	Symmetrical	V. Leptokutric	Planer cross stratified
B4D T	16.48	3.42	V.fine	M. well sorted	VF skewed	V. platykurtic	
HO1 T	11.03	0.85	Fine	M. sorted	Symmetrical	Mesokurtic	Bioturbated
HO2 B	22.94	76.84	Fine	M. sorted	Symmetrical	V. Leptokutric	Trough
HO3 M	12.60	2.78	Fine	M. well sorted	Fine Skewed	V. Leptokutric	Inter bedded
HO4 T	17.44	10.96	Fine	M. well sorted	Fine Skewed	V.Leptokutric	Bioturbated
HO5 B	20.54	27.26	Fine	Well sorted	Symmetrical	V. Leptokutric	Planer cross stratified
HO6 F	21.82	13.99	V.fine	M. well sorted	VF skewed	V. platykurtic	Inter bedded
HO6 G	12.32	2.55		NA	NA	NA	Inter bedded
HO6 H	24.99	66.55	Fine	M. well sorted	Fine Skewed	V. Leptokutric	Parrallel laminated
S1 T	17.27	23.49	Fine	M. sorted	Symmetrical	V. Leptokutric	Inter bedded
S3	23.04	120.95	Fine	Well sorted	VC skewed	V. platykurtic	Inter bedded
S8	25.06	58.28	V.fine	M. well sorted	Fine Skewed	Platykurtic	Inter bedded
S10 B	28.79	233.77	Fine	M. well sorted	VF skewed	V. platykurtic	Massive FG S.St
S13	17.74	28.97	Fine	M. well sorted	C. skewed	Platykurtic	Inter bedded
S14 T	19.51	10.80	V.fine	M. well sorted	Fine Skewed	Mesokurtic	Inter bedded
S20	22.88	76.74	Fine	M. well sorted	Fine Skewed	V. Leptokutric	Inter bedded
S22 T	27.40	2000.32	Mediu m	Well sorted	Symmetrical	V. Leptokutric	Massive MG S.St
S22 B	28.38	2007.37	Mediu m	Well sorted	Symmetrical	V. Leptokutric	Massive MG S.St
S24 T	29.27	1622.59	Mediu m	V. well sorted	Fine Skewed	V. Leptokutric	Massive MG S.St
S24 B	25.30	1557.45	Mediu m	V. well sorted	Fine Skewed	V. Leptokutric	Massive MG S.St
S26 T	28.20	2200.40	Mediu m	M. well sorted	VF skewed	V. platykurtic	Massive MG S.St
S26 B	30.44	2238.31	Mediu m	M. well sorted	VF skewed	V. platykurtic	Massive MG S.St
S29 B	19.81	21.77	Fine	M. well sorted	C. skewed	V. Leptokutric	Planer cross stratified
S32 T	21.70	64.42	Fine	M. well sorted	C. skewed	Mesokurtic	Massive FG S.St
S11	22.78	286.00	Fine	M. well sorted	VF skewed	V. platykurtic	Massive FG S.St
S27 T	20.98	75.89	Fine	M. well sorted	C. skewed	V. Leptokutric	Inter bedded
S28 T	25.07	183.81	Fine	M. sorted	Symmetrical	V. Leptokutric	Planer cross stratified

Mod.=Moderate; V.- Very; VF = Very Fine; C.-Coarse; VC = Very Coarse; FG S.St = Fine grained Sandstone; MG S.St = Medium grained Sandstone



**Figure 4.27 Porosity versus the log of permeability cross plot of the Miri Formation sandstones from all four studied outcrops. The cross plot shows four reservoir rock classes: high quality (class I), moderate quality (class II), low quality (class III) and very low quality (class IV). Class I: Medium-grained mature sandstone; low clay minerals, well to very well sorted, Avg. Illite = 0.4% (S22B, S22T, S24B, S24T, S26B and S26T); Class II: Very fine to fine-grained mature sandstone; 5-10% of clay minerals; moderately well sorted - well-sorted, Avg. Illite = 9.58% (T1B, T1T, T2B, T2T, T3T, Ho2B, Ho6H, S3, S8, S10B and S20); Class III: Very fine -fine-grained, mature sandstone; >10% of clay minerals, and moderately well sorted - well-sorted, Avg. Illite = 11.45% (T3T, B4cT, B4dT, Ho4T, S1T, S13, S14T, S29B and B4cT); Class IV: Very fine -fine-grained mature – immature sandstone 10 - 15% of clay minerals, moderately well sorted - well-sorted, calcite cement and bioturbated, Avg. Illite = 13.57% (B2T, Ho1T, Ho3M and Ho6G).**

## 4.7 Geochemistry

The major oxides, trace elements and rare earth elements (REEs) concentrations of clastic sedimentary rocks of the Miri Formation are reported in table 4.7 a, b, c.

### 4.7.1 Major Oxides

The geochemical classification plot of Herron (1988) has been used in this study and the clastic sedimentary rocks of the Miri Formation. **Fig 4.28** shows, the sandstone samples are classified as quartz arenite (n=3), sublitharenite (n=8), Fe-sandstone (n=2), litharenite (n=3), while the sandstone interbedded mudstone samples are mostly classified as litharenite (n=4), arkose (n=1), sublitharenite (n=1), shale (n=1) and mudstone samples are classified as mostly wacke (n=4), litharenite (n=1) and shale (n=1). Though the samples are classified into various lithotypes, the field-based names are followed in the discussion as a significant number of samples collected are sandstone interbedded mudstone or vice-versa.

The most abundant major oxides across all the study samples are  $\text{SiO}_2$  and  $\text{Al}_2\text{O}_3$ . A significant variation of  $\text{SiO}_2$  is observed within the lithotypes where: sandstones (80.17-97.34 wt%), sandstone interbedded mudstone (65.59-94.23 wt%), and mudstone (70.78-79.53 wt%).  $\text{Al}_2\text{O}_3$  is relatively higher in mudstone/silts and sandstone interbedded mudstone/silt (11.72-18.37 wt%) and (3.64-19.28 wt%) than obtained in the sandstones (1.54-10.56 wt%). An increasing variation in  $\text{K}_2\text{O}$  concentration is observed in all lithotypes as 0.29-1.89 wt%, 0.66-3.26 and 2.01-3.10wt% in sandstones, sandstone interbedded mudstone and mudstone respectively.  $\text{Fe}_2\text{O}_3$  values obtained across the lithotypes also show decent variation as 0.45-5.05 wt%, 0.8-7.98 wt% and 3.28-7.30 wt% in sandstones, sandstone interbedded mudstone and mudstone respectively, while  $\text{MgO}$  shows a decreasing variation as 0.06-2.45 wt%, 0.25-2.48 wt% and 0.09-1.82 wt% in sandstones, sandstone interbedded mudstone and mudstone respectively.  $\text{MnO}$ ,  $\text{CaO}$ ,  $\text{Na}_2\text{O}$ ,  $\text{TiO}$  and  $\text{P}_2\text{O}_5$  concentration was relatively lower than 1wt% in all lithotypes except one which recorded a  $\text{CaO}$  value of 4.23 wt% due to the presence of calcite cement.

**Table 4.7a The major oxides (in Wt.%) trace element concentration (in ppm) of sandstones (n=17) of the Miri Formation**

Sample No.	S10T	S11	S14 T	S22 T	S24 B	S26 T	S29 T	S32 T	T1 T	T2 T	T3 T	B2 T	B4D T	Ho2 B	Ho4 B	Ho5 T	H06HT	Avg.
SiO <sub>2</sub>	84.71	92.38	89.20	96.98	97.06	97.34	86.42	92.02	84.58	87.88	88.46	80.17	88.85	86.42	93.79	92.06	91.08	89.96
Al <sub>2</sub> O <sub>3</sub>	10.56	3.17	6.37	1.90	1.54	1.57	8.20	4.95	9.57	7.31	6.89	7.19	6.44	4.46	3.65	4.42	5.49	5.51
Fe <sub>2</sub> O <sub>3</sub> *	1.38	3.58	2.06	0.45	0.81	0.48	2.42	1.08	2.10	1.86	1.99	3.62	1.88	5.05	1.01	1.27	1.28	1.90
MnO	0.01	0.01	0.01	0.01	0.01	0.01	0.01	0.01	0.01	0.01	0.02	0.06	0.01	0.06	0.01	0.01	0.01	0.02
MgO	0.65	0.11	0.42	0.07	0.06	0.10	0.60	0.45	0.92	0.69	0.62	2.45	0.65	2.03	0.27	0.61	0.37	0.65
CaO	0.03	0.01	0.03	0.01	0.02	0.01	0.03	0.03	0.05	0.10	0.05	4.23	0.12	0.63	0.10	0.15	0.04	0.33
Na <sub>2</sub> O	0.14	0.02	0.27	0.07	0.04	0.06	0.28	0.15	0.42	0.35	0.30	0.44	0.38	0.22	0.20	0.24	0.28	0.23
K <sub>2</sub> O	1.89	0.44	1.18	0.36	0.33	0.29	1.49	0.90	1.75	1.35	1.24	1.29	1.14	0.83	0.71	0.82	1.08	1.01
TiO <sub>2</sub>	0.59	0.24	0.43	0.11	0.11	0.12	0.53	0.38	0.55	0.42	0.42	0.51	0.47	0.31	0.25	0.39	0.34	0.36
P <sub>2</sub> O <sub>5</sub>	0.04	0.05	0.04	0.04	0.03	0.03	0.03	0.03	0.05	0.04	0.04	0.09	0.05	0.05	0.03	0.04	0.04	0.04
K <sub>2</sub> O/Al <sub>2</sub> O <sub>3</sub>	0.18	0.14	0.19	0.19	0.22	0.19	0.18	0.18	0.18	0.18	0.18	0.18	0.18	0.19	0.19	0.19	0.20	0.18
SiO <sub>2</sub> /Al <sub>2</sub> O <sub>3</sub>	8.02	29.12	14.00	51.04	63.22	62.06	10.54	18.58	8.84	12.02	12.84	11.15	13.79	19.39	25.71	20.83	16.60	23.40
Al <sub>2</sub> O <sub>3</sub> /TiO <sub>2</sub>	17.88	13.48	14.67	17.09	13.82	12.92	15.60	13.08	17.45	17.34	16.32	14.11	13.61	14.45	14.79	11.34	16.18	14.95
CIA	83.78	87.45	81.29	81.46	79.96	81.54	82.01	82.16	81.25	80.36	81.41	76.77	79.80	77.78	78.52	78.68	79.84	80.83
CIW	98.54	99.52	95.68	96.51	96.75	96.21	96.40	96.59	95.41	94.32	95.33	89.05	92.95	90.95	92.67	92.13	94.71	94.93
PIA	68.80	75.32	66.24	65.86	62.60	66.28	67.08	67.22	66.40	65.55	66.80	62.99	65.65	63.30	63.26	64.07	64.14	65.98
ICV	0.44	1.39	0.69	0.57	0.90	0.68	0.65	0.61	0.61	0.65	0.67	1.75	0.72	2.05	0.70	0.79	0.62	0.85
Ba	185	56	127	58	50	47	161	109	176	146	135	140	135	100	85	106	130	114.47
Sc	9	3	6	2	2	2	7	4	8	6	6	7	6	9	3	4	4	5.18
Be	1	1	1	1	1	1	2	1	1	1	2	1	1	1	1	1	1	1.12
Co	10.90	1.20	5.00	0.80	0.80	2.00	6.60	5.50	12.00	9.40	10.70	9.10	6.80	6.50	3.20	6.80	2.50	5.87
Cr	68.42	54.74	68.42	27.37	13.68	34.21	61.58	61.58	61.58	54.74	47.89	68.42	68.42	61.58	68.42	88.95	47.89	56.35
Cs	4.6	1	2.8	0.6	0.6	0.5	4	2	4	2.9	2.9	3	2.9	1.7	1.5	2.1	2.5	2.33
Ga	11.2	3.4	6.6	1.5	1.5	0.9	7.8	4.7	9.7	6.7	6.9	6.3	6.4	4	3.7	4.5	6	5.40
Hf	6.4	5.7	8.7	1.6	1.6	1.7	10	11.7	8.8	6.6	6.3	12.6	11.3	8.5	5.7	14.1	5.3	7.45
Nb	9.9	4.6	7.4	2.2	2	2.1	8.7	6.7	8.5	7.2	7.3	8.2	8	5	4.1	7.4	6	6.19
Rb	78.9	19	47.9	14	13	10.8	60.6	38.3	70.9	54.1	50.4	51.1	48.7	32.9	28.9	35.1	47.1	41.28
Sn	2	1	1	1	1	1	1	1	2	3	3	1	1	1	1	2	3	1.53
Sr	56.3	37.8	46.6	56.9	43.4	31.8	39.7	24.9	39.3	33.7	31.5	88.3	43.7	36.1	24.4	34.5	33.1	41.29
Ta	0.6	0.3	0.6	0.2	0.1	0.2	0.6	0.6	0.7	0.6	0.5	0.6	0.7	0.4	0.3	0.6	0.5	0.48
Th	8.6	3.7	7.1	2.3	2.2	2	9.2	7.3	9	7.3	7.3	9	7.7	5.8	4.8	6.6	5.5	6.20
U	2.5	1.1	2.1	0.6	0.6	0.5	2.4	2.2	2.8	1.8	1.8	2.6	2.2	1.8	1.3	2.1	1.4	1.75
V	67	25	48	14	12	12	54	31	60	46	44	48	39	44	24	29	32	37.00
W	1.7	1.1	1.8	0.6	1	2.1	1.9	1.7	2.1	1.6	1.6	2.1	1.5	1.3	1	2	1	1.54
Zr	255.8	224.2	349.8	59.9	59.8	64	392.5	472.7	335.5	260	240.4	505.5	458.7	352	228	575.5	209.1	296.67
Y	18.3	6.7	13.6	5.3	5.2	5.1	17.5	13.5	18.7	15.2	17.4	20.2	17.7	14.2	8.8	15.7	10.5	13.15
Mo	0.2	0.1	0.1	0.1	0.3	0.1	0.1	0.1	0.1	0.1	0.1	0.1	0.1	0.1	0.2	0.1	0.2	0.13
Cu	10.4	5.7	5.7	2	2.1	1.5	8.8	4.6	8.1	5	5.6	30.8	5.9	3.8	4	4.6	4.4	6.65
Pb	11.3	3.9	4.9	1.6	3.2	2.1	9.6	3.3	5.8	5	4.7	5.7	4.2	3.5	3.7	4.2	4.6	4.78
Zn	52	9	23	4	4	7	34	26	54	46	48	55	35	29	11	28	12	28.06

Sample No.	S10T	S11	S14 T	S22 T	S24 B	S26 T	S29 T	S32 T	T1 T	T2 T	T3 T	B2 T	B4D T	Ho2 B	Ho4 B	Ho5 T	H06HT	Avg.
Ni	14.1	1.8	6.8	1.2	0.8	2.7	11	8.6	22.5	15.8	15.4	12.9	12.3	8.5	4.3	8.7	4.5	8.94
As	5.8	2.1	3.2	3.5	3.3	2.1	6.5	2.4	4.9	3.6	3	3.8	2.4	3.3	4.6	3.4	2.9	3.58
(La/Yb) <sub>cn</sub>	7.74	8.72	8.10	9.22	7.93	9.20	7.62	7.32	7.07	7.71	8.29	6.43	6.73	7.43	8.68	7.48	8.65	7.90
(La/Lu) <sub>cn</sub>	7.67	8.30	7.67	9.86	8.17	8.43	7.02	6.71	6.82	7.39	7.82	5.98	6.23	7.40	8.37	6.36	7.73	7.53
Eu/Eu*	0.69	0.60	0.65	0.64	0.62	0.72	0.62	0.53	0.67	0.68	0.63	0.60	0.60	0.67	0.59	0.61	0.60	0.63
La/Sc	2.54	3.47	3.20	3.80	3.15	3.25	3.29	4.53	2.88	3.08	3.52	3.04	3.30	1.82	4.30	4.90	3.73	3.40
Th/Sc	0.96	1.23	1.18	1.15	1.10	1.00	1.31	1.83	1.13	1.22	1.22	1.29	1.28	0.64	1.60	1.65	1.38	1.24
Th/Cr	0.13	0.07	0.10	0.08	0.16	0.06	0.15	0.12	0.15	0.13	0.15	0.13	0.11	0.09	0.07	0.07	0.11	0.11
La/Co	2.10	8.67	3.84	9.50	7.88	3.25	3.48	3.29	1.92	1.97	1.97	2.34	2.91	2.52	4.03	2.88	5.96	4.03
Th/Co	0.79	3.08	1.42	2.88	2.75	1.00	1.39	1.33	0.75	0.78	0.68	0.99	1.13	0.89	1.50	0.97	2.20	1.44
Zr/Hf	39.97	39.33	40.21	37.44	37.38	37.65	39.25	40.40	38.13	39.39	38.16	40.12	40.59	41.41	40.00	40.82	39.45	39.39

Fe<sub>2</sub>O<sub>3</sub>\* = Total Fe expressed as Fe<sub>2</sub>O<sub>3</sub>. CIA = [Al<sub>2</sub>O<sub>3</sub>/(Al<sub>2</sub>O<sub>3</sub> + CaO\* + Na<sub>2</sub>O + K<sub>2</sub>O)] x 100 (Nesbitt and Young, 1982). PIA = 100 x (Al<sub>2</sub>O<sub>3</sub> - K<sub>2</sub>O)/(Al<sub>2</sub>O<sub>3</sub> + CaO\* + Na<sub>2</sub>O - K<sub>2</sub>O) (Fedo et al., 1995). [Al<sub>2</sub>O<sub>3</sub>/(Al<sub>2</sub>O<sub>3</sub> + CaO + Na<sub>2</sub>O)\*100] (Harnois, 1988); ICV = (Fe<sub>2</sub>O<sub>3</sub> + K<sub>2</sub>O + Na<sub>2</sub>O + CaO + MgO + MnO + TiO<sub>2</sub>)/Al<sub>2</sub>O<sub>3</sub> (Cox et al., 1995). n = number of samples.

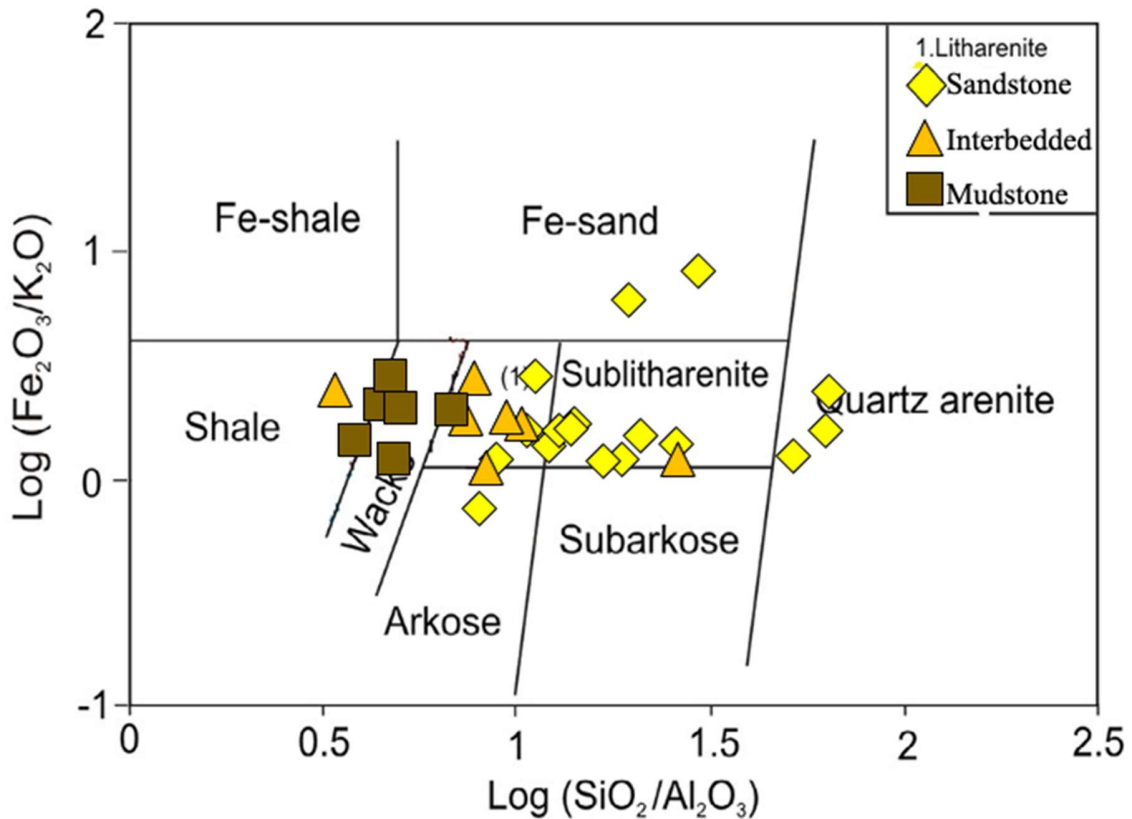


**Table 4.7b The major oxides (in Wt.%) and trace element concentrations (in ppm) of sandstone interbedded mudstone (n= 7) of the Miri Formation**

Sample No.	S1Top	S7	S13	S18Top	S25	H03 Bottom	Ho6G	Average
SiO <sub>2</sub>	85.92	65.59	80.79	94.23	84.41	81.37	84.34	82.38
Al <sub>2</sub> O <sub>3</sub>	8.39	19.28	10.40	3.64	10.16	10.99	9.02	10.27
Fe <sub>2</sub> O <sub>3</sub>	2.61	7.98	5.08	0.80	2.06	3.51	2.94	3.57
MnO	0.01	0.13	0.03	0.01	0.01	0.02	0.02	0.03
MgO	0.69	2.48	0.93	0.25	0.52	0.97	0.91	0.96
CaO	0.05	0.25	0.09	0.02	0.03	0.17	0.18	0.11
Na <sub>2</sub> O	0.28	0.19	0.27	0.12	0.27	0.40	0.41	0.28
K <sub>2</sub> O	1.50	3.26	1.83	0.66	1.87	1.93	1.59	1.80
TiO <sub>2</sub>	0.51	0.91	0.56	0.23	0.65	0.61	0.57	0.58
P <sub>2</sub> O <sub>5</sub>	0.05	0.07	0.05	0.03	0.04	0.05	0.05	0.05
K <sub>2</sub> O/Al <sub>2</sub> O <sub>3</sub>	0.18	0.17	0.18	0.18	0.18	0.18	0.18	0.18
SiO <sub>2</sub> /Al <sub>2</sub> O <sub>3</sub>	10.24	3.40	7.77	25.87	8.31	7.41	9.35	10.33
Al <sub>2</sub> O <sub>3</sub> /TiO <sub>2</sub>	16.58	21.21	18.43	15.57	15.70	18.09	15.87	17.35
CIA	82.19	84.10	82.76	82.09	82.53	81.53	80.66	82.27
CIW	96.31	98.05	96.88	96.47	97.28	95.15	94.02	96.31
PIA	67.53	69.88	68.19	67.19	67.37	67.22	66.45	67.69
ICV	0.67	0.79	0.84	0.58	0.53	0.69	0.73	0.69
Ba	155	275	178	84	180	181	171	174.86
Sc	7	22	10	3	8	8	7	9.29
Be	1	7	1	1	1	1	1	1.86
Co	8.4	30.1	8.9	2.7	5.2	11.5	10	10.97
Cr	68.42	102.63	129.99	41.05	75.26	136.84	102.63	93.83
Cs	4.2	10.5	5.3	1.4	5.1	5.6	4.9	5.29
Ga	11.1	20	10.2	3.6	10.2	10.7	9.6	10.77
Hf	7.8	5.2	7.3	2.9	7.4	6.1	12.6	7.04
Nb	9	13.3	9.2	4.4	10.4	9.9	10.1	9.47
Rb	64.3	144.9	78.3	27.3	76.3	84.8	71.5	78.20
Sn	2	4	2	1	2	2	2	2.14
Sr	41.2	61.6	47.4	28.5	62.3	50.3	51.8	49.01
Ta	0.6	0.9	0.8	0.3	0.7	0.7	0.7	0.67
Th	8.3	14.7	9.2	3.8	9.5	10.3	9.9	9.39
U	2.3	3.8	2.5	0.9	2.6	2.5	2.8	2.49
V	56	136	67	25	68	65	58	67.86
W	1.6	2.5	2.2	10.6	1.8	2.2	1.9	3.26
Zr	298	191.6	292.3	112.9	293.1	236.1	506.2	275.74
Y	16.7	43.2	18.9	8.4	19.1	19.6	19.8	20.81
Mo	0.2	0.3	0.2	0.1	0.2	0.8	0.2	0.29
Cu	17.9	29	13.4	4	12.3	135	21	33.23
Pb	7.7	17	10.9	2.7	9	16.9	10.2	10.63
Zn	48	96	52	14	19	138	68	62.14
Ni	16.2	45.9	20.2	4.2	6.1	22.1	18.8	19.07
As	5.9	9	6.5	2.5	12.2	7.6	5.4	7.01
(La/Yb) <sub>cn</sub>	8.17	6.81	7.84	9.51	8.08	8.71	7.66	8.11
(La/Lu) <sub>cn</sub>	7.71	6.59	8.00	9.50	7.88	7.99	7.24	7.84
Eu/Eu*	0.67	0.71	0.66	0.64	0.64	0.66	0.64	0.66
La/Sc	2.97	1.76	2.39	3.97	3.23	3.18	3.79	3.04
Th/Sc	1.19	0.67	0.92	1.27	1.19	1.29	1.41	1.13
Th/Cr	0.12	0.14	0.07	0.09	0.13	0.08	0.10	0.10
La/Co	2.48	1.29	2.69	4.41	4.96	2.21	2.65	2.95
Th/Co	0.99	0.49	1.03	1.41	1.83	0.90	0.99	1.09
Zr/Hf	38.21	36.85	40.04	38.93	39.61	38.70	40.17	38.93
Rb/Sr	1.56	2.35	1.65	0.96	1.22	1.69	1.38	1.54

**Table 4.7c The major oxides (in Wt.%) and trace element concentrations (in ppm) of mudstones (n=6) of the Miri Formation**

Sample No.	S4	S17	S31	B1	B3	Ho6C	Average
SiO <sub>2</sub>	72.12	71.57	74.88	79.53	70.78	75.61	74.08
Al <sub>2</sub> O <sub>3</sub>	16.11	15.10	14.92	11.72	18.37	15.60	15.31
Fe <sub>2</sub> O <sub>3</sub>	5.89	7.30	5.40	4.00	4.51	3.28	5.06
MnO	0.08	0.13	0.01	0.04	0.03	0.02	0.05
MgO	1.71	1.82	0.90	1.18	1.55	1.22	1.40
CaO	0.22	0.33	0.03	0.21	0.15	0.09	0.17
Na <sub>2</sub> O	0.29	0.40	0.31	0.55	0.54	0.60	0.45
K <sub>2</sub> O	2.79	2.60	2.65	2.01	3.10	2.69	2.64
TiO <sub>2</sub>	0.81	0.78	0.86	0.72	0.90	0.85	0.82
P <sub>2</sub> O <sub>5</sub>	0.07	0.09	0.04	0.06	0.08	0.07	0.07
K <sub>2</sub> O/Al <sub>2</sub> O <sub>3</sub>	0.17	0.17	0.18	0.17	0.17	0.17	0.17
SiO <sub>2</sub> /Al <sub>2</sub> O <sub>3</sub>	4.48	4.74	5.02	6.79	3.85	4.85	4.95
Al <sub>2</sub> O <sub>3</sub> /TiO <sub>2</sub>	19.99	19.41	17.29	16.19	20.35	18.37	18.60
CIA	83.07	82.04	83.32	80.94	82.96	82.30	82.44
CIW	97.02	95.53	97.82	94.01	96.48	95.90	96.13
PIA	68.70	67.91	68.50	67.05	68.94	68.11	68.20
ICV	0.73	0.88	0.68	0.74	0.59	0.56	0.70
Ba	237.00	221.00	239.00	190.00	264.00	257.00	234.67
Sc	13.00	14.00	12.00	10.00	14.00	11.00	12.33
Be	2.00	2.00	1.00	2.00	2.00	3.00	2.00
Co	17.20	14.90	4.50	10.40	14.50	15.30	12.80
Cr	82.10	88.95	82.10	88.95	88.95	82.10	85.53
Cs	8.50	7.90	8.00	6.00	10.20	8.70	8.22
Ga	16.90	14.70	15.40	11.50	18.30	16.50	15.55
Hf	5.00	5.90	7.30	13.30	6.10	7.10	7.45
Nb	11.90	11.60	13.50	11.80	14.20	13.90	12.82
Rb	116.00	109.60	113.30	86.10	132.50	121.70	113.20
Sr	3.00	2.00	4.00	4.00	3.00	3.00	3.17
Sr	57.80	60.00	51.50	58.80	78.00	70.80	62.82
Ta	0.90	0.90	1.00	0.80	1.00	1.00	0.93
Th	13.00	12.40	12.30	12.20	15.70	13.90	13.25
U	3.10	3.20	3.00	3.50	3.60	3.10	3.25
V	107.00	97.00	97.00	81.00	118.00	91.00	98.50
W	2.20	2.10	2.60	5.60	2.80	2.90	3.03
Zr	196.20	220.40	268.60	519.90	227.80	263.00	282.65
Y	30.70	27.60	24.50	25.70	27.70	28.00	27.37
Mo	0.30	0.20	0.10	0.20	0.30	0.30	0.23
Cu	26.50	20.20	11.60	25.90	37.10	22.40	23.95
Pb	20.70	16.30	11.90	15.80	19.80	17.40	16.98
Zn	69.00	58.00	28.00	69.00	84.00	82.00	65.00
Ni	30.70	24.90	6.20	23.60	30.60	33.20	24.87
As	14.20	8.10	7.40	7.30	12.80	8.00	9.63
(La/Yb) <sub>cn</sub>	7.38	7.64	8.20	7.24	8.41	7.98	7.81
(La/Lu) <sub>cn</sub>	7.67	7.41	7.91	7.08	8.11	7.76	7.66
Eu/Eu*	0.69	0.70	0.65	0.65	0.68	0.67	0.67
La/Sc	2.50	2.19	2.67	3.07	2.68	3.13	2.71
Th/Sc	1.00	0.89	1.03	1.22	1.12	1.26	1.09
Th/Cr	0.16	0.14	0.15	0.14	0.18	0.17	0.16
La/Co	1.89	2.06	7.11	2.95	2.59	2.25	3.14
Th/Co	0.76	0.83	2.73	1.17	1.08	0.91	1.25
Zr/Hf	39.24	37.36	36.79	39.09	37.34	37.04	37.81
Rb/Sr	2.01	1.83	2.20	1.46	1.70	1.72	1.82



**Figure 4.28 Geochemical Classification Plot of Siliciclastic rocks of the Miri Formation using  $\text{Log} (\text{Fe}_2\text{O}_3/\text{K}_2\text{O})$  vs  $\text{Log} (\text{SiO}_2/\text{Al}_2\text{O}_3)$  (Herron, 1988).**

## 4.7.2 Trace Elements

The trace elements are grouped into four groups based on their geochemical behaviours, which are transitional trace elements (TTE: Sc, V, Cr, Mn, Co, Ni, Cu, Zn); large ion lithophile elements (LILE; Rb, Cs, Ba, Sr), high field strength elements (HFSE; Zr, Hf, Nb, Ta, Y, Th, U, Ta and W) and rare earth elements (REE: La, Ce, Pr, Nd, Sm, Eu, Gd, Tb, Dy, Ho, Er, Tm, Yb and Lu).

### 4.4.2.1 TTE (Sc, V, Cr, Mn, Co, Ni, Cu and Zn)

The TTEs are widely distributed in the different lithotypes and, as expected, are highly concentrated in mudstone and interbedded mudstone compared to sandstone. The V, Cr, Mn, Co, Ni, Cu and Zn concentrations in sandstone interbedded mudstone and mudstone show a significant difference (i.e., 25.00-136.00 ppm and 41.10-136.84 ppm, <0.00- 1006.80 ppm and 77.45-1006.80

ppm, 2.70-30.10 and 4.50-17.20 ppm, 2.50-12.20 and 7.30-14.20 ppm, 4.00-135.00 ppm and 11.60-37.10 ppm, 14.00-138.00 ppm and 28.00-84.00 ppm) respectively. The sandstone samples have a lower concentration of TTEs compared to the other lithotypes (**Fig 4.29 A**).

#### **4.7.2.1 LILE (Rb, Cs, Ba, Sr and Be)**

LILEs show a significantly lower concentration in sandstone samples (i.e., Rb 10.80-78.90 ppm, Cs 0.50-4.60 ppm, Ba 47.00-185.00 ppm, Sr 24.40-88.30 ppm and Be 1.00-2.00 ppm), while variation among sandstone interbedded mudstone and mudstone shows an increasing variation (i.e., Rb 27.30-144.90 ppm and 86.10-132.50 ppm, Cs 1.40-10.50 ppm and 6.00-10.20 ppm, Ba 84.00-275.00 ppm and 190.00-264.00 ppm, Sr 28.50-62.30 ppm and 51.50-78.00 ppm, Be, 1.00-7.00 ppm and 1.00-3.00 ppm) respectively. Rb shows a high positive correlation with K<sub>2</sub>O, TiO<sub>2</sub>, Al<sub>2</sub>O<sub>3</sub>, Ba, Ga and Cs, which confirms its association with clay minerals (**Appendix 5.0, Fig 6.20**).

Rb shows a positive correlation with Al<sub>2</sub>O<sub>3</sub> and K<sub>2</sub>O contents suggest the association of large ion lithophile elements in Al, Ti and K bearing minerals (e.g., Feng and Kerrich, 1990; Bauluz et al., 2000; Ali et al., 2014; Nagarajan et al., 2017; Nagarajan et al., 2021). The high abundance of Rb is due to the existence of very fine-grained clays and silts sediments. While the high variation of concentration of Sr is observed in sandstones. This is because Sr and Ba usually reside in plagioclase and K-feldspar, respectively (Puchett, 1972; Ben-Awuah et al., 2017) and the effect of calcite cement in selected samples.

#### **4.7.2.2 HFSE (Zr, Hf, Nb, Ta, Y, Th, U, and W)**

HFSEs have a small ionic radius with a higher charge and possess higher resistance from the weathering processes. With respect to that, these elements can survive longer in sediments although the sediments undergo multiple cycles of deposition (recycling) and can provide significant information about the source rocks (McLennan et al., 1990; Nagarajan et al., 2014, 2015, 2017; 2021). Zr concentration is relatively high in all lithotypes (i.e. >575.50 ppm), i.e. in sandstones (59.80-575.50 ppm), sandstone interbedded mudstone (112.90-506.20 ppm) and mudstone (196.20-519.90 ppm), thus, indicating the effects of the recycling and sorting effect (McLennan et al., 1993). Hf also shows similar distribution as Zr in all lithotypes (**Fig 4.29 A**),

i.e., in sandstones 1.60-14.10 ppm, sandstone interbedded mudstone 2.9-12.60 ppm and mudstone/silt 5.00-13.30ppm. The high concentration of Zr and Hf among the HFSE's are due to the presence of heavy minerals (i.e. zircon) as seen in the SEM (Fig 4.34) and petrographic analysis (Fig 4.16 A, B and C). Th and U content are higher in mudstone and sandstone interbedded mudstone compared to sandstone where the concentrations in mudstone for Th range from 12.20-15.70 ppm and U from 3.00-3.66 ppm, Th concentration in sandstone interbedded mudstone ranges of 3.80-14.70 ppm and U in the ranges of 0.90-3.80 ppm and the lowest concentrations for both Th and U are recorded in sandstones i.e., 2.00-9.20 ppm and 0.50-2.80 ppm respectively.

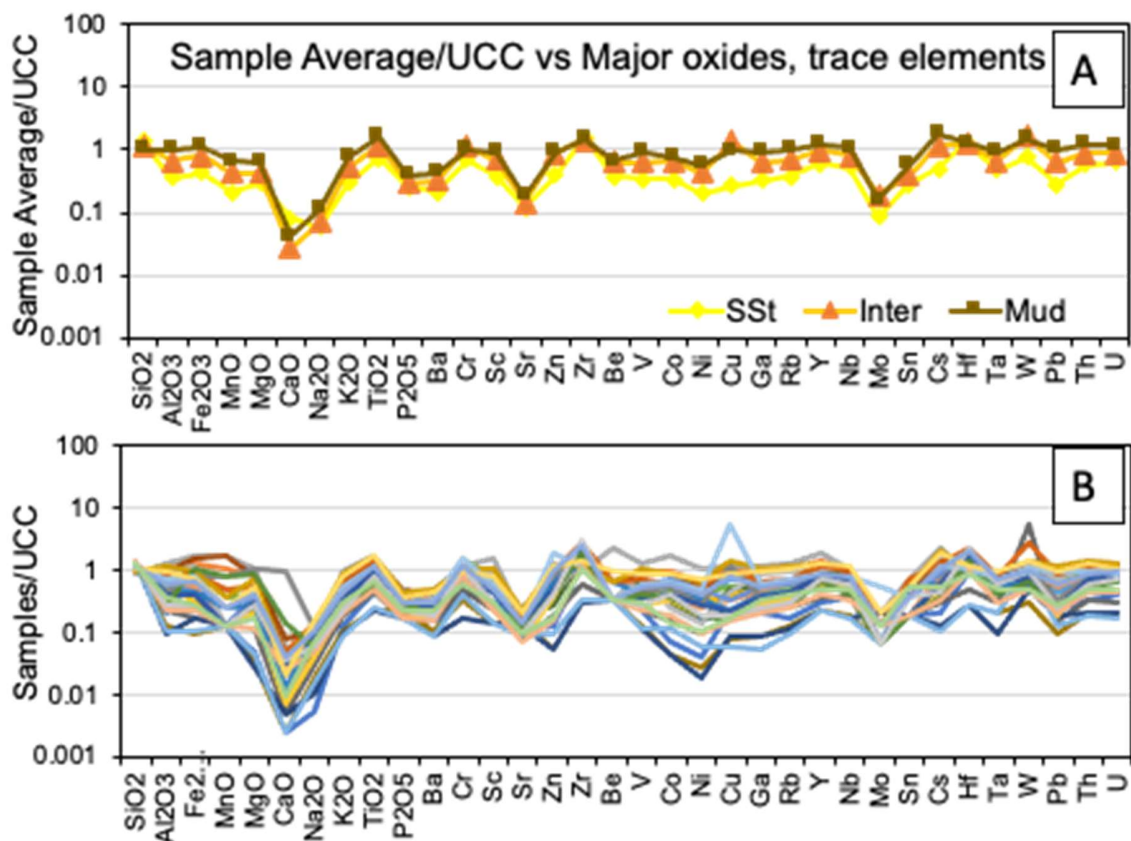


Figure 4.29A- UCC-normalized multi-elements plot based on the average oxide/elemental composition of various lithotypes of the Miri Formation. B- UCC-normalized multi-elements plot for different lithotypes of the Miri Formation.

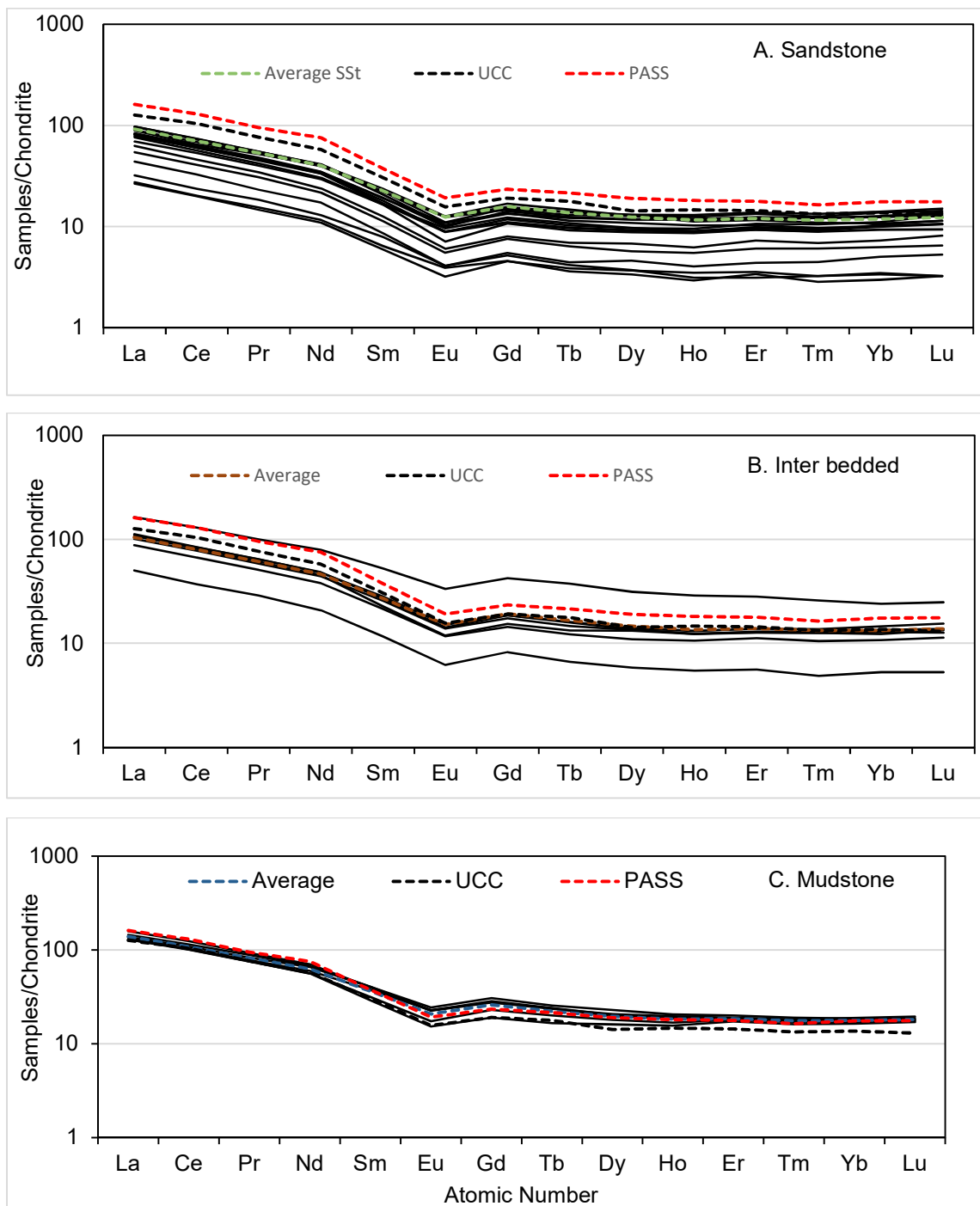
### 4.7.2.3 Rare Earth Elements (REEs)

REEs are known to be the least soluble elements, which make them relatively immobile during processes such as; low-grade metamorphism, hydrothermal alteration and weathering (Rollinson, 1993). The total REE concentration (Table 4.8) is higher in sandstone interbedded

mudstone (54.37-201.88 ppm) and mudstone (147.62-181.54 ppm) compared to that of sandstone (29.32-108.57 ppm). Chondrite normalized plot of all the lithotypes shows an LREE enrichment  $(La/Yb)_{cn}$  range from 6.43-9.33, 6.81-9.51 and 7.24-8.41 for sandstone, sandstone interbedded mudstone and mudstone respectively, also an almost flat HREE  $(Gd/Yb)_{cn}$  ranging from 1.03-1.57, 1.13-1.77 and 1.28-1.65 for sandstone, sandstone interbedded mudstone and mudstone respectively (**Fig 4.30 A, B and C**). Eu shows negative anomalies  $(Eu/Eu^*)$  ranging from 0.53-0.72, 0.64-0.71 and 0.65-0.70 for sandstones, interbedded sandstone/mudstone and mudstone respectively (**Fig 4.30 A, B and C**).

**Table 4.8: Statistical summary of REE values of the three lithotypes in the Miri Formation.**

<b>lithotype</b>	<b>REE</b>	<b>La</b>	<b>Ce</b>	<b>Pr</b>	<b>Nd</b>	<b>Sm</b>	<b>Eu</b>	<b>Gd</b>	<b>Tb</b>	<b>Dy</b>	<b>Ho</b>	<b>Er</b>	<b>Tm</b>	<b>Yb</b>	<b>Lu</b>
Sandstone	Max	23.00	45.40	5.11	18.80	3.51	0.71	3.35	0.53	3.22	0.71	2.20	0.33	2.25	0.37
	Min	6.30	12.20	1.36	5.00	0.88	0.18	0.90	0.13	0.83	0.16	0.50	0.07	0.48	0.08
Interbedded	Max	38.70	79.40	9.27	36.20	7.75	1.88	8.43	1.35	7.71	1.57	4.51	0.64	3.86	0.61
	Min	11.90	22.60	2.68	9.50	1.72	0.35	1.64	0.24	1.44	0.30	0.90	0.12	0.85	0.13
Mudstone	Max	37.50	76.40	8.64	32.30	5.98	1.37	6.10	0.92	5.63	1.12	3.21	0.47	3.03	0.48
	Min	30.70	61.60	6.99	25.70	4.31	0.86	3.77	0.60	3.95	0.85	2.77	0.40	2.65	0.42



**Figure 4.30. Chondrite normalized REE pattern for the siliciclastic rocks of the Miri Formation (A – sandstone; B. sandstone interbedded mudstone and C. mudstone)**

## 4.8 Discussion

### 4.8.1 Paleo weathering

The weathering of sediment can indicate the degree of alteration in which rock or sediment have undergone due to exposure to weathering agents at some point in time. Key factors that govern the weathering processes include tectonic influences, climate and geomorphology of the area. The mineralogical and geochemical composition of the original rocks is being affected by these weathering processes (Nesbitt et al., 1996). Many weathering indices are proposed to calculate the intensity of weathering in which the CIA (Chemical Index of Alteration by Nesbitt and Young, 1982), and PIA (Plagioclase Index of Alteration by Fedo et al., 1995) are frequently used by many authors. Weathering intensity of rocks are categorized based on the CIA values, where non-weathered or fresh parent rock have CIA value lesser than 50, weak weathering has CIA ranging from 50-70 and indicating in an arid and cold climate (Fedo et al., 1996 and Yan et al., 2010), moderate weathering rocks has CIA values ranging 70-80 indicating in a warm and humid climate condition (Nesbitt and Young, 1982) and intensely weathered rocks have CIA greater than 80, indicating in a humid hot climate. PIA values are also calculated in addition to CIA to support the interpretation, which mainly describes Ca-rich end member of feldspar (plagioclase) hydrolyses since this mineral is most abundant in silicate rocks. In general, chemical weathering strongly affects the major-element geochemistry and mineralogy of the siliciclastic sediments (Fedo et al., 1995; Nesbitt and Young, 1982), where larger labile cations ( $Al^{3+}$ ,  $Ba^{2+}$ , and  $Rb^{+}$ ) remain fixed in the weathering profile preferentially over smaller cations ( $Ca^{2+}$ ,  $Na^{+}$ ,  $K^{+}$ , and  $Sr^{2+}$ ), which are selectively leached. These chemical signatures are ultimately transferred to the sedimentary record, thus providing a useful tool for monitoring source-area weathering conditions.

In order to better understand the paleoweathering history of the Miri Formation siliciclastic sedimentary rocks, CIA and PIA values are calculated and A-CN-K and A-CNK-FM ternary plots are also adopted. The calculated CIA values for the Miri Formation are in the ranges 72 to 85 for sandstone, 78 to 82 for sandstone interbedded mudstone and 78 to 81 for mudstone respectively.



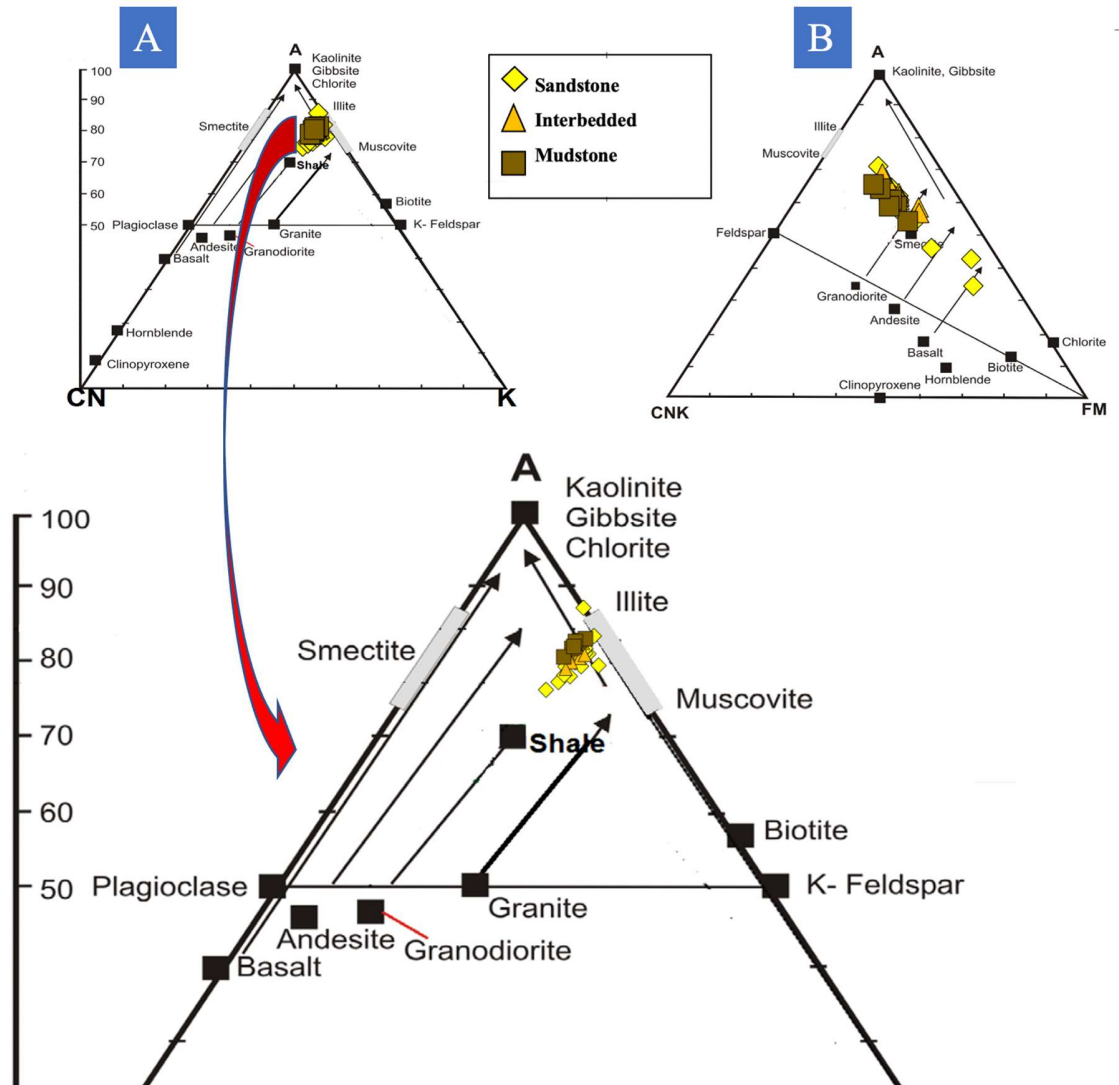
The high CIA values ( $>75$ ) observed in the study samples indicate moderate to intensive chemical weathering. The PIA values of the Miri Formation range from 80 to 98 for sandstone, 89 to 96 for sandstone interbedded mudstone and 89 to 95 for mudstone respectively. The PIA values of the study samples suggest moderate to intense chemical weathering in the source area. However, sedimentary recycling might have influenced the higher values of these geochemical indices by the enrichment of quartz and heavy minerals, in particular, in the sandstones.

The weathering history of both recent and ancient sediments can be calculated in terms of  $\text{Al}_2\text{O}_3$  (A),  $\text{CaO}^*+\text{Na}_2\text{O}$  (CN), and  $\text{K}_2\text{O}$  (K) molecular ratios (Nesbitt and Young, 1984; Nesbitt, 2003) by plotting the A-CN-K ternary diagram. The A-CN-K plot (**Fig 4.31 A**; Nesbitt and Young, 1982), where all the samples plot away from the average shale composition and are clustered at the illite point, which indicates that the study samples have a significant amount of illite. Likewise, the samples are more clustered on the A-K line, which indicates that a significant amount of  $\text{Na}_2\text{O}$  and  $\text{CaO}$  has been removed from the bulk composition due to chemical weathering (e.g. Khan and Khan, 2015). The samples are also plotted on a weathering trend derived from UCC/granodiorite, which indicates that these sediments are derived from felsic rocks-dominated source areas. An A-CN-K-FM plot (**Fig 4.31 B**) also supports this interpretation, where, the samples plot from smectite toward illite, following the predicted weathering trend of granodiorite than mafic source rocks. Generally, stronger chemical weathering indicates that the source area has experienced warm and humid climate conditions (Nesbitt and Young, 1982).

Illite is the most dominant mineral, based on XRD analysis of the 6 studied samples, which supports the weathering trend observed on the A-CN-K and A-CN-K-FM plots.

Based on the weathering intensity scale (WIS) proposed by Meunier et al. (2013), the studied samples reveal a trend of illitization thus, illite correction was carried out (**Table 4.9**). The  $\text{M}^+ - 4\text{Si} - \text{R}^{2+}$  plot enables the transformation that sediments undergo according to the type and intensity of the possible diagenetic reaction during burial. The studied samples plot towards the 4Si point (**Fig 4.32 A and B**), signifying kaolinite and quartz enrichment zone, which is clearly the ultimate silicate clay-product of weathering. The intensity of weathering ( $\Delta 4\text{Si}$ ) is determined by considering the  $\Delta 4\text{Si}$  percentage granodiorite as the source. Based on the  $\Delta 4\text{Si}$  versus

$R^{3+}/(R^{3+}+R^{2+}+M^{+})$  plot (**Fig4.32 D**), most of the studied samples plot in the gray zone (Physical mixture), which is the effect that points to multi-source sediments (mixing of fresh rock debris with clays, carbonates or Fe-Al- oxyhydroxides; Meunier et al., 2013).



**Figure 4.31 (A) A-CN-K and (B) A-CN-K-FM (after Nesbitt and Young, 1984; Nesbitt and Wilson, 1992) plots showing the weathering trend for the siliciclastic rocks of the Miri Formation.**

**Table 4.9 The corrected composition of the Miri Formation after subtraction of illite contribution.**

Samples	SiO <sub>2</sub> cor	Al <sub>2</sub> O <sub>3</sub> cor	Fe <sub>2</sub> O <sub>3</sub> cor	MnOcor	MgOcor	CaOcor	Na <sub>2</sub> Ocor	K <sub>2</sub> Ocor	ΔK <sub>2</sub> O	%illite
S1T	80.12	4.70	2.49	0.01	0.49	0.05	0.28	0.29	1.29	13.0
S4	60.10	8.47	5.64	0.08	1.30	0.22	0.29	0.29	1.20	12.2
S7	51.29	10.19	7.68	0.13	1.99	0.25	0.19	0.29	2.49	25.2
S10T	77.03	5.67	1.22	0.01	0.39	0.03	0.14	0.29	2.97	30.0
S11	91.67	2.72	3.57	0.01	0.09	0.01	0.02	0.29	1.60	16.1
S13	73.38	5.69	4.92	0.03	0.67	0.09	0.27	0.29	0.15	1.5
S14T	84.93	3.66	1.97	0.01	0.28	0.03	0.27	0.29	1.54	15.5
S17	60.45	8.03	7.07	0.13	1.45	0.33	0.40	0.29	0.89	8.9
S18T	92.46	2.51	0.77	0.01	0.19	0.02	0.12	0.29	2.31	23.3
S22T	96.64	1.68	0.45	0.01	0.06	0.01	0.07	0.29	0.37	3.7
S24B	96.87	1.41	0.80	0.01	0.05	0.02	0.04	0.29	0.07	0.7
S25	76.84	5.34	1.90	0.01	0.26	0.03	0.27	0.29	0.04	0.4
S26T	97.34	1.57	0.48	0.01	0.10	0.01	0.06	0.29	1.57	15.9
S29T	80.65	4.52	2.30	0.01	0.40	0.03	0.28	0.29	0.00	0.0
S31	63.50	7.69	5.16	0.01	0.51	0.03	0.31	0.29	1.20	12.1
S32 T	89.09	3.09	1.02	0.01	0.35	0.03	0.15	0.29	2.36	23.9
T1T	77.57	5.11	1.95	0.01	0.68	0.05	0.42	0.29	0.61	6.1
T2T	82.80	4.08	1.76	0.01	0.52	0.10	0.35	0.29	1.46	14.7
T3T	83.92	4.00	1.89	0.02	0.46	0.05	0.30	0.29	1.05	10.6
B1	71.25	6.45	3.83	0.04	0.90	0.21	0.55	0.29	0.94	9.5
B2T	75.36	4.13	3.52	0.06	2.29	4.23	0.44	0.29	1.72	17.4
B3	57.23	9.76	4.23	0.03	1.09	0.15	0.54	0.29	1.00	10.1
B4DT	84.76	3.84	1.80	0.01	0.51	0.12	0.38	0.29	2.81	28.4
Ho2B	83.83	2.81	5.00	0.06	1.94	0.63	0.22	0.29	0.85	8.6
H03B	73.49	5.98	3.34	0.02	0.70	0.17	0.40	0.29	0.54	5.4
Ho4B	91.79	2.37	0.97	0.01	0.20	0.10	0.20	0.29	1.64	16.5
Ho5T	89.52	2.80	1.22	0.01	0.52	0.15	0.24	0.29	0.42	4.2
Ho6C	64.07	8.26	3.04	0.02	0.83	0.09	0.60	0.29	0.53	5.3
Ho6G	78.09	5.05	2.81	0.02	0.69	0.18	0.41	0.29	2.40	24.2
H06HT	87.29	3.08	1.21	0.01	0.24	0.04	0.28	0.29	1.30	13.1

SiO<sub>2</sub>cor=SiO<sub>2</sub> corrected

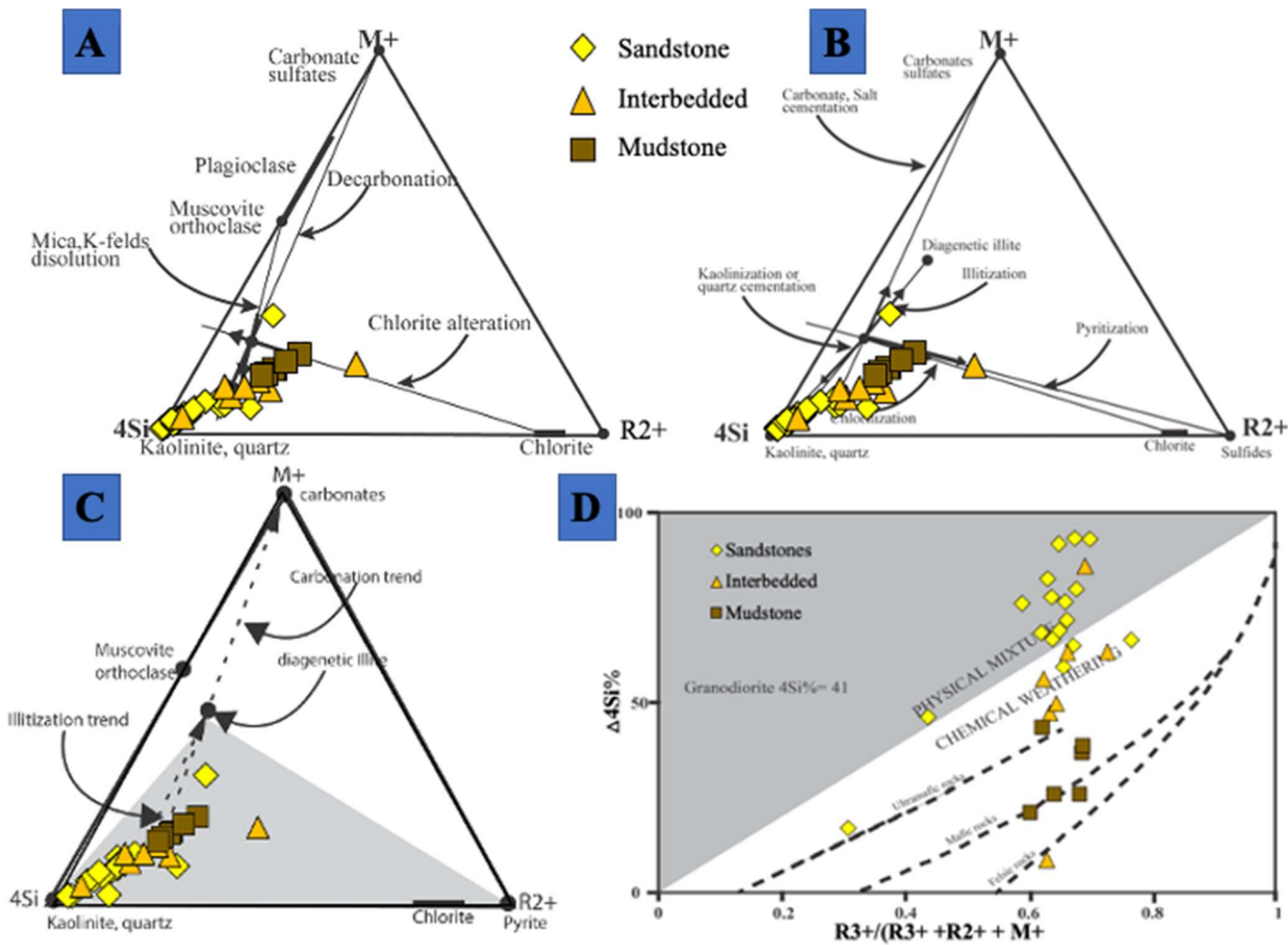
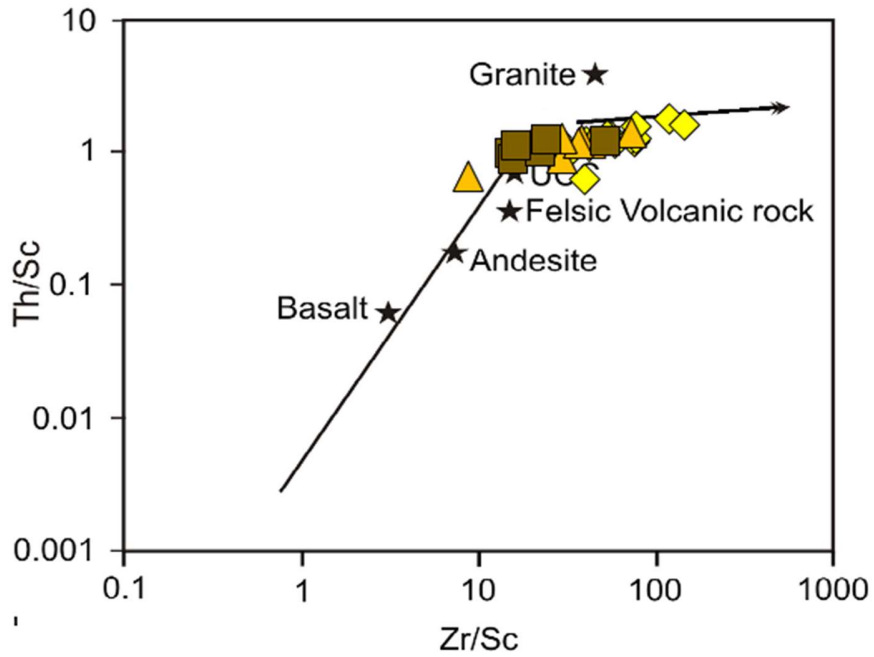


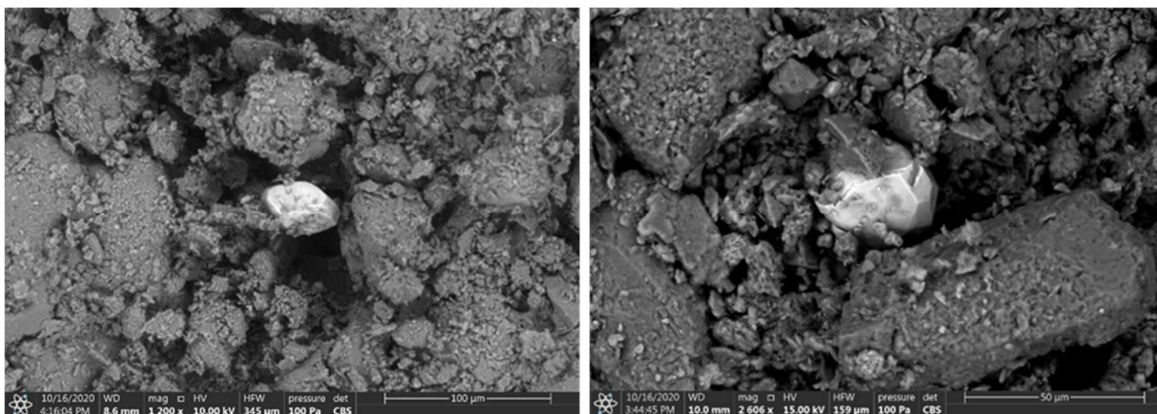
Figure 4.32. A-  $M^+ - 4Si - R^{2+}$  diagram shows the changes in sediments of the Miri Formation due to the dissolution of primary components, B.  $M^+ - 4Si - R^{2+}$  diagram shows the changes in sediments of the Miri Formation due to the effect of illitization, C.  $M^+ - 4Si - R^{2+}$  diagram shows all sediments plot in the grey area, which represents the domain of kaolinite-illite and pyrite. D-  $\Delta 4Si$  versus  $R^{3+}/(R^{3+} + R^{2+} + M^+)$  shows the majority of samples plotted in the physical mixture and few samples follow the trend of chemical weathering (after Meunier et al., 2013).

## 4.8.2 Sediment Sorting and Recycling

Sorting is the degree of mineral separation based upon the grain size, and as the mineral density increases, the degree of sorting increases, allowing for accurate measurement of the distribution of mineral grain size. Hydraulic sorting of minerals controls the distribution of Th, U, Zr, Hf, and Nb in siliciclastic sediments, which may affect the bulk composition of sedimentary rocks (Armstrong-Altrin, 2009). The Th/Sc versus Zr/Sc plot proposed by McLennan et al. (1993) is used to analyze the relationship between the composition of the source rock and the sedimentary processes. The Zr/Sc ratio is applied to investigate the enrichment of zircon since Zr is strongly enriched in zircon, while Sc also preserves the provenance signature like REEs. Zircon is rich in Zr and Hf and they are mainly associated with felsic igneous rocks, whereas mafic components have high concentrations of Sc. Therefore, the Zr/Sc versus Th/Sc plot (McLennan et al., 1993) is most suitable to evaluate the Zr enrichment during sediment sorting and also to understand the compositional difference between felsic and mafic compositions. On this plot (**Fig 4.33**), the samples deviate from the first trend and plot along with the second trend, which is the zircon concentration trend, indicating enriched zircon concentration by the accumulation of zircon minerals during sorting and recycling processes. In particular, sandstone and sandstone interbedded mudstone of the Miri Formation show high enrichment of zircon compared to mudstone, which is further confirmed by the SEM analysis (**Fig 4.34**). Some samples lie on the first trend, which were not subjected to sorting and weathering processes.

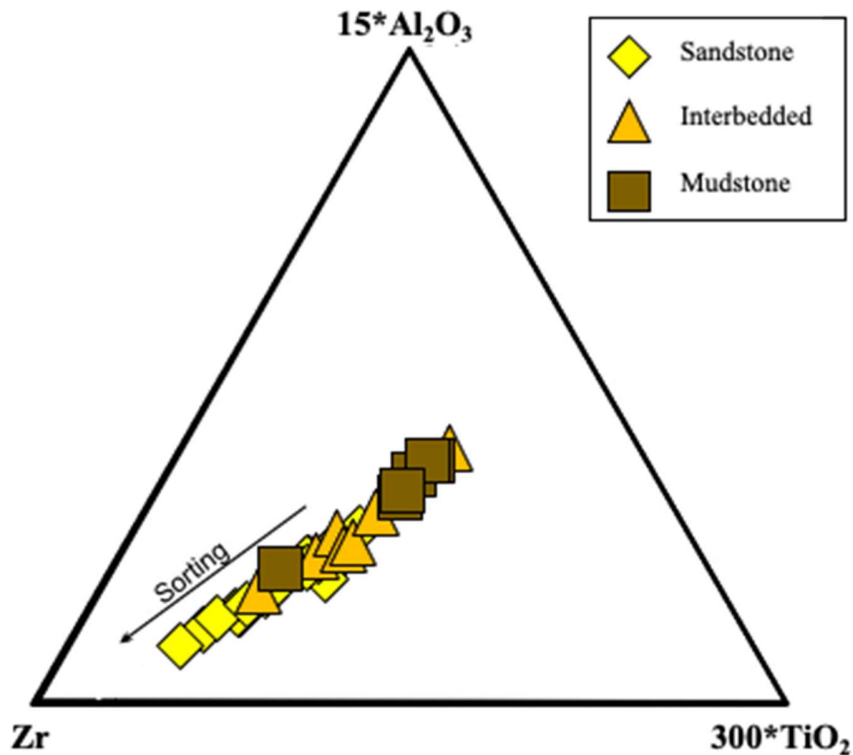


**Figure 4.33** Th/Sc versus Zr/Sc diagram for the siliciclastic rocks of the Miri Formation (after McLennan et al., 1993). The concentration of zircon due to sediment sorting and recycling can be seen along with the second Trend (increasing Zr/Sc ratios)



**Figure 4.34** SEM images of sandstone show the presence of zircon minerals

The  $\text{Al}_2\text{O}_3$ - $\text{TiO}_2$ -Zr ternary plot proposed by Garcia et al. (1994) disregards the weathering effects and illustrates the effect of sorting-related fractionation based on the proportion of these elements. Based on the  $\text{Al}_2\text{O}_3$ - $\text{TiO}_2$ -Zr ternary diagram (Fig 4.35), the study samples reveal that the variation in the  $\text{Al}_2\text{O}_3/\text{Zr}$  ratio is due to the recycling effect. Thus, the recycling process significantly controlled the provenance signature of the siliciclastic sediments of the Miri Formation.



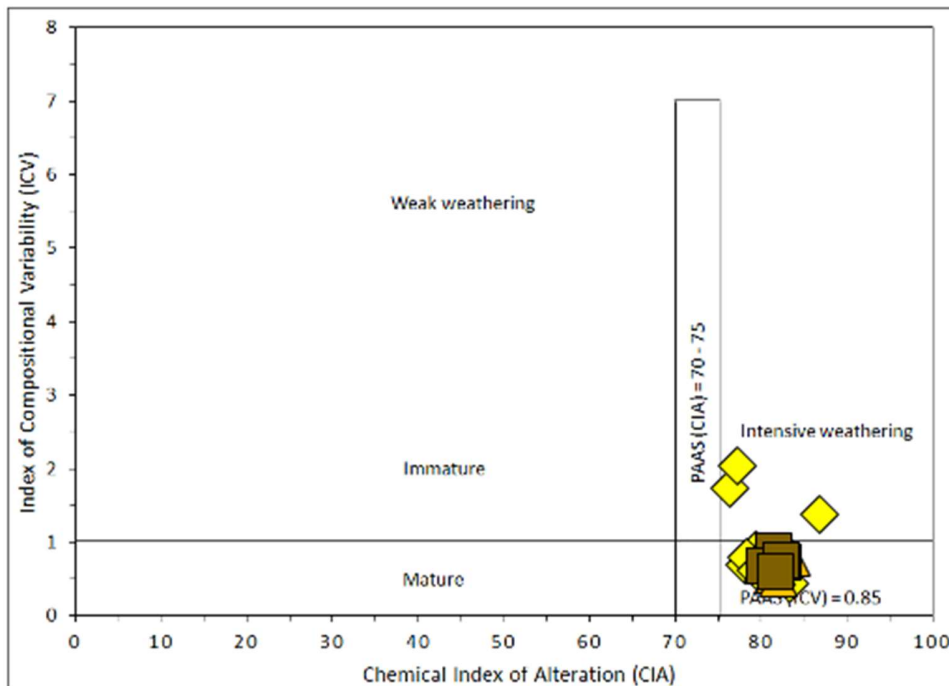
**Figure 4.35  $\text{Al}_2\text{O}_3$ -Zr- $\text{TiO}_2$  plot showing the sorting trend for the siliciclastic rocks of the Miri Formation. (after Garcia et al., 1994)**

To have a better understanding of sediment sorting and recycling, the maturity of the sediment is also taken into account. Maturity of sediments is governed by weathering and long transport distances of sediments whereby unstable minerals weather and sometimes partially disappear or entirely disappear from the original whole-rock composition, as well as the stable minerals shape becoming more rounded. Many researchers have defined maturity differently i.e., compositional maturity indicates the level of the chemical features in approaching the end product (Ingersoll et al., 2003). The degree of compositional maturity of the siliciclastic sediments is calculated by using the Index of Compositional Variability proposed by Cox et al. (1995) where;

ICV =  $(\text{Fe}_2\text{O}_3 + \text{K}_2\text{O} + \text{Na}_2\text{O} + \text{CaO} + \text{MgO} + \text{TiO}_2) / \text{Al}_2\text{O}_3$  and  $\text{K}_2\text{O} / \text{Al}_2\text{O}_3$  ratio (Armstrong-Altrin et al., 2015). Commonly, non-clay detrital minerals will devise higher ICV values compared to clay minerals. Whereas rock-forming minerals show ICV values greater than 0.84, alteration products such as kaolinite, illite, and muscovite have values lesser than 0.84 (Cox et al., 1995). Therefore, with increasing weathering and/or maturity of the siliciclastic sediments, ICV values decrease. The ICV values of the studied samples are generally  $< 1$  except for 3 samples with ICV values  $> 1$  (i.e. Fe rich sandstone (1.39), calcite cement sandstone (1.75) and organic-rich sandstone (2.05), suggesting that majority of the samples are compositionally mature and were likely subjected to weathering and recycling effects. While the high ICV values ( $>1$ ) recorded in the above-mentioned samples suggest chemical immaturity and enriched in CaO and  $\text{Fe}_2\text{O}_3$  content by the cement) formed during the post-depositional processes such as diagenesis. Moreover, in the CIA versus ICV plot (**Fig 4.36**), the chemically immature samples fall above the ICV values 1, which indicates that they consist of more rock-forming minerals than clay minerals. In addition, the three samples (S11, B2T and Ho2B) show ICV values  $>1$ , which are enriched in ferruginous ( $\text{Fe}_2\text{O}_3$  in S11 and HO2: 3.5 and 4.75wt.% respectively), and calcite cement (B2T: CaO = 3.9 wt.%) formed during the post-depositional period.

Feldspars and clay in the siliciclastic sediments can be determined by using the ratio between  $\text{K}_2\text{O}$  and  $\text{Al}_2\text{O}_3$ . Clay minerals show a value approaching zero in the  $\text{K}_2\text{O} / \text{Al}_2\text{O}_3$  ratio while alkali feldspars range from 0.4 to 1.0 (Cox et al., 1995). The average  $\text{K}_2\text{O} / \text{Al}_2\text{O}_3$  ratio in the studied samples is  $< 0.2$  (**Table 4.7**) and is comparable with illite (0.3). This observation is also supported by the mineralogy data and A-CN-K plot (**Fig. 4.31A**), where the samples are plotted between the average shale and illite compositions. A-CNK-FM plot also supports the abundance of illites that are enriched in smectite/chlorite (**Fig 4.31 B**), indicating moderate to high chemical maturity.





**Figure 4.36. CIA versus ICV plot showing the intensity of weathering and maturity of the siliciclastic rocks of the Miri Formation (Long et al., 2012). (please refer 4.35 for the legend of the samples' symbols).**

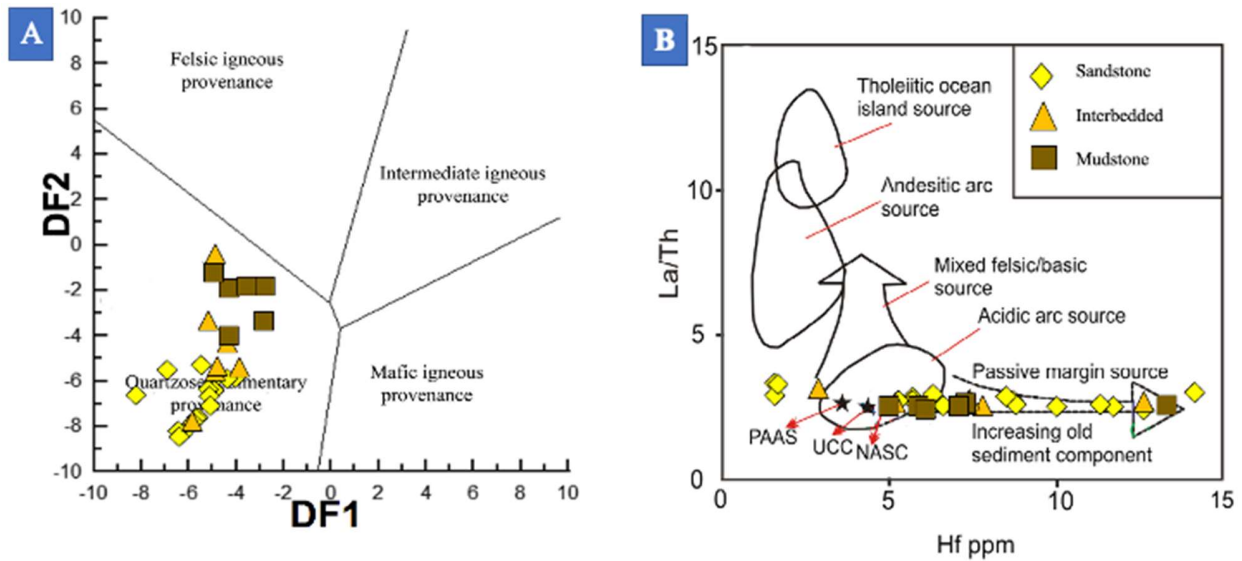
### 4.8.3 Source-rock Composition

An integrated approach using petrography, mineralogy and geochemistry is used to deduce the provenance of the Miri Formation sedimentary rocks. Provenance study using petrography has been studied by many researchers by examining the quartz microtextures (Krinsley and Donahue, 1968; Whalley and Krinsley, 1974; Krinsley and McCoy, 1977; Krinsley and Marshall, 1987; Itamiya et al., 2019, Hossain et al., 2020; Ramos-Vazquez and Armstrong-Altrin., 2020), the feldspar types (Pittman, 1970), lithic fragments (Pettijohn et al., 1987), and heavy mineral types (Asiedu et al., 2000; Morton, 1985; Patra et al., 2014). Petrographically, the Miri Formation sandstone is characterized by its textural features such as very fine to medium-grained, moderately to well sorted, and subangular to subrounded shapes, which indicate a moderate transport distance with an extensive reworking of the sandstones.

Based on the point counting results (**Table 4.1**), quartz is the most dominant mineral followed by lithic fragments and feldspars. The monocrystalline quartz accounts for over 80% of the total quartz composition compared to the polycrystalline quartz grains. Based on the provenance discriminant scheme of Dickson et al. (1983), the QFL triangle diagram (**Fig 4.40**) revealed the studied samples fall in the craton interior and recycled orogenic field. The occurrence of both stained and unstained monocrystalline quartz grains observed in the studied samples (**Fig 4.9, 4.20 and 4.12**), suggests that the quartz grains are mostly derived from plutonic igneous rocks (Basu et al., 1975). Moreover, the dominant occurrence of unstained quartz grains with inclusions (**Fig 4.12 C**) implies a granitic source (Basu et al., 1975; Potter, 1978; Hindix, 2000). This can further be supported by the presence of plutonic lithic fragments observed in the studied samples (**Fig 4.15 D**). The presence of polycrystalline quartz grains with five or more crystals exhibiting a straight or curved intercrystal boundary (**Fig 4.12 B**) also suggest a plutonic igneous rock source (Folk, 1974; Blatt et al., 1980). Plagioclase extinction angle using Michel-Levy's method the plagioclase feldspars are albite to andesite variety of anorthitic composition, which also revealed a felsic to the intermediate source. The lithic fragments observed (**Fig 4.15**) further revealed a recycled origin of the sedimentary or meta-sedimentary origin.

Geochemically, the major, trace and REEs are used by many researchers in order to identify sediment provenance due to their lower mobility nature. Based on the major elements provenance discrimination diagrams of Roser and Korsch (1988), the studied samples of the Miri Formation fall in the quartzose sedimentary provenance field (**Fig 4.37 A**). This implied that the source rocks were mostly felsic with a recycled nature. According to Roser and Korsch (1988), sediments derived from recycled orogenic provinces will fall in the quartzose sedimentary provenance field. Therefore, due to the uncertainty of provenance discrimination using major elements and the effect of multiple cycles of sediment, the provenance cannot be affirmed based on only major element concentration. Immobile elements are not affected by depositional processes, therefore the use Hf vs La/Th plot (Floyd and Leveridge, 1987), further address the provenance of the studied samples. In the Hf vs La/Th plot (**Fig 4.37 B**), the samples fall within the felsic source region, which is the acidic arc source comparable to UCC and NASC and extending towards the passive margin source, indicating the recycling of sediments from the sedimentary or meta-sedimentary terrain (i.e. Rajang Group of rocks in Borneo). Also, in this plot, samples are scattered horizontally with increasing values of Hf, which indicates that the recycling effect was significant and controlled the

selected heavy minerals and quartz. This confirms that the sediments are recycled from the sedimentary to metasedimentary rich source area (Rajang Group of rocks) which were originally derived from granitoids (granite and granodiorite rich) in the source region. The recycled nature of sediments is supported by enrichment of zircon (**Fig 4.35**) and Hf concentration trend in **Figure 4.37 B**.



**Figure 4.37. A. Major oxide-based provenance discrimination plot for the siliciclastic rocks of the Miri Formation (after Roser and Korsch, 1988). B. Hf vs. La/Th bi-plot shows the major provenance fields for the siliciclastic rocks of the Miri Formation (after Floyd and Leveridge, 1987).**

The felsic nature of the source region is further confirmed by the enrichment of LREE, depletion of HREE and a negative  $\text{Eu}/\text{Eu}^*$  anomaly on the chondrite normalized diagram (**Fig.4.30**). Also, trace element ratios of  $\text{La}/\text{Sc}$ ,  $\text{Th}/\text{Sc}$ ,  $\text{Th}/\text{Cr}$ ,  $\text{La}/\text{Co}$ ,  $\text{Th}/\text{Co}$ ,  $\text{Eu}/\text{Eu}^*$ , and  $(\text{La}/\text{Lu})_{\text{cn}}$  are calculated (**Table 4.10**) and compared with similar ratios of the sediments derived from felsic and mafic rocks, UCC, PAAS and also with previous regional studies. These ratios confirm that the Miri Formation samples fall within the range of felsic source rock (**Table 4.10**) and similar results are reported from the previous study conducted on the Sibuti, Lambir and Tukai Formations (Nagarajan et al., 2017a,b), (**Table 4.11, 4.12**).

**Table 4.10: Range of elemental ratios of siliciclastic rocks of the Miri Formation, compared with those fine fractions derived from felsic and mafic source rocks, Upper Continental Crust (UCC), and Post-Archean Australian Shale (PAAS).**

Lithotypes / Element ratio	Range of Elemental Ratios of the Miri Formation <sup>1</sup>				Range of the fine fractions from <sup>3</sup>						
	SSt (n=17)	SSt intr Mdst (n=7)	Mdst (n=6)	Granite <sup>2</sup>	TTG <sup>2</sup>	Felsic volcanic rocks	Andesite <sup>2</sup>	Felsic Source <sup>3</sup>	Mafic Source <sup>3</sup>	UCC <sup>4</sup>	PASS <sup>5</sup>
La/Sc	1.82- 4.90	1.76- 3.97	2.19- 3.13	8.00	1.79	2.80	0.90	0.70– 27.7	0.40– 1.10	2.21	2.40
Th/Sc	0.64- 1.83	0.67- 1.41	0.89- 1.26	3.60	0.71	0.90	0.22	0.64– 18.1	0.05– 0.40	0.79	0.90
Th/Cr	0.06- 0.16	0.07- 0.14	0.14- 0.18	2.25	0.30	1.50	0.10	0.067– 4.0	0.002– 0.045	0.13	0.13
La/Co	1.92- 9.50	1.29- 4.96	1.89- 2.95	13.33	1.79	5.60	0.90	1.4– 22.4	0.14– 0.38*	1.76	1.66
Th/Co	0.68- 3.08	0.49- 1.83	0.76- 1.17	6.00	0.71	1.80	0.22	0.30– 7.5	0.04– 1.4*	0.63	0.63
Zr/Hf	37.38- 41.41	36.84- 40.18	37.04- 39.24	-	-	-	-	-	-	33.00	42.00
Eu/Eu*	0.53- 0.72	0.64- 0.71	0.65- 0.70	-	-	-	-	0.40– 0.94	0.70– 1.02	0.63	0.65
(La/Lu)cn	5.98- 9.86	6.59- 9.50	7.08- 8.11	-	-	-	-	3.00– 27	-	9.73	15.15

i.e., <sup>1</sup>Present study, <sup>2</sup>Condie (1993), <sup>3</sup>Cullers and Podkovyroy (2002), <sup>4</sup>McLennan (2001), <sup>5</sup>Taylor and McLennan (1985) (SSt – Sandstone; SSt intr Mdst – sandstone interbedded mudstone; Mdst – mudstone; TTG – Tonalite Trondhjemite granite; UCC – Upper Continental Crust and PAAS – Post Archean Australian Shale

**Table 4.11 Range of elemental ratios of siliciclastic rocks of the Miri Formation, compared with published data from Nagarajan et al. (2017a) of the Sibuti and Lambir Formations.**

Lithotypes / Element ratio	Range of Elemental Ratios of the Miri Formation <sup>1</sup>			Sibuti Formation <sup>2</sup>		Lambir Formation <sup>2</sup>			
	Sst (n=17)	Sst intr Mdst (n=7)	Mdst (n=6)	Wacke (n=3)	Wacke (n=10)	Litharenite (n=10)	Arkose (n=4)	Fe-Sand (n=2)	Quartz arenite (n=1)
La/Sc	1.82- 4.90	1.76- 3.97	2.19- 3.13	2.42- 3.14	2.09- 2.93	2.59- 5.37	4.22- 6.40	2.26- 3.18	5.7
Th/Sc	0.64- 1.83	0.67- 1.41	0.89- 1.26	0.90- 0.96	0.82- 1.10	0.94- 1.97	1.55- 2.45	0.76- 1.20	2.1
Th/Cr	0.06- 0.16	0.07- 0.14	0.14- 0.18	0.16- 0.20	0.13- 0.19	0.17- 0.23	0.14- 0.20	0.16- 0.19	-
La/Co	1.92- 9.50	1.29- 4.96	1.89- 2.95	2.42- 4.40	1.18-10.90	1.74- 15.80	5.28- 9.17	3.18- 3.23	5.7
Th/Co	0.68- 3.08	0.49- 1.83	0.76- 1.17	0.96- 1.28	0.45- 3.53	0.63- 5.95	1.98- 3.63	1.09- 1.20	2.1
Zr/Hf	37.38-41.41	36.84- 40.18	37.04- 39.24	-	-	-	-	-	-
Eu/Eu*	0.53- 0.72	0.64- 0.71	0.65- 0.70	0.66- 0.76	0.59- 0.76	0.56- 0.71	0.55- 0.72	0.64- 0.72	0.59
(La/Lu)cn	5.98- 9.86	6.59- 9.50	7.08- 8.11	8.16- 8.62	7.19-10.49	5.75- 7.46	4.68- 7.94	6.70- 7.32	6.23

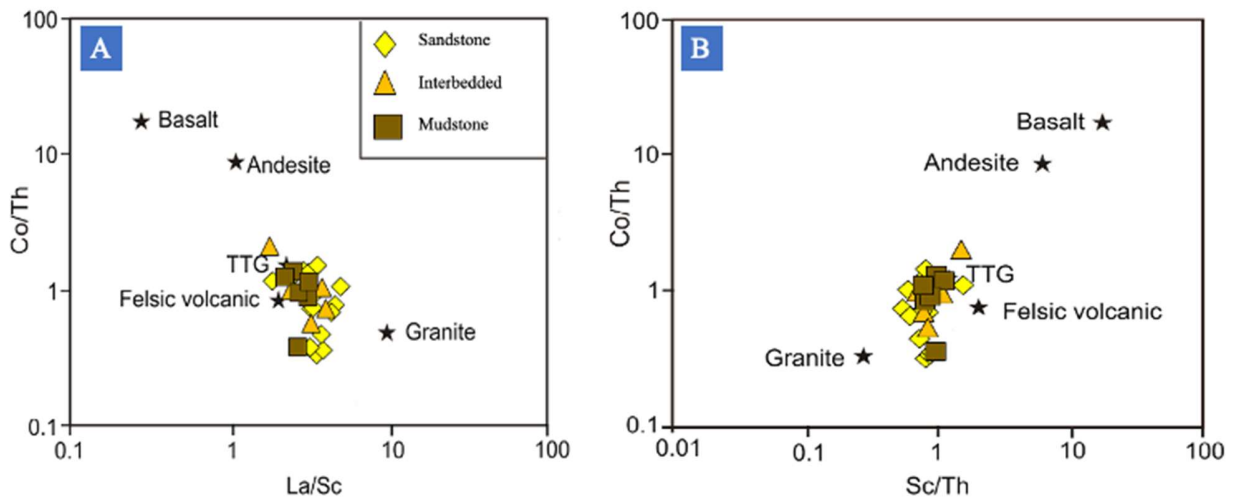
i.e., <sup>1</sup>Present study, <sup>2</sup>Nagarajan et al. (2017a). SSt – Sandstone; SSt intr Mdst – sandstone interbedded mudstone; Mdst – mudstone

**Table 4.12 Range of REE of siliciclastic rocks of the Miri Formation, compared with published data from Nagarajan et al. (2017b) of the Tukau Formations.**

Lithotypes/ Element ratio	Range of REE's of the Miri Formation <sup>1</sup>			Range of REE's of the Tukau Formation <sup>2</sup>
	Sandstone n=17	Interbedded n=7	Mudstone n=6	Sandstones and mudstones n=31
La/Sc	1.82- 4.90	1.76- 3.97	2.19- 3.13	2.09 – 6.40
Th/Sc	0.64- 1.83	0.67- 1.41	0.89- 1.26	0.76 – 2.45
Th/Cr	0.06- 0.16	0.07- 0.14	0.14- 0.18	0.13 – 0.23
La/Co	1.92- 9.50	1.29- 4.96	1.89- 2.95	1.18 – 15.80
Th/Co	0.68- 3.08	0.49- 1.83	0.76- 1.17	0.45 – 5.95
Zr/Hf	37.38-41.41	36.84- 40.18	37.04- 39.24	38.75 – 56.22
Eu/Eu*	0.53- 0.72	0.64- 0.71	0.65- 0.70	0.55 – 0.76
(La/Lu)cn	5.98- 9.86	6.59- 9.50	7.08- 8.11	4.68- 10.49

i.e., <sup>1</sup>Present study, <sup>2</sup>Nagarajan et al. (2017b).

Based on the A-CN-K plot (**Fig 4.32 A**) the provenance of the sediments can be extrapolated; accordingly, the studied samples show the source rocks are granitoids (granodiorite to granitic rocks). Similarly, the trace elements Co/Th ratios vs La/Sc and Sc/Th ratios plot (**Fig 4.38 A and B**) also confirm the contribution from the mixing of felsic igneous rocks, showing all the study samples falling toward felsic volcanic and TTG, which confirms the mixing of felsic source rocks rather than mixing of mafic rocks with the granitic rocks to show an intermediate character. The depletion of Co/Th and shows a vertical declining trend that can be linked to the presence of Th bearing minerals due to recycling.



**Figure 4.38 A- Co/Th vs. La/Sc and B- Co/Th vs. Sc/Th plots show the provenance characters of the Miri Formation studied samples.**

#### 4.8.4 The possible provenance area

Petrographic and geochemical characteristics of the study samples all point to the recycled origin. By integrating both results, the studied samples of the Miri Formation samples indicate a felsic rich source region and recycled from sedimentary to meta-sedimentary region (see **Fig 4.33, Fig 4.37 A and B, Fig 4.38 A and B**). The possible source composition is established based on the results obtained, the relative contribution from the end members of granite, felsic volcanic rocks (FVR) and tonalite- trondhjemite granodiorite (TTG).

Many researchers have considered the mixing calculation as a significant tool for identifying the possible provenance (Hegde and Chavadi, 2009; Madhavaraju, 2015; Armstrong-Altrin et al., 2015; Wani, 2017; Asiedu et al., 2019). The relative source area (end members) contribution to the study area is calculated by solving the equation proposed by Hegde and Chavadi (2009). The end members of granite, FVR, TTG and andesite from Condi, (1993) and Cullers and Podkovyroy, (2002) to solve the equation  $Y_1A+Y_2B+Y_3C+Y_4D=Y$ . The relative contribution of the end members is quantitatively constrained from the concentration of Th, La, Yb and Co (**Table 4.13**). The Miri Formation represents the mixing of granite, FVR and TTG in the ratio of 40:10:50 respectively.

**Table 4.13 Trace element abundances (ppm) of the end members used in mixing calculations.**

Source /Elements	Th	La	Yb	Co	Total
A.Granites <sup>b</sup>	18	40	3.2	3	64.20
B.Felsic volcanic rocks <sup>b</sup>	10.2	28	2.9	6	47.10
C.TTG (granodiorite) <sup>b</sup>	10	25	1.7	14	50.70
D. Sandstone <sup>a</sup>	6.20	16.56	1.47	5.87	30.10
E. Interbedded <sup>a</sup>	9.39	24.71	2.14	10.97	47.22
F. Mudstone <sup>a</sup>	13.25	32.97	2.87	12.80	61.89

a-This study, b-Cullers and Podkovyroy, (2002),

The possible source rocks located near the study area REE patterns are also compared with the Miri Formation REE pattern (**Fig 4.39**). Source rocks considered include the Kelalan Formation (turbidites; an average of sandstone and mudstone; Nagarajan et al., 2021), TTG, FVR, Cratonic sandstone and Granite (Condi, 1993). The mixing of granite, TTG and Kelalan Formation in the ratio of 15:30:55 is the best fit with the Miri Formation REE pattern (**Table 4.14**). Based on the mixing calculation and the REE pattern, the Miri Formation sediments are mainly recycled from the Rajang Group of sedimentary to metasedimentary rocks which is further confirmed by the presence of meta sedimentary lithics in many sandstone samples. The parent source rocks must be derived from felsic rich source rocks in particular granitoids are the main sources.

The previous study by Nagarajan et al. (2017b) reported zircon geochronology data for the Tukai Formation, which is also partly age equivalent (Mid-Miocene to Pliocene). Based on the age of the zircon crystals extracted from the Tukai Formation, three major source areas (2 young

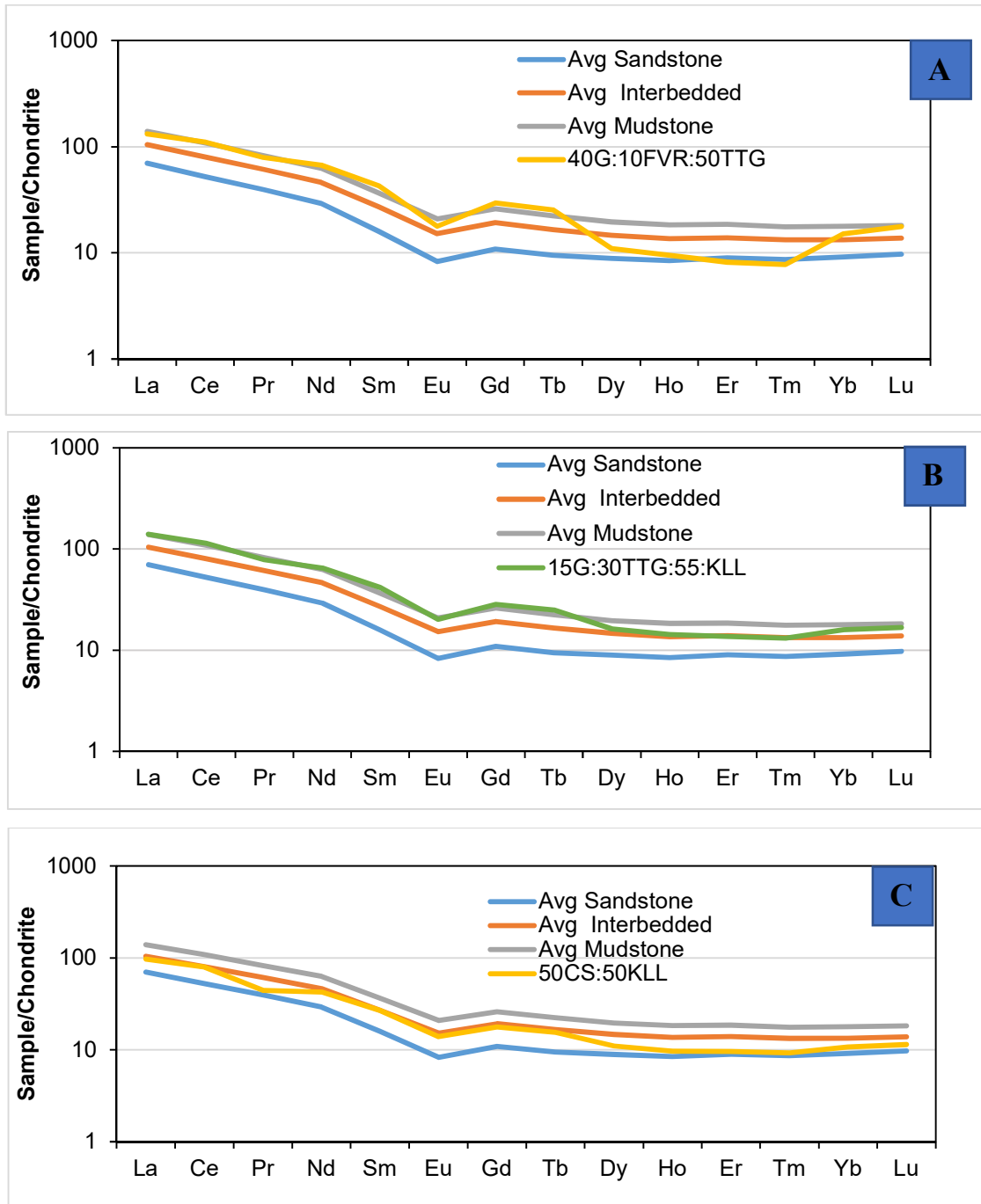


age clusters and one old age cluster) were identified such as the Schwaner Mountains and Tin Belt of the Malaysia Peninsular granitoids were the important sources for the Rajang Group, which have been recycling since Paleogene to present-day (Hutchison, 2005; Kessler and Jong 2015a; Jong et al., 2016; Nagarajan et al., 2014, 2015, 2017; Van Hattum et al., 2003, 2013; Nagarajan et al., 2017b; 2019).

**Table 4.14 Comparison of end members mixing calculation of the Miri Formation with the possible source rocks.**

Elements	Average concentration Miri Formation			Mixing end-member			Mixing result
	Sandstone <sup>a</sup>	Interbedded <sup>a</sup>	Mudstone <sup>a</sup>	Granite <sup>b</sup>	TTG <sup>b</sup>	Kelalan Formation <sup>c</sup>	15:30:55
	ppm	ppm	ppm	ppm	ppm	ppm	ppm
La	16.56	24.71	32.97	40	25	35.74	139.91
Ce	32.07	49.06	66.55	94	47	75.08	113.37
Pr	3.67	5.67	7.64	18.3	-	8.23	78.34
Nd	13.35	21.10	28.68	46	19.5	30.52	64.63
Sm	2.35	3.99	5.40	8.8	4.6	6.32	41.74
Eu	0.47	0.86	1.17	0.9	1.1	1.22	20.20
Gd	2.16	3.83	5.18	7.63	4.67	5.61	28.28
Tb	0.34	0.60	0.80	1.15	0.76	0.91	24.92
Dy	2.19	3.60	4.83	6.75	-	5.43	16.26
Ho	0.46	0.74	1.00	1.29	-	1.06	14.20
Er	1.43	2.22	2.96	3.27	-	3.07	13.63
Tm	0.21	0.33	0.44	0.48	-	0.46	13.10
Yb	1.47	2.14	2.87	3.2	1.7	2.85	15.88
Lu	0.24	0.34	0.45	0.54	0.28	0.45	16.77

a-study area, b- Condie (1993), c- Nagarajan et al. (2021)



**Figure 4.39 A.** Chondrite normalized REE pattern for the siliciclastic rocks of the Miri Formation compared with mixed pattern ratio of 40:10:50 (granite: TTG: Kelalan Formation). **B.** Chondrite normalized REE pattern for the siliciclastic rocks of the Miri Formation compared with mixed pattern ratio of 15:30:55 (granite: TTG: Kelalan Formation). **C.** Chondrite normalized REE pattern for the siliciclastic rocks of the Miri Formation compared with mixed pattern ratio of 50:50 (Cratonic sandstone: Kelalan Formation).

### 4.8.5 Tectonic setting

Petrographically, the tectonic setting of the Miri Formation is determined using the QFL ternary plot (Dickinson and Suczek, 1979). Based on the QFL plot, most of the studied sandstone samples fall in the recycled orogenic field with few samples fall in the craton interior (Fig 4.40). The folding and faulting events of sedimentary or metasedimentary terrains are correlated with sources of recycled orogens, which causes the detritus of rocks to be recycled into related basins (Dickinson and Suczek, 1979; Dickinson et al., 1983; Dickinson, 1985 and 1988). The petrographic composition observed from the studied samples such as monocrystalline and polycrystalline quartz, sedimentary and metasedimentary lithic fragments suggests a collision of orogens (Dickinson and Suczek, 1979).

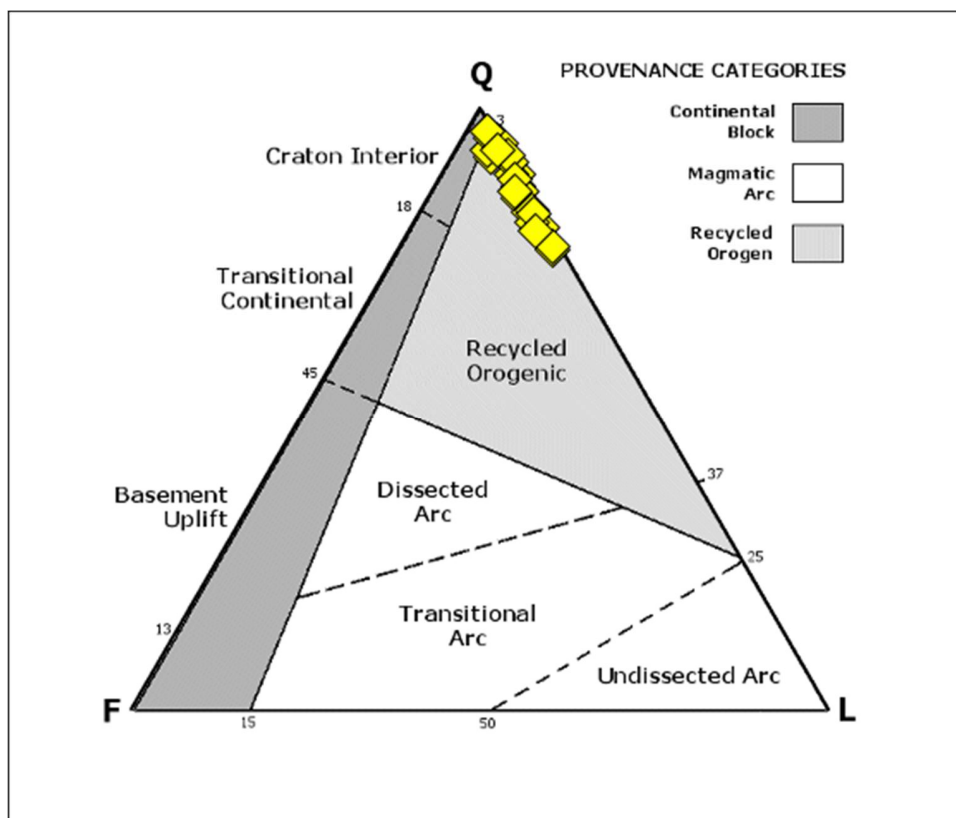
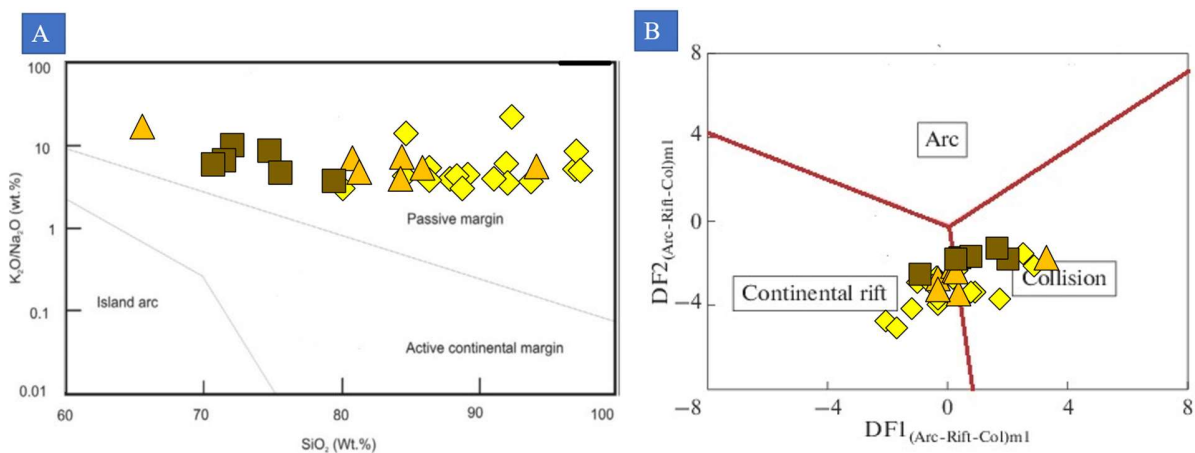


Figure 4.40. QFL Diagram (after Dickinson, 1970) for determination of tectonic settings. Showing the majority of the sandstone samples falling in the recycled orogenic and two samples falling on the craton interior.

Tectonic settings can also be deduced based on the sediment composition, major, trace and rare earth element geochemistry. This has been proposed by many researchers (Bailey, 1981; Bhatia, 1983; Bhatia and Crook, 1986; Roser and Korsch, 1986; Girty et al., 1993; McLennan et al. 1993; Verma and Armstrong-Altrin, 2013, 2016). As mentioned in the literature review, caution is taken when using major oxides for inferring tectonic settings due to the effects of syn and post-depositional processes (e.g. Nagarajan et al., 2021).

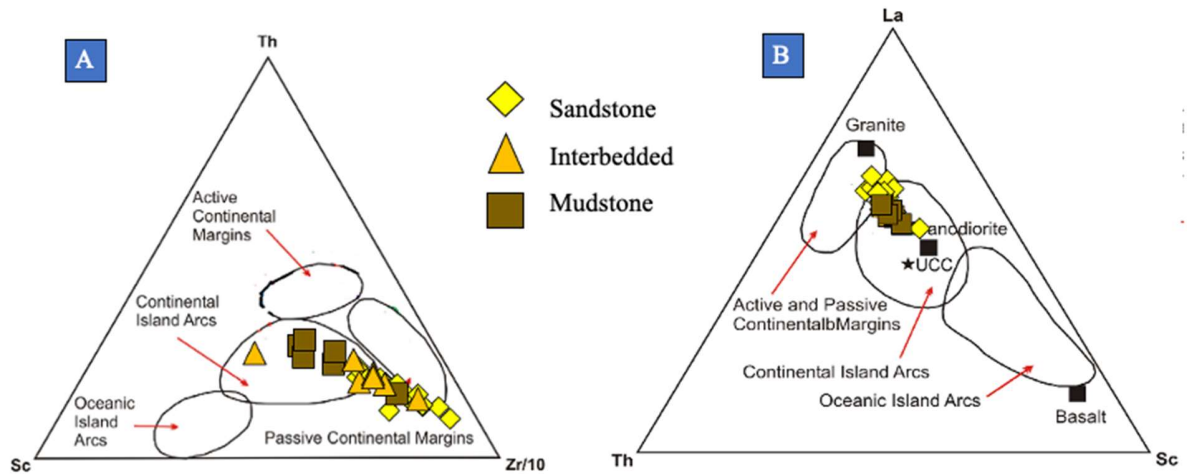
Based on the  $K_2O/Na_2O$ - $SiO_2$  discrimination diagram of Roser and Korsch, (1986), all the Miri Formation samples are plotted in the passive margin field (Fig. 4.41 A), which shows consistency with the provenance of the Miri Formation sediments being dominated by recycled sedimentary to the metasedimentary source region. Similarly, based on the discriminant-function multi-dimensional diagram of Verma and Armstrong-Altrin, (2013), the Miri Formation samples plot in both the collisional field and rift field (Fig. 4.41 B) belonging to the passive margin, which coincides with the regional tectonic setting of NW Borneo during the deposition of the Miri Formation sediments.



**Figure 4.41 A- $K_2O/Na_2O$  vs.  $SiO_2$  tectonic discrimination diagram for Siliciclastic rocks of the Miri Formation (Roser and Korsch 1986). B-Discriminant-function multi-dimensional diagram (Verma and Armstrong-Altrin, 2013) showing the tectonic setting for the Miri Formation.**

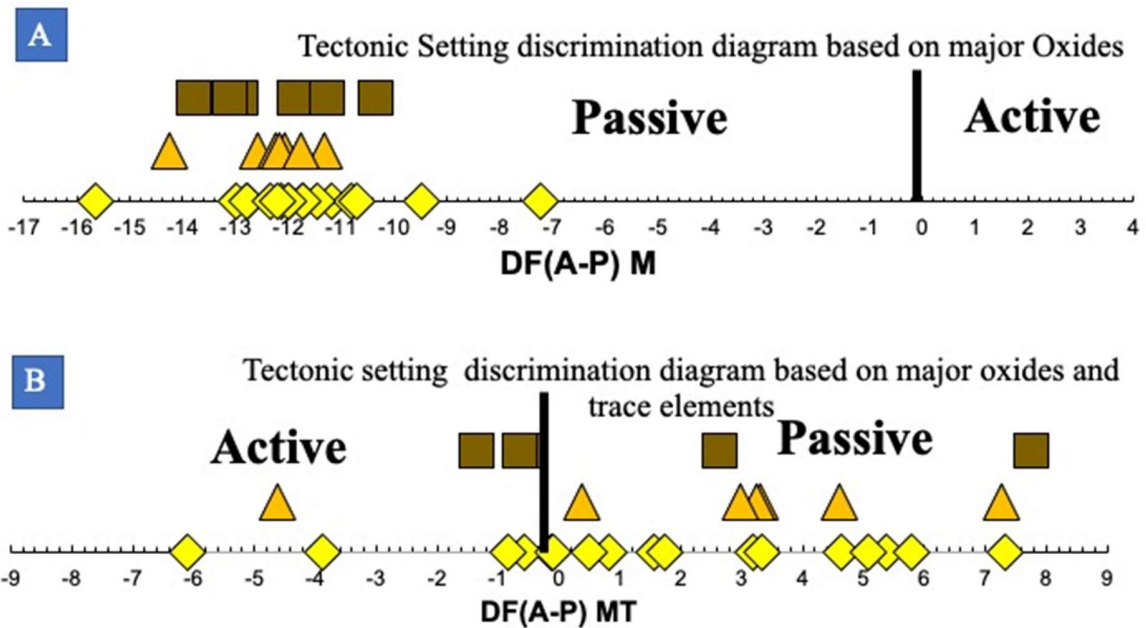
Also based on the trace elements discriminant diagrams; Th-Sc-Zr/10 and La-Th-Sc ternary diagram (Fig. 4.42 A and B) the tectonic setting is inferred. On the Th-Sc-Zr/10 ternary plot, the studied samples of the Miri Formation indicate a continental island arc and also passive continental margins while on the La-Th-Sc ternary diagram the studied samples also suggest a continental

island arc with few samples falling in the active and passive continental margins and also showing a possible source from granitoid rocks (granite-granodiorite).



**Figure 4.42. A-Th-Sc-Zr/10 ternary plot shows the major tectonic fields for the siliciclastic rocks of the Miri Formation. B-La-Th-Sc ternary plot showing the major tectonic area of the sediments with the possible source rocks**

The new discriminant diagrams proposed by Verma and Armstrong-Altrin (2016) are also taken into account to further discriminate the tectonic setting for the Miri Formation. Based on the major oxides discriminant diagrams, all the samples fall in the passive margin setting (**Fig. 4.43 A**) while based on the major – trace element based discriminant plot, the majority of the samples fall in the passive margin setting and few fall in the active tectonic boundary (**Fig. 4.43 B**).



**Figure 4.43** Tectonic setting discrimination diagram based on major oxides and major oxides and trace elements. (A) Oxides  $DF(A-P) M = (3.0005 \times ilr1TiM) + (-2.8243 \times ilr2AIM) + (-1.0596 \times ilr3FeM) + (-0.7056 \times ilr4MnM) + (-0.3044 \times ilr5MgM) + (-0.6277 \times ilr6CaM) + (-1.1838 \times ilr7NaM) + (1.5915 \times ilr8KM) + (0.1526 \times ilr9PM) - 5.9948$ , and (B) based on trace element  $DF(A-P)MT = (3.2683 \times ilr1TiMT) + (5.3873 \times ilr2AIMT) + (1.5546 \times ilr3FeMT) + (3.2166 \times ilr4MnMT) + (4.7542 \times ilr5MgMT) + (2.0390 \times ilr6CaMT) + (4.0490 \times ilr7NaMT) + (3.1505 \times ilr8KMT) + (2.3688 \times ilr9PMT) + (2.8354 \times ilr10CrMT) + (0.9011 \times ilr11NbMT) + (1.9128 \times ilr12NiMT) + (2.9094 \times ilr13VMT) + (4.1507 \times ilr14YMT) + (3.4871 \times ilr15ZrMT) - 3.2088$  for the Miri Formation (after Verma and Armstrong-Altrin, 2016).

To better understand the tectonic setting derived from the geochemical data based on the discrimination diagrams, the result from the studied Miri Formation samples mostly falls in the passive margin with slight involvement of active margin, similar tectonic setting reported for nearby formations in the region (e.g., Nagarajan et al., 2017 a,b). Therefore, the regional geology of the NW Boneo is compared with results obtained from the studied samples. The Sarawak orogeny plays a vital role in sediment supply during the Late Eocene (Hutchison, 2007). This sediment supply caused a transition from flysch to molasses in the NW Borneo due to the folding, trusting and uplift of the Rajang Group turbidites flysch located at the eastern part of the Miri zone (Kessler and Jong, 2015; Jong et al., 2016; Kessler et al., 2020).

Early Miocene, the rifting and potential subduction of the proto-South China sea occurred with the continuous sediment supply from the Rajang Group until Middle Miocene. By that time, the tectonic event slowed, resulting due to the uplift of the Boneo landmass. According to Kessler

and Jong (2015), the transitional changes that occurred from muddy Middle Miocene shelf (Setep shale and Sibuti Formation) to a more sand prone Middle Miocene to late Miocene formations (Lambir, Belait, Miri, Tukai and Seria Formation) can be attributed to regional tectonism, which cause the rise of the Boneo landmass. This event in addition to the climate condition enhanced the erosion of Rajang/Crocker Formations and deposited sand-rich sedimentary rocks during the Neogene in the northern part of Borneo.

Based on the regional tectonism, the tectonic setting of the studied area reported based on petrography and geochemistry can be attributed to the possibility of the northern part of Borneo having a collisional tectonic setting at the time and the passive rifts might have developed along faulted margins in the zones of continental collision (e.g., Ingersoll, 1988). Rifts are common along the collisional boundaries due to irregularities of continental margins and by normal faulting due to non-perpendicular collision (e.g., Condie, 2011). The result of the study area is affirmed by comparing the regional results and result from older formations as mentioned earlier.

#### **4.8.6 Influential parameter on the Miri Formation reservoir properties.**

Influential parameters affecting the reservoir quality of the Miri Formation reservoir rocks include the depositional environment, grain characteristics (grain size, grain shape and sorting) and diagenesis. The depositional environment (lithofacies) of the Miri Formation has already been discussed by Siddique et al. (2017). This study focuses on the textural and diagenetic influences on reservoir quality.

##### **4.8.6.1 Textural influence on the reservoir properties.**

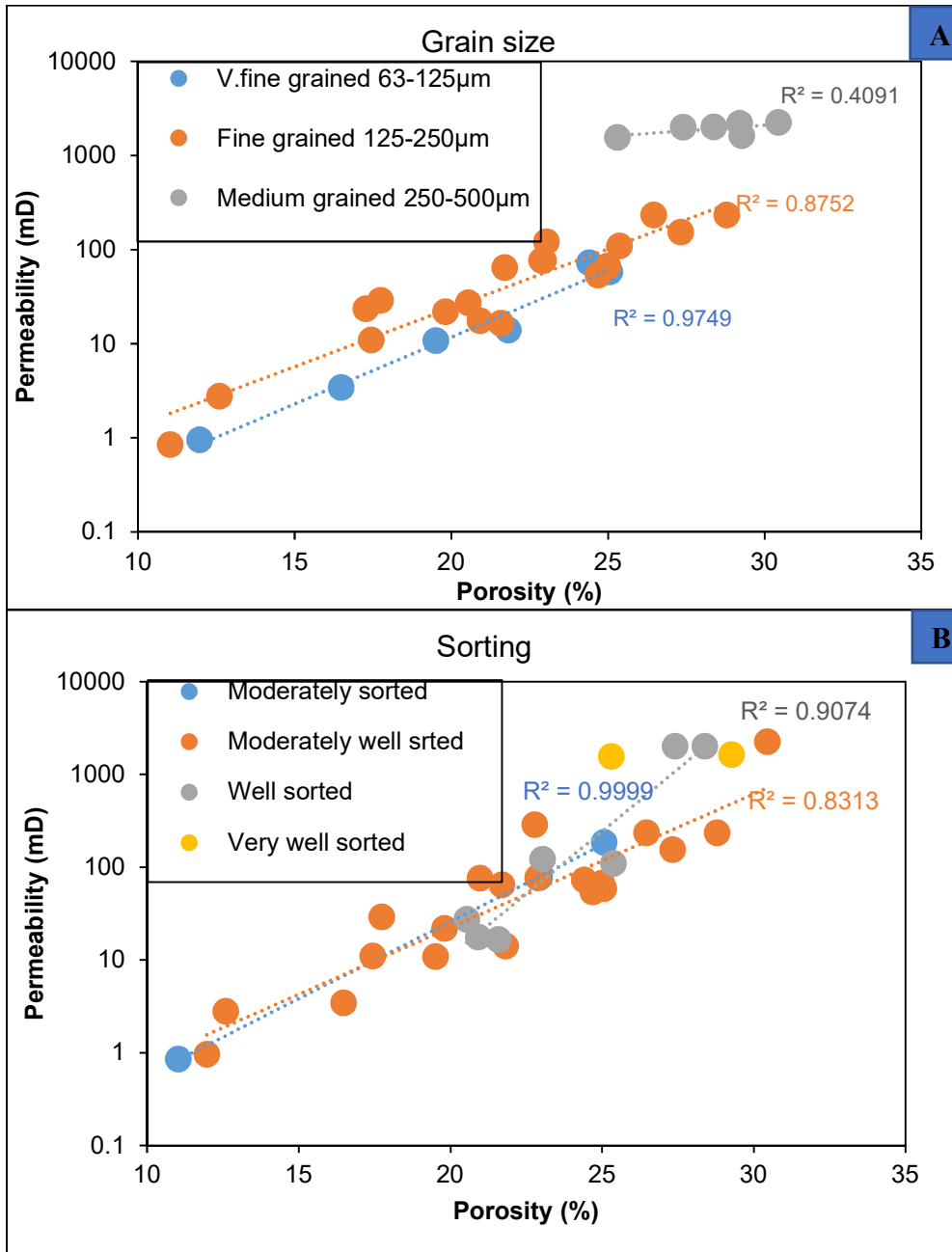
Grain size, grain shape and sorting are some of the factors influencing the reservoir properties. Grain size in reservoir rocks can have a significant effect on permeability due to the smaller grains having a narrower pore throat (Yu et al., 2018; Bukar et al., 2020; Baiyegunhi et al., 2020; Makeen et al., 2021).

Based on the grain size analysis, the studied core samples are subdivided into three-grain size classes of very fine-grained (63- 125  $\mu\text{m}$ ), fine-grained (125-250  $\mu\text{m}$ ) and medium-grained

(250-500  $\mu\text{m}$ ) to have a better understanding on the influence of grain size on the reservoir quality of the Miri Formation (**Fig 4.44 A**). The medium-grained sandstones are clustered above 25% porosity and  $>1000\text{mD}$  permeability (**Fig 4.44 A**), which suggest that the medium-grained sandstones have excellent reservoir quality among the sandstone type based on the grain size. While the fine and very fine-grained sandstone samples are having a very good reservoir quality with porosity and permeability ranging 15-30% and 10-100 mD. As observed in the studied samples, porosity is dependent on the grain size and permeability reduces as grain size decreases (Makeen et al., 2016; Chen et al., 2019; Makeen et al., 2021).

The sorting of the studied samples varies between moderately sorted and very well sorted (**Table 4.6**). Based on the porosity and permeability cross plot (**Fig 4.44 B**), the sorting of studied samples shows an increase in both porosity and permeability as sorting increases. Thus, based on the absence of significant differences observed in the sorting indices of the studied sandstones, the sorting of the studied samples is therefore considered either subordinate or not relevant given that diagenetic overprint has greater control in defining the reservoir quality of the Miri Formation.





**Figure 4.44. A. Porosity and permeability cross plot of the Miri Formation based on grain size, B. Porosity and permeability cross plot of the Miri Formation based on sorting.**

#### 4.8.6.2 Diagenetic influences on reservoir quality.

The reservoir quality of the Miri Formation is controlled by diagenetic processes that either increase or reduce the porosity and permeability of the studied samples. The main diagenetic processes observed in the study area include compaction, bioturbation, cementation, clay minerals and dissolution.

Compaction is one of the diagenetic processes observed in the studied samples, which affects both porosity and permeability. Many researchers have made use of the burial depth using well data to compare the effects caused due to increasing depth of burial (Rahman et al., 2016; Liu et al., 2020; Li et al., 2021). The porosity and permeability data obtained from the study area is compared with the grain contacts observed in all the studied samples to evaluate the effect of overburden load or younger sediments during burial (**Fig 4.9 A-F, Fig 4.10 G-L, Fig 4.23 A, B, C and D**). Generally, sutured and line contacts with the formation of pseudomatrix are observed in the older studied samples belonging to the hospital outcrop. The occurrence of sutured, line contact and pseudomatrix has a significant effect on the reservoir properties of the studied samples while point contacts are generally observed across all studied samples. This shows that compaction has a significant influence on the reservoir quality of the older sediments of the Miri Formation.

The influences of authigenic clay minerals on the reservoir quality of the Miri Formation are also observed. The common clay minerals observed based on SEM analysis are illite, illite/smectite, chlorite and kaolinite. Illite is the most dominant clay mineral observed in the studied samples, the morphology of illite observed on the SEM analysis resembles the morphology of kaolinite, which occurs as pore bridging and pore-filling showing both booklets and vermicular stacked plates. Illite is formed from the illitization of kaolinite and alteration of feldspar and muscovite (Bjørlykke and Jahren, 2012; Rahman and Worden, 2016; Yuan et al., 2019). The morphological nature of the observed illite in the studied samples has a negative impact on the reservoir permeability by blocking the intergranular pores (**Fig 4.24 C & D**). The pore bridging illite reduces the air permeability of the studied samples due to the change in the intergranular pore

network from macropores to micropores. The illite percentage is driven based on the WIS diagenetic illite (**Table 4.9**), using the illite % is given by  $\Delta K_2O \times 100/9.9$ .

Based on the cross plot of porosity and permeability versus illite percentage, a significant reduction of permeability is observed as illite percentage increase (**Fig 4.45 B**) but no influence on the porosity (**Fig 4.45 A**).

Grain coating chlorite (**Fig 4.24 E**) in the studied samples is mostly observed in the medium-grained sandstones, while pore filling chlorites are generally observed in most of the studied samples. Grain coating chlorite observed in the studied samples tends to preserve the intergranular porosity. Two factors can be considered; (i) chlorite lined pore throats exhibit the highest effective radii and therefore similarly high values of permeability are expected and (ii) these chlorite “rims” inhibit the growth of quartz cement that would otherwise fill up the pore spaces (**Fig 4.27 Class I**). The coating chlorite forms around the detrital grains as rims observed in the SEM analysis (**Appendix 3.0 Fig 6.6, 6.7, 6.8**). The pore-filling chlorites are mostly observed with either pyrite or illite. The occurrence of chlorite as a pore filling mineral tends to have a negative effect on the studied samples by reducing the pore throat thus affecting the reservoir quality. The source of chlorite is not certain, but it has been reported by many researchers to be generated by the alteration of pre-existing Fe rich minerals such as pyrite and glauconite, metasedimentary lithic fragments and Fe-Mg- rich lithic fragments (Gould et al., 2010; Worden et al., 2020; Bukar et al., 2021).

Calcite cement type is observed in a few of the studied samples (**Fig 4.17 D and Fig 4.24 H, I**), which are observed as crystalline poikilotopic calcites that are considered to be precipitated from alkaline water during eodiagenesis (Liu et al., 2014; Lai et al., 2015). The calcite cement observed in the studied sample tend to block the pore throat which reduces the porosity and permeability to very low values (**Fig 4.27 class IV**).

Bioturbation is observed in the studied samples due to the action of organisms associated with trace fossils such as *Ophiomorpha*. The burrowing action of these organisms in the study area reworked sedimentary clay and silt grade materials from overlying beds into underlying and previously clean sand graded beds. This process of “injection” of clay or silt into the sand can

lead to the growth of Fe- clays during diagenesis (Worden et al., 2020). Pyrite and chlorite are observed as pore blocking clay minerals in most of the bioturbated sandstones (**Fig 4.25 J**). As mentioned previously, reducing the pore throat radii has a negative effect on the porosity and permeability.

The reservoir quality of the Miri Formation is either positively or negatively affected by different diagenetic events. Compaction, bioturbation, authigenic and detrital clay minerals (illite, illite/smectite and illite/chlorite) and calcite cement show a negative influence on the quality of the reservoir of the Miri Formation, while grain coating chlorite shows a positive influence on the reservoir quality by preserving the pore throat from blocking by silica cement.

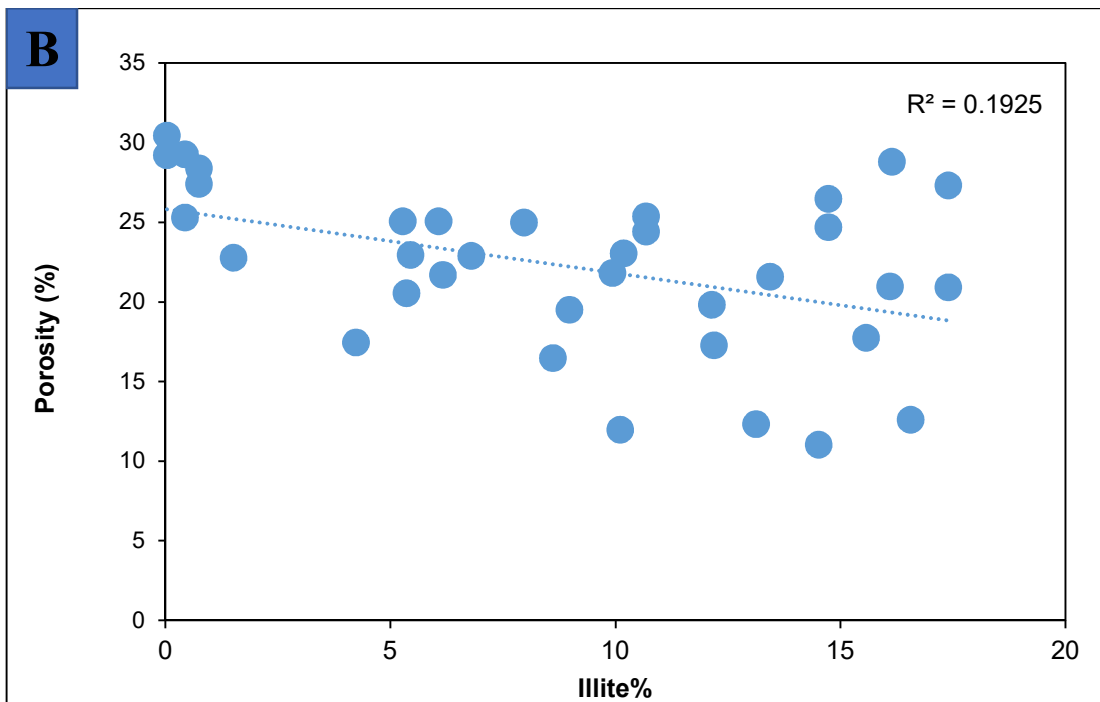
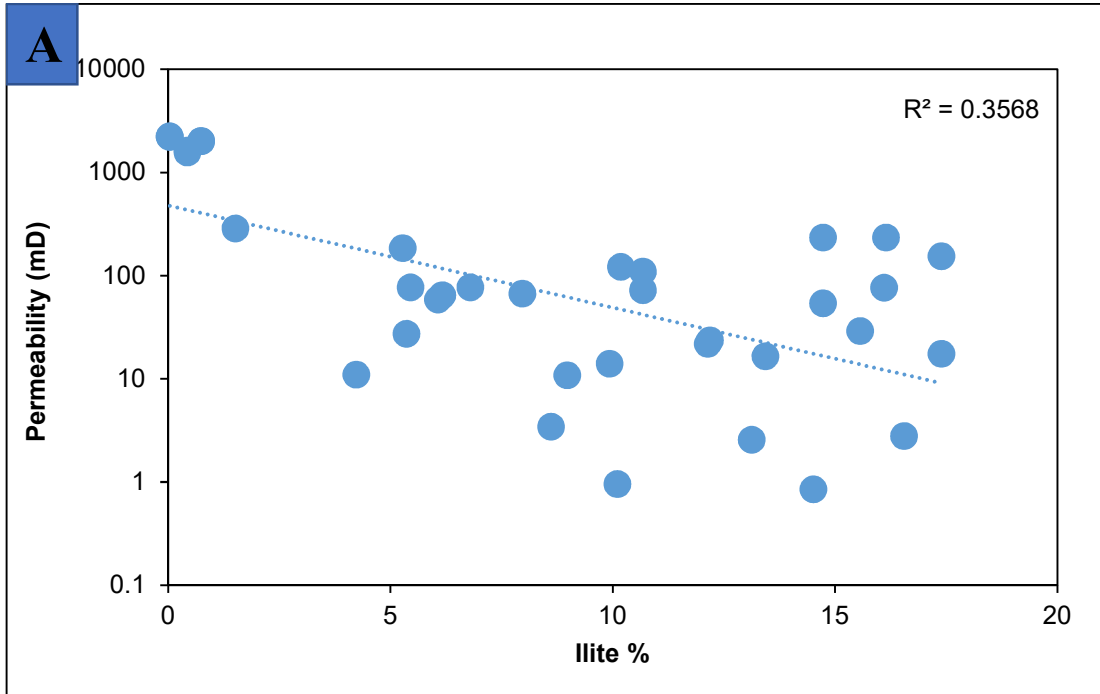


Figure 4.45 A- Cross plot shows the studied sandstones relationship of porosity Vs illite %, B- Cross plot shows the relationship of permeability Vs illite %.

# CHAPTER 5

## CONCLUSION AND FUTURE RECOMMENDATIONS

### 5.1 Introduction

As mentioned earlier, the main objectives of this study are (i) to identify the mineralogical composition of the rocks in the Miri Formation and their implications for diagenesis, (ii) to study the geochemical composition of the rocks in the Miri Formation and (iii) determine their implication on paleo weathering, sediment provenance and possible tectonic setting and (iv) to assess the petrophysical characteristics of the rocks in the Miri Formation and determine their possible control on reservoir quality. Based on the proposed integrated approach, the major outcomes and future recommendations are discussed in this chapter.

### 5.2 Conclusion

An integrated approach based on petrography and geochemistry is used to classify the Miri Formation studied samples. The studied samples are geochemically composed of quartz arenite, sublitharenite, litharenite, wacke and Fe-sandstone. This result matches the petrographic classification of the sandstones using the QFL diagram. The studied samples of the Miri Formation are further petrographically characterized based on their textural features. The studied sandstone samples are texturally mature with grain size ranging from very fine to medium-grained, moderately well sorted to very well sorted and sub-angular to sub-rounded grains.

Based on geochemistry, the weathering intensity of the studied samples of the Miri Formation was deduced based on CIA, PIA, A-CN-K, A-CNK-FM, WIS, and CIA versus ICV plot reveal that the studied samples underwent moderate to intensive chemical weathering and are chemically mature. WIS further confirms the intensity of the weathering and also the diagenetic trend of the studied samples.

The provenance of the Miri Formation is deduced based on an integrated approach of petrography, mineralogy, geochemistry and quartz microtextures. Based on the petrography and quartz microtextural analysis of the Miri Formation, the textural features indicate a moderate transportation distance with an extensive reworking. The provenance discriminant diagram (QFL) reveals the recycled nature of the studied samples. Based on the quartz grains crystallinity and extinction, the studied samples revealed a plutonic igneous rock source with recycled metasedimentary rocks. Quartz microtextures also reveal a crystalline source rock. The provenance based on multiple geochemical discriminant diagrams also reveals that the Miri Formation studied samples source as felsic to intermediate characteristics and derived from a sedimentary to metasedimentary rocks dominated source region (Rajang Group). The mixing model based on selected trace elements endmembers revealed the source rock character of granite, FVR and TTG, in the ratio of 40:10:50. Similarly, the REE pattern of siliciclastic rocks of the Miri Formation is comparable to source rock Kelalan Formation (turbidites) of Rajang Group and cratonic sandstone, which further confirms the recycling of sediments. The sediments of the Miri Formation are derived from recycled sedimentary/metasedimentary rocks of older nearby formations of the Rajang Group as the major source and minor contribution from granitoids (recycled fresh lithics from the source region), which are deposited in an evolving passive continental margin setting.

The reservoir properties and diagenetic influences of the Miri Formation were studied through integrated methods of petrophysical analysis, petrography, SEM, XRD and geochemistry. The reservoir quality shows four classes of reservoir rocks in the Miri Formation. Class I: the high quality with average porosity and permeability of 28.33 % and 1937.74 mD respectively, Class II: moderate quality with an average porosity and permeability of 24.29 % and 116.57 mD respectively, Class III: low quality with an average porosity and permeability of 19.31 % and 17.46 mD respectively and Class IV: very low quality with an average porosity and permeability of 11.98 % and 1.78 mD respectively. The reservoir quality has been positively and negatively influenced by different diagenetic events. Grain coating chlorites preserve the sandstone pore throats yielding a high reservoir quality rock, while the reservoir quality is negatively influenced by diagenetic events such as compaction, pore-blocking diagenetic minerals, calcite cement, iron oxide cement and bioturbation.

### **5.3 Future Recommendations**

The Provenance characters of the Miocene sediments can be further investigated through heavy mineral analysis, heavy mineral chemistry and zircon geochronology. also, the exposures of the Miri Formation in and around Miri City are limited. If any oil company, if they share the core data, which will be useful to investigate the complete picture of the Miri Formation. In addition, the clay seamer morphology and their chemistry can be further explored.



# References

- Abdullah, F., Shaaban, F., Khalaf, F., Bahaman, F., Akbar, B., & Al-Khamiss, A. (2017).** Petrophysics and hydrocarbon potential of Paleozoic rocks in Kuwait. *Journal of Asian Earth Sciences*, 148, 105-120.
- Abieda, H. S., Harith, Z. Z. T., & Rahman, A. H. A. (2005).** Depositional controls on petrophysical properties and reservoir characteristics of Middle Miocene Miri Formation sandstones, Sarawak. *Geol. Soc. Malaysia, Bulletin* 51, 63 -75.
- Abu-Zeid, M. M., Baghdady, A. R., & El-Etr, H. A. (2001).** Textural attributes, mineralogy and provenance of sand dune fields in the greater Al Ain area, United Arab Emirates. *Journal of Arid Environments*, 48(4), 475-499.
- Adepehin, E. J., Ali, C. A., Zakaria, A. A., & Sali, M. S. (2019).** An overview of 20 years' hydrocarbon exploration studies and findings in the Late Cretaceous-to-Tertiary onshore Central Sarawak, NW Borneo: 1997–2017 in retrospect. *Journal of Petroleum Exploration and Production Technology*, 9(3), 1593-1614.
- Akinlua, A., Ngola, A., Fadipe, O., & Adekola, S. (2016).** Petrography and geochemistry of sandstone samples of Vischkuil formation, Karoo Supergroup, South Africa. *Journal of Petroleum Exploration and Production Technology*, 6(2), 159-167.
- Al-Hurban, A., & Gharib, I. (2004).** Geomorphological and sedimentological characteristics of coastal and inland sabkhas, Southern Kuwait. *Journal of arid environments*, 58(1), 59-85.
- Al-Laboun, A., AL-QURAISHI, A. B. D. U. R. R. A. H. M. A. N., Zaman, H., & Benaafi, M. (2014).** Reservoir characterization of the Burqan Formation sandstone from Midyan Basin, northwestern Saudi Arabia. *Turkish Journal of Earth Sciences*, 23(2), 204-214.
- Al-Saleh, S., & Khalaf, F. I. (1982).** Surface textures of quartz grains from various recent sedimentary environments in Kuwait. *Journal of Sedimentary Research*, 52(1), 215-225.
- Ali, S. A., Clark, W. J., Moore, W. R., & Dribus, J. R. (2010).** Diagenesis and reservoir quality. *Oilfield Review*, 22(2), 14-27.
- Ali, S., Stattegger, K., Garbe-Schönberg, D., Kuhnt, W., Kluth, O., & Jabour, H. (2014).** Petrography and geochemistry of Cretaceous to quaternary siliciclastic rocks in the Tarfaya basin, SW Morocco: implications for tectonic setting, weathering, and provenance. *International Journal of Earth Sciences*, 103(1), 265-280.
- Anani, C. Y., Kwayisi, D., Agra, N. A., & Asiedu, D. K. (2018).** Provenance of shales and sandstones from the Devonian Accraian Group, southern Ghana. *Geosciences Journal*, 22(3).
- Armstrong-Altrin, J. S., & Natalhy-Pineda, O. (2014).** Microtextures of detrital sand grains from the Tecolutla, Nautla, and Veracruz beaches, western Gulf of Mexico, Mexico: implications for depositional environment and paleoclimate. *Arabian Journal of Geosciences*, 7(10), 4321-4333.
- Armstrong-Altrin, J. S., & Verma, S. P. (2005).** Critical evaluation of six tectonic setting discrimination diagrams using geochemical data of Neogene sediments from known tectonic settings. *Sedimentary Geology*, 177(1-2), 115-129.
- Armstrong-Altrin, J. S., Lee, Y. I., Verma, S. P., & Ramasamy, S. (2004).** Geochemistry of sandstones from the Upper Miocene Kudankulam Formation, southern India:

implications for provenance, weathering, and tectonic setting. *Journal of Sedimentary Research*, 74(2), 285-297.

- Armstrong-Altrin, J. S., Nagarajan, R., Balaram, V., & Natalhy-Pineda, O. (2015).** Petrography and geochemistry of sands from the Chachalacas and Veracruz beach areas, western Gulf of Mexico, Mexico: constraints on provenance and tectonic setting. *Journal of South American Earth Sciences*, 64, 199-216.
- Armstrong-Altrin, J. S., Nagarajan, R., Lee, Y. I., Zubillaga, J. J. K., & Saldaña, L. P. C. (2014).** Geochemistry of sands along the San Nicolás and San Carlos beaches, Gulf of California, Mexico: implications for provenance and tectonic setting. *Turkish Journal of Earth Sciences*, 23(5), 533-558.
- Armstrong-Altrin, J. S., Nagarajan, R., Madhavaraju, J., Rosalez-Hoz, L., Lee, Y. I., Balaram, V., and Avila-Ramírez, G. (2013).** Geochemistry of the Jurassic and Upper Cretaceous shales from the Molango Region, Hidalgo, eastern Mexico: Implications for source-area weathering, provenance, and tectonic setting. *Comptes Rendus Geoscience*, 345(4), 185-202.
- Asiedu, D. K., Suzuki, S., & Shibata, T. (2000).** Provenance of sandstones from the Wakino Subgroup of the Lower Cretaceous Kanmon Group, northern Kyushu, Japan. *Island Arc*, 9(1), 128-144.
- Augustsson, C. (2021).** Influencing Factors on Petrography Interpretations in Provenance Research—A Case-Study Review. *Geosciences*, 11(5), 205.
- Baig, M. O., Harris, N. B., Ahmed, H., & Baig, M. O. A. (2016).** Controls on reservoir diagenesis in the Lower Goru sandstone formation, Lower Indus Basin, Pakistan. *Journal of Petroleum Geology*, 39(1), 29-47.
- Baiyegunhi, C., Liu, K., & Gwavava, O. (2017).** Diagenesis and reservoir properties of the Permian Ecca Group sandstones and mudrocks in the Eastern Cape Province, South Africa. *Minerals*, 7(6), 88.
- Baiyegunhi, T. L., Liu, K., Gwavava, O., & Baiyegunhi, C. (2020).** Petrography and Tectonic Provenance of the Cretaceous Sandstones of the Bredasdorp Basin, off the South Coast of South Africa: Evidence from Framework Grain Modes. *Geosciences*, 10(9), 340.
- Bakkiaraj, D., Nagendra, R., Nagarajan, R., & Armstrong-Altrin, J. S. (2010).** Geochemistry of sandstones from the Upper Cretaceous Sillakkudi Formation, Cauvery Basin, southern India: implication for provenance. *Journal of the Geological Society of India*, 76(5), 453.
- Baldermann, A., Abdullayev, E., Taghiyeva, Y., Alasgarov, A., & Javad-Zada, Z. (2020).** Sediment petrography, mineralogy and geochemistry of the Miocene Islam Dağ Section (Eastern Azerbaijan): Implications for the evolution of sediment provenance, palaeo-environment and (post-) depositional alteration patterns. *Sedimentology*, 67(1), 152-172.
- Bassis, A., Hinderer, M., & Meinhold, G. (2016).** Petrography and geochemistry of Palaeozoic quartz-rich sandstones from Saudi Arabia: implications for provenance and chemostratigraphy. *Arabian Journal of Geosciences*, 9(5), 400.
- Bell, R., & Jessop, R. (1974).** Exploration and geology of the west Sulu Basin, Philippines. *The APPEA Journal*, 14(1), 21-28.
- Basu, A. (2017).** Chapter 2 - Evolution of Siliciclastic Provenance Inquiries: A Critical Appraisal. In Mazumder, R (Eds), *Sediment Provenance: Influences on Compositional Change from Source to Sink* pp. 5-23.

- Beitler, B., Parry, W. T., & Chan, M. A. (2005).** Fingerprints of fluid flow: Chemical diagenetic history of the Jurassic Navajo Sandstone, southern Utah, USA. *Journal of Sedimentary Research*, 75(4), 547-561.
- Ben-Awuah, J., & Eswaran, P. (2015).** Effect of bioturbation on reservoir rock quality of sandstones: a case from the Baram Delta, offshore Sarawak, Malaysia. *Pet Explor Dev* 4 (2): 223–231.
- Ben-Awuah, J., Padmanabhan, E., & Sokkalingam, R. (2017).** Geochemistry of Miocene sedimentary rocks from offshore West Baram Delta, Sarawak Basin, Malaysia, South China Sea: implications for weathering, provenance, tectonic setting, paleoclimate and paleoenvironment of deposition. *Geosciences Journal*, 21(2), 167-185.
- Berrezueta, E., Cuervas-Mons, J., Rodríguez-Rey, Á., & Ordóñez-Casado, B. (2019).** Representativity of 2D Shape Parameters for Mineral Particles in Quantitative Petrography. *Minerals*, 9(12), 768.
- Bessa, A. E., Ngueutchoua, G., & Ndjigui, P. D. (2018).** Mineralogy and geochemistry of sediments from Simbock Lake, Yaoundé area (southern Cameroon): provenance and environmental implications. *Arabian journal of geosciences*, 11(22), 1-18.
- Bhatia, M. R., & Crook, K. A. (1986).** Trace element characteristics of graywackes and tectonic setting discrimination of sedimentary basins. *Contributions to mineralogy and petrology*, 92(2), 181-193.
- Bhattacharya, J. P., Copeland, P., Lawton, T. F., & Holbrook, J. (2016).** Estimation of source area, river paleo-discharge, paleoslope, and sediment budgets of linked deep-time depositional systems and implications for hydrocarbon potential. *Earth-Science Reviews*, 153, 77-110.
- Bhattacharyya, K., & Das, S. (2015).** Sandstone petrology and geochemistry of the Kolhan Basin, Eastern India: implications for basin tectonics. *J Geol Geosci*, 4(2), 6.
- Bjørlykke, K. (1998).** Clay mineral diagenesis in sedimentary basins—a key to the prediction of rock properties. Examples from the North Sea Basin. *Clay minerals*, 33(1), 15-34.
- Bjørlykke, K. (2014).** Relationships between depositional environments, burial history and rock properties. Some principal aspects of diagenetic process in sedimentary basins. *Sedimentary Geology*, 301, 1-14.
- Bjørlykke, K., & Jahren, J. (2012).** Open or closed geochemical systems during diagenesis in sedimentary basins: Constraints on mass transfer during diagenesis and the prediction of porosity in sandstone and carbonate reservoirs *Geohorizon. AAPG bulletin*, 96(12), 2193-2214.
- Boggs, S. (1968).** Experimental study of rock fragments. *Journal of Sedimentary Research*, 38(4), 1326-1339.
- Bracciali, L., Marroni, M., Pandolfi, L., Rocchi, S., Arribas, J., Critelli, S., & Johnsson, M. J. (2007).** Geochemistry and petrography of Western Tethys Cretaceous sedimentary covers (Corsica and Northern Apennines): from source areas to configuration of margins. *Special papers-geological society of america*, 420, 73.
- Bukar, M., Worden, R. H., Bukar, S., & Shell, P. (2021).** Diagenesis and its controls on reservoir quality of the Tambar oil field, Norwegian North Sea. *Energy Geoscience*, 2(1), 10-31.
- Caja, M. A., Marfil, R., Lago, M., Salas, R., & Ramseyer, K. (2007).** Provenance discrimination of Lower Cretaceous synrift sandstones (eastern Iberian Chain, Spain): Constraints from detrital modes, heavy minerals, and geochemistry. *SPECIAL PAPERS-GEOLOGICAL SOCIETY OF AMERICA*, 420, 181.

- Caracciolo, L. (2020).** Sediment generation and sediment routing systems from a quantitative provenance analysis perspective: Review, application and future development. *Earth-Science Reviews*, 209, 103226.
- Casas-Peña, J. M., Ramírez-Fernández, J. A., Velasco-Tapia, F., Alemán-Gallardo, E. A., Augustsson, C., Weber, B., Frei, D., & Jenchen, U. (2021).** Provenance and tectonic setting of the Paleozoic Tamatán Group, NE Mexico: Implications for the closure of the Rheic Ocean. *Gondwana Research*, 91, 205-230.
- Cassel, M., Piégay, H., Lavé, J., Vaudor, L., Sri, D. H., Budi, S. W., & Lavigne, F. (2018).** Evaluating a 2D image-based computerized approach for measuring riverine pebble roundness. *Geomorphology*, 311, 143-157.
- Cawood, P. A. (1983).** Modal composition and detrital clinopyroxene geochemistry of lithic sandstones from the New England Fold Belt (east Australia): A Paleozoic forearc terrane. *Geological Society of America Bulletin*, 94(10), 1199-1214.
- Chaudhuri, A., Chatterjee, A., Banerjee, S., & Ray, J. S. (2021).** Tracing multiple sources of sediments using trace element and Nd isotope geochemistry: provenance of the Mesozoic succession in the Kutch Basin, western India. *Geological Magazine*, 158(2), 359-374.
- Chayes, F. (1949).** A simple point counter for thin-section analysis. *American Mineralogist: Journal of Earth and Planetary Materials*, 34(1-2), 1-11.
- Chen, J., Yao, J., Mao, Z., Li, Q., Luo, A., Deng, X., & Shao, X. (2019).** Sedimentary and diagenetic controls on reservoir quality of low-porosity and low-permeability sandstone reservoirs in Chang101, upper Triassic Yanchang Formation in the Shanbei area, Ordos Basin, China. *Marine and Petroleum Geology*, 105, 204-221.
- Cheng, J.E. (2019).** Implication of reservoir characteristics based on overview of structure and sedimentology of outcrops along Bintulu-Niah-Miri areas. *Malaysian Journal of Geosciences (MJG)* 3(2), 12-22.
- Chima, P., Baiyegunhi, C., Liu, K., & Gwavava, O. (2018).** Diagenesis and rock properties of sandstones from the Stormberg Group, Karoo Supergroup in the Eastern Cape Province of South Africa. *Open Geosciences*, 10(1), 740-771.
- Chima, P., Baiyegunhi, C., Liu, K., & Gwavava, O. (2018).** Petrography, modal composition and tectonic provenance of some selected sandstones from the Molteno, Elliot and Clarens Formations, Karoo Supergroup, in the Eastern Cape Province, South Africa. *Open Geosciences*, 10(1), 821-833.
- Chougong, D. T., Bessa, A. Z. E., Ngueutchoua, G., Yongue, R. F., Ntyam, S. C., & Armstrong-Altrin, J. S. (2021).** Mineralogy and geochemistry of Lobé River sediments, SW Cameroon: Implications for provenance and weathering. *Journal of African Earth Sciences*, 183, 104320.
- Church, M., Coniglio, M., Hardie, L. A., & Longstaffe, F. J. (2005).** *Encyclopedia of sediments and sedimentary rocks*. Springer.
- Condie, K. C. (1993).** Chemical composition and evolution of the upper continental crust: contrasting results from surface samples and shales. *Chemical geology*, 104(1-4), 1-37.
- Condie, K.C. (2011).** *Earth as an Evolving Planetary System*, second ed. Elsevier, Great Britain (574pp. ISBN: 978-0-12-385227-4).
- Cottingham, K. (1951).** The Geologist's Vocabulary. *The Scientific Monthly*, 72(3), 154-163.
- Cox, R., Lowe, D. R., & Cullers, R. L. (1995).** The influence of sediment recycling and basement composition on evolution of mudrock chemistry in the southwestern United States. *Geochimica et Cosmochimica Acta*, 59(14), 2919-2940.

- CozzENs, A. B. (1931).** Rates of wear of common minerals. *Washington University Studies, Science and Technology*, 5, 71-80.
- Crook, K. A. (1974).** Lithogenesis and geotectonics: the significance of compositional variation in flysch arenites (graywackes). *Soc. Econ. Paleont. Mineral. Spec. Publ.*, 1974, 19, 304-310.
- Cullers, R. L. (1995).** The controls on the major-and trace-element evolution of shales, siltstones and sandstones of Ordovician to Tertiary age in the Wet Mountains region, Colorado, USA. *Chemical Geology*, 123(1-4), 107-131.
- Cullers, R. L. (2000).** The geochemistry of shales, siltstones and sandstones of Pennsylvanian–Permian age, Colorado, USA: implications for provenance and metamorphic studies. *Lithos*, 51(3), 181-203.
- Cullers, R. L., & Podkovyrov, V. N. (2000).** Geochemistry of the Mesoproterozoic Lakhanda shales in southeastern Yakutia, Russia: implications for mineralogical and provenance control, and recycling. *Precambrian Research*, 104(1-2), 77-93.
- De Rosa, S. S., Shipton, Z. K., Lunn, R. J., Kremer, Y., & Murray, T. (2018).** Along-strike fault core thickness variations of a fault in poorly lithified sediments, Miri (Malaysia). *Journal of Structural Geology*, 116, 189-206.
- Deng, C., Sun, G., Sun, D., Han, J., Yang, D., & Tang, Z. (2019).** Morphology, trace elements, and geochronology of zircons from monzogranite in the Northeast Xing’an Block, northeastern China: constraints on the genesis of the host magma. *Mineralogy and Petrology*, 113(5), 651-666.
- Denge, E., & Baiyegunhi, C. (2021).** Geochemical and Petrographical Characteristics of the Madzaringwe Formation Coal, Mudrocks and Sandstones in the Vele Colliery, Limpopo Province, South Africa: Implications for Tectonic Setting, Provenance and Paleoweathering. *Applied Sciences*, 11(6), 2782.
- Dickinson, W. R. (1985).** Interpreting provenance relations from detrital modes of sandstones. In *Provenance of arenites* (pp. 333-361). Springer, Dordrecht.
- Dickinson, W. R., & Suczek, C. A. (1979).** Plate tectonics and sandstone compositions. *Aapg Bulletin*, 63(12), 2164-2182.
- Dickinson, W. R., Beard, L. S., Brakenridge, G. R., Erjavec, J. L., Ferguson, R. C., Inman, K. F., ... & Ryberg, P. T. (1983).** Provenance of North American Phanerozoic sandstones in relation to tectonic setting. *Geological Society of America Bulletin*, 94(2), 222-235.
- Doornkamp, J. C., & Krinsley, D. (1971).** Electron microscopy applied to quartz grains from a tropical environment. *Sedimentology*, 17(1-2), 89-101.
- Dostal, J., & Keppie, J. D. (2009).** Geochemistry of low-grade clastic rocks in the Acatlán Complex of southern Mexico: Evidence for local provenance in felsic–intermediate igneous rocks. *Sedimentary Geology*, 222(3-4), 241-253.
- Dumoulin, J. A., Jones III, J. V., Bradley, D. C., Till, A. B., Box, S. E., & O’Sullivan, P. (2018).** Neoproterozoic–early Paleozoic provenance evolution of sedimentary rocks in and adjacent to the Farewell terrane (interior Alaska). *Geosphere*, 14(2), 367-394.
- Fantle, M. S., Barnes, B. D., & Lau, K. V. (2020).** The role of diagenesis in shaping the geochemistry of the marine carbonate record. *Annual Review of Earth and Planetary Sciences*, 48, 549-583.
- Fathy, D., Wagreeich, M., Ntaflos, T., & Sami, M. (2021).** Provenance Characterization of Campanian Lacustrine Organic-Rich Mudstones on the Southern Tethyan Margin, Egypt. *ACS Earth and Space Chemistry*, 5(2), 197-209.

- Fedo, C. M., Wayne Nesbitt, H., & Young, G. M. (1995).** Unraveling the effects of potassium metasomatism in sedimentary rocks and paleosols, with implications for paleoweathering conditions and provenance. *Geology*, 23(10), 921-924.
- Folk, R. L. (1974).** Petrology of sedimentary rocks: Hemphill Pub. Co., Austin, Texas, 63.
- Folk, R. L. (1980).** Petrology of sedimentary rocks (pp. 26–27). Austin, Texas: Hemphill.
- Galim, T., Breitfeld, H. T., Hall, R., & Sevastjanova, I. (2017).** Provenance of the Cretaceous–Eocene Rajang Group submarine fan, Sarawak, Malaysia from light and heavy mineral assemblages and U-Pb zircon geochronology. *Gondwana Research*, 51, 209-233.
- Garzanti, E., Doglioni, C., Vezzoli, G., & Ando, S. (2007).** Orogenic belts and orogenic sediment provenance. *The Journal of Geology*, 115(3), 315-334.
- Garzanti, E., He, J., Barbarano, M., Resentini, A., Li, C., Yang, L., Yang, S., & Wang, H. (2021).** Provenance versus weathering control on sediment composition in tropical monsoonal climate (South China)-2. Sand petrology and heavy minerals. *Chemical Geology*, 564, 119997.
- Garzanti, E., Padoan, M., Setti, M., López-Galindo, A., & Villa, I. M. (2014).** Provenance versus weathering control on the composition of tropical river mud (southern Africa). *Chemical Geology*, 366, 61-74.
- Garzanti, E., Vermeesch, P., Padoan, M., Resentini, A., Vezzoli, G., & Ando, S. (2014).** Provenance of passive-margin sand (Southern Africa). *The Journal of Geology*, 122(1), 17-42.
- Getaneh, W. (2002).** Geochemistry provenance and depositional tectonic setting of the Adigrat Sandstone northern Ethiopia. *Journal of African Earth Sciences*, 35(2), 185-198.
- Giles, M. R., Indrelid, S. L., Beynon, G. V., Amthor, J., Worden, R. H., & Morad, S. (2000).** The origin of large-scale quartz cementation: evidence from large data sets and coupled heat-fluid mass transport modelling. special publication-international association of sedimentologists, 29, 21-38.
- Gould, K., PE-PIPER, G. E. O. R. G. I. A., & Piper, D. J. (2010).** Relationship of diagenetic chlorite rims to depositional facies in Lower Cretaceous reservoir sandstones of the Scotian Basin. *Sedimentology*, 57(2), 587-610.
- Grimes, C. B., Wooden, J. L., Cheadle, M. J., & John, B. E. (2015).** “Fingerprinting” tectono-magmatic provenance using trace elements in igneous zircon. *Contributions to Mineralogy and Petrology*, 170(5), 1-26.
- Guadagnin, F., Junior, F. C., Magalhães, A. J., Alessandretti, L., Bállico, M. B., & Jelinek, A. R. (2015).** Sedimentary petrology and detrital zircon U–Pb and Lu–Hf constraints of Mesoproterozoic intracratonic sequences in the Espinhaço Supergroup: Implications for the Archean and Proterozoic evolution of the São Francisco Craton. *Precambrian Research*, 266, 227-245.
- Hall, R. (1996).** Reconstructing Cenozoic SE Asia. Geological Society, London, Special Publications, 106(1), 153-184.
- Harnois, L. (1988).** The CIW index: a new chemical index of weathering. *SedG*, 55(3), 319-322.
- He, J., Garzanti, E., Dinis, P., Yang, S., & Wang, H. (2020).** Provenance versus weathering control on sediment composition in tropical monsoonal climate (South China)-1. Geochemistry and clay mineralogy. *Chemical Geology*, 558, 119860.
- Herron, M. M. (1988).** Geochemical classification of terrigenous sands and shales from core or log data. *Journal of Sedimentary Research*, 58(5), 820-829.

- Hood, A.v.S., Planavsky, N. J., Wallace, M. W., & Wang, X. (2018).** The effects of diagenesis on geochemical paleoredox proxies in sedimentary carbonates. *Geochimica et Cosmochimica Acta*, 232, 265-287.
- Hossain, H. M. Z., Roser, B. P., & Kimura, J. I. (2010).** Petrography and whole-rock geochemistry of the Tertiary Sylhet succession, northeastern Bengal Basin, Bangladesh: Provenance and source area weathering. *Sedimentary Geology*, 228(3-4), 171-183.
- Hossain, H. Z., Armstrong-Altrin, J. S., Jamil, A. H. M. N., Rahman, M. M., Hernández-Coronado, C. J., & Ramos-Vázquez, M. A. (2020).** Microtextures on quartz grains in the Kuakata beach, Bangladesh: implications for provenance and depositional environment. *Arabian Journal of Geosciences*, 13(7), 1-12.
- Hou, Q., Mou, C., Han, Z., Wang, Q., Tan, Z., & Ge, X. (2020).** Petrography and geochemistry of the Lower Silurian sandstones from the Angzanggou Formation in the North Qilian Belt, China: implications for provenance, weathering and tectonic setting. *Geological Magazine*, 157(3), 477-496.
- Hutchison, C.S. (2005).** *Geology of North-West Borneo*. Elsevier, p. 421.
- Ibrahim, C. A., Light, L., Mennie, J., & Ngu, C. K. (2012).** Foresee the unforeseen: modeling West Baram Delta overpressure. In *PGCE 2012*.
- Ingersoll, R. V. (1988).** Tectonics of sedimentary basins. *Geological Society of America Bulletin*, 100(11), 1704-1719.
- Ismail, m. N., & Abdul Rahman, S. H. (2017).** Wave-dominated shoreline deposits in the late miocene sedimentary. *Geological Behavior (GBR)* 1(2), 14-19
- Itamiya, H., Sugita, R., & Sugai, T. (2019).** Analysis of the surface microtextures and morphologies of beach quartz grains in Japan and implications for provenance research. *Progress in Earth and Planetary Science*, 6(1), 43.
- Jafarzadeh, M., & Hosseini-Barzi, M. (2008).** Petrography and geochemistry of Ahwaz Sandstone Member of Asmari Formation, Zagros, Iran: implications on provenance and tectonic setting. *Revista Mexicana de Ciencias Geológicas*, 25(2), 247-260.
- Jalal, P., & Ghosh, S. K. (2012).** Provenance of the Late Neogene Siwalik sandstone, Kumaun Himalayan Foreland Basin: Constraints from the metamorphic rank and index of detrital rock fragments. *Journal of earth system science*, 121(3), 781-792.
- Ji, H., Tao, H., Wang, Q., Ma, D., & Hao, L. (2019).** Petrography, geochemistry, and geochronology of Lower Jurassic sedimentary rocks from the Northern Tianshan (West Bogda area), Northwest China: Implications for provenance and tectonic evolution. *Geological Journal*, 54(3), 1688-1714.
- Jia, T. Y., & Rahman, A. H. A. (2009).** Comparative analysis of facies and reservoir characteristics of Miri Formation (Miri) and Nyalau Formation (Bintulu), Sarawak. *Bulletin of the Geological Society of Malaysia*, 55 ,39 – 45
- Jong, J., Kessler, F., Noon, S., & Tan, T. T. Q. (2016).** Structural development, deposition model and petroleum system of Paleogene carbonate of the Engkabang-Karap Anticline, Onshore Sarawak. *Berita Sedimentologi*, 34, 5-25.
- Kalińska-Nartiša, E., Alexanderson, H., Nartišs, M., Stevic, M., & Kaiser, K. (2017).** Sedimentary features reveal transport paths for Holocene sediments on the Kristianstad coastal plain, SE Sweden. *GFF*, 139(2), 147-161.
- Kanhaiya, S., Singh, B. P., & Srivastava, V. K. (2017).** Surface textures of detrital quartz grains derived from Bundelkhand granite in the Khurar River, central India. Vietnam: Geo-

spatial technology and Earth resources. Publishing House for Science and Technology, 575-581.

- Kassab, M. A., Hassanain, I. M., & Salem, A. M. (2014).** Petrography, diagenesis and reservoir characteristics of the pre-Cenomanian sandstone, Sheikh Attia area, East Central Sinai, Egypt. *Journal of African Earth Sciences*, 96, 122-138.
- Kelly, J. L., Fu, B., Kita, N. T., & Valley, J. W. (2007).** Optically continuous silcrete quartz cements of the St. Peter Sandstone: high precision oxygen isotope analysis by ion microprobe. *Geochimica et Cosmochimica Acta*, 71(15), 3812-3832.
- Kennedy, M., (2015).** Practical Petrophysics. Elsevier, Amsterdam.
- Kennedy, M. (2015).** Practical petrophysics. Elsevier.
- Kessler, F. L., & Jong, J. (2015).** Tertiary uplift and the Miocene evolution of the NW Borneo shelf margin. *Berita Sedimentologi*, 33, 21-46.
- Kessler, F. L., Jong, J., & Madon, M. (2020).** Sedimentary record of Paleogene sequences in Penyu and Malay basins, offshore Peninsular Malaysia. *Berita Sedimentologi*, 46.
- Kettanah, Y. A., Armstrong-Altrin, J. S., & Mohammad, F. A. (2020).** Petrography and geochemistry of siliciclastic rocks of the Middle Eocene Gercus Formation, northern Iraq: Implications for provenance and tectonic setting. *Geological Journal*.
- Kettanah, Y. A., Armstrong-Altrin, J. S., & Mohammad, F. A. (2021).** Petrography and geochemistry of siliciclastic rocks of the Middle Eocene Gercus Formation, northern Iraq: Implications for provenance and tectonic setting. *Geological Journal*, 56(5), 2528-2549.
- Khidir, A., & Catuneanu, O. (2010).** Reservoir characterization of Scollard-age fluvial sandstones, Alberta foredeep. *Marine and Petroleum Geology*, 27(9), 2037-2050.
- Krinsley, D. (1980).** Scanning electron microscope examination of quartz sandgrain microtextures. *Geological Quarterly*, 24(2), 217-232.
- Krinsley, D. H., & Donahue, J. (1968).** Environmental interpretation of sand grain surface textures by electron microscopy. *Geological Society of America Bulletin*, 79(6), 743-748.
- Krinsley, D. H., & Funnell, B. M. (1965).** Environmental history of quartz sand grains from the Lower and Middle Pleistocene of Norfolk, England. *Quarterly Journal of the Geological Society*, 121(1-4), 435-456.
- Krinsley, D. H., & Marshall, J. R. (1987).** Sand grain textural analysis: an assessment. In *Clastic particles. Scanning electron microscopy and shape analysis of sedimentary and volcanic clasts* (pp. 2-15).
- Krinsley, D. H., & McCoy, F. W. (1977).** Significance and origin of surface textures on broken sand grains in deep-sea sediments. *Sedimentology*, 24(6), 857-862.
- Krinsley, D., & Takahashi, T. (1964).** A technique for the study of surface textures of sand grains with electron microscopy. *Journal of Sedimentary Research*, 34(2), 423-426.
- Krumbein, W. C., & Sloss, L. L. (1951).** Stratigraphy and sedimentation (Vol. 71, No. 5, p. 401). LWW.
- Kunming, W., Zongqi, W., Yingli, Z., & Gang, W. (2015).** Geochronology and geochemistry of mafic rocks in the Xuhe, Shaanxi, China: implications for petrogenesis and mantle dynamics. *Acta Geologica Sinica-English Edition*, 89(1), 187-202.
- Lai, J., Wang, G., Chen, J., Wang, S., Zhou, Z., & Fan, X. (2017).** Origin and distribution of carbonate cement in tight sandstones: The Upper Triassic Yanchang Formation Chang 8 oil layer in west Ordos Basin, China. *Geofluids*, 2017.
- Lai, J., Wang, G., Ran, Y., & Zhou, Z. (2015).** Predictive distribution of high-quality reservoirs of tight gas sandstones by linking diagenesis to depositional facies: Evidence from Xu-2



sandstones in the Penglai area of the central Sichuan basin, China. *Journal of Natural Gas Science and Engineering*, 23, 97-111.

- Levorsen, A.I. and Berry, F.A., 1967.** Geology of petroleum (Vol. 8). San Francisco: WH Freeman.
- Li, B., Zhuang, X., Liu, X., Wu, C., Zhou, J., & Ma, X. (2016).** Mineralogical and geochemical composition of Middle Permian Lucaogou Formation in the southern Junggar Basin, China: implications for paleoenvironment, provenance, and tectonic setting. *Arabian Journal of Geosciences*, 9(3), 174.
- Li, W., Fan, T., Gao, Z., Wu, Z., Li, Y. N., Zhang, X., Zhang, H., & Cao, F. (2021).** Impact of Diagenesis on the Low Permeability Sandstone Reservoir: Case Study of the Lower Jurassic Reservoir in the Niudong Area, Northern Margin of Qaidam Basin. *Minerals*, 11(5), 453.
- Li, Y. N., Shao, L., Xu, J., Hou, H., Tang, Y., Yuan, Y., & Zhang, J. (2020).** Application of channel-belt scaling relationships to early Middle Jurassic source-to-sink system evolution in the southern Junggar Basin. *Marine and Petroleum Geology*, 117, 104356.
- Li, Z., Liu, Q., Zhu, H., Zhang, X., Li, M., & Zhao, Q. (2021).** Compositional relationship between the source-to-sink segments and their sedimentary response to diverse geomorphology types in the intrabasinal lower uplift of continental basins. *Marine and Petroleum Geology*, 123, 104716.
- Lindsey, D. A. (1999).** An evaluation of alternative chemical classifications of sandstones (No. 99-346). US Geological Survey.
- Liu, E. J., Cashman, K. V., & Rust, A. C. (2015).** Optimising shape analysis to quantify volcanic ash morphology. *GeoResJ*, 8, 14-30.
- Liu, L., Li, Y., Dong, H., & Sun, Z. (2020).** Diagenesis and reservoir quality of Paleocene tight sandstones, Lishui Sag, East China Sea Shelf Basin. *Journal of Petroleum Science and Engineering*, 195, 107615.
- Liu, S., Huang, S., Shen, Z., Lü, Z., & Song, R. (2014).** Diagenetic fluid evolution and water-rock interaction model of carbonate cements in sandstone: An example from the reservoir sandstone of the Fourth Member of the Xujiahe Formation of the Xiaoquan-Fenggu area, Sichuan Province, China. *Science China Earth Sciences*, 57(5), 1077-1092.
- Long, X., Yuan, C., Sun, M., Xiao, W., Wang, Y., Cai, K., & Jiang, Y. (2012).** Geochemistry and Nd isotopic composition of the Early Paleozoic flysch sequence in the Chinese Altai, Central Asia: evidence for a northward-derived mafic source and insight into Nd model ages in accretionary orogen. *Gondwana Research*, 22(2), 554-566.
- Mackie, W. (1897).** The sands and sandstones of eastern Moray. *Transactions of the Edinburgh Geological Society*, 7(3), 148-172.
- Madhavaraju J, JCGy B, Hussain SM, Mohan SP (2009)** Microtextures on quartz grains in the beach sediments of Puerto Peñasco and Bahia Kino, Gulf of California, Sonora, Mexico. *Rev Mex Cienc Geol* 26:367–379
- Madhavaraju, J., & Ramasamy, S. (1999).** Microtextures on quartz grains of Campanian-Maastrichtian sediments of Ariyalur Group of Tiruchirapalli Cretaceous, Tamil Nadu-Implication on depositional environments. *Journal of the Geological Society of India*, 54(6), 647-658.
- Madhavaraju, J., Lee, Y. I., Armstrong-Altrin, J. S., & Hussain, S. M. (2006).** Microtextures on detrital quartz grains of upper Maastrichtian-Danian rocks of the Cauvery Basin,

Southeastern India: implications for provenance and depositional environments. *Geosciences Journal*, 10(1), 23-34.

- Madhavaraju, J., Armstrong-Altrin, J. S., James, R. A., & Hussain, S. M. (2021).** Palaeoenvironment and provenance signatures inferred from quartz grain surface features: A case study from Huatabampu and Altata beaches, Gulf of California, Mexico. *Journal of South American Earth Sciences*, 103441.
- Madhavaraju, J., Pacheco-Olivas, S. A., González-León, C. M., Espinoza-Maldonado, I. G., Sanchez-Medrano, P. A., Villanueva-Amadoz, U., Monreal, R., Pi-Puig, T., Ramírez-Montoya, E. & Grijalva-Noriega, F. J. (2017).** Mineralogy and geochemistry of the lower Cretaceous siliciclastic rocks of the Morita formation, Sierra San Jose section, Sonora, Mexico. *Journal of South American Earth Sciences*, 76, 397-411.
- Madhavaraju, J., Ramasamy, S., Mohan, S. P., Hussain, S. M., Gladwin Gnana Asir, N., & Stephen Pitchaimani, V. (2004).** Petrography and surface textures on quartz grains of Nimar Sandstone, Bagh Beds, Madhya Pradesh-Implications for provenance and depositional environment. *Journal of the Geological Society of India*, 64(6), 747-762.
- Mahaney, W. C., Stewart, A., & Kalm, V. (2001).** Quantification of SEM microtextures useful in sedimentary environmental discrimination. *Boreas*, 30(2), 165-171.
- Makeen, Y. M., Abdullah, W. H., Ayinla, H. A., Hakimi, M. H., & Sia, S. G. (2016).** Sedimentology, diagenesis and reservoir quality of the upper Abu Gabra Formation sandstones in the Fula Sub-basin, Muglad Basin, Sudan. *Marine and Petroleum Geology*, 77, 1227-1242.
- Makeen, Y. M., Shan, X., Ayinla, H. A., Adepehin, E. J., Ayuk, N. E., Yelwa, N. A., ... & Fan, D. (2021).** Sedimentology, petrography, and reservoir quality of the Zarga and Ghazal formations in the Keyi oilfield, Muglad Basin, Sudan. *Scientific Reports*, 11(1), 1-22.
- Malaza, N., Liu, K., & Zhao, B. (2016).** Petrology and geochemistry of clastic sedimentary rocks as evidences for provenance of the Late Palaeozoic Madzaringwe Formation, Tshipise-Pafuri Basin, South Africa. *Science China Earth Sciences*, 59(12), 2411-2426.
- Margolis, S. V., & Krinsley, D. H. (1974).** Processes of formation and environmental occurrence of microfeatures on detrital quartz grains. *American Journal of Science*, 274(5), 449-464.
- Maslov, A. V., Podkovyrov, V. N., Mizens, G. A., Nozhkin, A. D., Fazliakhmetov, A. M., Malinovsky, A. I., Khudoley, A. K., Kotava, L. N., Kuptosova, A. V., Gareev, E. Z., & Zainullin, R. I. (2016).** Tectonic setting discrimination diagrams for terrigenous rocks: a comparison. *Geochemistry International*, 54(7), 569-583.
- Mathew, M. J., Menier, D., Siddiqui, N., Kumar, S. G., & Authemayou, C. (2016a).** Active tectonic deformation along rejuvenated faults in tropical Borneo: Inferences obtained from tectono-geomorphic evaluation. *Geomorphology*, 267, 1-15.
- Mathew, M. J., Menier, D., Siddiqui, N., Ramkumar, M., Santosh, M., Kumar, S., & Hassaan, M. (2016b).** Drainage basin and topographic analysis of a tropical landscape: Insights into surface and tectonic processes in northern Borneo. *Journal of Asian Earth Sciences*, 124, 14-27.
- Matter, A., & Ramseyer, K. (1985).** Cathodoluminescence microscopy as a tool for provenance studies of sandstones. In *Provenance of arenites* (pp. 191-211). Springer, Dordrecht.
- Maynard, J. B. (1984).** Composition of plagioclase feldspar in modern deep-sea sands: relationship to tectonic setting. *Sedimentology*, 31(4), 493-501.

- Mazumder, R. (2017).** Sediment provenance: influence on compositional change from source to sink. In *Sediment Provenance* (pp. 1-4). Elsevier.
- McLennan, S. M., Hemming, S., McDaniel, D. K., & Hanson, G. N. (1993).** Geochemical approaches to sedimentation, provenance, and tectonics. *Special Papers-Geological Society of America*, 21-21.
- Menier, D., Mansor, Y., Sautter, B., Pubellier, M., Estournes, G., Meng Choong, C., Ghosh Deva, P., Proust, J.N. and Goubert, E., (2014),** May. Geomorphology and regional stratigraphic model of Cenozoic deposits from "Continental to Marine" of Western Peninsular Malaysia and Strait of Malacca. In *EGU General Assembly Conference Abstracts* (Vol. 16).
- Milliken, K. L., Mack, L. E., & Land, L. S. (1994).** Elemental mobility in sandstones during burial; whole-rock chemical and isotopic data, Frio Formation, South Texas. *Journal of Sedimentary Research*, 64(4a), 788-796.
- Mode, A. W., Anyiam, O. A., & Anigbogu, E. C. (2016).** The effect of diagenesis on reservoir quality of Mamu Sandstone, Anambra Basin, Nigeria. *Journal of the Geological Society of India*, 87(5), 583-590.
- Mohammadi, A., Burg, J. P., & Guillong, M. (2020).** The Siah Cheshmeh-Khoy-Misho-Tabriz fault (NW Iran) is a cryptic neotethys suture: evidence from detrital zircon geochronology, Hf isotopes, and provenance analysis. *International Geology Review*, 1-21.
- Monicard, R. P. (1980).** Properties of reservoir rocks: core analysis (Vol. 5). Editions Technip.
- Morad, S., Ketzer, J. M., & De Ros, L. F. (2000).** Spatial and temporal distribution of diagenetic alterations in siliciclastic rocks: implications for mass transfer in sedimentary basins. *Sedimentology*, 47, 95-120.
- Mounteney, I., Burton, A. K., Farrant, A. R., Watts, M. J., Kemp, S. J., & Cook, J. M. (2018).** Heavy mineral analysis by ICP-AES a tool to aid sediment provenancing. *Journal of Geochemical Exploration*, 184, 1-10.
- Nagarajan, R., Armstrong-Altrin, J. S., Kessler, F. L., & Jong, J. (2017a).** Petrological and geochemical constraints on provenance, paleoweathering, and tectonic setting of clastic sediments from the Neogene Lambir and Sibuti Formations, northwest Borneo. In *Sediment provenance* (pp. 123-153). Elsevier.
- Nagarajan, R., Armstrong-Altrin, J. S., Kessler, F. L., Hidalgo-Moral, E. L., Dodge-Wan, D., & Taib, N. I. (2015).** Provenance and tectonic setting of Miocene siliciclastic sediments, Sibuti Formation, northwestern Borneo. *Arabian Journal of Geosciences*, 8(10), 8549-8565.
- Nagarajan, R., Armstrong-Altrin, J. S., Nagendra, R., Madhavaraju, J., & Moutte, J. (2007b).** Petrography and geochemistry of terrigenous sedimentary rocks in the Neoproterozoic Rabanpalli Formation, Bhima Basin, Southern India: implications for paleoweathering conditions, provenance and source rock composition. *Journal-Geological Society of India*, 70(2), 297.
- Nagarajan, R., Franz L, K., Jong, J., Muthuvairavasamy, R., Muhammad, A.A., Dayong, V., Shanmugarajah, L., Vusak, N., Sivanasvaran, K. & Kinanthi, D., (2021).** Geochemistry of the Palaeocene-Eocene Upper Kelalan Formation, NW Borneo: Implications on palaeoweathering, tectonic setting, and provenance. *Geological Journal*.
- Nagarajan, R., Madhavaraju, J., Nagendra, R., Altrin, J. S. A., & Moutte, J. (2007a).** Geochemistry of Neoproterozoic shales of the Rabanpalli Formation, Bhima Basin,

Northern Karnataka, southern India: implications for provenance and paleoredox conditions. *Revista Mexicana de Ciencias Geológicas*, 24(2), 150-160.

- Nagarajan, R., Roy, P. D., Jonathan, M., Lozano, R., Kessler, F. L., & Prasanna, M. V. (2014).** Geochemistry of Neogene sedimentary rocks from Borneo Basin, East Malaysia: Paleo-weathering, provenance and tectonic setting. *Chemie der Erde-Geochemistry*, 74(1), 139-146.
- Nagarajan, R., Roy, P. D., Kessler, F. L., Jong, J., Dayong, V., & Jonathan, M. P. (2017b).** An integrated study of geochemistry and mineralogy of the Upper Tunku Formation, Borneo Island (East Malaysia): Sediment provenance, depositional setting and tectonic implications. *Journal of Asian Earth Sciences*, 143, 77-94.
- Nesbitt, H. W., Young, G. M., McLennan, S. M., & Keays, R. R. (1996).** Effects of chemical weathering and sorting on the petrogenesis of siliciclastic sediments, with implications for provenance studies. *The Journal of Geology*, 104(5), 525-542.
- Nesbitt, H., & Young, G. M. (1989).** Formation and diagenesis of weathering profiles. *The Journal of Geology*, 97(2), 129-147.
- Niki, T., Saito, S., & Gladish, D. K. (2019).** A novel thin section preparation and staining protocol to increase contrast and resolution of cell details for light microscopy. *Biotechnic & Histochemistry*, 94(7), 522-526.
- Nowrouzi, Z., Moussavi-Harami, R., Mahboubi, A., Gharai, M. H. M., & Ghaemi, F. (2014).** Petrography and geochemistry of Silurian Niur sandstones, Derenj Mountains, East Central Iran: implications for tectonic setting, provenance and weathering. *Arabian Journal of Geosciences*, 7(7), 2793-2813.
- O'Sullivan, G. J., Chew, D. M., Morton, A. C., Mark, C., & Henrichs, I. A. (2018).** An integrated apatite geochronology and geochemistry tool for sedimentary provenance analysis. *Geochemistry, Geophysics, Geosystems*, 19(4), 1309-1326.
- Ohta, T. (2004).** Geochemistry of Jurassic to earliest Cretaceous deposits in the Nagato Basin, SW Japan: implication of factor analysis to sorting effects and provenance signatures. *Sedimentary Geology*, 171(1-4), 159-180.
- Osae, S., Asiedu, D. K., Banoeng-Yakubo, B., Koeberl, C., & Dampare, S. B. (2006).** Provenance and tectonic setting of Late Proterozoic Buem sandstones of southeastern Ghana: Evidence from geochemistry and detrital modes. *Journal of African Earth Sciences*, 44(1), 85-96.
- Pacle, N. A. D., Dimalanta, C. B., Ramos, N. T., Payot, B. D., Faustino-Eslava, D. V., Queaño, K. L., & Yumul Jr, G. P. (2017).** Petrography and geochemistry of Cenozoic sedimentary sequences of the southern Samar Island, Philippines: clues to the unroofing history of an ancient subduction zone. *Journal of Asian Earth Sciences*, 142, 3-19.
- Paikaray, S., Banerjee, S., & Mukherji, S. (2008).** Geochemistry of shales from the Paleoproterozoic to Neoproterozoic Vindhyan Supergroup: Implications on provenance, tectonics and paleoweathering. *Journal of Asian Earth Sciences*, 32(1), 34-48.
- Pang, H., Pan, B., Garzanti, E., Gao, H., Zhao, X., & Chen, D. (2018).** Mineralogy and geochemistry of modern Yellow River sediments: Implications for weathering and provenance. *Chemical Geology*, 488, 76-86.
- Parker, A. (1970).** An index of weathering for silicate rocks. *Geological Magazine*, 107(6), 501-504.
- Parry, W. T. (2011).** Composition, nucleation, and growth of iron oxide concretions. *Sedimentary Geology*, 233(1-4), 53-68.

- Peterknecht, K. M., & Tietz, G. F. (2011).** Chattermark trails: surface features on detrital quartz grains indicative of a tropical climate. *Journal of Sedimentary Research*, 81(2), 153-158.
- Pettijohn, F. J. (1975).** *Sedimentary rocks* (Vol. 3). New York: Harper & Row.
- Pettijohn, F. J., Potter, P. E., & Siever, R. (1987).** Introduction and source materials. In *Sand and sandstone* (pp. 1-21). Springer, New York, NY.
- Pettijohn, F. J., Potter, P. E., & Siever, R. (2012).** *Sand and sandstone*. Springer Science & Business Media.
- Pitard, F. F. (1993).** Pierre Gy's sampling theory and sampling practice: heterogeneity, sampling correctness, and statistical process control. CRC press, 271.
- Pittman, E. D. (1963).** Use of zoned plagioclase as an indicator of provenance. *Journal of Sedimentary Research*, 33(2), 380-386.
- Pittman, E. D. (1970).** Plagioclase feldspar as an indicator of provenance in sedimentary rocks. *Journal of Sedimentary Research*, 40(2).
- Pittman, E. D., & Larese, R. E. (1991).** Compaction of lithic sands: experimental results and applications. *AAPG bulletin*, 75(8), 1279-1299.
- Potter, P. E. (1978).** Petrology and chemistry of modern big river sands. *The Journal of Geology*, 86(4), 423-449.
- Potter, P. E. (1994).** Modern sands of South America: composition, provenance and global significance. *Geologische Rundschau*, 83(1), 212-232.
- Potter, P. E., Maynard, J. B., & Depetris, P. J. (2005).** *Mud and mudstones: Introduction and overview*. Springer Science & Business Media.
- Rahman, M. J. J., & Worden, R. H. (2016).** Diagenesis and its impact on the reservoir quality of Miocene sandstones (Surma Group) from the Bengal Basin, Bangladesh. *Marine and Petroleum Geology*, 77, 898-915.
- Rahman, M. N. I. A., & Tahir, S. H. (2017).** Measured Section for The Possible Stratotype Of The Miri Formation, At Miri Hill, North Sarawak, Malaysia. *Geological Behavior (GBR)* 2(2), 10-16.
- Ramkumar, M., Santosh, M., Nagarajan, R., Li, S. S., Mathew, M., Menier, D., Ramkumar, M., Santosh, M., Nagarajan, R., Li, S.S., Mathew, M., Menier, D., Siddiqui, N.A., & Poppelreiter, M. C. (2018).** Late Middle Miocene volcanism in Northwest Borneo, Southeast Asia: Implications for tectonics, paleoclimate and stratigraphic marker. *Palaeogeography, Palaeoclimatology, Palaeoecology*, 490, 141-162.
- Ramos-Vázquez, M. A., & Armstrong-Altrin, J. S. (2021).** Microtextures on quartz and zircon grain surfaces in the Barra del Tordo and Tesoro beaches, northwestern Gulf of Mexico. *Arabian Journal of Geosciences*, 14(11), 1-12.
- Ramos-Vázquez, M.A., & Armstrong-Altrin, J.S. (2020).** Provenance and palaeoenvironmental significance of microtextures in quartz and zircon grains from the Paseo del Mar and Bosque beaches, Gulf of Mexico. *Journal of Earth System Science*, 129(1), 1-16.
- Rijks, E. J. H. (1981).** Baram Delta geology and hydrocarbon occurrence. *Roduit, N. I. C. O. L. A. S.* (2005). Two complementary efficient methods to quantify porosity types in digital images of thin sections with the software JMicroVision. In *Abstract, Scenic Sedimentology, 24th IAS Meeting*.
- Rodrigues, A. G., & Goldberg, K. (2014).** Primary composition and diagenetic patterns of sandstones from Barra de Itiúba Formation in Atalaia High, Sergipe Sub-Basin. *Brazilian Journal of Geology*, 44(4), 545-560.

- Roser, B. P., & Korsch, R. J. (1986).** Determination of tectonic setting of sandstone-mudstone suites using SiO<sub>2</sub> content and K<sub>2</sub>O/Na<sub>2</sub>O ratio. *The Journal of Geology*, 94(5), 635-650.
- Ru, K., & Pigott, J. D. (1986).** Episodic rifting and subsidence in the South China Sea. *AAPG Bulletin*, 70(9), 1136-1155.
- Ryan, K. M., & Williams, D. M. (2007).** Testing the reliability of discrimination diagrams for determining the tectonic depositional environment of ancient sedimentary basins. *Chemical Geology*, 242(1-2), 103-125.
- Saigal, G. C., Morad, S., Bjorlykke, K., Egeberg, P. K., & Aagaard, P. (1988).** Diagenetic albitization of detrital K-feldspar in Jurassic, Lower Cretaceous, and Tertiary clastic reservoir rocks from offshore Norway; I, Textures and origin. *Journal of Sedimentary Research*, 58(6), 1003-1013.
- Saminpanya, S., Duangkrayom, J., Jintasakul, P., & Hanta, R. (2014).** Petrography, mineralogy and geochemistry of Cretaceous sediment samples from western Khorat Plateau, Thailand, and considerations on their provenance. *Journal of Asian Earth Sciences*, 83, 13-34.
- Schieber, J. (1992).** A combined petrographical—geochemical provenance study of the Newland Formation, Mid-Proterozoic of Montana. *Geological Magazine*, 129(2), 223-237.
- Schowalter, T. T. (1979).** Mechanics of secondary hydrocarbon migration and entrapment. *AAPG Bulletin*, 63(5), 723-760.
- Schwab, F. L. (1975).** Framework mineralogy and chemical composition of continental margin-type sandstone. *Geology*, 3(9), 487-490.
- Selvaraj, K., & Chen, C. T. A. (2006).** Moderate chemical weathering of subtropical Taiwan: constraints from solid-phase geochemistry of sediments and sedimentary rocks. *The Journal of Geology*, 114(1), 101-116.
- Siddiqui, N. A., Rahman, A. H. A., Sum, C. W., Mathew, M. J., & Menier, D. (2016).** Onshore sandstone facies characteristics and reservoir quality of Nyalau Formation, Sarawak, East Malaysia: an analogue to subsurface reservoir quality evaluation. *Arabian Journal for Science and Engineering*, 41(1), 267-280.
- Siddiqui, N. A., Rahman, A. H. A., Sum, C. W., Mathew, M. J., Hassaan, M., & Menier, D. (2017).** Generic hierarchy of sandstone facies quality and static connectivity: an example from the Middle-Late Miocene Miri Formation, Sarawak Basin, Borneo. *Arabian Journal of Geosciences*, 10(11), 237.
- Song, Y. H., & Choi, M. S. (2009).** REE geochemistry of fine-grained sediments from major rivers around the Yellow Sea. *Chemical Geology*, 266(3-4), 328-342.
- Suttner, L. J. (1974).** Sedimentary petrographic provinces: an evaluation.
- Suttner, L. J., Basu, A., & Mack, G. H. (1981).** Climate and the origin of quartz arenites. *Journal of Sedimentary Research*, 51(4), 1235-1246.
- Switzer, A. D., & Pile, J. (2015).** Grain size analysis. *Handbook of sea-level research*, 331.
- Tawfik, H. A., Ghandour, I. M., Maejima, W., Armstrong-Altrin, J. S., & Abdel-Hameed, A. M. T. (2017).** Petrography and geochemistry of the siliciclastic Araba Formation (Cambrian), east Sinai, Egypt: implications for provenance, tectonic setting and source weathering. *Geological Magazine*, 154(1), 1-23.
- Taylor, B., & Hayes, D. E. (1983).** Origin and history of the South China Sea basin. *The Tectonic and Geologic Evolution of Southeast Asian Seas and Islands: Part 2*, 27, 23-56.
- Taylor, S. R., & McLennan, S. M. (1985).** The continental crust: its composition and evolution.

- Taylor, T. R., & Land, L. S. (1996).** Association of allochthonous waters and reservoir enhancement in deeply buried Miocene sandstones: Picaroon field, Corsair trend, offshore Texas.
- Taylor, T. R., Giles, M. R., Hathon, L. A., Diggs, T. N., Braunsdorf, N. R., Birbiglia, G. V., Kittridge, M. G., Macaulay, C. I., & Espejo, I. S. (2010).** Sandstone diagenesis and reservoir quality prediction: Models, myths, and reality. *AAPG bulletin*, 94(8), 1093-1132.
- Tiab, D., & Donaldson, E. C. (2016).** Porosity and permeability. *Petrophysics. Theory and Practice of Measuring Reservoir Rock and Fluid Transport Properties*. 4th ed. Elsevier, Amsterdam, 67-186.
- Tijani, M. N., Nton, M. E., & Kitagawa, R. (2010).** Textural and geochemical characteristics of the Ajali Sandstone, Anambra Basin, SE Nigeria: implication for its provenance. *Comptes Rendus Geoscience*, 342(2), 136-150.
- Togunwa, O. S., & Abdullah, W. H. (2017).** Geochemical characterization of Neogene sediments from onshore West Baram Delta Province, Sarawak: paleoenvironment, source input and thermal maturity. *Open Geosciences*, 9(1), 302-313.
- Totten, M. W., Hanan, M. A., & Weaver, B. L. (2000).** Beyond whole-rock geochemistry of shales: the importance of assessing mineralogic controls for revealing tectonic discriminants of multiple sediment sources for the Ouachita Mountain flysch deposits. *Geological Society of America Bulletin*, 112(7), 1012-1022.
- Trevena, A. S., & Nash, W. P. (1981).** An electron microprobe study of detrital feldspar. *Journal of Sedimentary Research*, 51(1), 137-150.
- Tucker, M. E. (Ed.). (2009).** *Sedimentary petrology: an introduction to the origin of sedimentary rocks*. John Wiley & Sons.
- Ulfa, Y., Sapari, N., & Harith, Z. Z. T. (2011).** Combined Tide and Storm Influence on Facies Sedimentation of Miocene Miri Formation, Sarawak. *Eksplorium*, 32(2), 77-90.
- Usman, M., Siddiqui, N. A., Mathew, M., Zhang, S., El-Ghali, M. A., Ramkumar, M., Jameel, M., & Zhang, Y. (2020).** Linking the influence of diagenetic properties and clay texture on reservoir quality in sandstones from NW Borneo. *Marine and Petroleum Geology*, 104509.
- van der Zee, W., & Urai, J. L. (2005).** Processes of normal fault evolution in a siliciclastic sequence: a case study from Miri, Sarawak, Malaysia. *Journal of Structural Geology*, 27(12), 2281-2300.
- Van Hattum, M. W. A., Hall, R., Pickard, A. L., & Nichols, G. J. (2013).** Provenance and geochronology of Cenozoic sandstones of northern Borneo. *Journal of Asian Earth Sciences*, 76, 266-282.
- Verma, S. P., & Armstrong-Altrin, J. S. (2013).** New multi-dimensional diagrams for tectonic discrimination of siliciclastic sediments and their application to Precambrian basins. *Chemical Geology*, 355, 117-133.
- Verma, S. P., & Armstrong-Altrin, J. S. (2016).** Geochemical discrimination of siliciclastic sediments from active and passive margin settings. *Sedimentary Geology*, 332, 1-12.
- Vos, K., Vandenberghe, N., & Elsen, J. (2014).** Surface textural analysis of quartz grains by scanning electron microscopy (SEM): From sample preparation to environmental interpretation. *Earth-Science Reviews*, 128, 93-104.
- Wannier, M., Lesslar, P., Lee, C., Raven, H., Sorkhabi, R., & Ibrahim, A. (2011).** Geological Excursions Around Miri, Sarawak. *EcoMedia Software*, p. 279.

- Wasel, S. O. (2012).** Microtextures of quartz grain surface from recent sedimentary environments along Al-khowkhah-Al-mokha coastal area, southern Red Sea, Yemen. *Journal of King Abdulaziz University: Marine Sciences*, 179(822), 1-30.
- Weltje, G. J. (2006).** Ternary sandstone composition and provenance: an evaluation of the 'Dickinson model'. Geological Society, London, Special Publications, 264(1), 79-99.
- Weltje, G. J., & von Eynatten, H. (2004).** Quantitative provenance analysis of sediments: review and outlook. *Sedimentary Geology*, 171(1-4), 1-11.
- Whalley, W. B., & Krinsley, D. H. (1974).** A scanning electron microscope study of surface textures of quartz grains from glacial environments. *Sedimentology*, 21(1), 87-105.
- Wilkinson, M. (1991).** The concretions of the Bearerraig Sandstone Formation: geometry and geochemistry. *Sedimentology*, 38(5), 899-912.
- Worden, R. H., Griffiths, J., Wooldridge, L. J., Utley, J. E. P., Lawan, A. Y., Muhammed, D. D., Simon, N., & Armitage, P. J. (2020).** Chlorite in sandstones. *Earth-Science Reviews*, 204, 103105.
- Worden, R.H. & Burley, S.D. (2003).** Sandstone diagenesis: the evolution of sand to stone. *Sandstone Diagenesis: Recent and Ancient*, 4, pp.3-44.
- Worden, R.H. & Morad, S. (2003).** Clay minerals in sandstones: controls on formation, distribution and evolution. *Clay mineral cements in sandstones*, pp.1-41.
- Xie, Y., & Chi, Y. (2016).** Geochemical investigation of dry-and wet-deposited dust during the same dust-storm event in Harbin, China: Constraint on provenance and implications for formation of aeolian loess. *Journal of Asian Earth Sciences*, 120, 43-61.
- Xinlu, H. U., Shuzhen, Y., Mouchun, H. E., Zhenju, D., & Bin, C. H. E. N. (2015).** Geochemistry, U-Pb geochronology and Sr-Nd-Hf isotopes of the Early Cretaceous volcanic rocks in the northern Da Hinggan Mountains. *Acta Geologica Sinica-English Edition*, 89(1), 203-216.
- Xiong, C., Chen, H., Niu, Y., Chen, A., Zhang, C., Li, F., Xu, S., & Yang, S. (2019).** Provenance, depositional setting, and crustal evolution of the Cathaysia Block, South China: Insights from detrital zircon U–Pb geochronology and geochemistry of clastic rocks. *Geological journal*, 54(2), 897-912.
- Yang, L., Wang, C., Bagas, L., Du, B., & Zhang, D. (2019).** Mesozoic–Cenozoic sedimentary rock records and applications for provenance of sediments and affiliation of the Simao Terrane, SW China. *International Geology Review*, 61(18), 2291-2312.
- Yarincik, K. M., Murray, R. W., & Peterson, L. C. (2000).** Climatically sensitive eolian and hemipelagic deposition in the Cariaco Basin, Venezuela, over the past 578,000 years: Results from Al/Ti and K/Al. *Paleoceanography*, 15(2), 210-228.
- Yu, Y., Lin, L., Zhai, C., Wang, Y., Li, Y., & Guo, Y. (2018).** Diagenesis and reservoir characteristics analysis of the Late Triassic Xujiahe Formation tight gas sandstone in the northern Sichuan Basin, China. *Energy Exploration & Exploitation*, 36(4), 743-763.
- Yuan, G., Cao, Y., Gluyas, J., Cao, X., & Zhang, W. (2018).** Petrography, fluid-inclusion, isotope, and trace-element constraints on the origin of quartz cementation and feldspar dissolution and the associated fluid evolution in arkosic sandstones. *AAPG Bulletin*, 102(5), 761-792.
- Yuan, G., Cao, Y., Schulz, H. M., Hao, F., Gluyas, J., Liu, K., Yang, T., Wang, Y., Xi, K., & Li, F. (2019).** A review of feldspar alteration and its geological significance in sedimentary basins: From shallow aquifers to deep hydrocarbon reservoirs. *Earth-science reviews*, 191, 114-140.



- Zaid, S. M. (2012).** Provenance, diagenesis, tectonic setting and geochemistry of Rudies sandstone (lower Miocene), Warda Field, Gulf of Suez, Egypt. *Journal of African Earth Sciences*, 66, 56-71
- Zaid, S. M. (2015).** Geochemistry of sandstones from the Pliocene Gabir Formation, north Marsa Alam, Red Sea, Egypt: implication for provenance, weathering and tectonic setting. *Journal of African Earth Sciences*, 102, 1-17.
- Zaid, S. M. (2017).** Petrography and geochemistry of the Middle Miocene Gebel El Rusas sandstones, Eastern Desert, Egypt: Implications for provenance and tectonic setting. *Journal of Earth System Science*, 126(7), 103.
- Zaid, S. M. (2020).** Petrography and geochemistry of the Lower Carboniferous Abu Durba sandstones, West Central Sinai, Egypt. *Arabian Journal of Geosciences*, 13(16), 1-18.
- Zaid, S. M., Elbadry, O., Ramadan, F., & Mohamed, M. (2015).** Petrography and geochemistry of Pharaonic sandstone monuments in Tall San Al Hagr, Al Sharqiya Governorate, Egypt: implications for provenance and tectonic setting. *Turkish Journal of Earth Sciences*, 24(4), 344-364.
- Zhang, M., Yu, Y., Choi, J., Cai, K., & Shi, M. (2020).** Petrography and geochemistry of clastic sedimentary rocks as evidence for the provenance of the Jurassic stratum in the Daqingshan area. *Open Geosciences*, 12(1), 1350-1368.
- Zhao, M. Y., & Zheng, Y. F. (2015).** The intensity of chemical weathering: Geochemical constraints from marine detrital sediments of Triassic age in South China. *Chemical geology*, 391, 111-122.
- Zhiming, L., Jiajun, L., Ruizhong, H., Mingqin, H., Yuping, L., & Chaoyang, L. (2003).** Tectonic setting and nature of the provenance of sedimentary rocks in Lanping Mesozoic-Cenozoic Basin: Evidence from geochemistry of sandstones. *Chinese Journal of Geochemistry*, 22(4), 352-360.
- Zou, C., Zhu, R., Tao, S., Hou, L., Yuan, X., Zhang, G., Song, Y., Niu, Dong, J., D., Wu, X., Liu, S., Jiang, L., Wang, S., Guo, Q., Yang, Z., Zhang, Y., Zhou, C., Bai. B. (2017).** *Unconventional Petroleum Geology* (2<sup>nd</sup> ed.). pp.3-48. Elsevier, Amsterdam, Netherlands. <https://doi.org/10.1016/B978-0-12-812234-1.01001-3>
- Zuo, X., Li, C., Zhang, J., Ma, G., & Chen, P. (2020).** Geochemical characteristics and depositional environment of the Shahejie Formation in the Binnan Oilfield, China. *Journal of Geophysics and Engineering*, 17(3), 539-551.

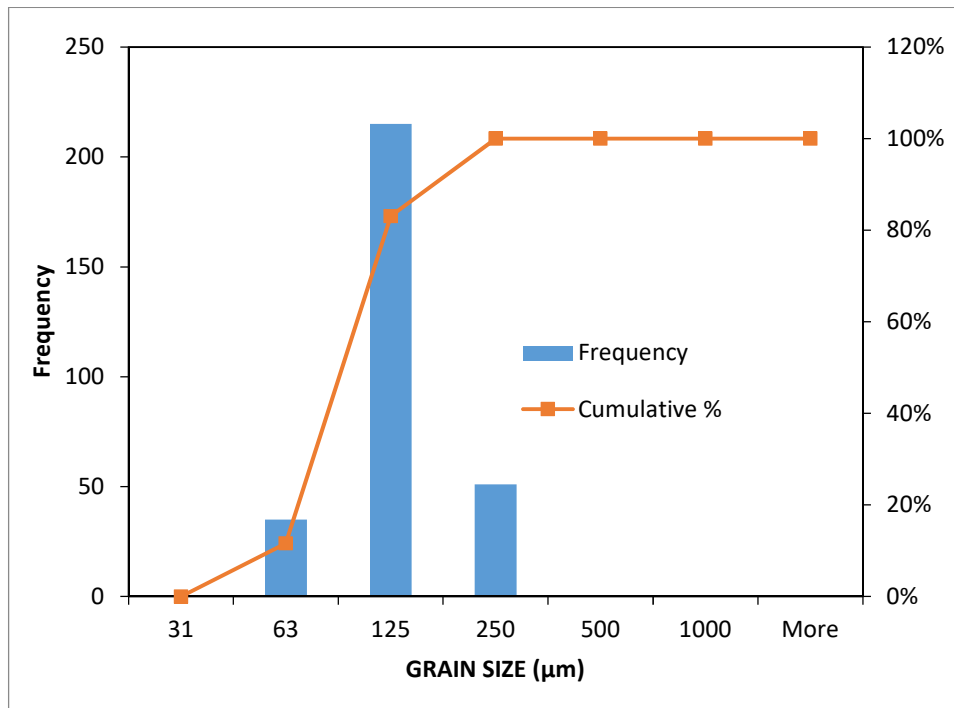
*“Every reasonable effort has been made to acknowledge the owners of copyright material. I would be pleased to hear from any copyright owner who has been omitted or incorrectly acknowledged.”*

# Appendix 1.0

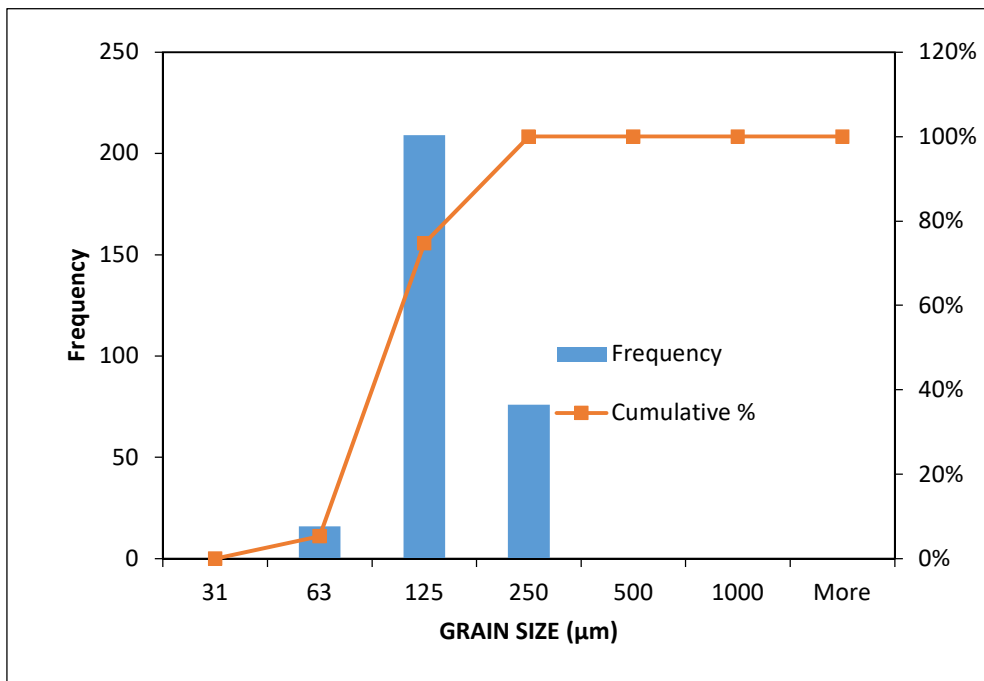
## Grain size analysis

Tanjung Lobang

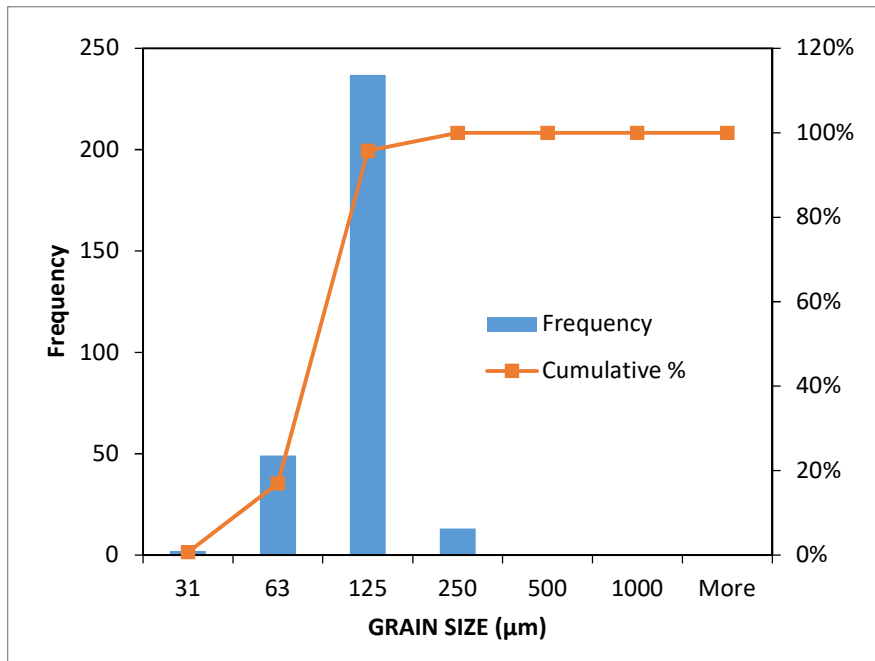
Sample Number T1 B		
GRAIN SIZE ( $\mu\text{m}$ )	Frequency	Cumulative %
31	0	0.00%
63	35	11.63%
125	215	83.06%
250	51	100.00%
500	0	100.00%
1000	0	100.00%



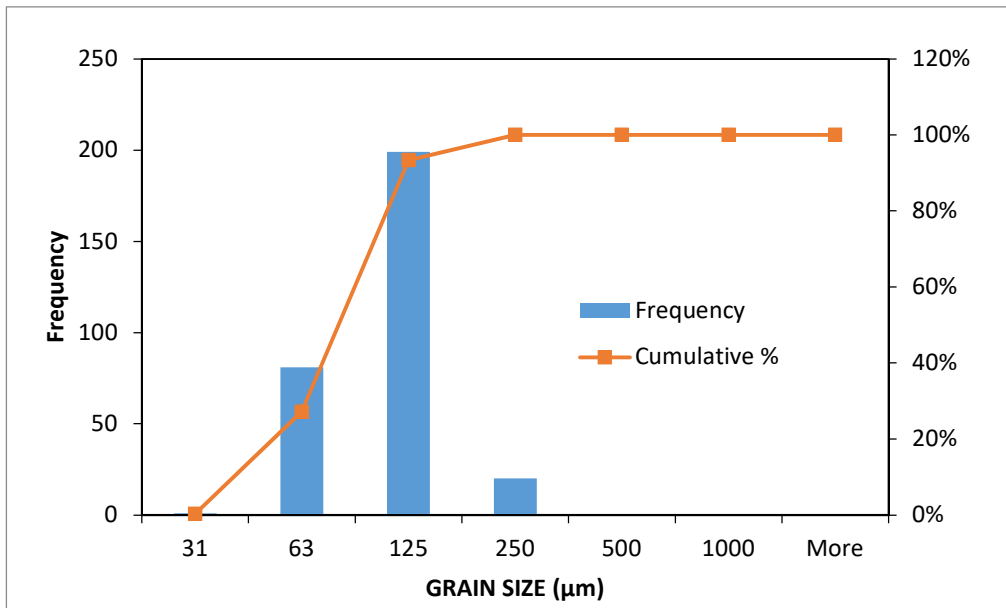
Sample Number: T1 T		
GRAIN SIZE ( $\mu\text{m}$ )	Frequency	Cumulative %
31	0	0.00%
63	16	5.32%
125	209	74.75%
250	76	100.00%
500	0	100.00%
1000	0	100.00%



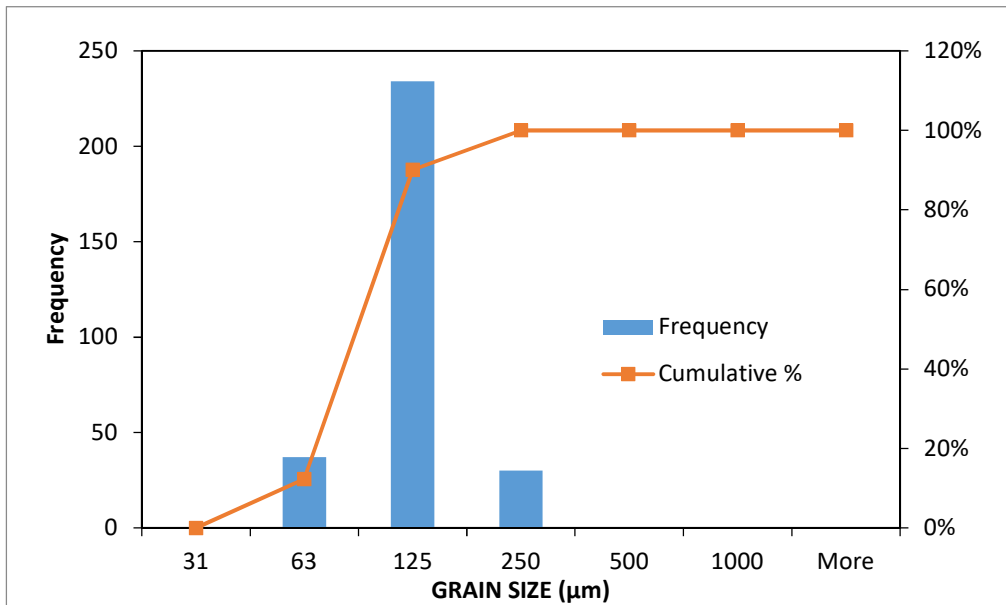
Sample Number: T2 B		
Grain Size ( $\mu\text{m}$ )	Frequency	Cumulative %
31	2	0.66%
63	49	16.94%
125	237	95.68%
250	13	100.00%
500	0	100.00%
1000	0	100.00%



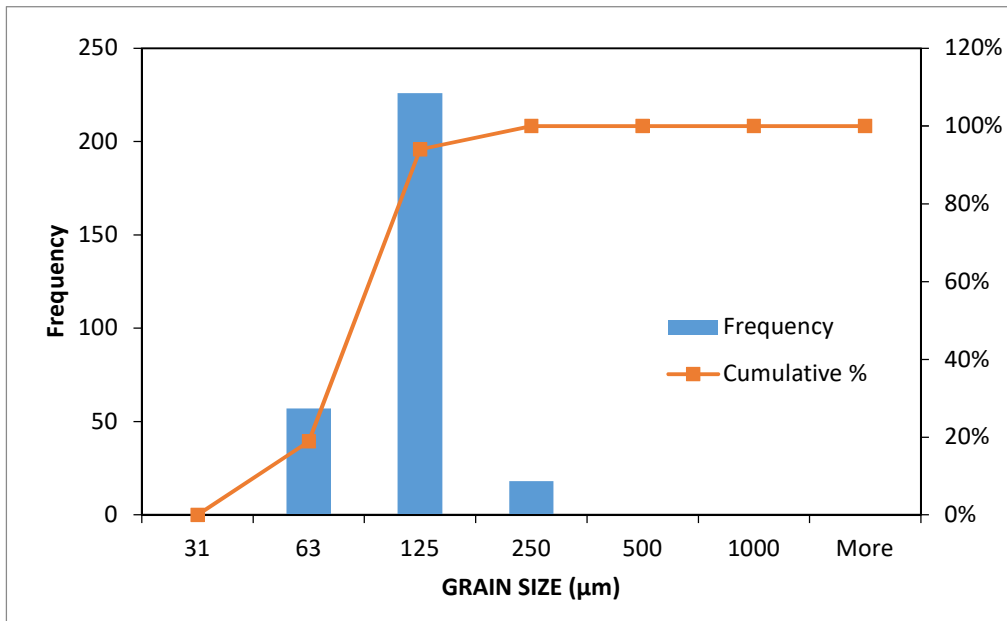
Sample Number T2 T		
GRAIN SIZE ( $\mu\text{m}$ )	Frequency	Cumulative %
31	1	0.33%
63	81	27.24%
125	199	93.36%
250	20	100.00%
500	0	100.00%
1000	0	100.00%



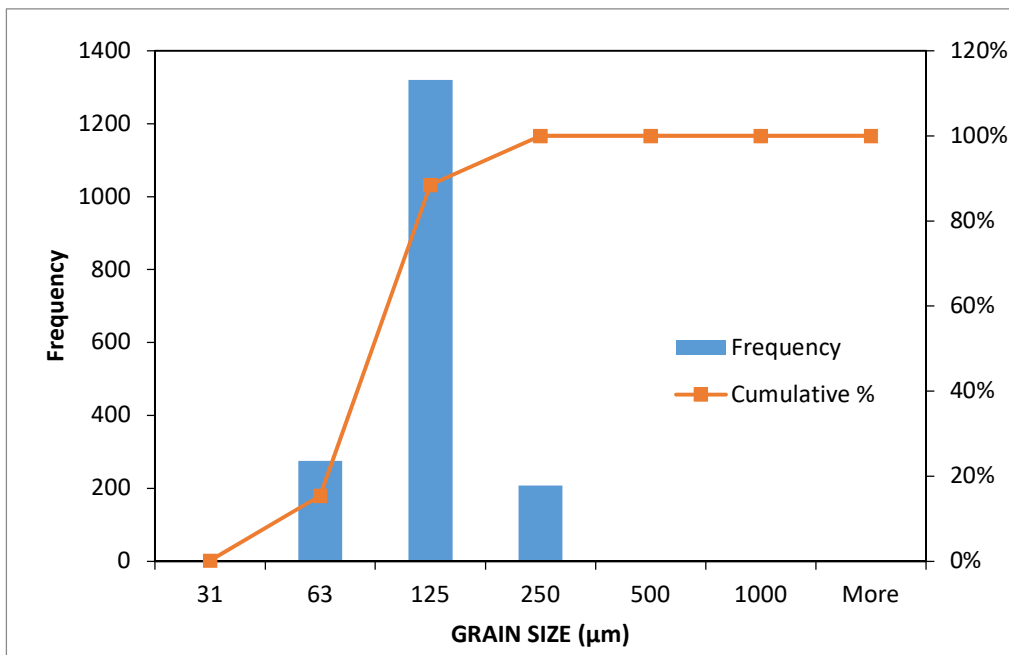
Sample Number T3 B		
GRAIN SIZE ( $\mu\text{m}$ )	Frequency	Cumulative %
31	0	0.00%
63	37	12.29%
125	234	90.03%
250	30	100.00%
500	0	100.00%
1000	0	100.00%



Sample Number T3 T		
GRAIN SIZE ( $\mu\text{m}$ )	Frequency	Cumulative %
31	0	0.00%
63	57	18.94%
125	226	94.02%
250	18	100.00%
500	0	100.00%
1000	0	100.00%



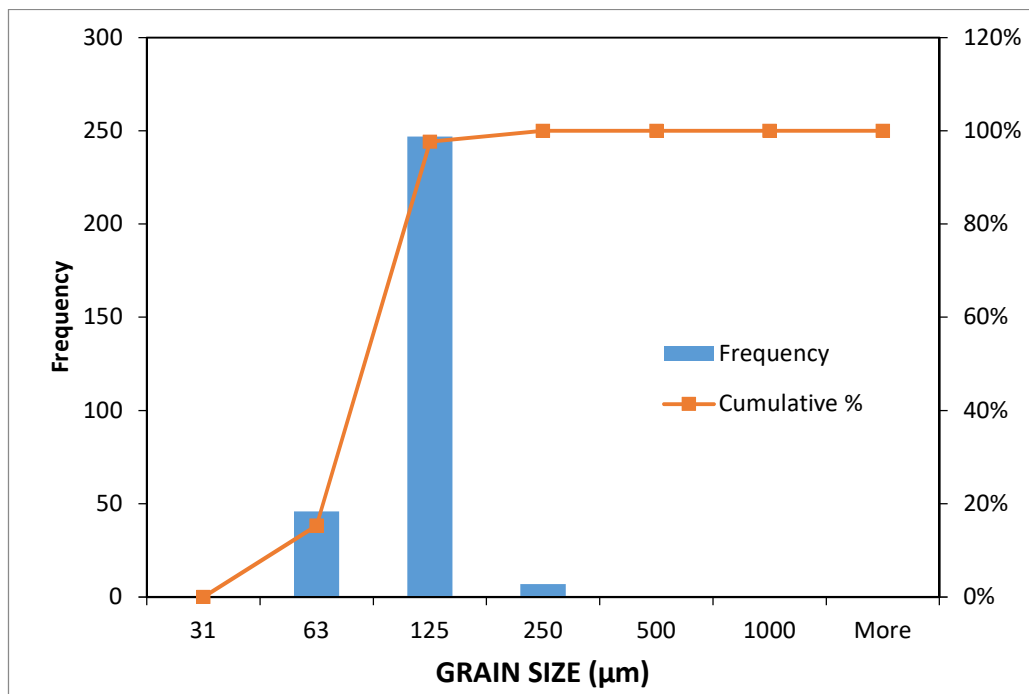
All studied samples of Tanjung Lobang outcrop		
GRAIN SIZE ( $\mu\text{m}$ )	Frequency	Cumulative %
31	3	0.17%
63	275	15.39%
125	1320	88.48%
250	208	100.00%
500	0	100.00%
1000	0	100.00%



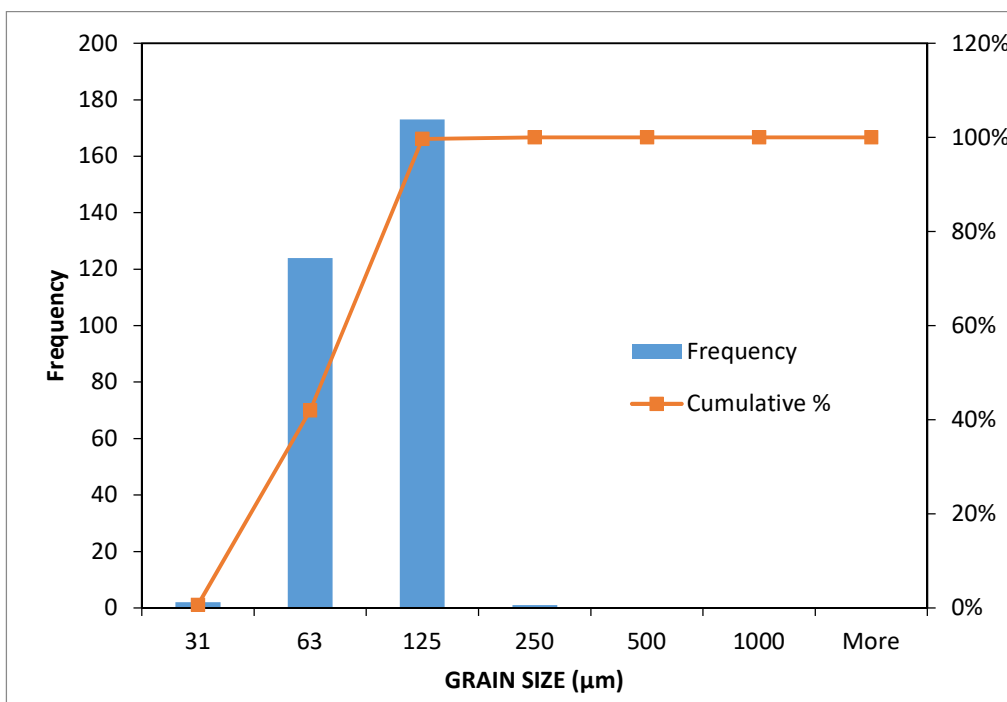


**Bomba outcrop**

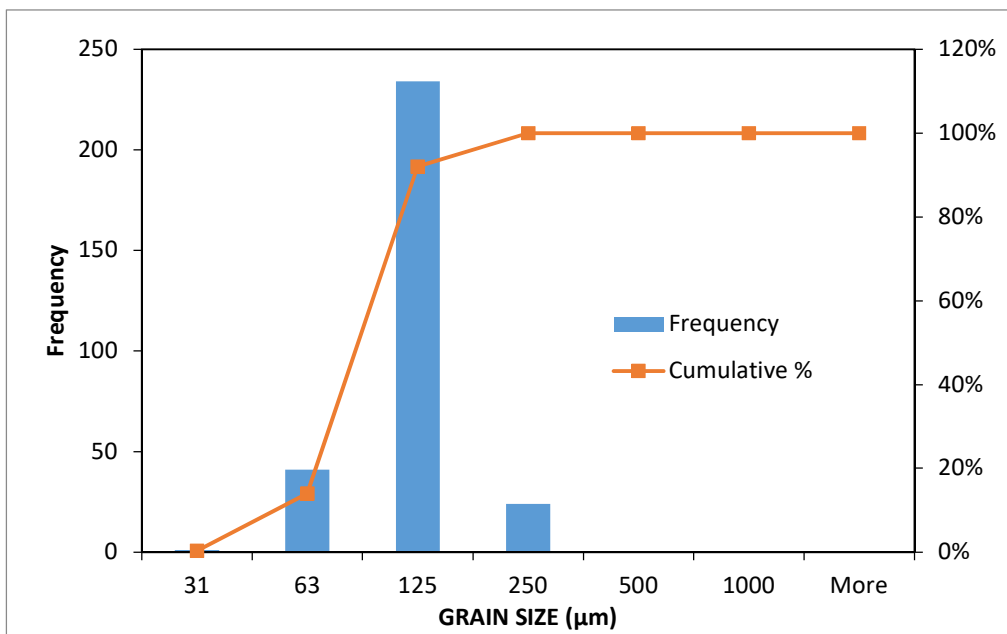
Sample Number B2 B		
GRAIN SIZE ( $\mu\text{m}$ )	Frequency	Cumulative %
31	0	0.00%
63	46	15.33%
125	247	97.67%
250	7	100.00%
500	0	100.00%
1000	0	100.00%



Sample Number B2 T		
GRAIN SIZE ( $\mu\text{m}$ )	Frequency	Cumulative %
31	2	0.67%
63	124	42.00%
125	173	99.67%
250	1	100.00%
500	0	100.00%
1000	0	100.00%

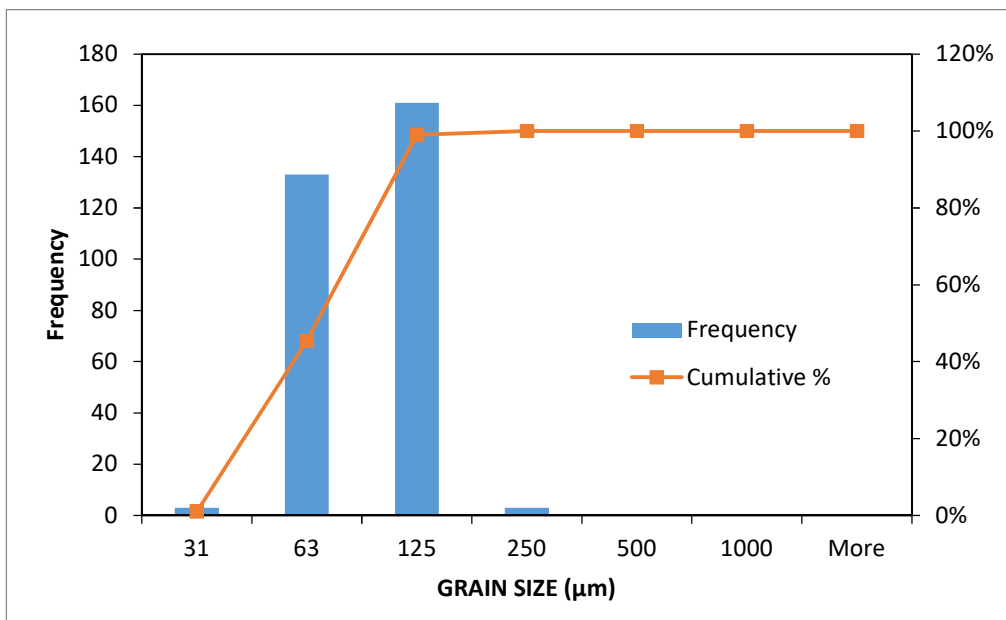


Sample Number B4c T		
GRAIN SIZE ( $\mu\text{m}$ )	Frequency	Cumulative %
31	1	0.33%
63	41	14.00%
125	234	92.00%
250	24	100.00%
500	0	100.00%
1000	0	100.00%

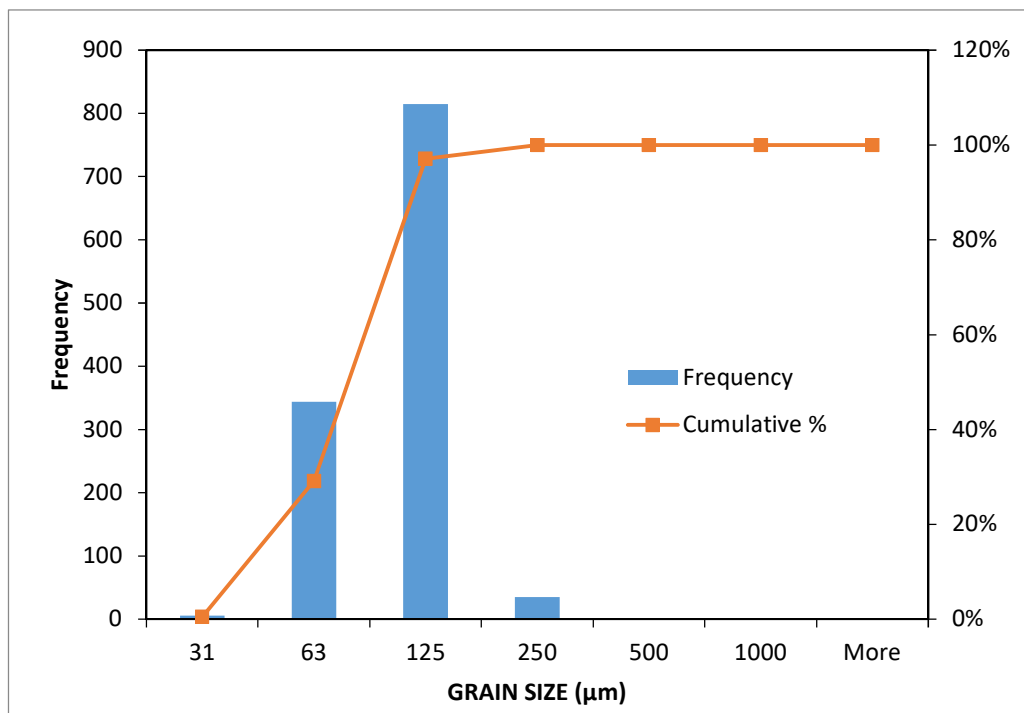


\

Sample Number B4D T		
GRAIN SIZE ( $\mu\text{m}$ )	Frequency	Cumulative %
31	3	1.00%
63	133	45.33%
125	161	99.00%
250	3	100.00%
500	0	100.00%
1000	0	100.00%

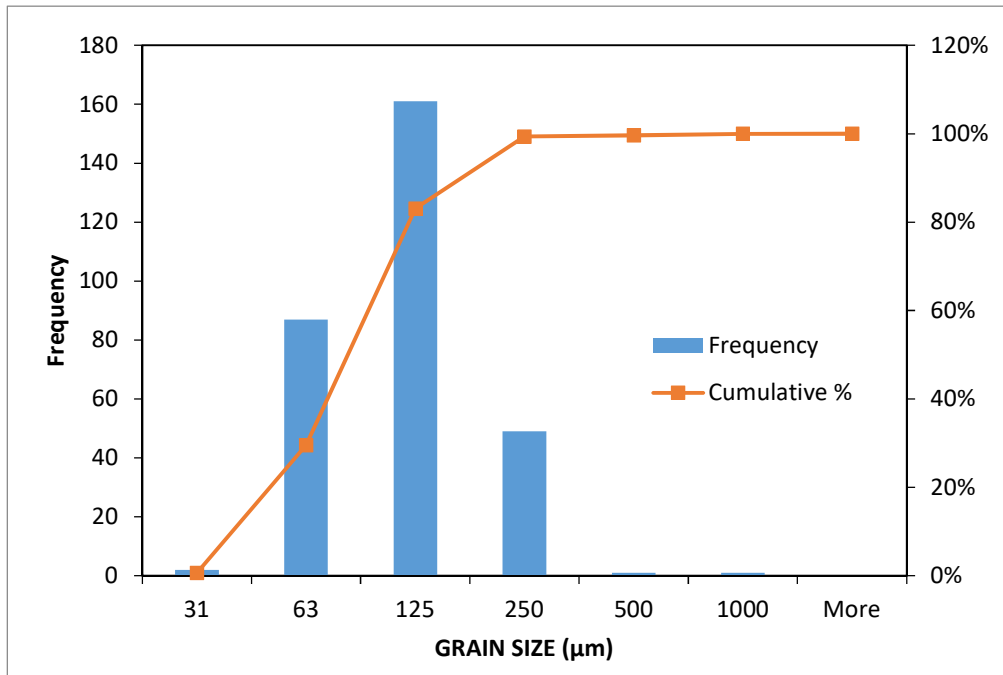


All studied samples of bomba outcrop		
GRAIN SIZE ( $\mu\text{m}$ )	Frequency	Cumulative %
31	6	0.50%
63	344	29.17%
125	815	97.08%
250	35	100.00%
500	0	100.00%
1000	0	100.00%

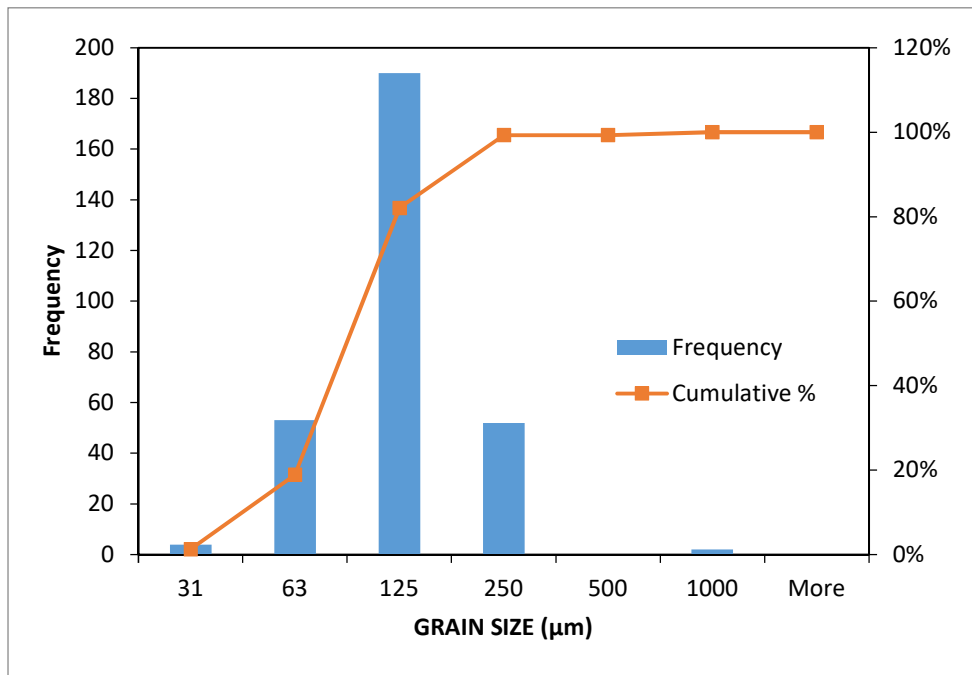


## Hospital Outcrop

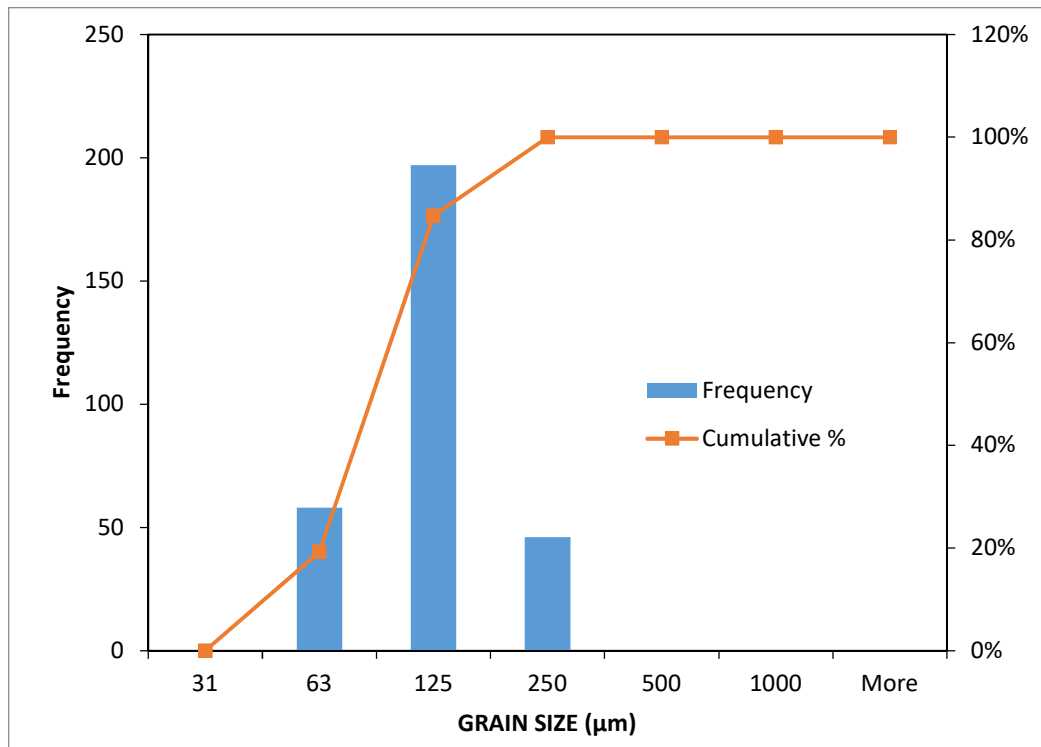
Sample Number HO1 T		
GRAIN SIZE ( $\mu\text{m}$ )	Frequency	Cumulative %
31	2	0.66%
63	87	29.57%
125	161	83.06%
250	49	99.34%
500	1	99.67%
1000	1	100.00%



Sample Number HO2 B		
GRAIN SIZE ( $\mu\text{m}$ )	Frequency	Cumulative %
31	4	1.33%
63	53	18.94%
125	190	82.06%
250	52	99.34%
500	0	99.34%
1000	2	100.00%

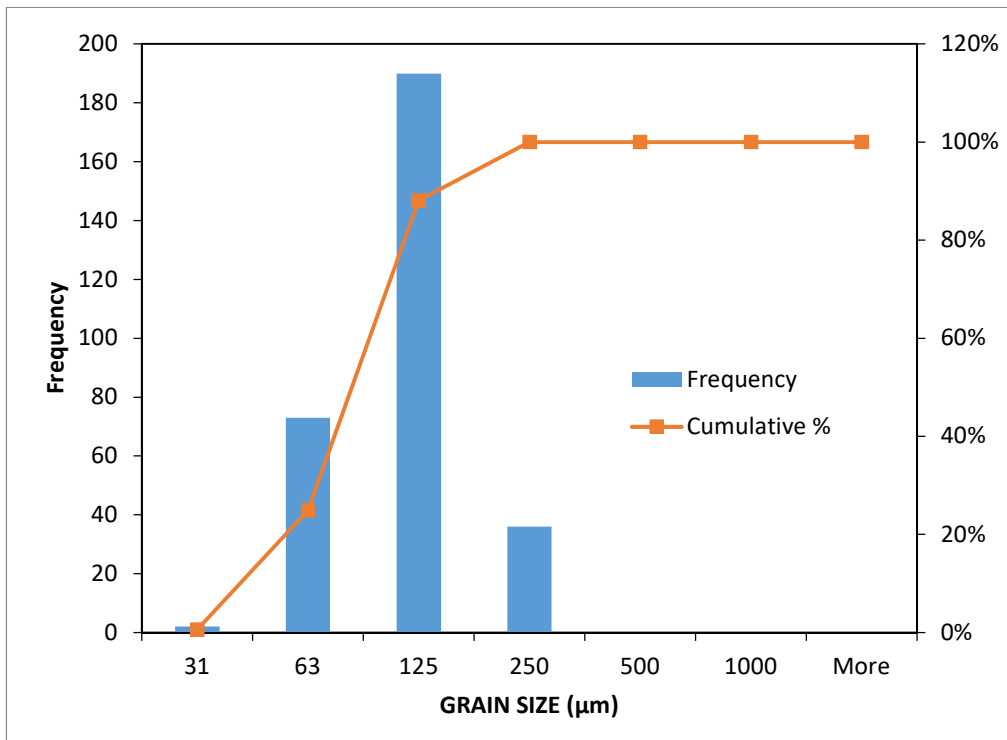


Sample Number HO3 M		
GRAIN SIZE ( $\mu\text{m}$ )	Frequency	Cumulative %
31	0	0.00%
63	58	19.27%
125	197	84.72%
250	46	100.00%
500	0	100.00%
1000	0	100.00%

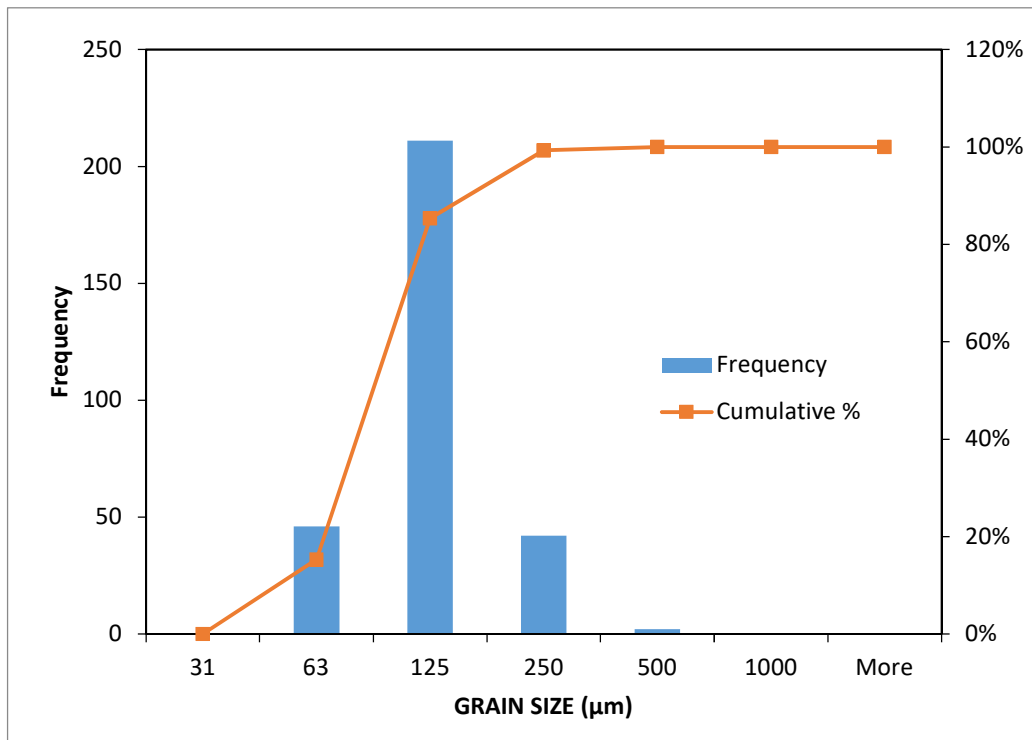




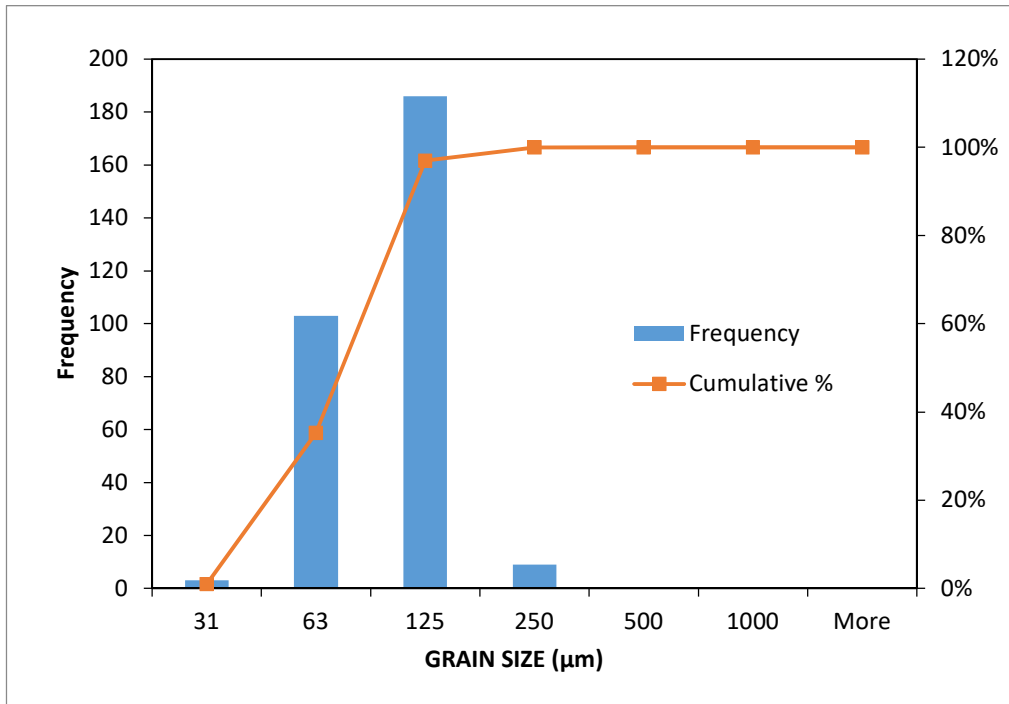
Sample Number HO4 T		
GRAIN SIZE ( $\mu\text{m}$ )	Frequency	Cumulative %
31	2	0.66%
63	73	24.92%
125	190	88.04%
250	36	100.00%
500	0	100.00%
1000	0	100.00%



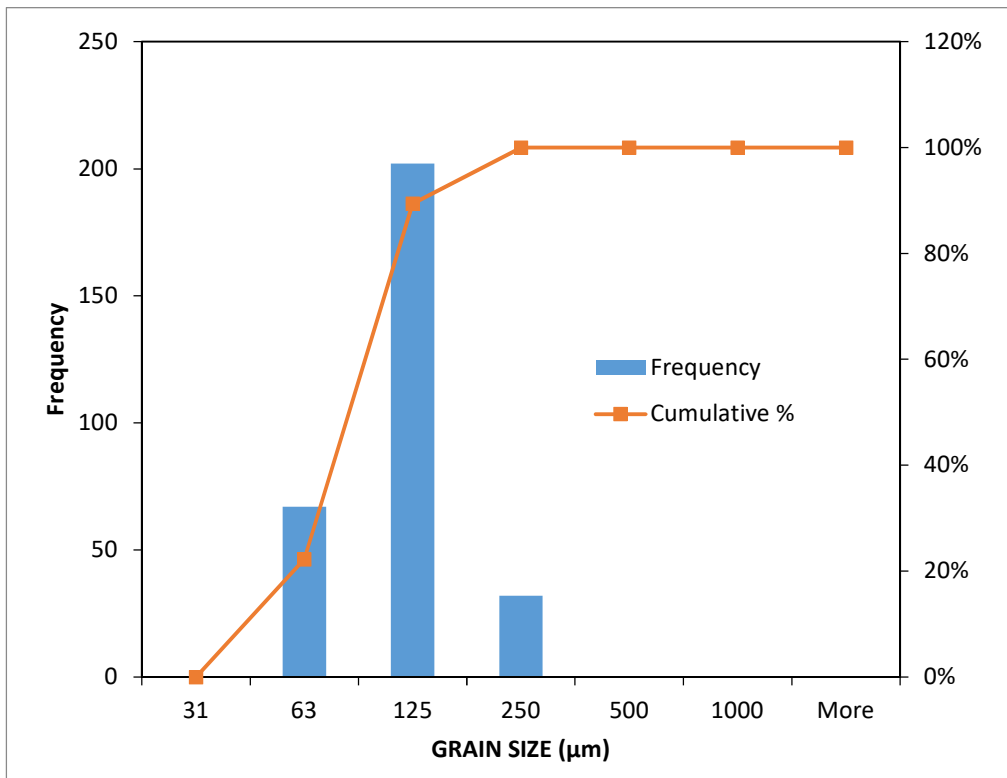
Sample Number HO5 B		
GRAIN SIZE ( $\mu\text{m}$ )	Frequency	Cumulative %
31	0	0.00%
63	46	15.28%
125	211	85.38%
250	42	99.34%
500	2	100.00%
1000	0	100.00%



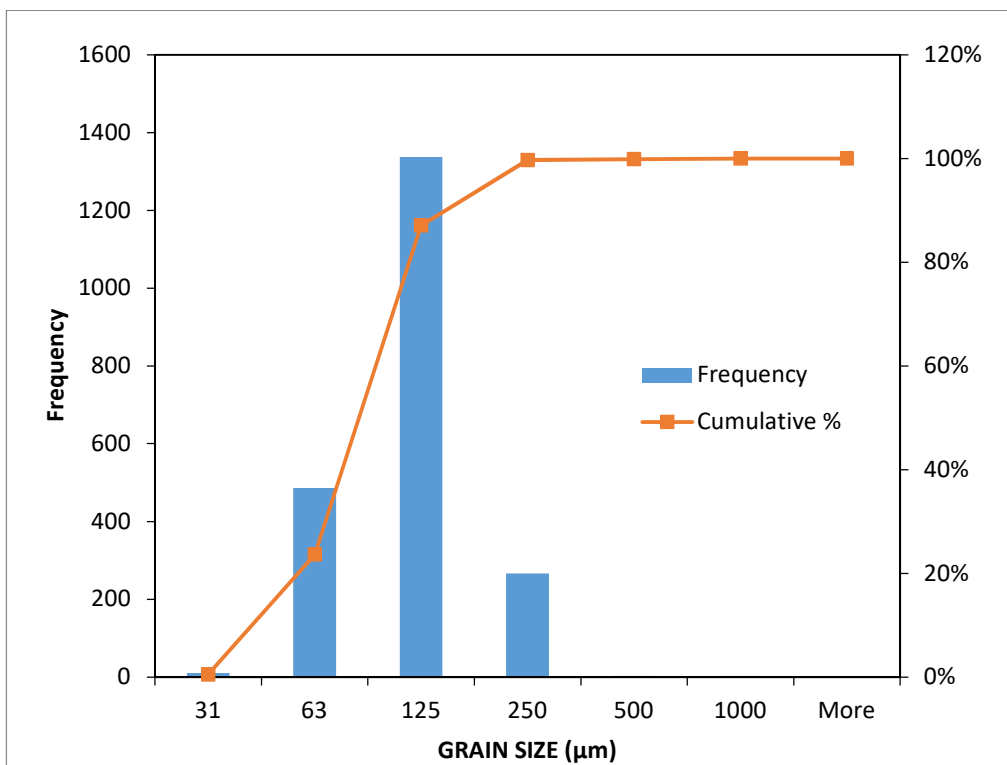
Sample Number HO6f		
GRAIN SIZE ( $\mu\text{m}$ )	Frequency	Cumulative %
31	3	1.00%
63	103	35.22%
125	186	97.01%
250	9	100.00%
500	0	100.00%
1000	0	100.00%



Sample Number HO6h		
GRAIN SIZE ( $\mu\text{m}$ )	Frequency	Cumulative %
31	0	0.00%
63	67	22.26%
125	202	89.37%
250	32	100.00%
500	0	100.00%
1000	0	100.00%

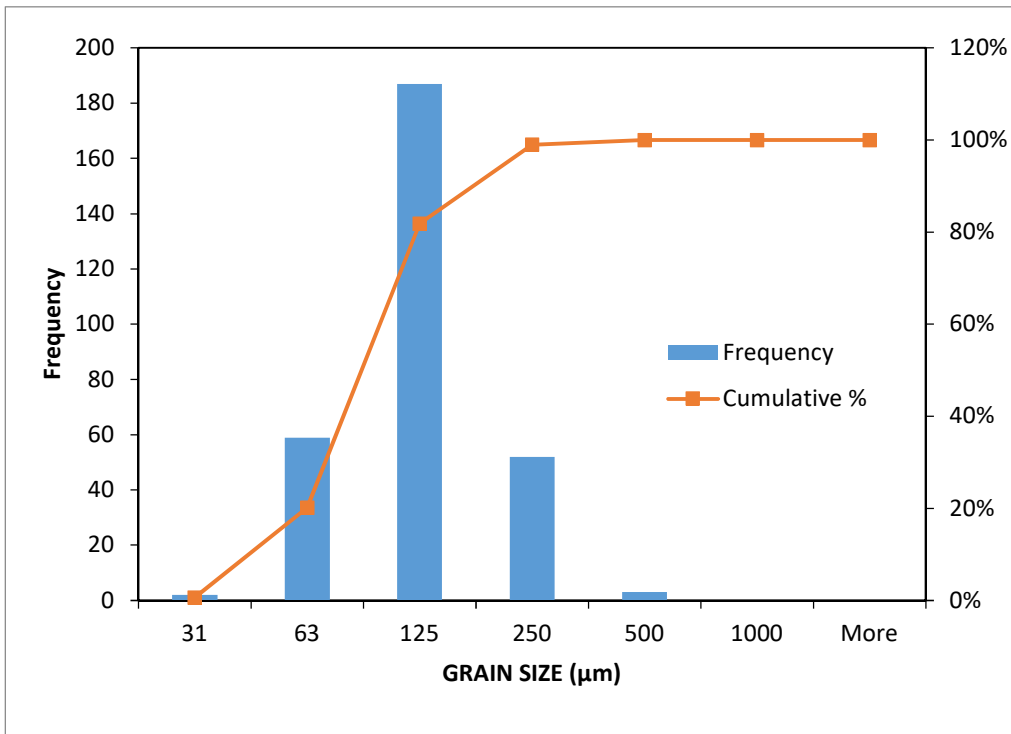


<b>All studied samples of Hospital outcrop</b>		
<b>GRAIN SIZE (<math>\mu\text{m}</math>)</b>	<b>Frequency</b>	<b>Cumulative %</b>
31	11	0.52%
63	487	23.64%
125	1337	87.09%
250	266	99.72%
500	3	99.86%
1000	3	100.00%

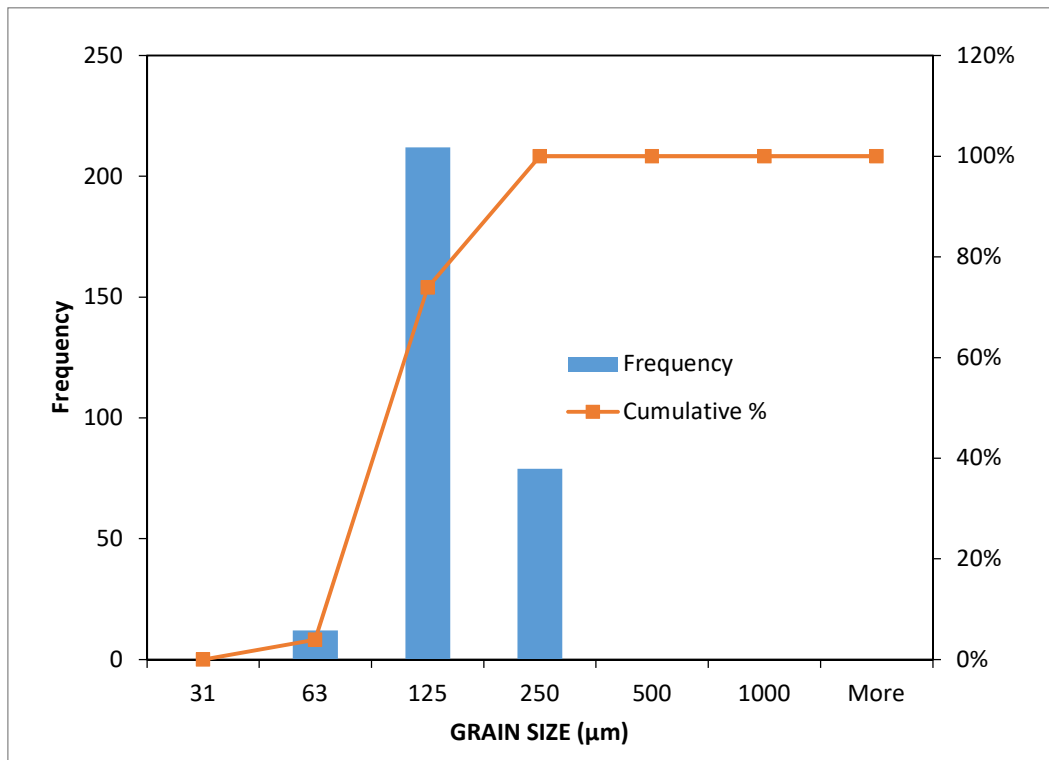


## Taman Awam outcrop

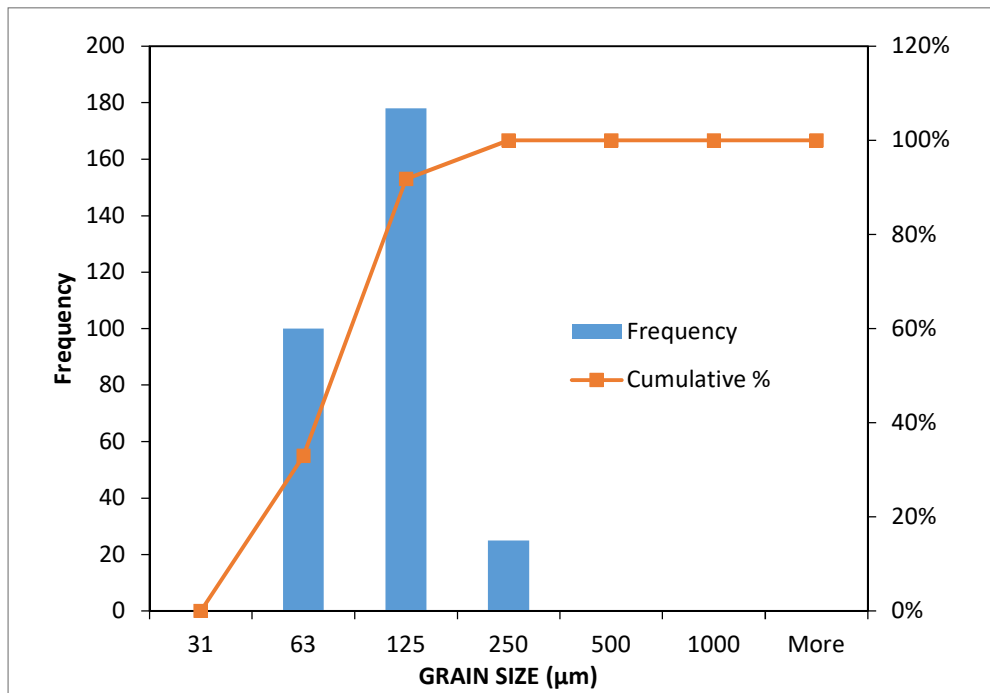
Sample Number S1 T		
GRAIN SIZE ( $\mu\text{m}$ )	Frequency	Cumulative %
31	2	0.66%
63	59	20.13%
125	187	81.85%
250	52	99.01%
500	3	100.00%
1000	0	100.00%



Sample Number S3		
GRAIN SIZE ( $\mu\text{m}$ )	Frequency	Cumulative %
31	0	0.00%
63	12	3.96%
125	212	73.93%
250	79	100.00%
500	0	100.00%
1000	0	100.00%

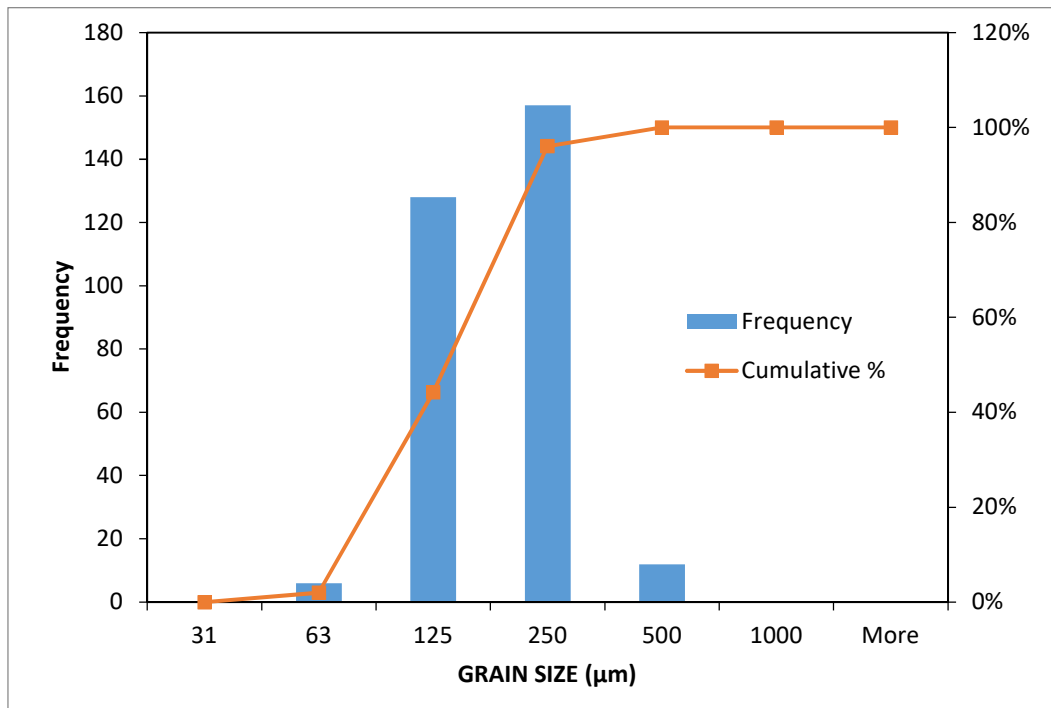


Sample Number S8		
GRAIN SIZE ( $\mu\text{m}$ )	Frequency	Cumulative %
31	0	0.00%
63	100	33.00%
125	178	91.75%
250	25	100.00%
500	0	100.00%
1000	0	100.00%

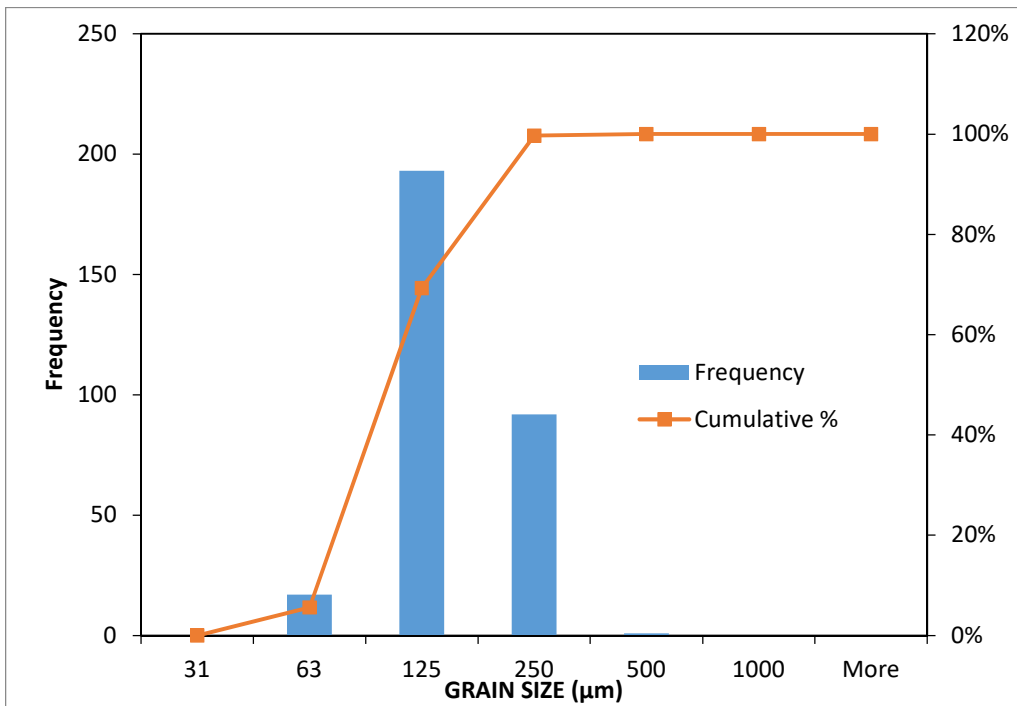




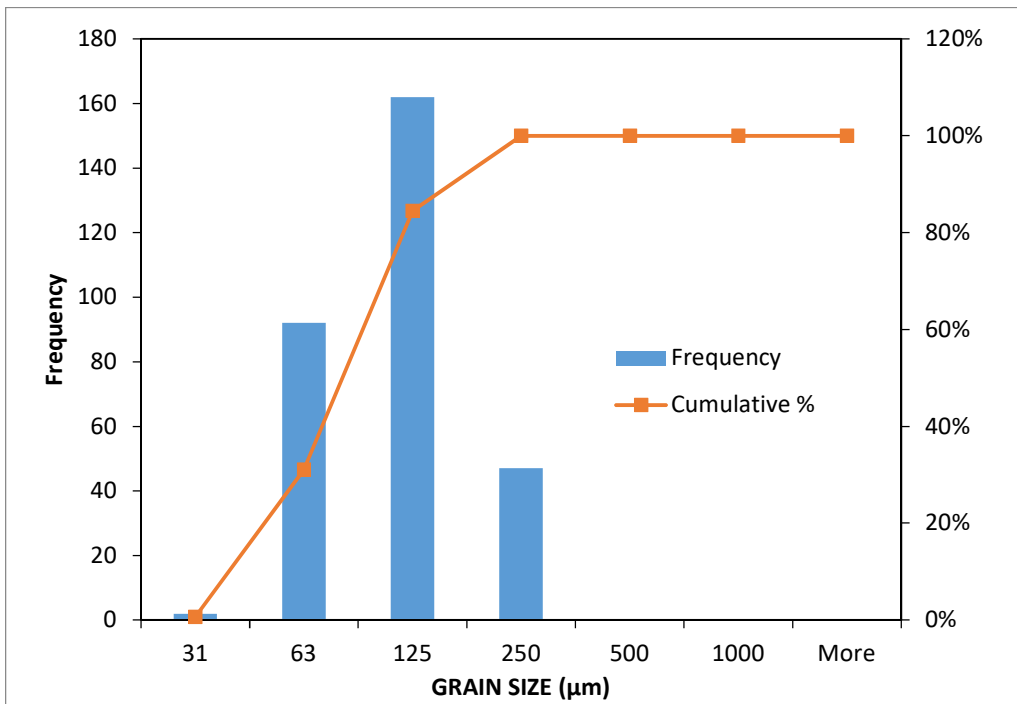
Sample Number S10 B		
GRAIN SIZE ( $\mu\text{m}$ )	Frequency	Cumulative %
31	0	0.00%
63	6	1.98%
125	128	44.22%
250	157	96.04%
500	12	100.00%
1000	0	100.00%



Sample Number S13		
GRAIN SIZE ( $\mu\text{m}$ )	Frequency	Cumulative %
31	0	0.00%
63	17	5.61%
125	193	69.31%
250	92	99.67%
500	1	100.00%
1000	0	100.00%

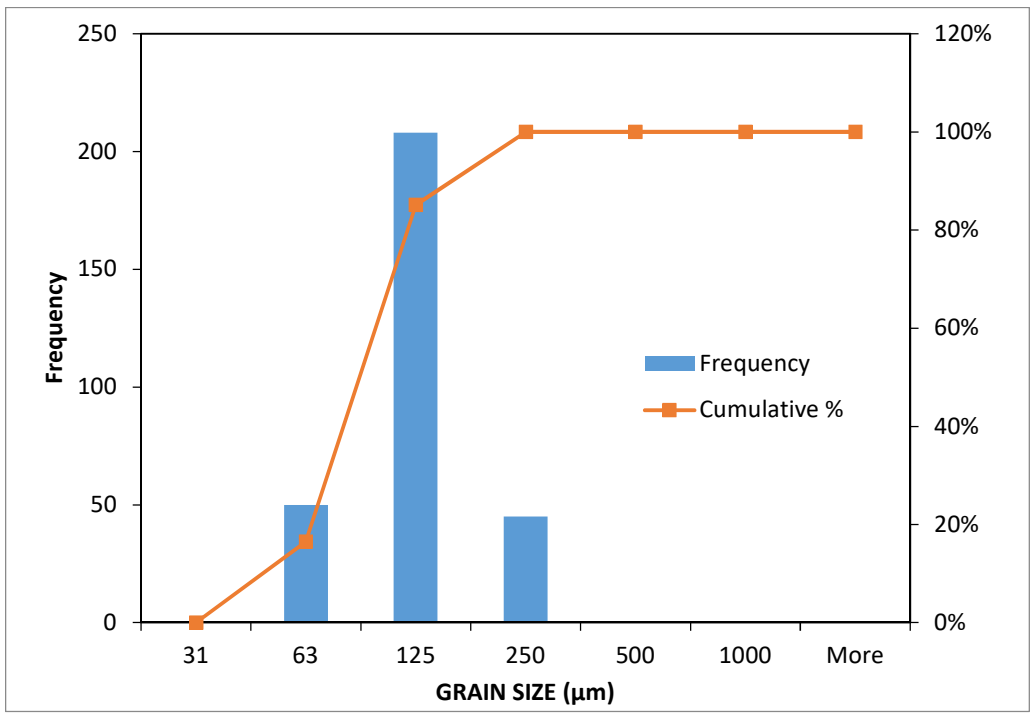


Sample Number S14 T		
GRAIN SIZE ( $\mu\text{m}$ )	Frequency	Cumulative %
31	2	0.66%
63	92	31.02%
125	162	84.49%
250	47	100.00%
500	0	100.00%
1000	0	100.00%

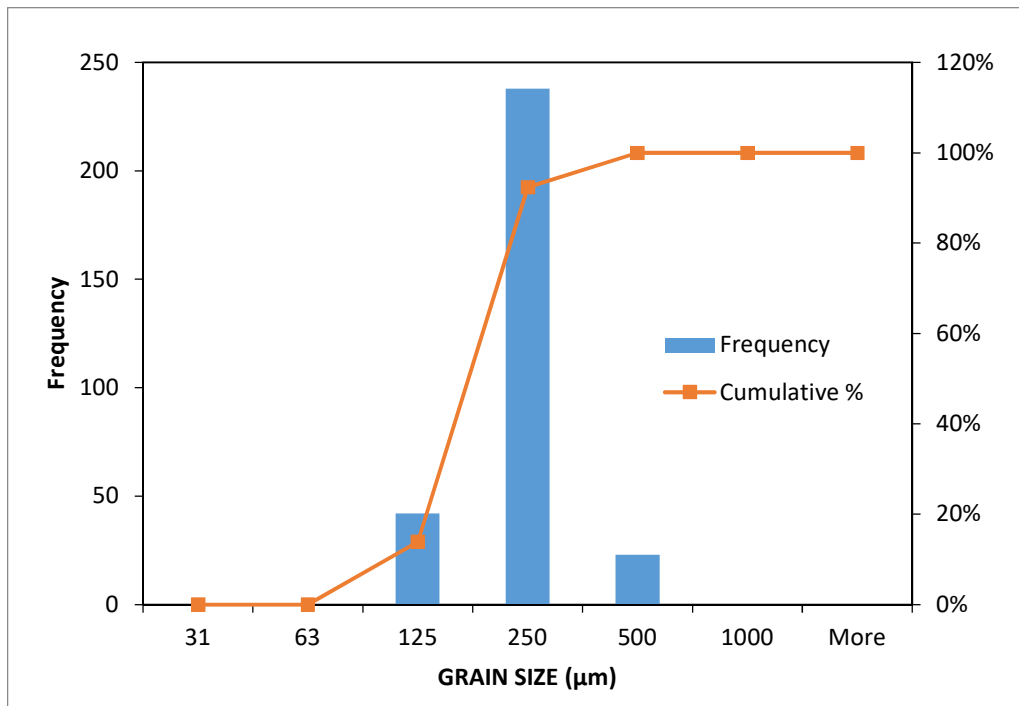


\

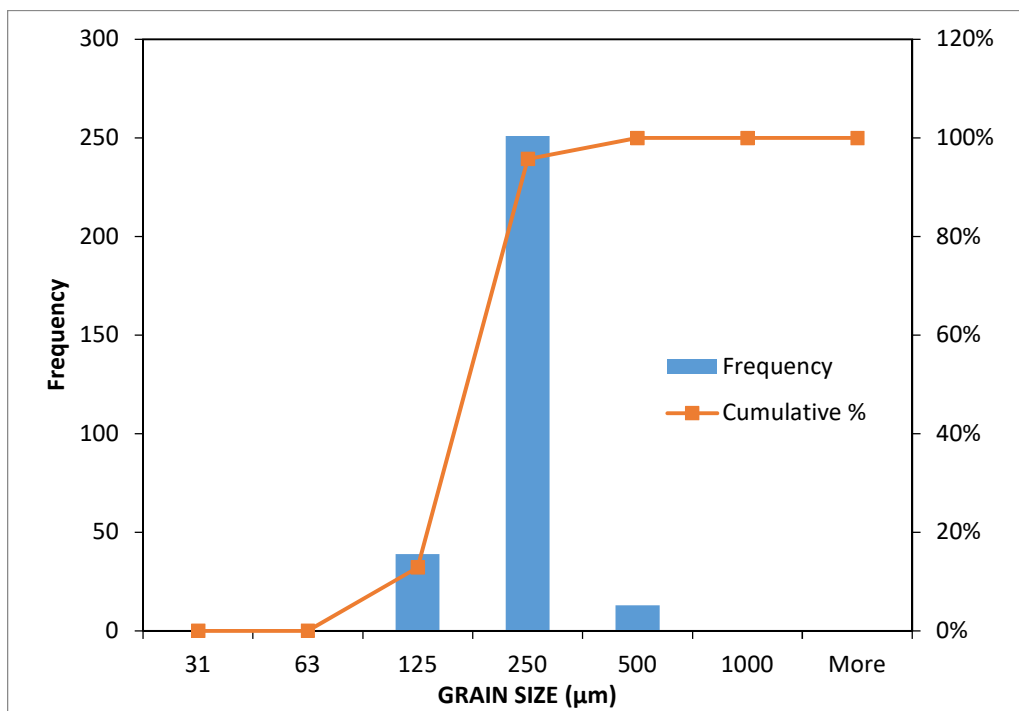
Sample Number S20		
GRAIN SIZE ( $\mu\text{m}$ )	Frequency	Cumulative %
31	0	0.00%
63	50	16.50%
125	208	85.15%
250	45	100.00%
500	0	100.00%
1000	0	100.00%



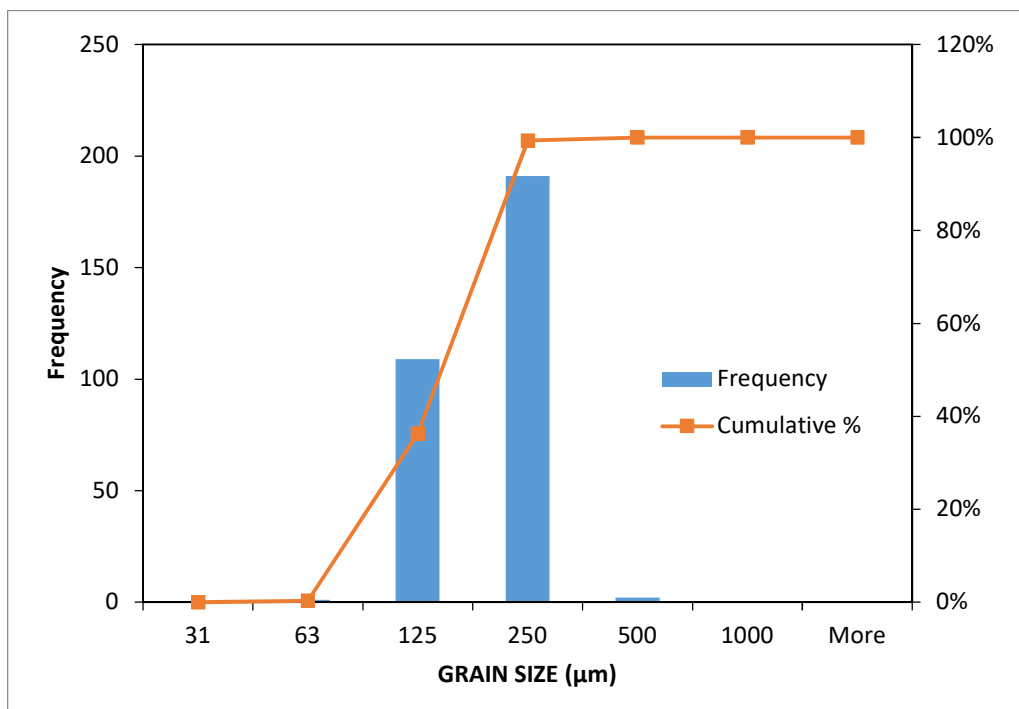
Sample Number S22 B		
GRAIN SIZE ( $\mu\text{m}$ )	Frequency	Cumulative %
31	0	0.00%
63	0	0.00%
125	42	13.86%
250	238	92.41%
500	23	100.00%
1000	0	100.00%



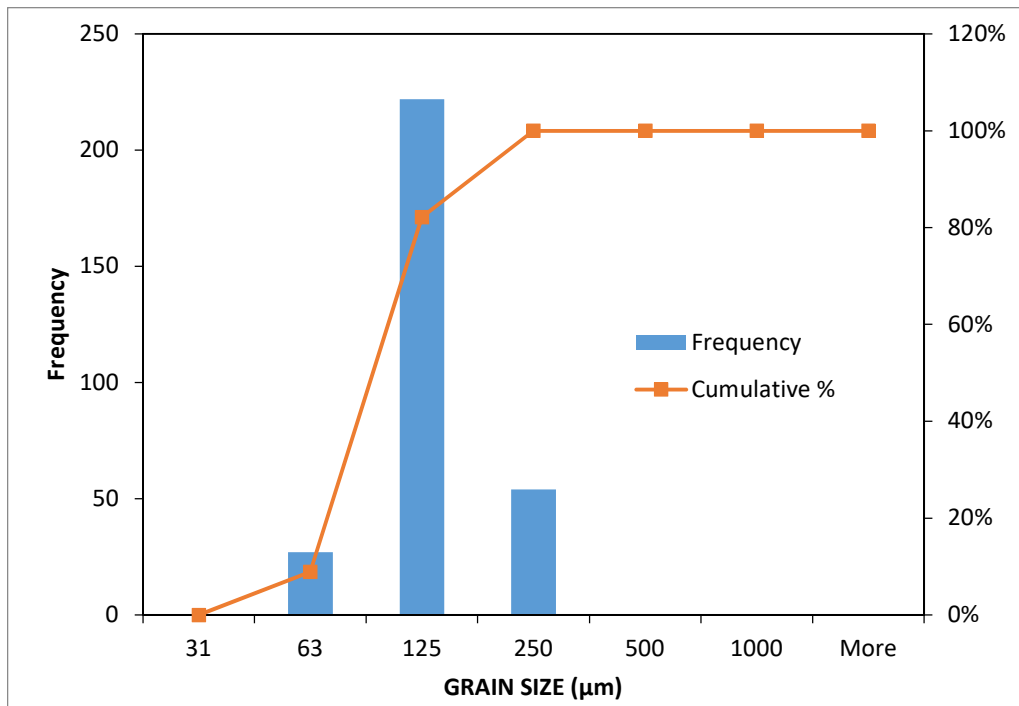
Sample Number S24		
GRAIN SIZE ( $\mu\text{m}$ )	Frequency	Cumulative %
31	0	0.00%
63	0	0.00%
125	39	12.87%
250	251	95.71%
500	13	100.00%
1000	0	100.00%



Sample Number S26 B		
GRAIN SIZE ( $\mu\text{m}$ )	Frequency	Cumulative %
31	0	0.00%
63	1	0.33%
125	109	36.30%
250	191	99.34%
500	2	100.00%
1000	0	100.00%

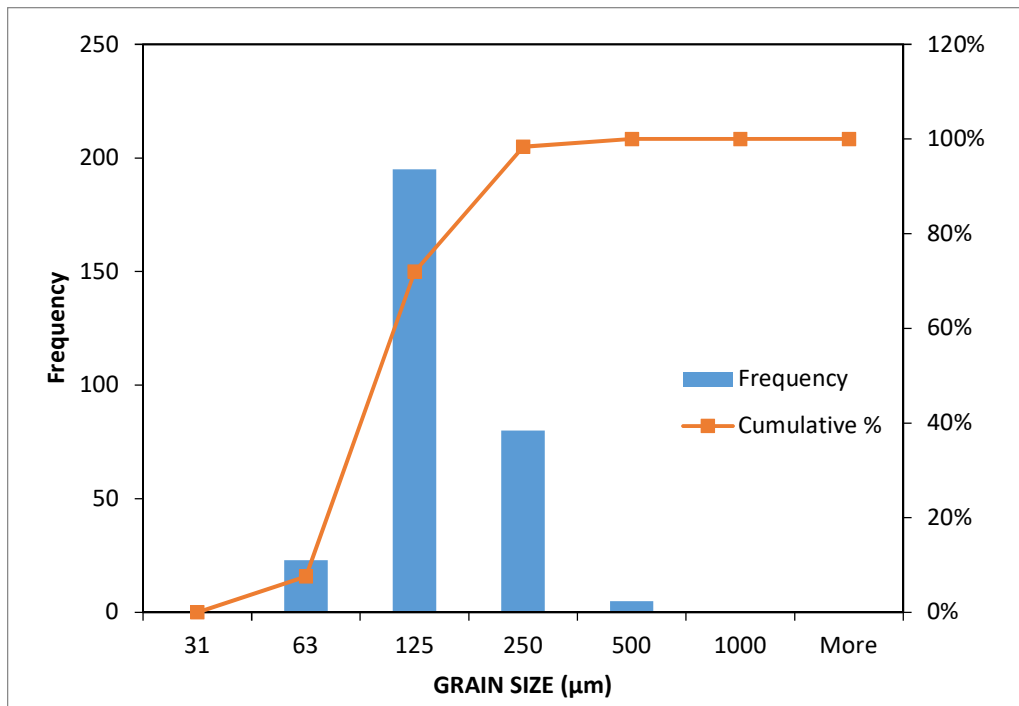


<b>Sample Number S229 B</b>		
<i>GRAIN SIZE</i> ( $\mu\text{m}$ )	<i>Frequency</i>	<i>Cumulative</i> %
31	0	0.00%
63	27	8.91%
125	222	82.18%
250	54	100.00%
500	0	100.00%
1000	0	100.00%

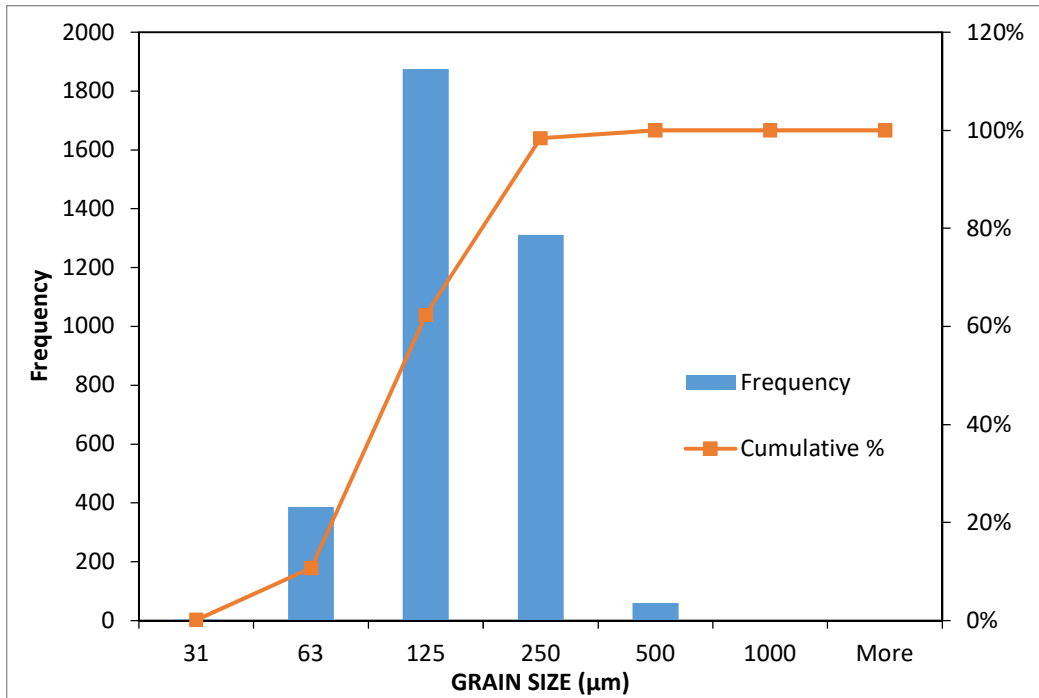




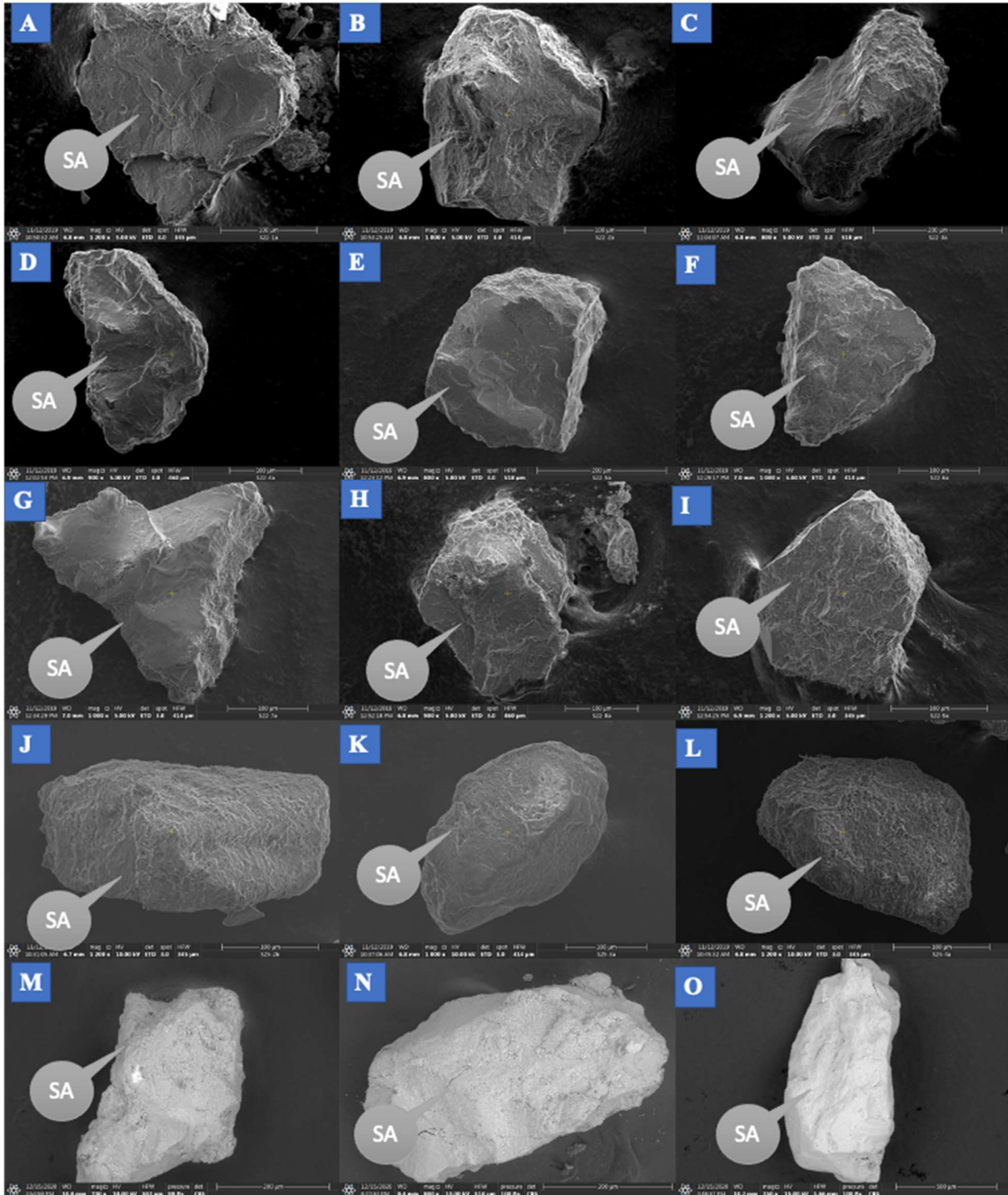
Sample Number S32 T		
GRAIN SIZE ( $\mu\text{m}$ )	Frequency	Cumulative %
31	0	0.00%
63	23	7.59%
125	195	71.95%
250	80	98.35%
500	5	100.00%
1000	0	100.00%



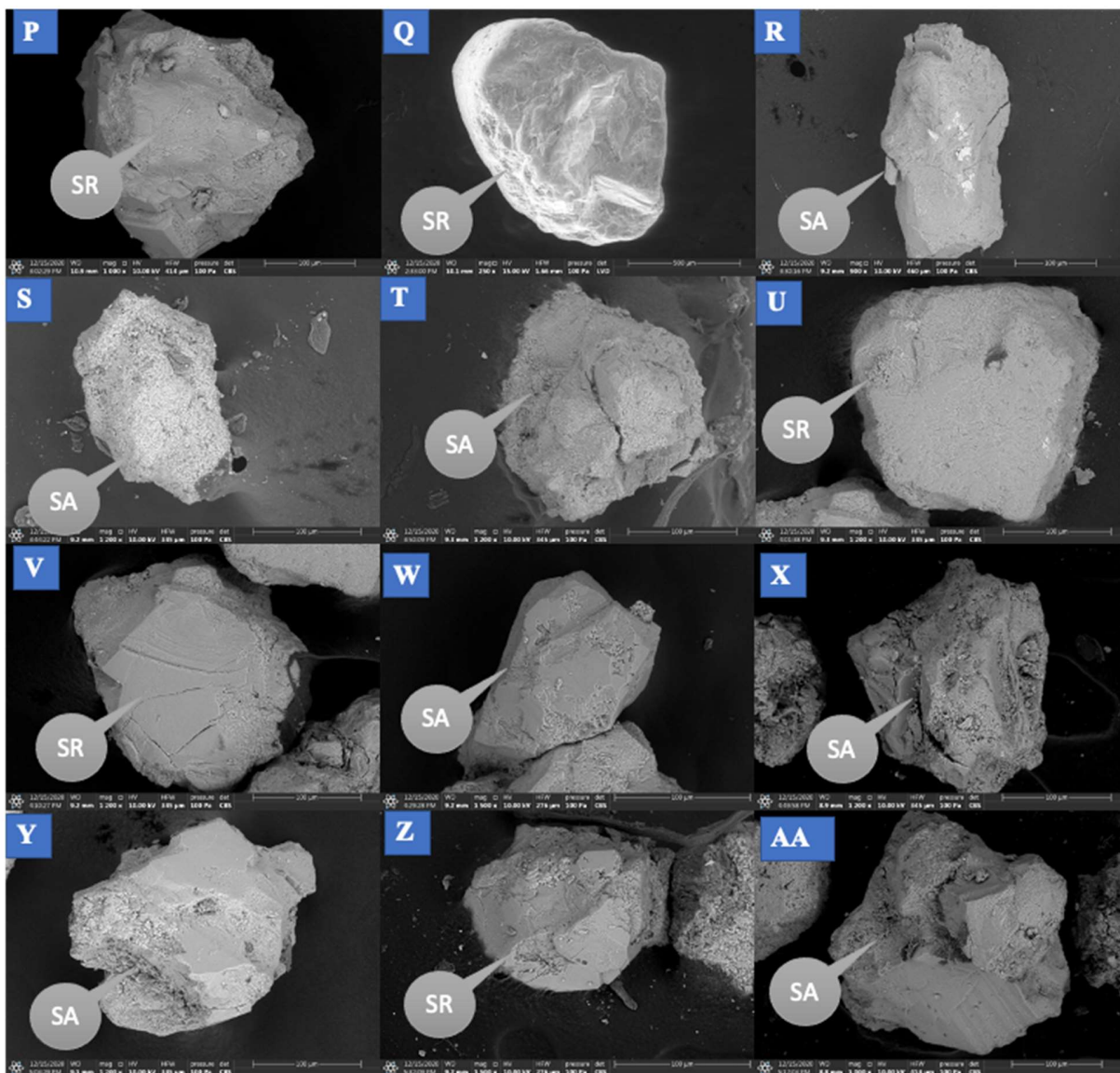
All studied samples of Taman awam		
GRAIN SIZE ( $\mu\text{m}$ )	Frequency	Cumulative %
31	4	0.11%
63	387	10.75%
125	1875	62.32%
250	1311	98.38%
500	59	100.00%
1000	0	100.00%



## Appendix 2.0 Quartz grains shape



**Figure 7.1.** SEM images of grain shape of quartz grains from the Miri Formation (SA= sub-angular, SR= sub- rounded)



**Figure 7.2. SEM images of grain shape of quartz grains from the Miri Formation (SA= sub-angular, SR= sub- rounded)**

## Appendix 3.0 Clay minerals

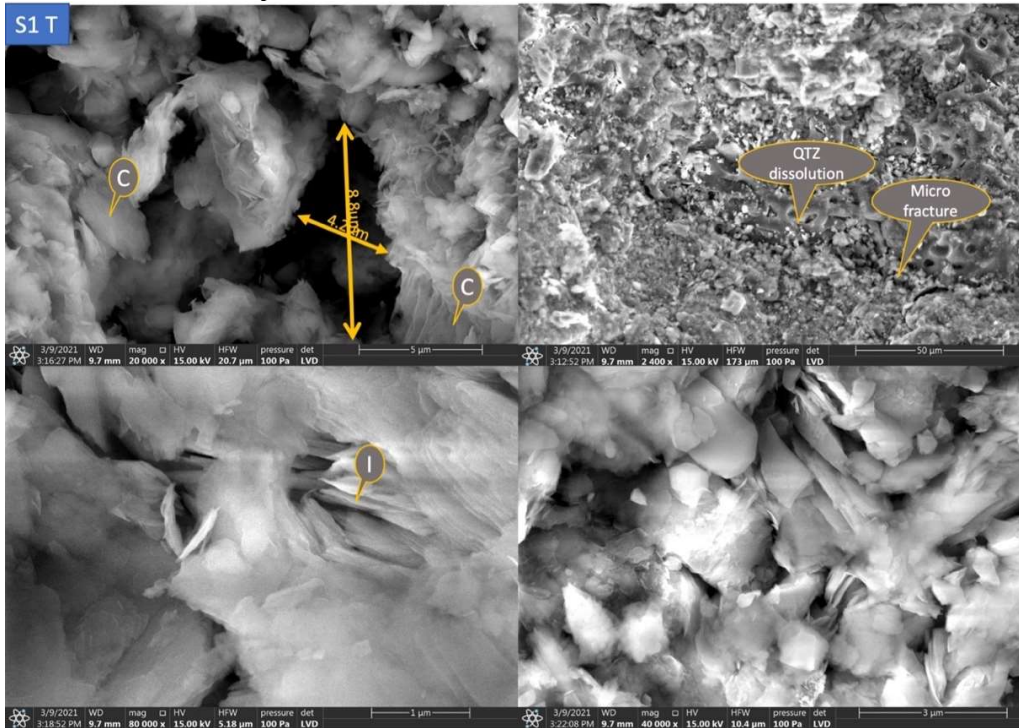


Figure 7.3. SEM images showing pore throat, microfractures and illite in S1T

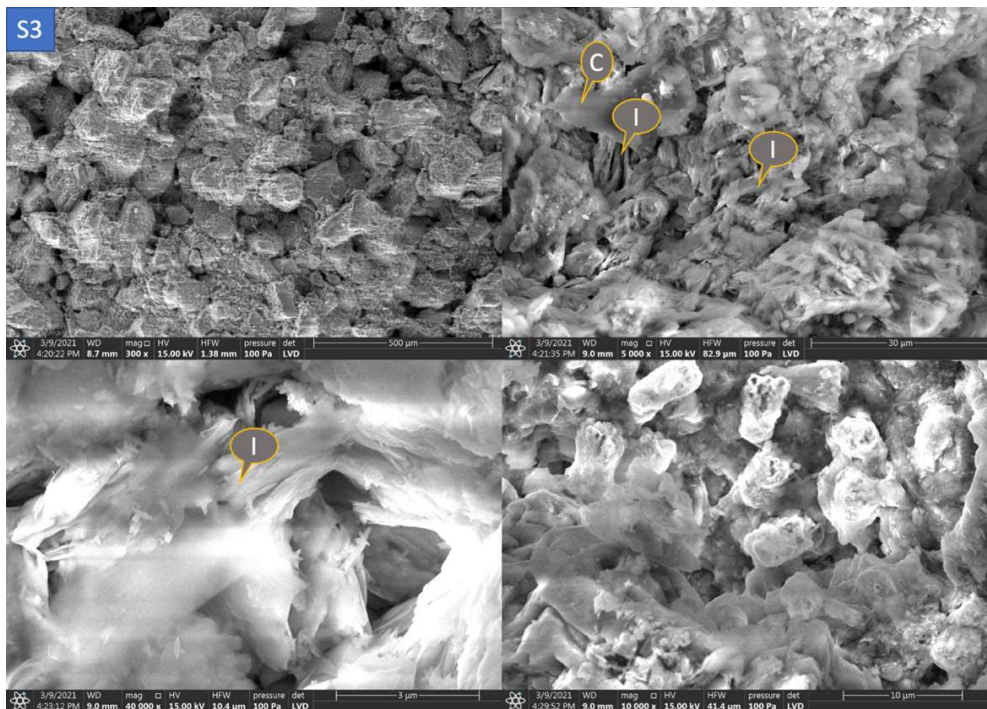
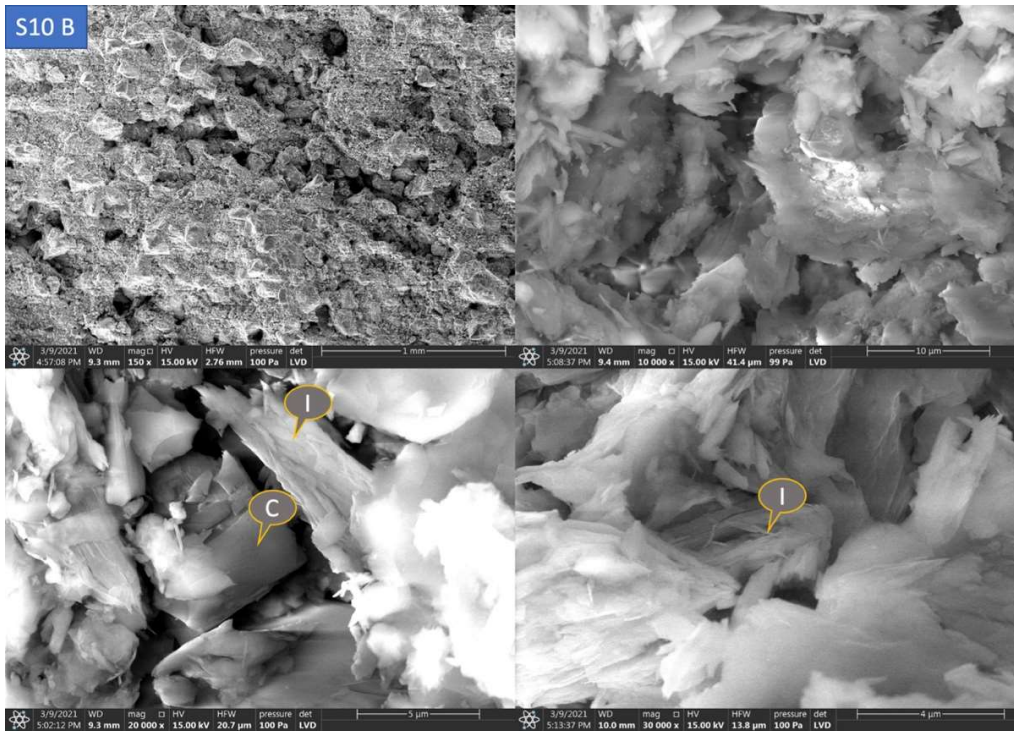
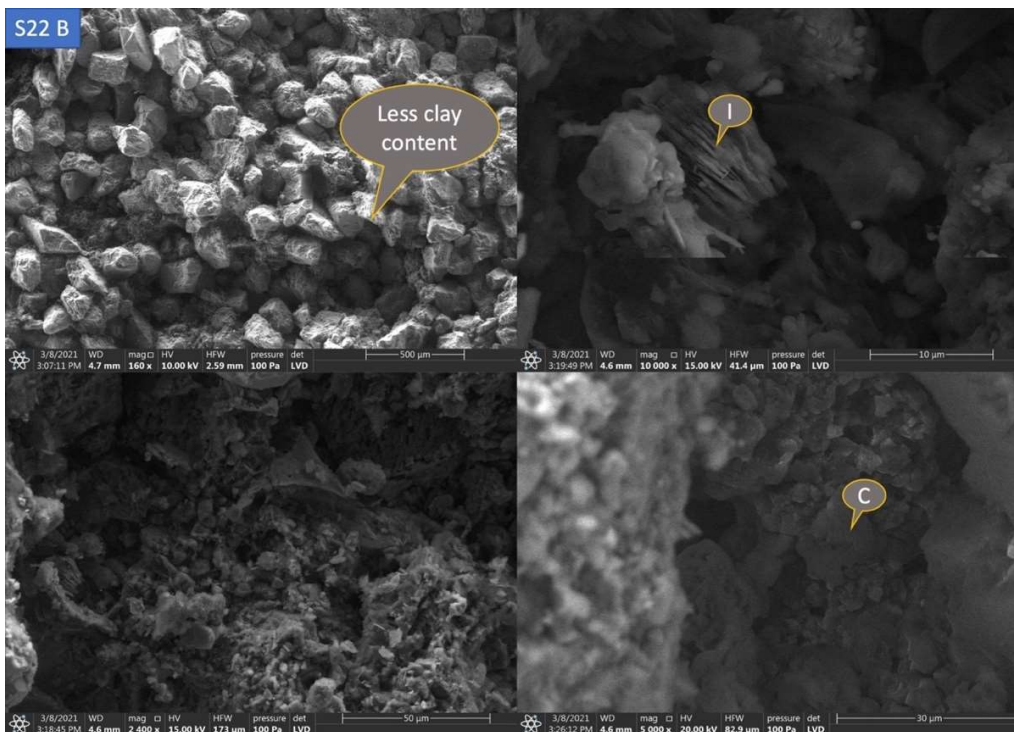


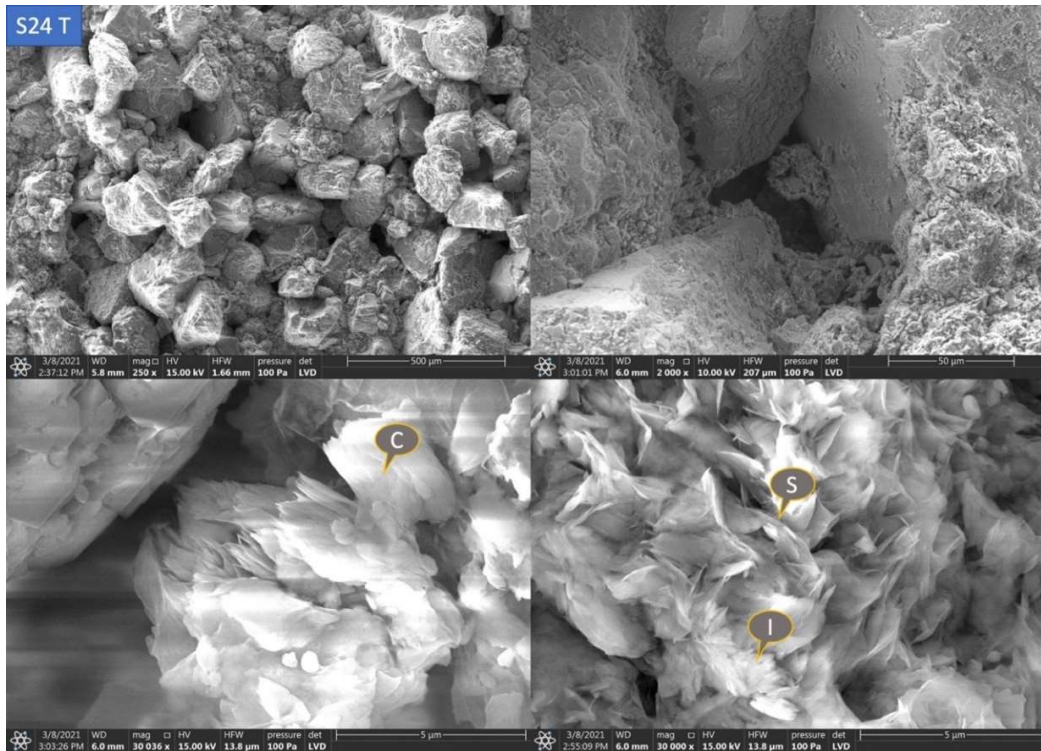
Figure 7.4. SEM images showing overall grains with clay minerals, (chlorite and illite) in S3



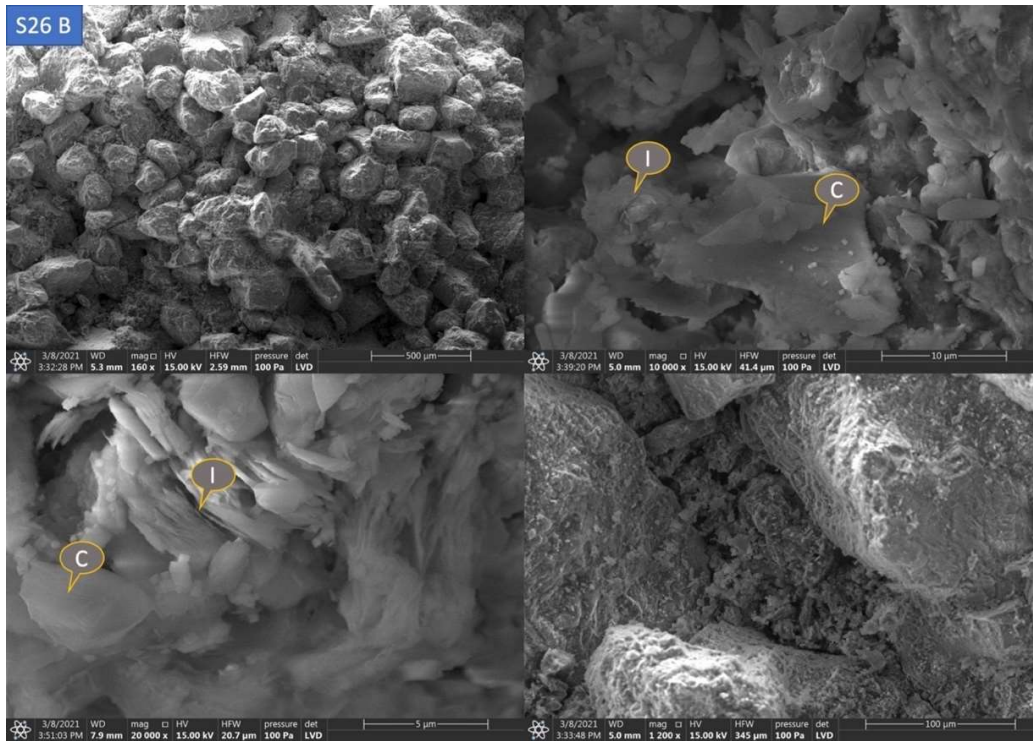
**Figure 7.5. SEM images showing overall grains with clay minerals and pore space, chlorite and illite in S10B**



**Figure 7.6 SEM images showing overall grains with less clay minerals and pore space, chlorite and illite in S22B**



**Figure 7.7. SEM images showing overall grains with less clay minerals and pore space, grain coating chlorite, smectite and illite in S24T**



**Figure 7.8 SEM images showing overall grains with less clay minerals and pore space, grain coating chlorite and illite in S26T**

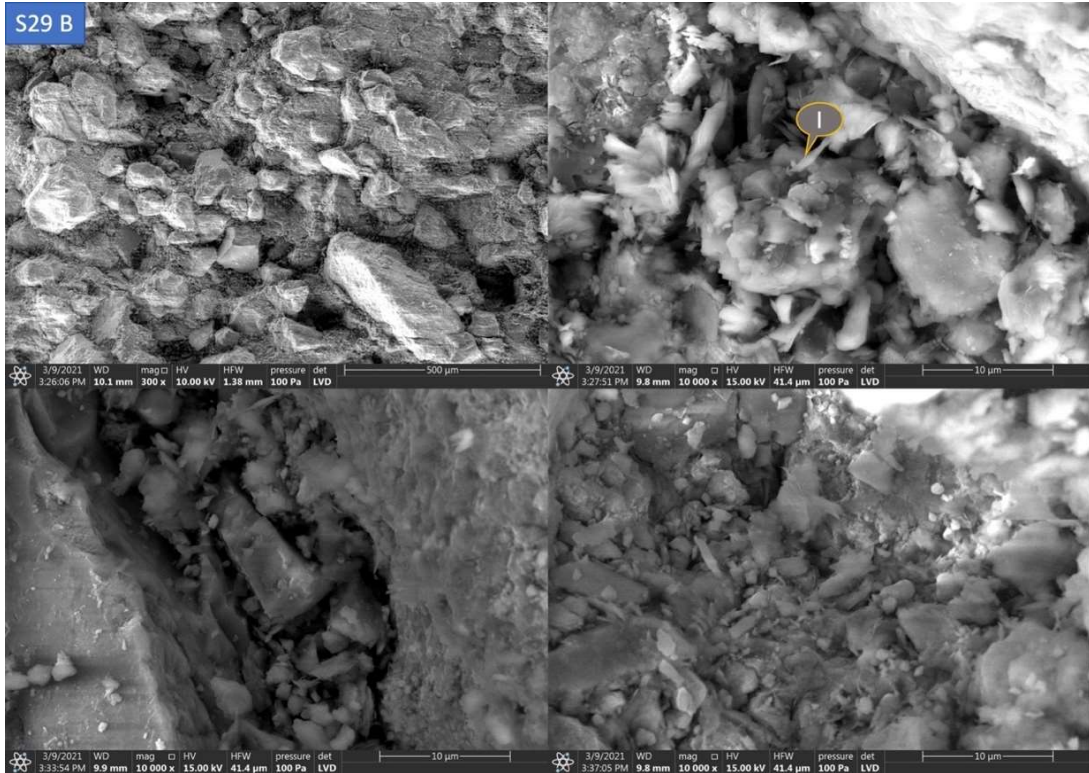


Figure 7.9. SEM images showing overall grains with clay minerals mostly illite in S29B

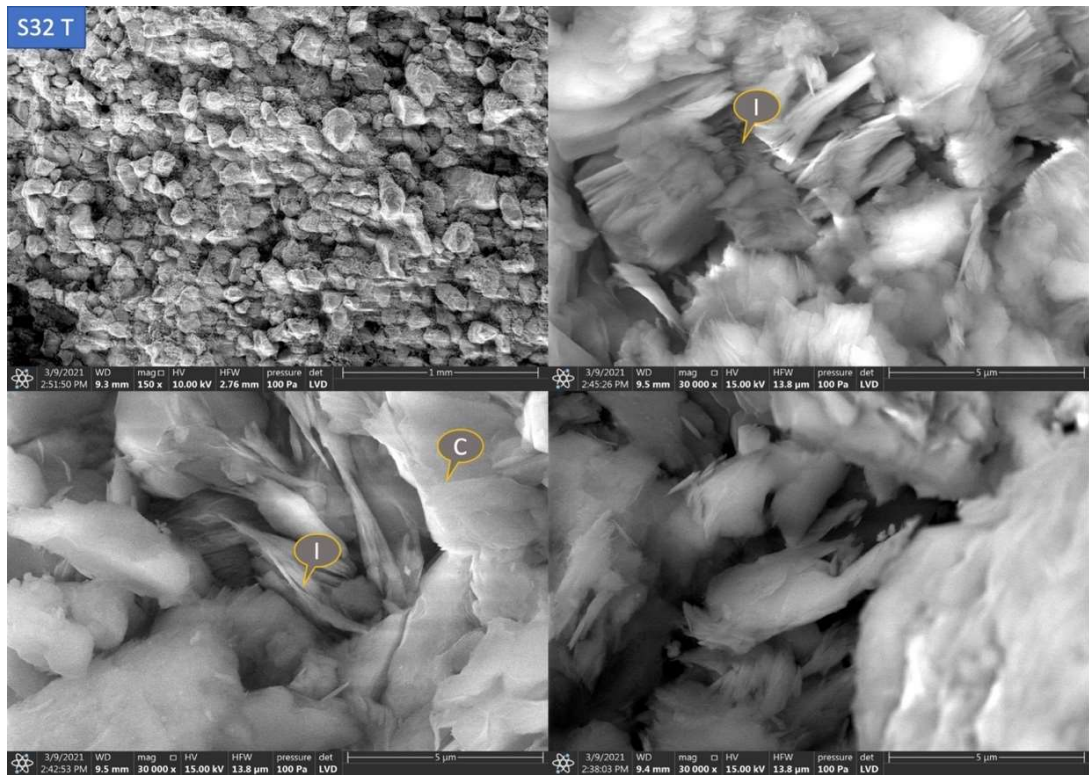
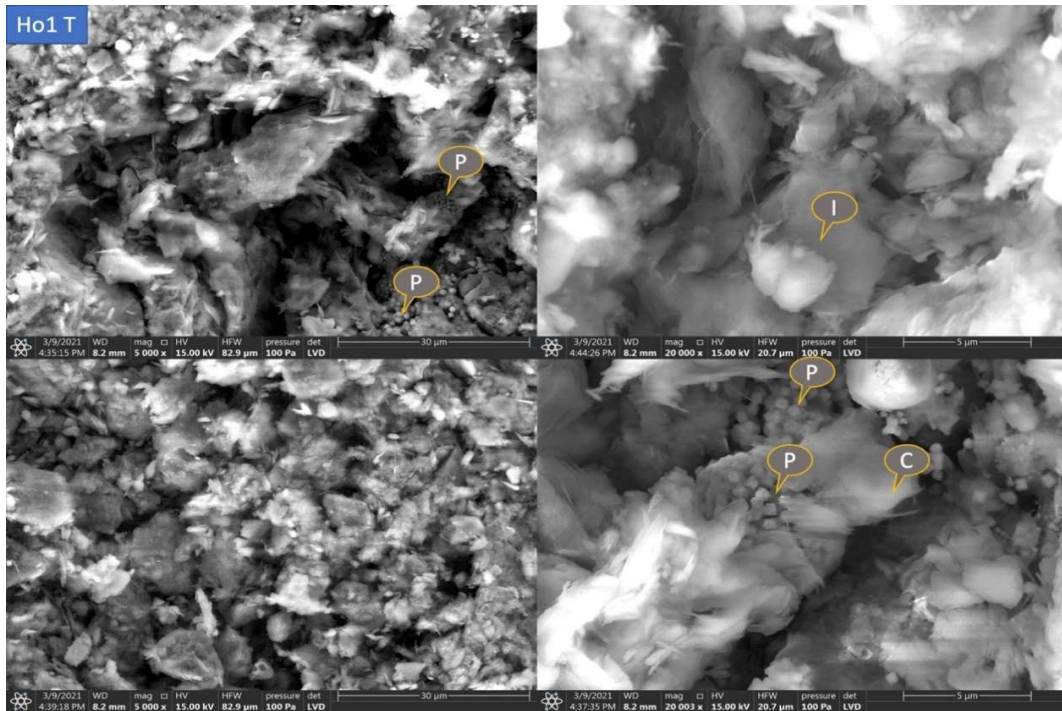
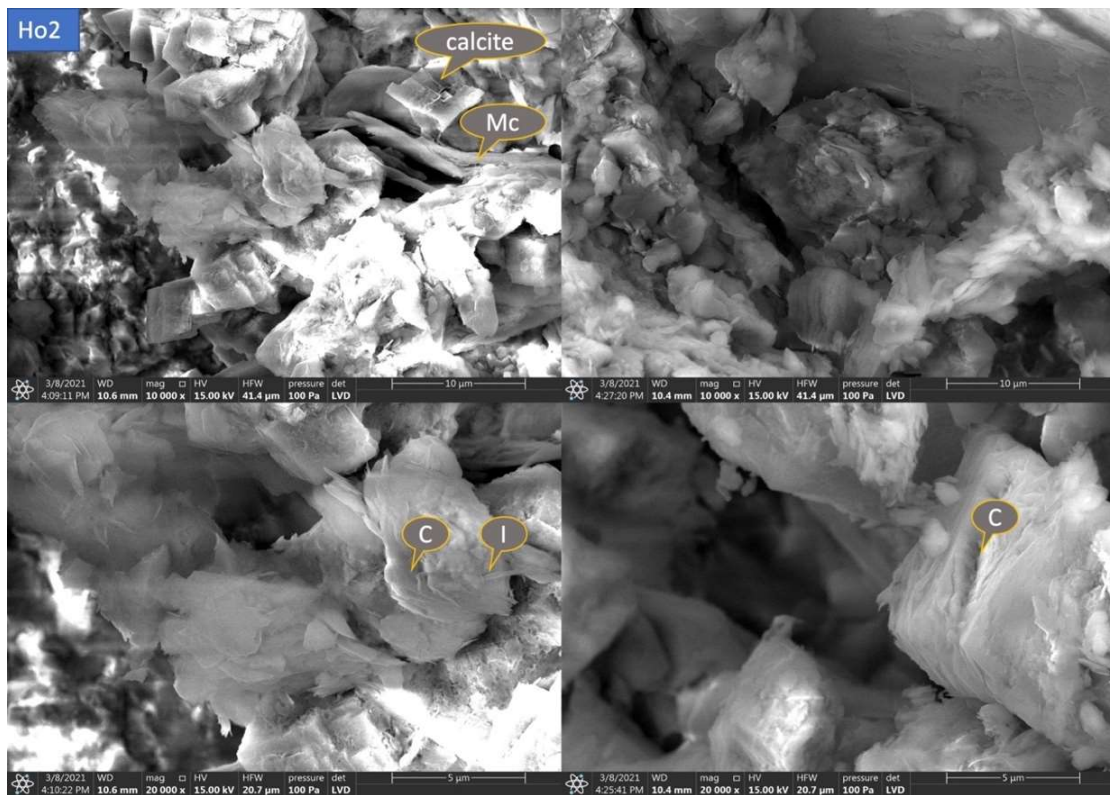


Figure 7.10. SEM images showing overall grains with clay minerals and pore space, grain coating chlorite and pore-blocking illite in S32T

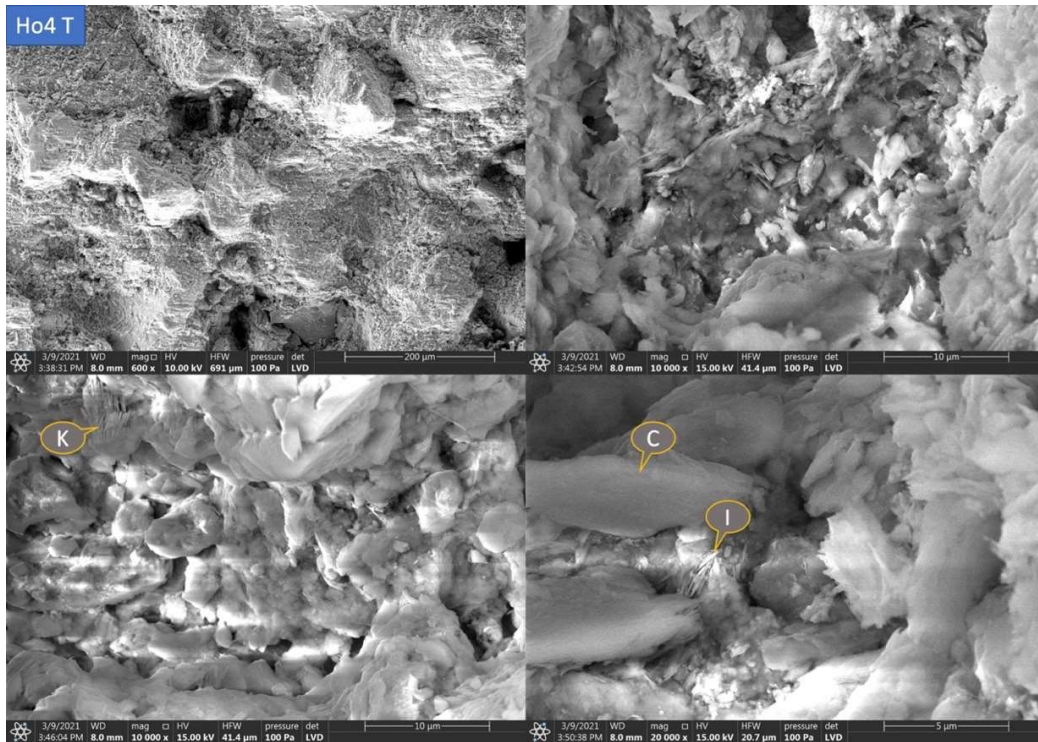




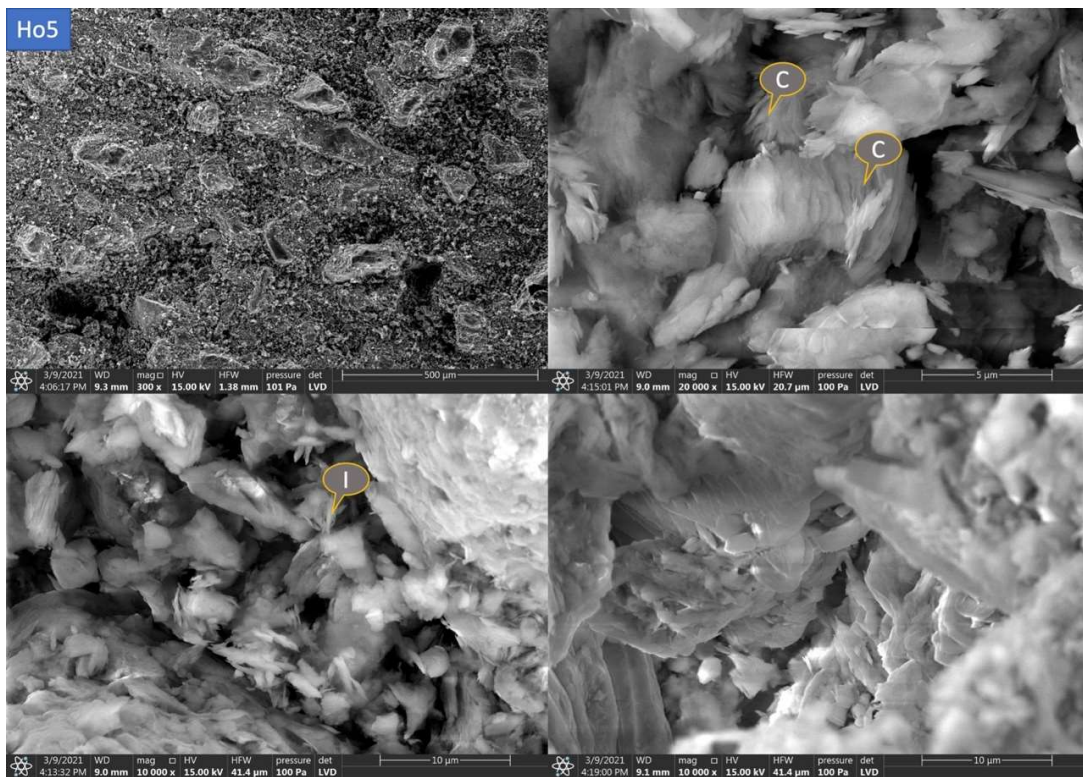
**Figure 7.11 SEM images showing overall grains with clay minerals and pore space, grain coating chlorite, pore-blocking pyrite and illite in HO1T**



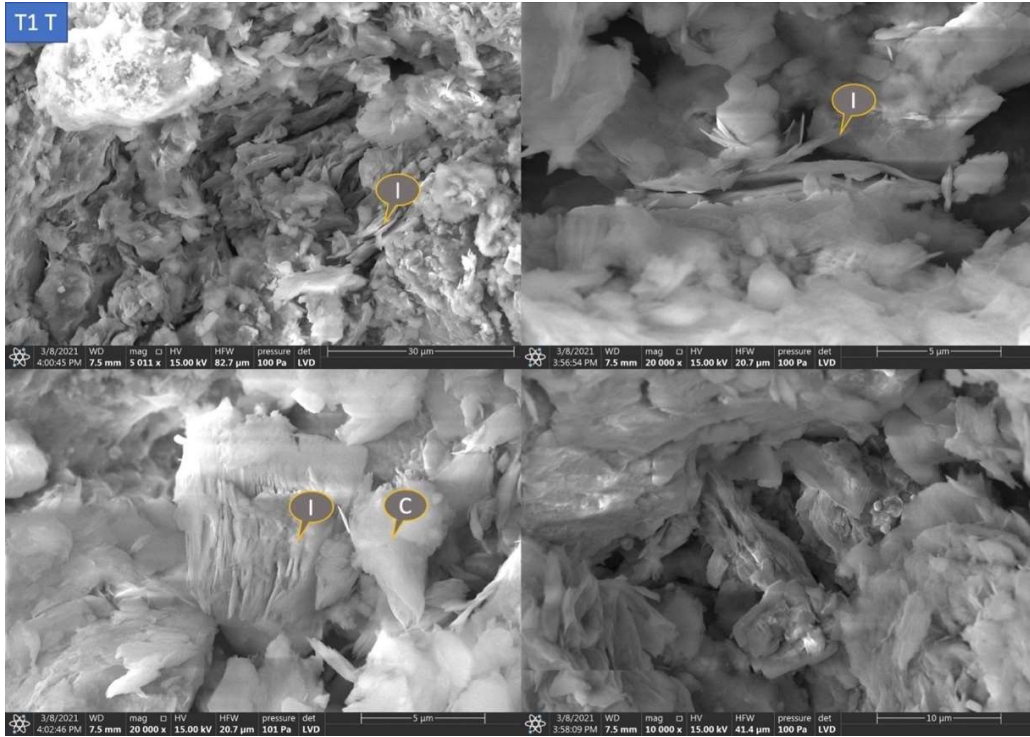
**Figure 7.12 SEM images showing calcite cement, pore-blocking illite and pore-blocking chlorite in HO2**



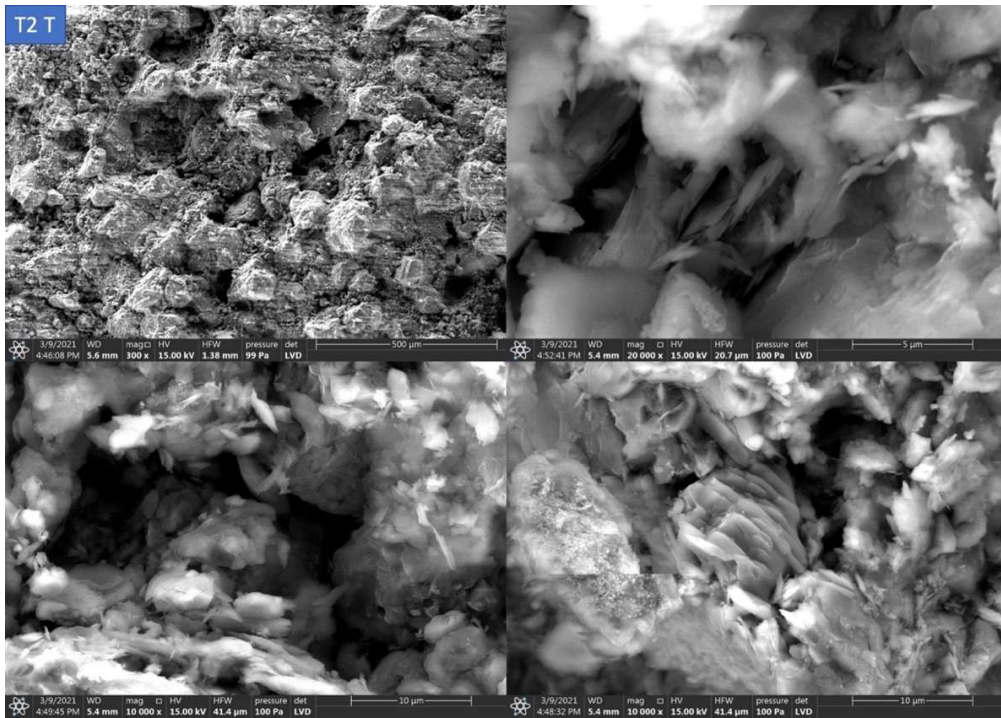
**Figure 7.13 SEM images showing overall grains with clay minerals and pore space, pore-blocking chlorite and illite in HO4T**



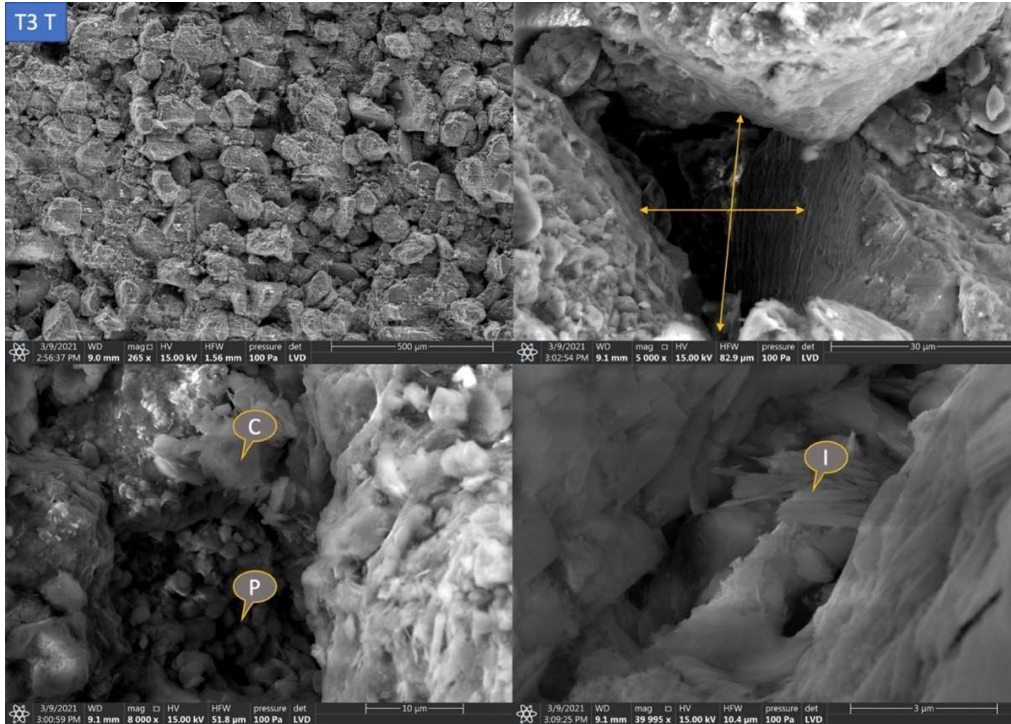
**Figure 7.14 SEM images showing overall grains with high clay minerals and less pore space, pore-blocking illite in HO5**



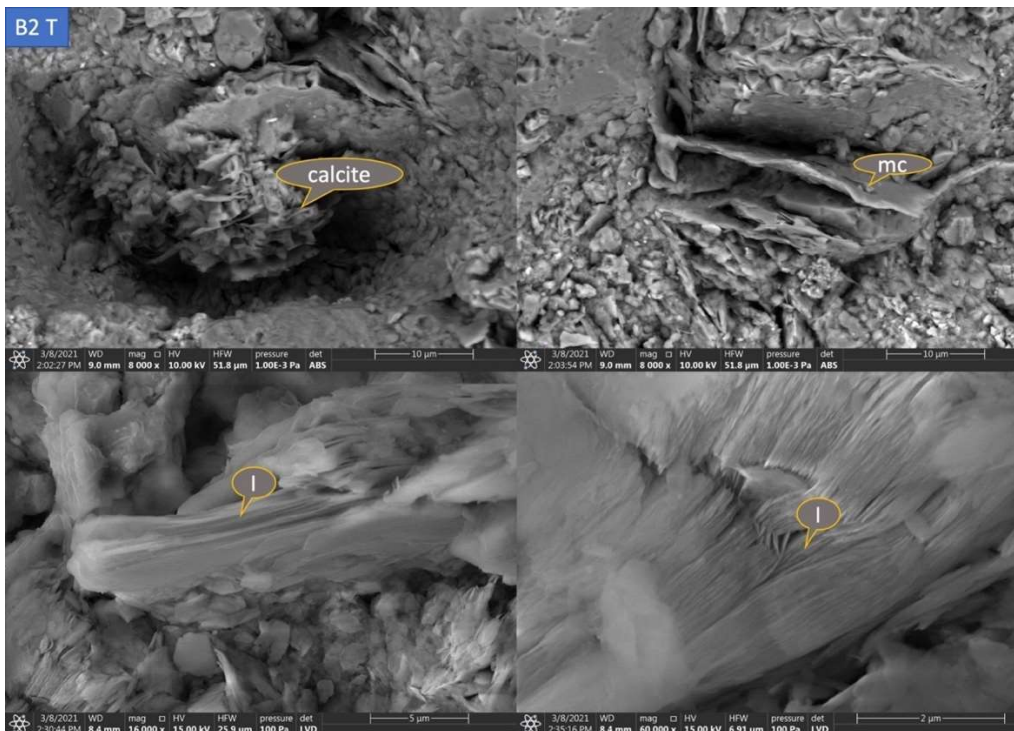
**Figure 7.15 SEM images showing pore-blocking illite and chlorite in T1 T**



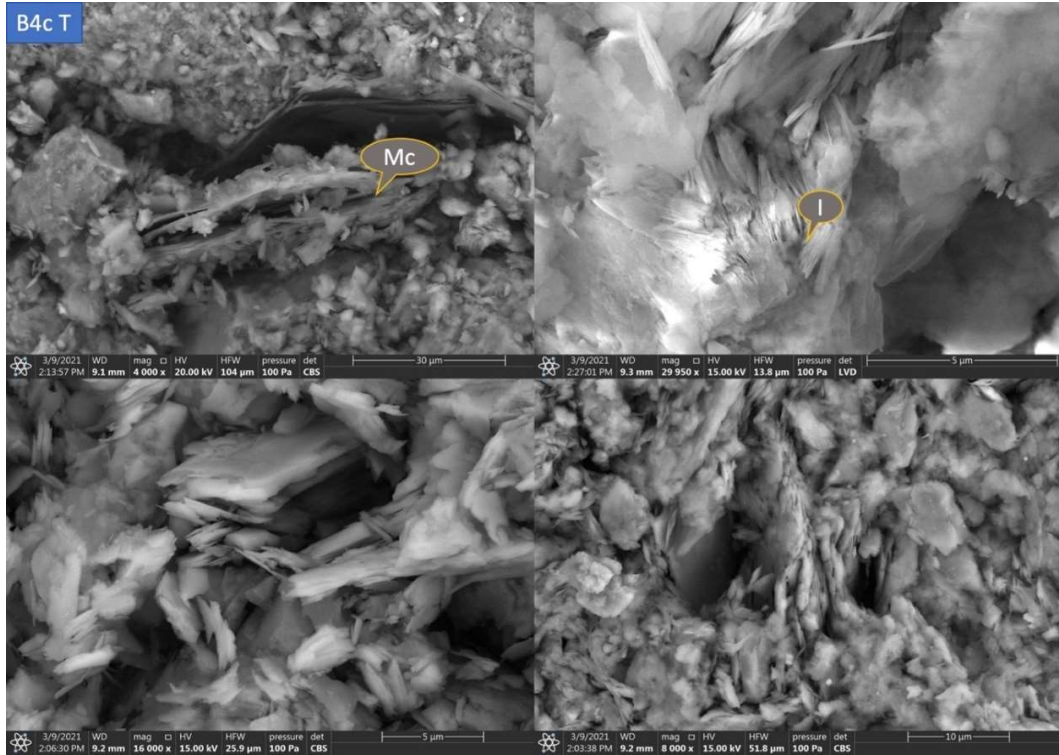
**Figure 7.16 SEM images showing overall grain with pore space, pore-blocking clay minerals in T2 T**



**Figure 7.17. SEM images showing overall grain with pore space, pore-blocking illite and Chlorite in T3 T**



**Figure 7.18. SEM images showing pore-blocking calcite and illite in B2 T**



**Figure 7.19. SEM images showing pore-blocking illite in B4C T**

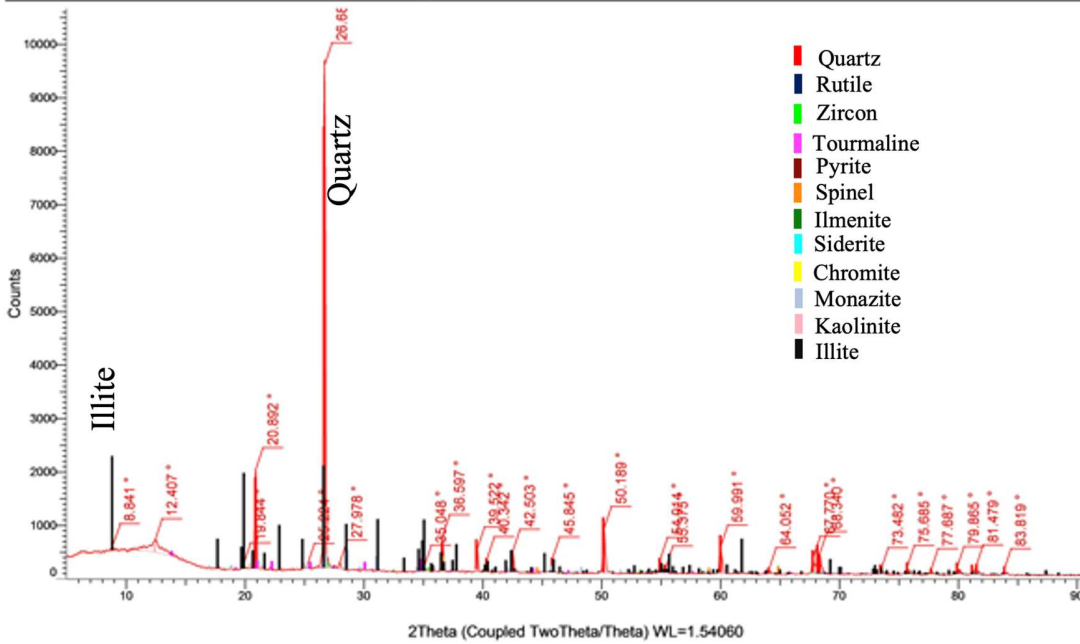
# Appendix 4.0 - XRD results

**Table 7.1 XRD results for the studied samples of the Miri Formation.**

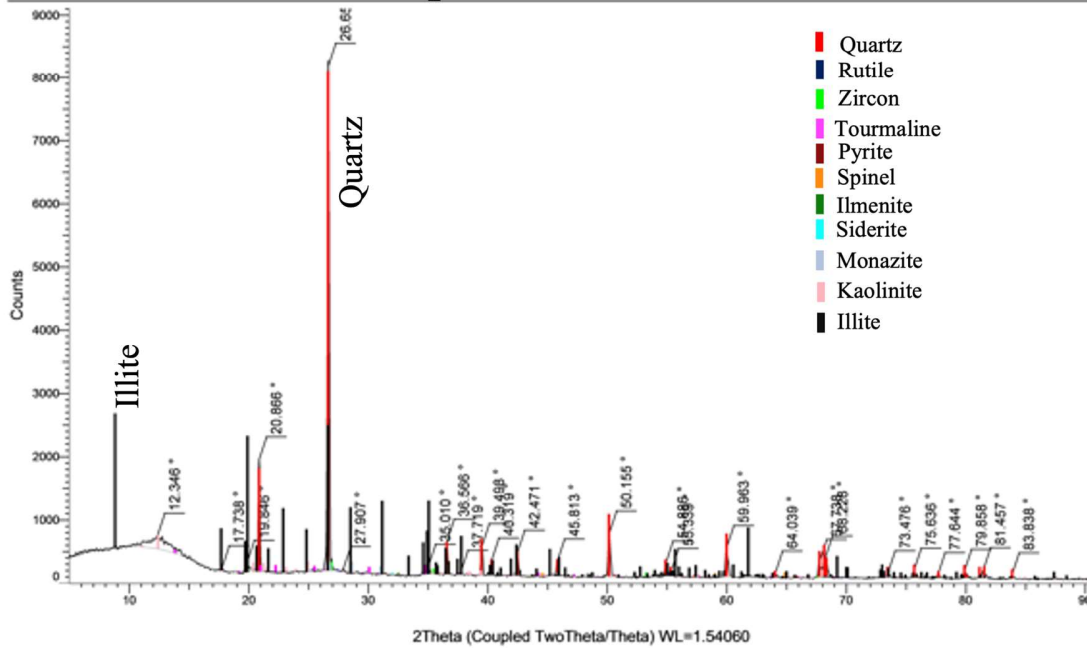
<u>Sample/ minerals</u>	<u>Quartz</u>	<u>Rutile</u>	<u>Zircon</u>	<u>Tourmaline</u>	<u>Pyrite</u>	<u>Spinel</u>	<u>Ilmenite</u>	<u>Siderite</u>	<u>Chromite</u>	<u>Monazite</u>	<u>Kaolinite</u>	<u>Illite</u>
HO5T	Y	Y	Y	Y	N	Y	Y	Y	N	Y	Y	Y
B3	Y	Y	Y	Y	Y	Y	Y	Y	N	Y	Y	Y
B4DT	Y	Y	Y	Y	N	Y	Y	Y	N	Y	Y	Y
S7	Y	Y	Y	Y	Y	Y	Y	Y	Y	Y	Y	Y
S10T	Y	Y	Y	Y	Y	Y	Y	Y	N	Y	Y	Y
T2T	Y	Y	Y	Y	Y	Y	Y	Y	N	Y	Y	Y

Note: Y= present, N= absent.

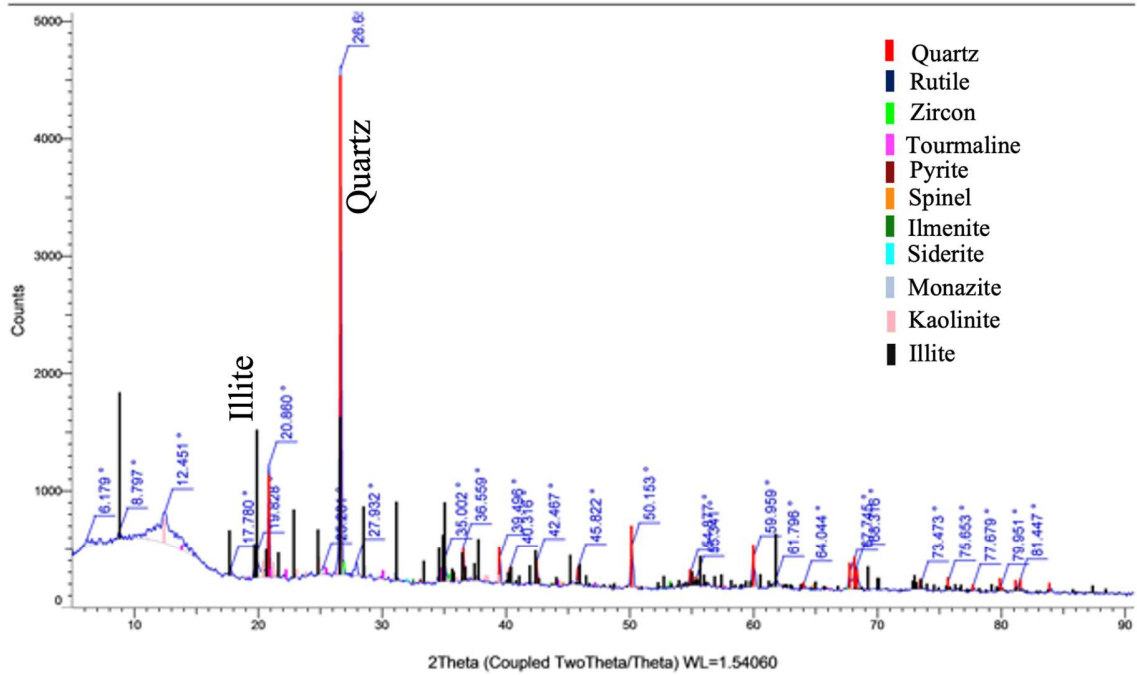
(Coupled TwoTheta/Theta) **T2Top**



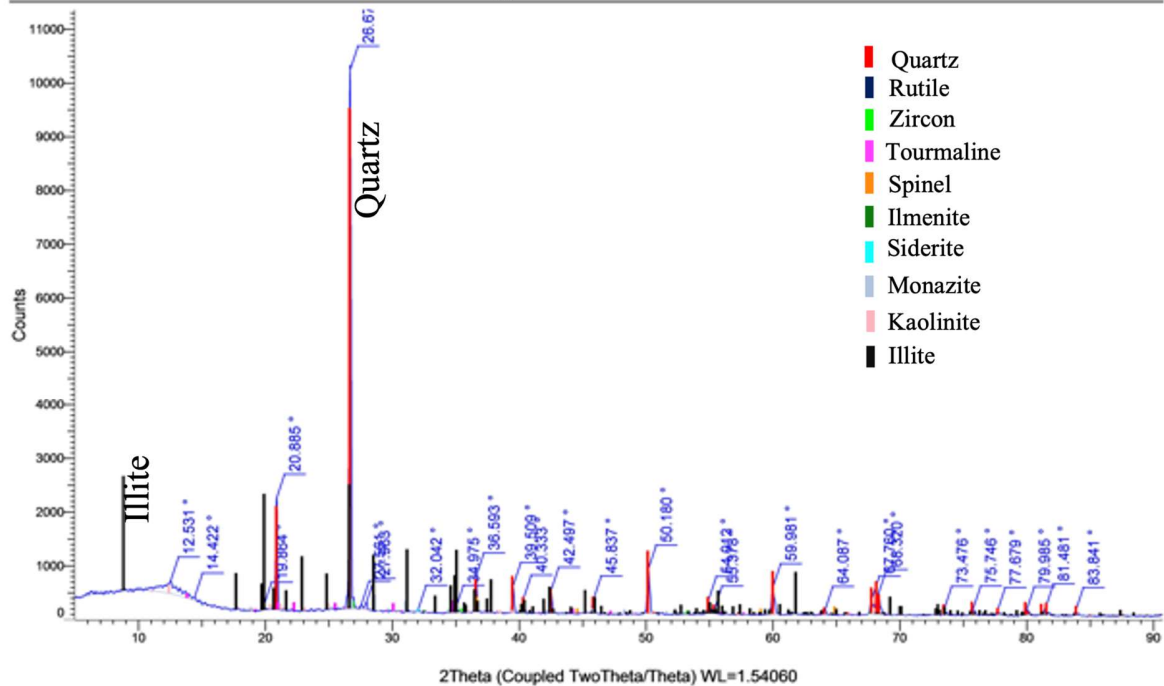
(Coupled TwoTheta/Theta) **S10Top**



(Coupled TwoTheta/Theta) **B3**

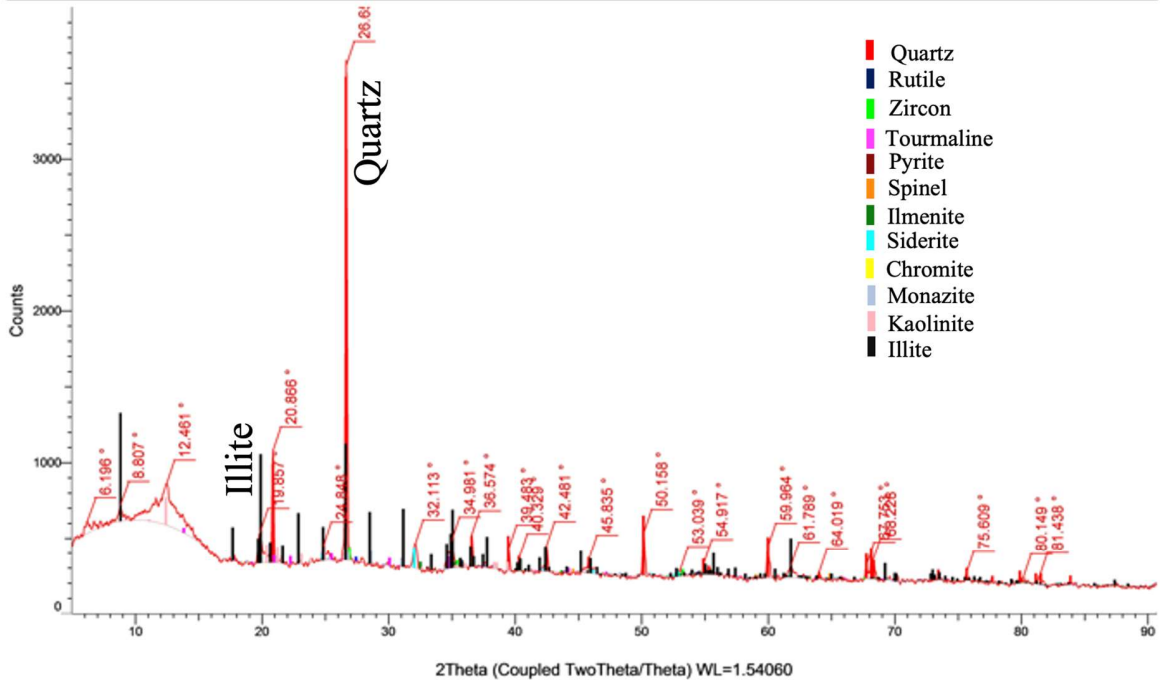


(Coupled TwoTheta/Theta) **B4D Top**

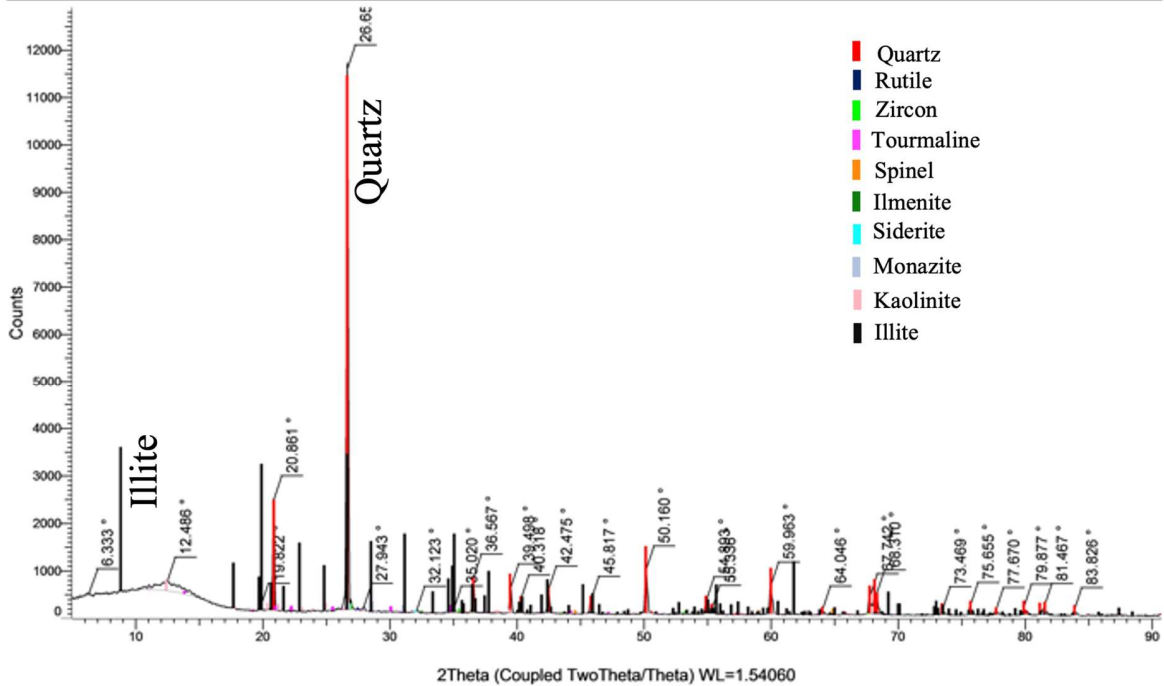




(Coupled TwoTheta/Theta) **S7**



(Coupled TwoTheta/Theta) **Ho5Top**



# Appendix 5.0 Geochemistry calculations

**Table 7.2 Geochemical parameters for tectonic setting, paleoweathering, sorting and provenance.**

Sample No.	Tectonic setting		Paleoweathering						Sorting			Provenance	
	Dfl (A-R-C)	DF2(A-R-C)	A%	CNK%	FM%	A%	CN%	K%	15*Al <sub>2</sub> O <sub>3</sub>	Zr	300*TiO <sub>2</sub>	DF1	DF2
S1T	-0.40	-2.69	62.11	13.46	24.42	82.19	3.15	14.66	21.8624	51.8	26.367	-5.59	-4.91
S4	1.99	-1.81	59.68	12.16	28.16	83.07	2.55	14.37	35.5522	28.9	35.577	-1.96	-4.30
S7	3.22	-1.71	57.77	10.92	31.32	84.10	1.67	14.22	38.3823	25.4	36.188	-0.39	-4.89
S10T	1.66	-3.64	72.13	13.96	13.91	83.78	1.24	14.98	26.7827	43.3	29.967	-5.88	-4.04
S11	-2.15	-4.74	43.33	6.22	50.45	87.45	0.42	12.13	13.8967	65.5	20.621	-5.55	-6.90
S13	0.10	-2.11	56.00	11.67	32.33	82.76	2.67	14.57	25.2626	47.3	27.409	-3.36	-5.17
S14T	-1.10	-2.86	61.74	14.21	24.05	81.29	3.67	15.04	16.597	60.8	22.632	-6.35	-5.13
S17	1.59	-1.29	54.85	12.01	33.14	82.04	3.84	14.13	33.2998	32.4	34.304	-1.26	-4.92
S18T	0.26	-3.38	66.28	14.46	19.26	82.09	3.00	14.90	22.9823	47.5	29.53	-7.80	-5.86
S22T	-1.28	-4.09	66.48	15.13	18.39	81.46	2.95	15.60	23.4081	49.2	27.392	-8.30	-6.25
S24Bo	-1.81	-5.06	55.05	13.80	31.15	79.96	2.68	17.36	19.8257	51.5	28.695	-8.21	-6.43
S25	-0.44	-3.19	68.24	14.45	17.31	82.53	2.31	15.16	23.8248	45.8	30.341	-5.42	-3.90
S26T	-0.43	-3.95	62.73	14.20	23.07	81.54	3.21	15.26	18.9804	51.6	29.389	-8.47	-6.42
S29T	-0.49	-2.64	63.00	13.82	23.18	82.01	3.06	14.93	18.2658	58.3	23.418	-5.77	-4.78
S31	-0.95	-2.52	61.66	12.34	25.99	83.32	1.86	14.82	29.7906	35.7	34.465	-1.87	-3.54
S32 T	0.83	-3.34	65.49	14.22	20.29	82.16	2.90	14.94	11.2475	71.6	17.197	-7.61	-5.61
T1T	0.17	-2.23	64.66	14.92	20.41	81.25	3.91	14.84	22.3067	52.1	25.562	-5.93	-4.38
T2T	0.06	-2.66	62.76	15.34	21.89	80.36	4.84	14.81	22.1048	52.4	25.494	-6.43	-4.93
T3T	0.23	-2.27	62.24	14.22	23.54	81.41	3.99	14.60	21.9668	51.1	26.925	-6.40	-5.17
B1	0.37	-1.75	59.60	14.03	26.36	80.94	5.16	13.90	19.2585	57	23.789	-4.04	-4.29
B2T	2.79	-2.09	46.57	14.09	39.34	76.77	9.45	13.78	14.077	66	19.958	-5.30	-5.49
B3	0.73	-1.73	65.12	13.38	21.50	82.96	3.03	14.02	35.5985	29.4	34.98	-1.87	-2.78
B4DT	-0.37	-2.79	60.75	15.38	23.87	79.80	6.05	14.15	13.8602	65.8	20.37	-6.69	-5.17
Ho2B	2.41	-1.48	34.78	9.94	55.28	77.78	7.74	14.48	13.071	68.8	18.094	-6.65	-8.21
H03B	0.14	-2.31	61.21	13.86	24.93	81.53	4.15	14.31	28.263	40.5	31.251	-4.34	-4.38

Sample No.	Tectonic setting		Paleoweathering						Sorting			Provenance	
	Df1 (A-R-C)	DF2(A-R-C)	A%	CNK%	FM%	A%	CN%	K%	15*Al <sub>2</sub> O <sub>3</sub>	Zr	300*TiO <sub>2</sub>	DF1	DF2
Ho4B	-0.41	-3.63	61.62	16.85	21.52	78.52	6.22	15.26	15.3417	63.9	20.744	-7.65	-5.71
Ho5T	0.70	-3.35	58.98	15.98	25.04	78.68	6.72	14.60	8.73861	75.9	15.409	-7.83	-5.80
Ho6C	0.23	-1.84	66.52	14.31	19.17	82.30	3.51	14.19	31.1289	35	33.888	-3.40	-2.85
Ho6G	0.18	-2.36	60.04	14.40	25.57	80.66	5.13	14.21	16.6647	62.3	21.001	-5.37	-4.79
H06H													
T	-0.62	-3.01	64.35	16.24	19.40	79.84	4.46	15.70	20.9359	53.2	25.876	-7.09	-5.10

## Tectonic Setting Verma and Armstrong-Altrin. (2016) major oxides.

**Table 7.3 Normalized major oxides composition of the Miri Formation samples.**

	SiO <sub>2</sub>	Al <sub>2</sub> O <sub>3</sub>	Fe <sub>2</sub> O <sub>3</sub>	MnO	MgO	CaO	Na <sub>2</sub> O	K <sub>2</sub> O	TiO <sub>2</sub>	P <sub>2</sub> O <sub>5</sub>	MultiplySiO <sub>2</sub> - P <sub>2</sub> O <sub>5</sub>	Root 10
S1T	85.92	8.39	2.61	0.01	0.69	0.05	0.28	1.50	0.51	0.05	0.007723311	0.61486582
S4	72.12	16.11	5.89	0.08	1.71	0.22	0.29	2.79	0.81	0.07	9.208502102	1.24858726
S7	65.59	19.28	7.98	0.13	2.48	0.25	0.19	3.26	0.91	0.07	31.66524234	1.41272712
S10T	84.71	10.56	1.38	0.01	0.65	0.03	0.14	1.89	0.59	0.04	0.001652401	0.52700114
S11	92.38	3.17	3.58	0.01	0.11	0.01	0.02	0.44	0.24	0.05	1.31027E-06	0.25806905
S13	80.79	10.40	5.08	0.03	0.93	0.09	0.27	1.83	0.56	0.05	0.147843903	0.82600056
S14T	89.20	6.37	2.06	0.01	0.42	0.03	0.27	1.18	0.43	0.04	0.000874459	0.49450873
S17	71.57	15.10	7.30	0.13	1.82	0.33	0.40	2.60	0.78	0.09	44.87160815	1.46284113
S18T	94.23	3.64	0.80	0.01	0.25	0.02	0.12	0.66	0.23	0.03	8.2394E-06	0.31016268
S22T	96.98	1.90	0.45	0.01	0.07	0.01	0.07	0.36	0.11	0.04	6.92899E-08	0.19233883
S24Bo	97.06	1.54	0.81	0.01	0.06	0.02	0.04	0.33	0.11	0.03	6.68597E-08	0.19165335
S25	84.41	10.16	2.06	0.01	0.52	0.03	0.27	1.87	0.65	0.04	0.003952894	0.57503134
S26T	97.34	1.57	0.48	0.01	0.10	0.01	0.06	0.29	0.12	0.03	4.88436E-08	0.18572944
S29T	86.42	8.20	2.42	0.01	0.60	0.03	0.28	1.49	0.53	0.03	0.002265673	0.54390083
S31	74.88	14.92	5.40	0.01	0.90	0.03	0.31	2.65	0.86	0.04	0.054115171	0.74701944
S32 T	92.02	4.95	1.08	0.01	0.45	0.03	0.15	0.90	0.38	0.03	0.000109895	0.40188139
T1T	84.58	9.57	2.10	0.01	0.92	0.05	0.42	1.75	0.55	0.05	0.017044539	0.66551604
T2T	87.88	7.31	1.86	0.01	0.69	0.10	0.35	1.35	0.42	0.04	0.006923482	0.60818045
T3T	88.46	6.89	1.99	0.02	0.62	0.05	0.30	1.24	0.42	0.04	0.004941098	0.58800679
B1	79.53	11.72	4.00	0.04	1.18	0.21	0.55	2.01	0.72	0.06	1.93302368	1.06812903
B2T	80.17	7.19	3.62	0.06	2.45	4.23	0.44	1.29	0.51	0.09	33.0104787	1.41861707
B3	70.78	18.37	4.51	0.03	1.55	0.15	0.54	3.10	0.90	0.08	4.910721166	1.17250453
B4DT	88.85	6.44	1.88	0.01	0.65	0.12	0.38	1.14	0.47	0.05	0.009168071	0.6255007
Ho2B	86.42	4.46	5.05	0.06	2.03	0.63	0.22	0.83	0.31	0.05	0.45196526	0.92365653
H03B	81.37	10.99	3.51	0.02	0.97	0.17	0.40	1.93	0.61	0.05	0.262232527	0.87471919
Ho4B	93.79	3.65	1.01	0.01	0.27	0.10	0.20	0.71	0.25	0.03	9.96846E-05	0.39798141
Ho5T	92.06	4.42	1.27	0.01	0.61	0.15	0.24	0.82	0.39	0.04	0.001490021	0.52157798
Ho6C	75.61	15.60	3.28	0.02	1.22	0.09	0.60	2.69	0.85	0.07	0.73352681	0.96948613
Ho6G	84.34	9.02	2.94	0.02	0.91	0.18	0.41	1.59	0.57	0.05	0.14143388	0.82234744
H06H												
T	91.08	5.49	1.28	0.01	0.37	0.04	0.28	1.08	0.34	0.04	0.000407147	0.45811568

**Table 7.4 Isometric log-transformed ratios and discriminant function (DF (A-P)M) of the normalized major oxides of the Miri Formation samples.**

Samples	ilr1TiM	ilr2AlM	ilr3FeM	ilr4MnM	ilr5MgM	ilr6CaM	ilr7NaM	ilr8KM	ilr9PM	DF(A-P)M
S1T	0.13792876	-2.1337811	-1.2532834	3.68398369	-0.0987047	2.27457687	0.72066647	-0.8386902	2.33074772	-12.580992
S4	0.30956846	-2.0879791	-1.3430661	2.45765459	-0.2884452	1.59123456	1.36230518	-0.757067	2.77271911	-11.861438
S7	0.31187608	-2.1339393	-1.4989578	2.13387322	-0.512494	1.60356075	1.86135545	-0.7885619	2.87576887	-12.056293
S10T	-0.0807801	-2.4475656	-0.8349229	3.5460618	-0.1972011	2.60386816	1.25921924	-1.2032831	2.39525171	-15.665102
S11	0.06518552	-2.0485016	-2.2778656	2.90746266	0.75748678	2.98825145	2.3708388	-0.5030071	1.53519968	-11.728543
S13	0.26947704	-2.0682648	-1.5728117	2.96538218	-0.1045403	2.10341555	1.05937	-0.7505745	2.60124415	-11.309336
S14T	0.09189567	-2.0866527	-1.2346709	3.48914232	0.14063476	2.563612	0.57016609	-0.8188944	2.35400141	-12.156447
S17	0.44651863	-1.906141	-1.392323	2.16505167	-0.2007389	1.36907551	1.212717	-0.5424482	2.65681263	-10.317065
S18T	0.19916934	-2.0113338	-0.8247036	3.07192077	0.18100986	2.52194785	0.87204521	-0.7139186	2.19956957	-12.23407
S22T	0.38765197	-1.8700417	-0.7452534	2.64452914	0.91306062	2.72757521	0.93560872	-0.6009474	1.47977858	-11.193768
S24Bo	0.38548461	-1.6989887	-1.2461879	2.64133578	1.05098225	2.08300788	1.45621421	-0.5218021	1.74978994	-10.811129
S25	-0.0830931	-2.3445579	-1.1037456	3.62407537	0.09269494	2.68001794	0.72446596	-1.1098008	2.47328201	-14.253842
S26T	0.30047025	-1.7420684	-0.814334	2.61325322	0.55434147	2.69398442	1.04586459	-0.4312975	1.71827744	-10.69762
S29T	0.02450366	-2.2148429	-1.2915928	3.57429369	-0.0879778	2.63679501	0.60880465	-0.9514363	2.70191087	-12.778003
S31	-0.1022801	-2.4451048	-1.7123291	3.85811716	-0.1656495	2.90593491	0.81388989	-1.1954355	2.70477801	-13.775601
S32 T	0.04206416	-2.0507775	-0.8599922	3.30363114	-0.1038701	2.38101796	0.90020107	-0.760782	2.43981738	-12.997036
T1T	0.13690418	-2.1766901	-0.995325	3.75478535	-0.296439	2.36497574	0.42124664	-0.9107489	2.42337899	-12.796072
T2T	0.25903191	-2.0304424	-0.9687347	3.67420542	-0.1139209	1.64547248	0.51778736	-0.7498149	2.55537726	-12.347368
T3T	0.23430583	-2.0092785	-1.0546108	3.0240639	-0.0451086	2.25482803	0.63386924	-0.7000934	2.52220375	-11.467789
B1	0.27510493	-1.9558435	-1.1440406	2.93800046	-0.0921684	1.49319279	0.61486759	-0.5969699	2.6722562	-11.245239
B2T	0.72364358	-1.3253706	-0.8119913	2.82915658	-0.4993412	-1.0115627	1.08504519	0.08901124	2.65070901	-9.4883417
B3	0.18484652	-2.2468747	-1.1674243	3.27870173	-0.2561773	1.87855784	0.72617283	-0.9180842	2.58252613	-12.905789
B4DT	0.19679419	-1.9043966	-0.954824	3.69932166	-0.0330316	1.50172071	0.46399591	-0.5681177	2.36934839	-12.008439
Ho2B	0.77562759	-1.2848978	-1.4714776	2.44536011	-0.7194103	0.35797893	1.32798572	0.1013426	2.70826405	-7.2272441
H03B	0.2577977	-2.0662689	-1.2024117	3.37929855	-0.0942331	1.51375618	0.72031218	-0.7456344	2.65460025	-12.177847
Ho4B	0.33827647	-1.809086	-0.8041206	3.29490896	0.36364439	1.25343442	0.66602439	-0.5446207	2.42657697	-11.739535
Ho5T	0.20610203	-1.7448937	-0.7718219	3.53680991	-0.1355422	1.13043397	0.74231137	-0.4270625	2.41227782	-12.007712
Ho6C	0.09366257	-2.2685196	-1.0547692	3.47130224	-0.2093498	2.23097291	0.45071492	-0.9618732	2.55898614	-13.096453
Ho6G	0.26106049	-1.9557204	-1.1024784	3.32407668	-0.0877889	1.41184416	0.64975534	-0.6214059	2.60768507	-11.76822
H06H T	0.21274256	-2.0273813	-0.8928226	3.42076957	0.19521931	2.23222319	0.4691422	-0.8076002	2.28734811	-12.221024

Tectonic Setting Verma and Armstrong-Altrin. (2016) major oxides and trace elements.

**Table 7.5 Normalized major (%) and trace element (ppm) of the Miri Formation samples.**

Sample	SiO <sub>2</sub> MT	Al <sub>2</sub> O <sub>3</sub> MT	Fe <sub>2</sub> O <sub>3</sub> MT	MnOMT	MgOMT	CaOMT	Na <sub>2</sub> OMT	K <sub>2</sub> OMT	TiO <sub>2</sub> MT	P <sub>2</sub> O <sub>5</sub> MT	CrMT	NiMT	NbMT	VMT	YMT	ZrMT
S1T	85.87	8.38	2.61	0.01	0.68	0.05	0.28	1.50	0.51	0.05	0.00721	0.0017	0.0009	0.0059	0.0018	0.0314
S4	72.02	16.08	5.88	0.09	1.71	0.22	0.29	2.78	0.80	0.07	0.00918	0.0034	0.0013	0.0120	0.0034	0.0219
S7	65.45	19.24	7.96	0.15	2.47	0.25	0.19	3.25	0.91	0.07	0.01164	0.0052	0.0015	0.0154	0.0049	0.0217
S10T	84.67	10.55	1.38	0.01	0.65	0.03	0.14	1.89	0.59	0.04	0.00721	0.0015	0.0010	0.0071	0.0019	0.0270
S11	92.34	3.17	3.58	0.01	0.11	0.01	0.02	0.44	0.24	0.05	0.00560	0.0002	0.0005	0.0026	0.0007	0.0229
S13	80.72	10.39	5.07	0.03	0.93	0.09	0.27	1.83	0.56	0.05	0.01383	0.0021	0.0010	0.0071	0.0020	0.0311
S14T	89.14	6.36	2.06	0.01	0.42	0.03	0.27	1.18	0.43	0.04	0.00707	0.0007	0.0008	0.0050	0.0014	0.0361
S17	71.43	15.07	7.29	0.14	1.82	0.33	0.40	2.60	0.78	0.09	0.00987	0.0028	0.0013	0.0108	0.0031	0.0244
S18T	94.20	3.64	0.80	0.01	0.25	0.02	0.12	0.66	0.23	0.03	0.00418	0.0004	0.0004	0.0025	0.0009	0.0115
S22T	96.96	1.90	0.45	0.01	0.07	0.01	0.07	0.36	0.11	0.04	0.00277	0.0001	0.0002	0.0014	0.0005	0.0061
S24Bo	97.04	1.54	0.81	0.01	0.06	0.02	0.04	0.33	0.11	0.03	0.00138	0.0001	0.0002	0.0012	0.0005	0.0060
S25	84.36	10.15	2.06	0.01	0.52	0.03	0.26	1.86	0.65	0.04	0.00797	0.0006	0.0011	0.0072	0.0020	0.0311
S26T	97.32	1.57	0.48	0.01	0.10	0.01	0.06	0.29	0.12	0.03	0.00346	0.0003	0.0002	0.0012	0.0005	0.0065
S29T	86.37	8.19	2.42	0.01	0.60	0.03	0.28	1.49	0.53	0.03	0.00647	0.0012	0.0009	0.0057	0.0018	0.0412
S31	74.83	14.91	5.39	0.01	0.90	0.03	0.31	2.65	0.86	0.04	0.00885	0.0007	0.0015	0.0105	0.0026	0.0290
S32 T	91.95	4.95	1.08	0.01	0.45	0.03	0.15	0.90	0.38	0.03	0.00630	0.0009	0.0007	0.0032	0.0014	0.0483
T1T	84.53	9.56	2.10	0.01	0.92	0.05	0.42	1.75	0.55	0.05	0.00637	0.0023	0.0009	0.0062	0.0019	0.0347
T2T	87.83	7.31	1.86	0.01	0.69	0.10	0.35	1.35	0.42	0.04	0.00563	0.0016	0.0007	0.0047	0.0016	0.0267
T3T	88.41	6.88	1.99	0.02	0.62	0.05	0.30	1.23	0.42	0.04	0.00493	0.0016	0.0008	0.0045	0.0018	0.0247
B1	79.43	11.71	4.00	0.04	1.18	0.21	0.55	2.01	0.72	0.06	0.00946	0.0025	0.0013	0.0086	0.0027	0.0553
B2T	80.06	7.18	3.62	0.06	2.45	4.22	0.44	1.29	0.51	0.09	0.00741	0.0014	0.0009	0.0052	0.0022	0.0548
B3	70.72	18.36	4.51	0.03	1.55	0.15	0.54	3.10	0.90	0.08	0.00978	0.0034	0.0016	0.0130	0.0030	0.0251
B4DT	88.79	6.44	1.88	0.01	0.65	0.12	0.38	1.14	0.47	0.05	0.00704	0.0013	0.0008	0.0040	0.0018	0.0472
Ho2B	86.32	4.45	5.05	0.06	2.03	0.63	0.22	0.83	0.31	0.05	0.00654	0.0009	0.0005	0.0047	0.0015	0.0374
H03B	81.31	10.98	3.50	0.02	0.97	0.17	0.40	1.93	0.61	0.05	0.01457	0.0024	0.0011	0.0069	0.0021	0.0251
Ho4B	93.75	3.65	1.01	0.01	0.27	0.10	0.20	0.71	0.25	0.03	0.00703	0.0004	0.0004	0.0025	0.0009	0.0234
Ho5T	91.98	4.42	1.27	0.01	0.60	0.15	0.24	0.82	0.39	0.04	0.00911	0.0009	0.0008	0.0030	0.0016	0.0590
Ho6C	75.55	15.59	3.27	0.02	1.22	0.09	0.60	2.69	0.85	0.07	0.00893	0.0036	0.0015	0.0099	0.0030	0.0286
Ho6G	84.25	9.01	2.93	0.02	0.90	0.18	0.41	1.59	0.57	0.05	0.01079	0.0020	0.0011	0.0061	0.0021	0.0532
H06H T	91.04	5.48	1.28	0.01	0.37	0.04	0.28	1.08	0.34	0.04	0.00492	0.0005	0.0006	0.0033	0.0011	0.0215

**Table 7.6 Product and 16Root of normalized oxides and trace elements of the Miri Formation.**

Samples	Sum	Product	16Root
S1T	100	3.0726E-17	0.09289009
S4	100	3.8314E-13	0.16747876
S7	100	5.2774E-12	0.19731091
S10T	100	7.134E-18	0.08478777
S11	100	2.6011E-23	0.03876565
S13	100	2.0203E-15	0.12066708
S14T	100	8.5977E-19	0.07428462
S17	100	1.3803E-12	0.18144623
S18T	100	1.6653E-22	0.0435355
S22T	100	2.3876E-26	0.02503933
S24Bo	100	5.8422E-27	0.02293038
S25	100	1.0715E-17	0.08697077
S26T	100	4.018E-26	0.02586729
S29T	100	6.9278E-18	0.08463251
S31	100	4.0035E-16	0.10905676
S32 T	100	8.9692E-20	0.06449811
T1T	100	9.4956E-17	0.09967706
T2T	100	9.4555E-18	0.08629392
T3T	100	5.9515E-18	0.08383287
B1	100	7.8711E-14	0.15170577
B2T	100	2.0242E-13	0.16093135
B3	100	2.7316E-13	0.16397445
B4DT	100	2.367E-17	0.09138766
Ho2B	100	3.9294E-16	0.10892941
H03B	100	3.645E-15	0.12520048
Ho4B	100	6.9627E-21	0.05497606
Ho5T	100	2.6314E-18	0.07966396
Ho6C	100	3.3355E-14	0.14377959
Ho6G	100	2.2609E-15	0.12151858
H06H T	100	4.4437E-20	0.06172829

**Table 7.7 Isometric log-transformed ratios of the normalized major oxides (%) and trace (ppm) of the Miri Formation samples.**

<b>Samples</b>	<b>ilr1TiMT</b>	<b>ilr2AlMT</b>	<b>ilr3FeMT</b>	<b>ilr4MnMT</b>	<b>ilr5MgMT</b>	<b>ilr6CaMT</b>	<b>ilr7NaMT</b>	<b>ilr8KMT</b>
S1T	-1.198	-3.676	-2.890	0.034	-1.823	0.525	-1.047	-2.620
S4	-1.110	-3.727	-3.082	0.114	-2.121	-0.267	-0.516	-2.650
S7	-1.079	-3.740	-3.202	2.620	-2.308	-0.217	0.022	-2.643
S10T	-1.372	-3.939	-2.417	1.892	-1.865	0.913	-0.449	-2.925
S11	-1.275	-3.596	-3.919	0.174	-0.973	1.234	0.598	-2.290
S13	-1.090	-3.638	-3.238	2.198	-1.860	0.323	-0.739	-2.563
S14T	-1.248	-3.634	-2.876	-0.593	-1.589	0.809	-1.202	-2.606
S17	-1.028	-3.609	-3.198	2.577	-2.104	-0.561	-0.738	-2.508
S18T	-1.189	-3.614	-2.525	1.306	-1.611	0.704	-0.964	-2.565
S22T	-1.054	-3.535	-2.511	0.812	-0.948	0.840	-0.971	-2.523
S24Bo	-1.116	-3.432	-3.085	0.691	-0.887	0.117	-0.530	-2.523
S25	-1.418	-3.886	-2.739	1.924	-1.631	0.932	-1.042	-2.890
S26T	-1.093	-3.351	-2.521	0.806	-1.245	0.869	-0.798	-2.290
S29T	-1.291	-3.733	-2.902	1.843	-1.786	0.915	-1.131	-2.705
S31	-1.462	-4.016	-3.378	2.117	-1.922	1.125	-0.985	-3.009
S32 T	-1.251	-3.544	-2.444	1.637	-1.773	0.688	-0.810	-2.485
T1T	-1.205	-3.726	-2.639	2.032	-2.029	0.608	-1.354	-2.700
T2T	-1.121	-3.624	-2.659	1.282	-1.896	-0.162	-1.308	-2.590
T3T	-1.143	-3.599	-2.741	0.607	-1.823	0.452	-1.188	-2.536
B1	-1.104	-3.548	-2.833	0.758	-1.873	-0.313	-1.210	-2.436
B2T	-0.814	-3.101	-2.696	1.417	-2.485	-3.025	-0.950	-1.962
B3	-1.206	-3.852	-2.870	2.477	-2.051	0.058	-1.113	-2.772
B4DT	-1.163	-3.474	-2.620	0.322	-1.788	-0.278	-1.335	-2.381
Ho2B	-0.735	-3.029	-3.322	1.460	-2.670	-1.620	-0.671	-1.913
H03B	-1.116	-3.653	-2.885	2.236	-1.868	-0.285	-1.097	-2.578
Ho4B	-1.061	-3.425	-2.518	1.503	-1.443	-0.579	-1.185	-2.410
Ho5T	-1.122	-3.278	-2.398	1.161	-1.850	-0.608	-1.015	-2.198
Ho6C	-1.255	-3.826	-2.707	1.719	-1.951	0.465	-1.334	-2.760
Ho6G	-1.090	-3.516	-2.758	2.210	-1.832	-0.358	-1.138	-2.423
H06H T	-1.204	-3.664	-2.628	1.604	-1.634	0.377	-1.405	-2.697



**Table 7.8 Isometric log-transformed ratios and discriminant function (DF (A-P)MT) of the normalized major oxides and trace elements of the Miri Formation samples.**

Samples	ilr9PMT	ilr10CrMT	ilr12NiMT	ilr11NbMT	ilr13VMT	ilr814YMT	ilr15ZrMT	DF(A-P)MT
S1T	0.538	2.437	3.840	4.390	2.656	3.832	1.050	-4.619
S4	0.868	2.769	3.735	4.630	2.543	3.756	1.968	-1.324
S7	1.010	2.699	3.493	4.667	2.456	3.571	2.136	7.270
S10T	0.662	2.349	3.885	4.210	2.395	3.655	1.109	0.835
S11	-0.263	1.845	5.140	4.224	2.620	3.899	0.508	4.640
S13	0.777	2.066	3.870	4.610	2.726	3.956	1.313	4.601
S14T	0.556	2.243	4.478	4.381	2.608	3.833	0.698	-6.107
S17	0.679	2.776	4.021	4.738	2.722	3.944	1.941	7.767
S18T	0.337	2.235	4.443	4.383	2.737	3.798	1.290	3.310
S22T	-0.454	2.101	5.121	4.523	2.769	3.715	1.375	5.361
S24Bo	-0.264	2.678	5.427	4.531	2.833	3.648	1.292	7.328
S25	0.682	2.278	4.710	4.183	2.400	3.633	0.997	0.365
S26T	-0.152	1.918	4.372	4.598	2.948	3.782	1.341	5.780
S29T	0.938	2.452	4.126	4.336	2.605	3.700	0.697	0.490
S31	0.880	2.394	4.895	4.133	2.259	3.594	1.284	-0.451
S32 T	0.705	2.218	4.127	4.351	2.903	3.714	0.279	1.546
T1T	0.623	2.623	3.610	4.530	2.676	3.809	1.022	-0.130
T2T	0.703	2.603	3.817	4.556	2.799	3.876	1.135	-0.572
T3T	0.675	2.702	3.813	4.514	2.812	3.716	1.182	-0.838
B1	0.822	2.646	3.941	4.591	2.764	3.881	0.978	-1.329
B2T	0.587	2.935	4.560	4.978	3.308	4.152	1.044	3.200
B3	0.717	2.688	3.734	4.456	2.444	3.850	1.819	2.640
B4DT	0.545	2.444	4.112	4.509	3.012	3.783	0.640	-3.887
Ho2B	0.681	2.682	4.605	5.097	3.034	4.135	1.035	5.080
Ho3B	0.811	2.051	3.818	4.574	2.790	3.955	1.554	3.257
Ho4B	0.549	1.961	4.635	4.664	2.992	3.969	0.826	3.343
Ho5T	0.630	2.067	4.316	4.456	3.169	3.770	0.291	-0.090
Ho6C	0.749	2.649	3.540	4.361	2.578	3.724	1.563	-0.631
Ho6G	0.795	2.308	3.957	4.538	2.883	3.929	0.799	2.990
H06H T	0.386	2.412	4.702	4.411	2.826	3.910	1.022	1.744

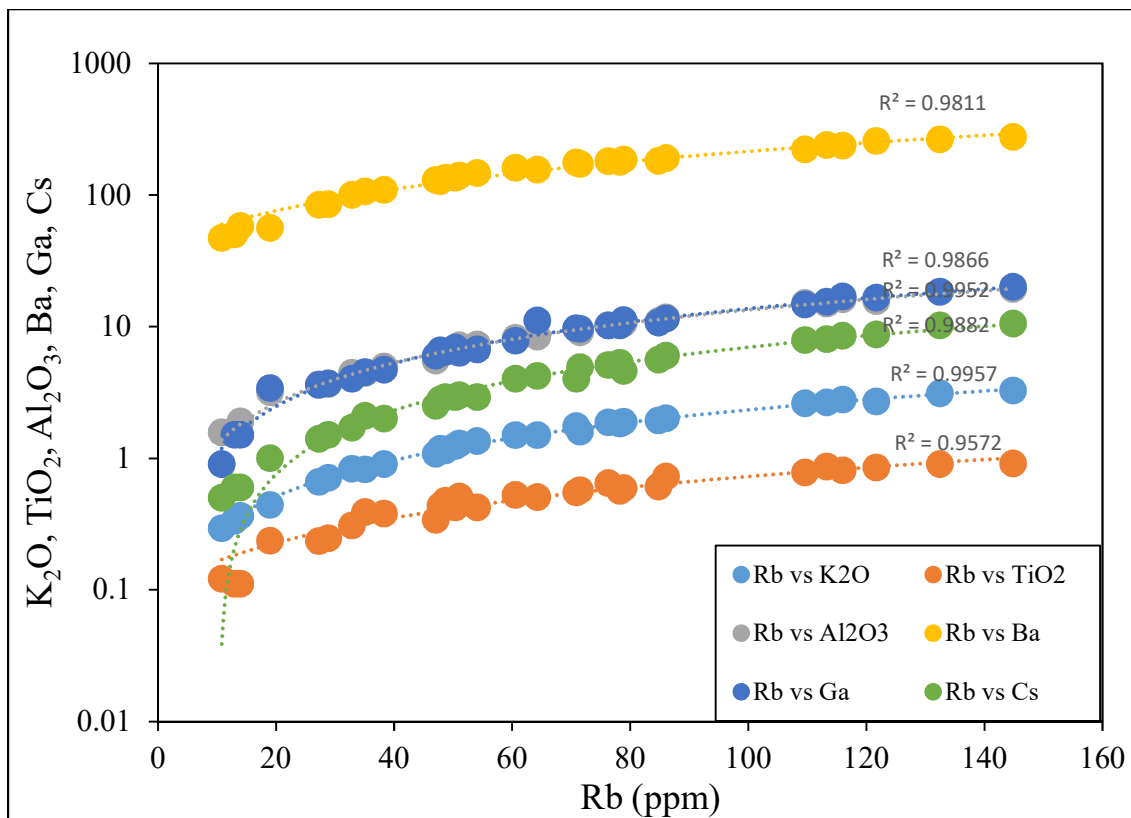


Figure 7.20 Bi-plot showing the correlation of Rb with K<sub>2</sub>O, TiO<sub>2</sub>, Al<sub>2</sub>O<sub>3</sub>, Ba, Ga, Cs.

## Appendix 6.0 Strata log key




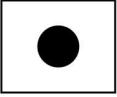


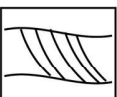
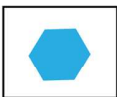
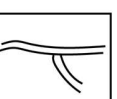



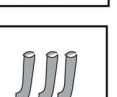
Legend			
	Sandstone		SEM - clay minerals
	Mudstone		XRD analysis
	Planar bedding or parallel lamination		Geochemical analysis
	Planar cross-stratification		Thin section (petrographic analysis)
	Hummocky cross-stratification		Porosity and permeability
	Trough cross bedding		
	Bioturbation		
	Burrow trace		

Figure 7.21: stratigraphic log legend of the Miri Formation.

**Table 7.9 REE values of the Miri Formation studied samples.**

Samples/REE's	La	Ce	Pr	Nd	Sm	Eu	Gd	Tb	Dy	Ho	Er	Tm	Yb	Lu
S1Top	20.8	40.9	4.72	17.3	3.17	0.66	2.86	0.44	2.69	0.58	1.8	0.26	1.73	0.28
S4	32.5	66.3	7.68	30.1	5.98	1.37	6.1	0.92	5.63	1.12	3.21	0.47	2.99	0.44
S7	38.7	79.4	9.27	36.2	7.75	1.88	8.43	1.35	7.71	1.57	4.51	0.64	3.86	0.61
S10Top	22.9	44.4	5.05	18.8	3.27	0.7	2.93	0.47	3.13	0.65	1.97	0.3	2.01	0.31
S11	10.4	20	2.14	7.9	1.27	0.23	1.09	0.16	1.13	0.22	0.7	0.11	0.81	0.13
S13	23.9	47.8	5.42	20.2	3.79	0.78	3.46	0.53	3.32	0.68	2.04	0.31	2.07	0.31
S14Top	19.2	37	4.2	15.3	2.51	0.5	2.19	0.35	2.25	0.49	1.57	0.23	1.61	0.26
S17	30.7	62.9	7.24	27.4	5.56	1.28	5.52	0.86	4.83	1.03	2.96	0.42	2.73	0.43
S18Top	11.9	22.6	2.68	9.5	1.72	0.35	1.64	0.24	1.44	0.3	0.9	0.12	0.85	0.13
S22Top	7.6	14.5	1.7	5.9	1.17	0.23	1.03	0.15	0.91	0.17	0.5	0.08	0.56	0.08
S24Bottom	6.3	12.2	1.36	5	0.88	0.18	0.9	0.14	0.9	0.19	0.57	0.08	0.54	0.08
S25	25.8	49.7	5.69	20.6	3.35	0.67	3.05	0.48	3.26	0.67	2.08	0.32	2.17	0.34
S26Top	6.5	12.4	1.43	5.3	0.95	0.22	0.91	0.13	0.83	0.16	0.54	0.07	0.48	0.08
S29Top	23	45.2	5.06	18.6	3.06	0.58	2.65	0.44	2.9	0.64	1.99	0.3	2.05	0.34
S31	32	62.3	7.04	25.7	4.31	0.86	3.77	0.6	3.95	0.85	2.77	0.4	2.65	0.42
S32 Top	18.1	34.5	3.9	13.9	2.45	0.4	2.13	0.33	2.16	0.47	1.49	0.22	1.68	0.28
T1ToP	23	45.4	5.11	18.6	3.25	0.7	3.11	0.5	3.21	0.68	2.14	0.31	2.21	0.35
T2Top	18.5	37.1	4.23	15.8	2.82	0.61	2.68	0.41	2.66	0.56	1.65	0.24	1.63	0.26
T3Top	21.1	39.6	4.81	18.4	3.51	0.71	3.35	0.53	3.15	0.61	1.85	0.27	1.73	0.28
B1	30.7	61.6	6.99	25.8	4.67	0.98	4.56	0.72	4.43	0.92	2.88	0.43	2.88	0.45
B2Top	21.3	41.9	4.87	18.1	3.3	0.62	3.03	0.5	3.22	0.71	2.2	0.33	2.25	0.37
B3	37.5	76.4	8.64	32.3	5.91	1.27	5.49	0.85	5.11	1.07	3.04	0.45	3.03	0.48
B4DTop	19.8	38.5	4.46	15.9	2.85	0.56	2.81	0.45	2.89	0.64	1.88	0.3	2	0.33
Ho2Bottom	16.4	32.6	3.71	13.4	2.45	0.54	2.46	0.39	2.39	0.49	1.49	0.22	1.5	0.23
H03Bottom	25.4	51.4	5.97	21.8	4.17	0.85	3.69	0.57	3.35	0.67	2.02	0.31	1.98	0.33
Ho4Bottom	12.9	24.9	2.86	9.9	1.68	0.31	1.51	0.23	1.4	0.3	0.97	0.15	1.01	0.16
Ho5Top	19.6	36.9	4.24	15.3	2.66	0.5	2.35	0.37	2.38	0.52	1.7	0.26	1.78	0.32
Ho6C	34.4	69.8	8.22	30.8	5.97	1.28	5.66	0.87	5	1.02	2.9	0.44	2.93	0.46
Ho6G	26.5	51.6	5.95	22.1	3.96	0.8	3.7	0.58	3.44	0.72	2.21	0.34	2.35	0.38
H06H Top	14.9	28.1	3.19	10.9	1.86	0.34	1.59	0.25	1.67	0.34	1.16	0.17	1.17	0.2

**Table 7.10 1: Detail of studied samples, analysis carried out and outcrop.**

<b>Sample Number</b>	<b>Type of sample</b>	<b>Analysis carried out</b>	<b>Outcrop</b>
HO1 B	Sandstone	Whole rock geochemistry and Thin section	Hospital outcrop
HO1 T	Sandstone	Thin section, Petrophysical analysis and SEM	Hospital Outcrop
HO2 B	Sandstone	Whole rock geochemistry, Thin section, Petrophysical analysis and SEM	Hospital Outcrop
HO2 T	Sandstone	Thin section	Hospital Outcrop
HO3 B	Mudstone	Whole rock geochemistry and Thin section	Hospital Outcrop
HO3 T	Sandstone	Thin section and Petrophysical analysis	Hospital Outcrop
HO4 B	Sandstone	Whole rock geochemistry and Thin section	
HO4 T	Sandstone	Petrophysical analysis and SEM	Hospital Outcrop
HO5 B	Sandstone	Petrophysical analysis and SEM	Hospital Outcrop
HO5 T	Sandstone	XRD analysis	Hospital Outcrop
HO6A	Mudstone	Whole rock geochemistry	Hospital Outcrop
HO6B	Sandstone	Whole rock geochemistry	Hospital Outcrop
HO6C	Mudstone	Whole rock geochemistry	Hospital Outcrop
HO6E	Mudstone	Whole rock geochemistry	Hospital Outcrop
HO6F	Sandstone	Whole rock geochemistry and petrophysical analysis	Hospital Outcrop
HO6G	Sandstone	Whole rock geochemistry and petrophysical analysis	Hospital Outcrop
HO6H T	Sandstone	Whole rock geochemistry, thin section and petrophysical analysis	Hospital Outcrop
B1	Mudstone	Whole rock geochemistry	Bomba Outcrop
B2 T	Sandstone	Whole rock geochemistry, thin section, SEM and petrophysical analysis	Bomba Outcrop

<b>Sample Number</b>	<b>Type of sample</b>	<b>Analysis carried out</b>	<b>Outcrop</b>
B3	Mudstone	Whole rock geochemistry and XRD analysis	Bomba Outcrop
B4C T	Sandstone	Whole rock geochemistry, thin section, SEM and petrophysical analysis	Bomba Outcrop
B4D B	Sandstone	Whole rock geochemistry	Bomba Outcrop
B4D T	Sandstone	Thin section, petrophysical analysis and XRD	Bomba Outcrop
S1 T	Sandstone	Whole rock geochemistry, thin section, SEM and petrophysical analysis	Taman Awam Outcrop
S3	Sandstone	Thin section, SEM and petrophysical analysis	Taman Awam Outcrop
S4	Mudstone	Whole rock geochemistry	Taman Awam Outcrop
S7	Mudstone	Whole rock geochemistry, thin section, XRD and petrophysical analysis	Taman Awam Outcrop
S10 B	Sandstone	Thin section, SEM, XRD and petrophysical analysis	Taman Awam Outcrop
S10 T	Sandstone	Whole rock geochemistry	Taman Awam Outcrop
S11	Sandstone	Whole rock geochemistry and thin section	Taman Awam Outcrop
S13	Mudstone	Whole rock geochemistry	Taman Awam Outcrop
S14 T	Sandstone	Whole rock geochemistry, thin section and petrophysical analysis	Taman Awam Outcrop
S17	Mudstone	Whole rock geochemistry	Taman Awam Outcrop
S18 T	Sandstone	Whole rock geochemistry and thin section	Taman Awam Outcrop
S20	Sandstone	Thin section and petrophysical analysis	Taman Awam Outcrop
S22 B	Sandstone	Thin section, petrophysical analysis and SEM	Taman Awam Outcrop
S22 T	Sandstone	Whole rock geochemistry, thin section and petrophysical analysis	Taman Awam Outcrop
S24 B	Sandstone	Thin section, SEM and petrophysical analysis	Taman Awam Outcrop

<b>Sample Number</b>	<b>Type of sample</b>	<b>Analysis carried out</b>	<b>Outcrop</b>
S24 T	Sandstone	Whole rock geochemistry, thin section and petrophysical analysis	Taman Awam Outcrop
S25 T	Mudstone	Whole rock geochemistry	Taman Awam Outcrop
S26 B	Sandstone	Thin section, SEM and petrophysical analysis	Taman Awam Outcrop
S26T	Sandstone	Whole rock geochemistry, thin section and petrophysical analysis	Taman Awam Outcrop
S29 B	Sandstone	Thin section, SEM and Petrophysical analysis	Taman Awam Outcrop
S29 T	Sandstone	Whole rock geochemistry and thin section analysis	Taman Awam Outcrop
S31	Mudstone	Whole rock geochemistry	Taman Awam Outcrop
S32 T	Sandstone	Whole rock geochemistry, thin section, SEM and petrophysical analysis	Taman Awam Outcrop
T1 B	Sandstone	Thin section and petrophysical analysis	Tajung Lobang
T1 T	Sandstone	Whole rock geochemistry, thin section, SEM and petrophysical analysis	Tajung Lobang
T2 B	Sandstone	Petrophysical analysis	Tajung Lobang
T2 T	sandstone	Whole rock geochemistry, thin section, SEM, XRD and petrophysical analysis	Tajung Lobang
T3 B	Sandstone	Petrophysical analysis	Tajung Lobang
T3 T	Sandstone	Whole rock geochemistry, thin section, SEM and petrophysical analysis	Tajung Lobang

**Table 7.10 2: Details of sample type, analysis conducted and total number of samples collected in each outcrop.**

<b>Hospital Outcrop</b>			
Analysis/Rock Type	Sandstones	Mudstones	Total Samples Collected
Petrography	7	1	<b>23 samples</b>
Geochemistry	7	4	
Petrophysics	8	-	
SEM	4	-	
XRD	1	-	
<b>Bomba Outcrop</b>			
Petrography	3		<b>12 samples</b>
Geochemistry	4	1	
Petrophysics	3	-	
SEM	2	-	
XRD	1	1	
<b>Taman Awam Outcrop</b>			
Petrography	15	1	<b>43 samples</b>
Geochemistry	10	6	
Petrophysics	14	-	
SEM	8	8	
XRD	1	1	
<b>Tanjung Lobang Outcrop</b>			
Petrography	4	-	<b>6 samples</b>
Geochemistry	3	-	
Petrophysics	6	-	
SEM	3	-	
XRD	1	-	

Detail of sample collection location and analysis conducted are represented in Fig. 4.1B, 4.3B, 4.5B and 4.7B.